# Effective interactions, structure and dynamics in charge-stabilized suspensions of impermeable and solvent-permeable particles

Inaugural-Dissertation

zur Erlangung des Doktorgrades
der Mathematisch-Naturwissenschaftlichen Fakultät
der Heinrich-Heine-Universität Düsseldorf

vorgelegt von

**Mariano E. Brito**
aus Cordoba, Argentinien

Düsseldorf, November 2020

aus dem Institute of Biological Information Processing (IBI-4)
Forschungszentrum Jülich GmbH

Gedruckt mit der Genehmigung der
Mathematisch-Naturwissenschaftlichen Fakultät der
Heinrich-Heine-Universität Düsseldorf

Referent: Prof. Dr.Gerhard Nägele

Koreferent: Prof. Dr. Jürgen Horbach

Tag der mündlichen Prüfung: 10.12.2020

# Abstract

In this thesis, we present a comprehensive theoretical study of effective colloidal interactions and related thermodynamic, structural, and dynamic properties of suspensions of charged, spherical colloidal particles suspended in an aqueous electrolyte solution. Two important classes of charge-stabilized particulate systems in the fluid phase state are investigated. Firstly, impermeable rigid colloidal particles constituting a generic model for aqueous suspensions of synthetic (e.g., polystyrene and silica) micro-spheres, and secondly ion- and solvent-permeable soft particles used as a model for suspensions of ionic microgels having a state-dependent size.

For both classes of suspensions, effective interaction potentials for pairs of microion-dressed colloids are derived using mean-field methods based, respectively, on Poisson-Boltzmann density functional theory, linear response theory and a multi-ion-species Ornstein-Zernike integral equation scheme. In averaging out the microionic degrees of freedom, a so-called volume energy contribution to the osmotic suspension pressure is obtained, and shown to be important at lower ionic strengths. Different thermodynamic routes for calculating the suspension pressure and osmotic compressibility are explored and compared, for suspensions in Donnan osmotic equilibrium with an electrolyte solution reservoir. On basis of a generalized virial equation, we analyze how the pressure is affected by the concentration dependence of the effective pair potential.

Using the derived effective pair potentials in conjunction with the thermodynamically self-consistent Rogers-Young integral equation method, static properties are calculated including the colloidal structure factor and radial distribution function. For strongly charged colloids where counterion condensation takes place, renormalized values are used for the colloid charge and electrostatic screening parameter entering the effective pair potential. We thoroughly analyze, and partially extend, the most commonly used renormalization methods and assess their respective performance in a broad range of suspension parameters. We demonstrate that good agreement with structural and pressure data from elaborate multi-component Monte-Carlo simulations is achieved when charge renormalization effects are properly accounted for. While counterion condensation always results in a renormalized colloid charge smaller than the bare one, we show that and explain why, for large concentration and small value of the bare charge, an effective charge larger than the bare one is observed. This peculiar effect can play a role in concentrated solutions of globular proteins.

The renormalized effective pair potentials and associated pair distribution functions are additionally employed in our semi-analytic calculations of dynamic properties where the solvent-mediated colloidal hydrodynamic interactions are accounted for. The studied properties include the hydrodynamic function, quantifying the influence of hydrodynamic interactions on short-time diffusion over different length scales, and the high-frequency and zero-frequency suspension viscosities.

Regarding our model for ionic microgels, two mean-field methods of calculating the crowding-dependent microgel radius are investigated, and their pros and cons assessed. We show that the counterion-induced deswelling of non-overlapping microgels enhances diffusion and the osmotic pressure, lowers the suspension viscosity, and significantly shifts the suspension crystallization point to larger concentrations.

The thesis provides a versatile toolbox of state-of-the-art, bottom-up methods for efficiently computing thermodynamic, structural and dynamic properties of suspensions of permeable and impermeable charged colloidal particles, using the single-particle characteristics.

# Zusammenfassung

Die vorliegende Dissertation beinhaltet eine umfassende theoretische Untersuchung von effektiven kolloidalen Wechselwirkungen und den daraus hervorgehenden thermodynamischen, strukturellen und dynamischen Eigenschaften von Suspensionen geladener kolloidaler Teilchen suspendiert in einer wässrigen Elektrolytlösung. Dazu untersuchen wir zwei wichtige Gruppen von ladungsstabilisierten kolloidalen Partikelsystemen im fluiden Phasenzustand. Zum einen sind dies harte, impermeable sphärische Teilchen, welche als generisches Modell für wässrige Suspensionen von synthetischen Mikroteilchen dienen, realisiert u.a. in Form von Polystyrol- und Silicapartikeln. Zum anderen untersuchen wir ionen-und lösungsmittelpermeable weiche Teilchen als ein Modellsystem für ionische Mikrogelteilchen, welche einen variablen, zustandsabhängigen Durchmesser aufweisen.

Für beide Gruppen von Suspensionen leiten wir effektive Wechselwirkungspotentiale für kolloidale Quasiteilchen, zusammengesetzt aus den nackten Teilchen und ihren neutralisierenden ionischen Ladungswolken, her. Dazu verwenden wir mittlere Feldtheoriemethoden basierend auf der Poisson-Boltzmann Dichtefunktionaltheorie, der linearen Antworttheorie und einer mehrkomponentigen Ornstein-Zernike Integralgleichungsmethode für ionische Mischungen. Als Folge der Integration über die mikroionischen Freiheitsgrade ergibt sich ein Beitrag zum osmotischen Suspensionsdruck, welcher sich aus einer sog. Volumenenergie ableitet. Wir zeigen, dass dieser Druckbeitrag wichtig ist für kleine Ionenstärken. Weiterhin analysieren wir unterschiedliche thermodynamische Zugänge für die Berechnung des Drucks und der osmotischen Kompressibilität einer Suspension im osmotischem (Donnan) Gleichgewicht mit einem Elektrolyt-Reservoir. Auf der Grundlage einer verallgemeinerten Virialgleichung analysieren wir, wie sich die Konzentrationsabhängigkeit des effektiven Paarpotentials auf den Systemdruck auswirkt.

Unter Verwendung der effektiven Paarpotentiale in Verbindung mit der thermodynamisch selbstkonsistenten Rogers-Young Integralgleichungsmethode berechnen wir statische Suspensionseigenschaften einschließlich dem kolloidalen statischen Strukturfaktor und der radialen Verteilungsfunktion. Die Gegenionenkondensation für hochgeladene Kolloidpartikel wird dabei berücksichtigt durch die Verwendung einer renormierten Kolloidladung und eines renormierten elektrostatischen Abschirmparameters in dem effektiven Paarpotential. Dazu untersuchen und verallgemeinern wir die am häufigsten verwendeten Renormierungsmethoden. Ihre Vor- und Nachteile diskutieren wir für einen breiten Parameterbereich. Wir zeigen, dass strukturelle Daten und der Systemdruck, erhalten aus aufwändigen, mehrkomponentigen Monte-Carlo Simulationen, gut reproduziert werden bei Verwendung einer geeigneten Renormierungsmethode. Während Gegenionenkondensation stets eine renormierte Ladung kleiner als die nackte Kolloidladung bedingt, ist das Gegenteil der Fall für die effektive

Ladung in einer konzentrierten Suspension schwach geladener Teilchen. Letzteres kann von Bedeutung sein für konzentrierte Lösungen globularer Proteine.

Die renormierten effektiven Paarpotentiale und zugehörigen Paarverteilungsfunktionen gehen zusätzlich ein in unsere semi-analytische Berechnung dynamischer Suspensionseigenschaften unter Berücksichtigung der durch das Lösungsmittel vermittelten hydrodynamischen Wechselwirkungen zwischen den Kolloiden. Wir studieren hier insbesondere die hydrodynamische Funktion, welche den Einfluss der hydrodynamischen Wechselwirkungen auf die Kurzzeitdiffusion bei unterschiedlichen Längenskalen beschreibt, sowie die Hochfrequenz- und statische Viskosität.

Im Rahmen unseres Modells für ionische Mikrogele verwenden und vergleichen wir zwei mittlere Feldtheoriemethoden für die Bestimmung des konzentrationsabhängigen Mikrogelradius. Wir zeigen, dass das durch Gegenionen induzierte Abschwellen nicht überlappender ionischer Mikrogele zu einer Erhöhung der Teilchendiffusion, Abnahme der Viskosität sowie einer deutlichen Verschiebung des Kristallisationspunkts hin zu größeren Konzentrationen führt.

Die vorliegende Dissertation stellt einen Fundus an vielseitig einsetzbaren bottom-up Methoden bereit, mit welchen sich thermodynamische, strukturelle und dynamische Eigenschaften von Suspensionen geladener permeabler und impermeabler Teichen effizient berechnen lassen, bei Verwendung der Einzelteilchencharakteristiken.

# Preface

The work presented in this thesis is partially published in a peer-reviewed international journal or in preparation. In the following, I list the publications, specify my personal contributions therein and denote where a specific publication is used in the thesis.

- **Modeling deswelling, thermodynamics, structure, and dynamics in ionic microgel suspensions**

  M. E. Brito, A. R. Denton and G. Nägele. *J. Chem. Phys.* **151**, 224901 (2019).

  The content of the publication was obtained in collaboration with A. R. Denton from North Dakota State University, USA. On basis of theoretical methods developed partially by A. R. Denton and G. Nägele, I performed all semi-analytic calculations and the data analysis, supported by helpful discussions with G. Nägele and A. R. Denton. The article was jointly written by me and G. Nägele. The content of this article is used in Subsec. 2.4.2 and Chapters 4 and 6.

- **Comparison of different methods for calculating effective colloidal charge, effective screening parameter and suspension osmotic pressure**

  M. E. Brito, J. Riest, A. R. Denton and G. Nägele. To be submitted (2021).

  Utilizing theoretical methods developed by A. R. Denton in conjunction with semi-analytic methods by J. Riest and G. Nägele, I did most of the calculations and data analysis with helpful discussions contributed by G. Nägele and A. R. Denton. The manuscript was written by me with some help by G. Nägele and A. R. Denton. The content of this article is used in Subsec. 2.4.3 and Chapters 3 and 7.

- **Effective electrostatic interactions in suspensions of surface-charged ionic microgels**

  M. E. Brito, M. O. Alziyadi, G. Nägele and A. R. Denton. To be submitted (2021).

  I have developed one of the theoretical models presented in this work and performed an important part of the data analysis, with helpful discussions contributed by G. Nägele and A. R. Denton. Part of the content of this work is used in Subsec. 2.4.3 and Chapter 8.

Additional publication by the author:

- **Self-assembly of pseudo-dipolar nanoparticles at low densities and strong coupling**

  M. E. Brito, M. A. Carignano and V. I. Marconi. *Sci. Rep.* **10**, 3971 (2020).

Previous thesis by the author:

- Diploma thesis: **Dipolar colloidal systems: Phases, dynamics of gelation and structural characterization**

  Supervisor: Prof. Dr. V. I. Marconi. Faculty of Mathematics, Astronomy, Physics and Computation, National University of Cordoba, Argentina, 2013.

# CONTENTS

**APPENDIX**

# Chapter One

# INTRODUCTION

Soft matter systems are widely present in our daily life. We can find them in products such as food, paints, inks, cosmetics, emulsions, foams and aerosols, as well as in many biological systems such as blood, protein solutions and the cytoplasm of cells. They are thus of great biological and medical importance, and have vast industrial applications. The soft mechanical nature of these systems is due the fact that their internal states can be easily modified by applying energy of the order of the thermal fluctuations. The rigidity of soft matter against mechanical deformations is hence many orders of magnitude smaller than that of atomic systems [1]. The softness is related to the mesoscopic size of the constituents and the types of interactions among them.

Since under standard ambient temperature and pressure conditions, a large variety of soft matter systems are in the liquid phase, a thorough theoretical understanding of the properties of fluids is of great importance. Differently from simple liquids, where one deals with one-component atomic or low-molecular systems of constituents typically with spherical symmetry and interacting via radially-symmetric (approximately) pairwise-additive potentials, fluid soft matter systems are “complex”. That is, they are solutions or suspensions which, owing to the large variety of constituent particles, are usually multi-component systems with complex many-body interactions.

An important subgroup of complex fluids are colloidal suspensions. These are suspensions of solid or liquid particles, in the size range from a few nanometers to tens of micrometers, dispersed in a low-molecular solvent such as water. The particles undergo Brownian motion, driven by the thermal agitation of the solvent molecules [2]. The intricate coupling among the colloidal particles and solvent brings about that changes in solvent quality, temperature, concentration of dissolved salt ions and pH can lead to very pronounced changes in the effective interactions between the suspension components, making these systems ideal for studying phase transitions [1]. In particular, the time scales for the phase changes are much slower than in atomic systems, allowing for an in-depth study of these changes. From an experimental point of view, the large size difference between colloidal particles and, in comparison, small solvent molecules allows to study the structural ordering and dynamics of the colloids by performing static and dynamic light scattering experiments using visible laser light [3], and direct observation of their real-space motion by means of video microscopy for larger particles [4]. Different from purified biological solutions, synthetic colloids are commonly polydisperse in size and interaction. Polydispersity tends to suppress crystallization as compared to a putative monodisperse suspension of same mean density and temperature [1].

Another important aspect of fluid-phase colloidal suspensions is their stabilization. Colloidal particles of same kind always experience an attractive so-called van der Waals force, caused by induced electromagnetic dipole-dipole interactions between the many atoms constituting the colloidal particles [2]. The attractive (effective) van der Waals potential tends to diverge as the particles come into contact. It decays as $r^{-6}$ for intermediate particle separations and, due to electromagnetic retardation effects, as $r^{-7}$ for very large distances [5]. Near to two-particles contact, van der Waals attraction combined with Born repulsion, the latter caused by overlapping of the atomic electronic clouds, gives rise to a deep potential minimum near contact, which can drive irreversible flocculation. To avoid this, stabilization mechanisms are needed providing an additional inter-particle repulsion. There are two major stabilization mechanisms, namely charge stabilization and steric stabilization, respectively.

Throughout this thesis, we focus on charge-stabilized suspensions of different kinds. These suspensions consist of colloidal particles (macroions) carrying ionizable chemical groups, suspended in a polar low-molecular solvent such as water [6]. The dissociation of so-called counterions from these functional groups into the solvent results in charged colloids with their charge sites located on their surfaces and/or in their interiors. Additionally to the particle-released counterions, there are commonly solvent-dissolved counter- and coions (microions). An electric double layer results from the buildup of an inhomogeneous mobile cloud of microions around each colloid, which carries a charge of opposite sign to that of the colloidal particles and tends to screen their electrostatic potential [6]. The overlap of the double layers of two colloids approaching each other leads to a repulsive force which stabilizes the particles against aggregation [5]. In case of solvent-permeable particles such as ionic microgels, the microion cloud extends also into the particle interior, where it can affect the equilibrium particle size.

In this thesis, we study theoretically the interactions in different fluid-phase, charge-stabilized dispersions formed by spherical charged colloids of different architecture, that coexist with the ions dissolved in a polar solvent. Two representative types of charge-stabilized suspensions are considered. The first one consists of impermeable rigid colloidal spheres, which are strongly charged on their surfaces, so nonlinear charge renormalization effects are operative. Examples that have been widely studied experimentally are aqueous suspensions of polystyrene and silica micro-spheres. As part of this thesis, different mean-field charge renormalization methods are investigated and compared, together with an assessment of their implications on structure, thermodynamics and dynamics. The second type are suspensions of weakly cross-linked spherical ionic microgel particles, which are permeated by the solvent and the microions. The electric repulsion of the cross-linked polyelectrolyte network forming the elastic "backbone" of a microgel particle is screened by dissolved counterions accumulated inside (and outside) its backbones. The delicate interplay of nonelectrostatic, elastic-entropic forces, tending to limit the microgel size, and electrostatic-entropic forces, tending to expand the size, give rise to a state-dependent mean particle size depending on temperature, pH, backbone charge, ionic strength and microgel concentration. In this thesis, the peculiar concentration dependence of ionic microgels and its impact on thermodynamics, structure and dynamics of microgel suspensions are explored in great detail. Standard experimental examples of ionic microgels, where a strong deswelling with increasing microgel concentration is observed, are aqueous suspensions of weakly cross-linked PNIPAM (Poly N-isopropylacrylamide) particles [7]. The multiresponsive character of the soft microgel systems allows for various industrial and biomedical applications, including drug-delivery vehicles, sensors, tunable microreactors and switchable membranes. Suspensions of hard- and impermeable charge-stabilized particles of practical and biological relevance are, among many others, aqueous paints and protein solutions.

Using the effective colloidal pair potentials derived and discussed in the thesis for charge-stabilized suspensions of rigid impermeable spheres and of soft ionic microgels, repectively, thermodynamic and equilibrium microstructural properties are calculated. These properties include the osmotic pressure and compressibility for a suspension in Donnan equilibrium with a salt reservoir, and colloidal pair distribution and static structure functions. For the latter functions, state-of-the-art integral equation methods are used and their results compared with simulation data. The pair distribution and static structural functions of the charged colloidal particles are employed, in turn, for the calculation of equilibrium and dynamic properties including wavenumber-dependent diffusion functions, and zero- and high-frequency suspension viscosities. The semi-analytic methods used in these calculations account for the solvent-mediated hydrodynamic interactions (HIs) between the particles, and for hydrodynamic solvent penetration effects inside the solvent- and microion-permeable microgels. In analyzing the inter-colloid interactions, we take advantage of the large size- and charge asymmetries between the big colloidal particles and the small microions and solvent molecules by tracing-out the degrees of freedom of the latter ones. This leads us to the determination of an effective Hamiltonian describing the microion- and solvent-averaged effective interaction between colloidal pseudo-particles, in the framework of an equivalent one-component picture. We restrict our analysis to monovalent microions where their correlations can be approximately disregarded, allowing thus for a mean-field treatment. By using different mean-field descriptions of the microion species, we derive the effective electrostatic colloidal pair potential and the so-called volume energy terms for the two considered hard- and soft particle systems.

For the impermeable hard colloids, the effective interaction between the pseudo-colloids is given by the standard double-layer DLVO (Derjaguin-Landau-Verwey-Overbeek) potential, with a renormalized effective colloid valence and screening parameter provided charge renormalization is operative. One target of our study is to assess when nonlinear effects causing charge renormalization become relevant in concentrated suspensions of strongly charged particles. Charge renormalization consists of introducing a renormalized effective macroion charge number (valence), $Z_{\text{eff}}$, which is different from the bare one $Z$, and a renormalized screening parameter, $\kappa_{\text{eff}}$, in the DLVO potential, quantifying hereby nonlinear screening effects. There are different charge-renormalization methods described in the current literature, providing in general different values for the renormalized interaction parameters, $Z_{\text{eff}}$ and $\kappa_{\text{eff}}$, in dependence of the bare interaction parameters $Z$ and $\kappa$ of a system. We have thoroughly analyzed, and partially extended, a selection of the most-commonly used charge renormalization methods, and have assessed their performance and applicability in a broad parameter range: from strongly to weakly charged particles, and from low to high ionic strengths. We have assessed the performance of the different methods by determining structural and thermodynamic properties from the respective effective pair potentials, in comparison with elaborate primitive-model (PM) simulations [8]. Our evaluation of different charge-renormalization schemes is helpful for the selection of reliable theoretical tools, e.g., for the interpretation of light, x-ray and neutron scattering data of charge-stabilized suspensions of impermeable particles.

Regarding solvent- and ion-permeable soft colloids, we determine the electrostatic contribution to the effective colloid interaction potential using a PM-based Ornstein-Zernike (OZ) integral equation scheme with linear mean spherical closure [9], and contrast with the equivalent linear response theory (LRT) prediction for the case of a uniform backbone charge distribution [10–12]. From the effective electrostatic interaction potential between permeable macroions taken together with an elastic Hertz potential and a Flory-Rehner free energy contribution, we compute the state-dependent equilibrium size of the microgels. Following earlier work by Denton *et al.* [10, 13–15], we model hereby the ionic microgels in a coarse-grained way as microion- and solvent-permeable, monodisperse elastic colloidal spheres, with the charged sites on the cross-linked polymer-gel backbone summarily described by a uniform charge distribution. This description is reasonable, under the proviso that the cross-linker density does not vary strongly along the microgel particle radius. We describe the elastic and solvent-interaction free energy contributions of a microgel using Flory-Rehner theory [16–18] for a likewise uniform cross-linker distribution.

For calculating the electrostatic semi-grand free energy contribution of microgels in a concentrated suspension, in Donnan equilibrium with a electrolyte reservoir, we use two different mean-field methods: First, the spherical Poisson-Boltzmann cell model (PBCM) approach of Denton and Tang [14], and second, a first-order thermodynamic perturbation theory (TPT) method of Weyer and Denton [15] based on a multi-colloid-center linear-response approach. The equilibrium microgel radius is obtained from minimizing the total suspension semi-grand free energy, which is equivalent to enforcing the balance of the total (intrinsic) pressure inside and outside a microgel. In combination with the derived effective electrostatic pair potential expression for ionic microgels and the volume energy expression in LRT [13], we explore thermodynamic, dynamic and equilibrium microstructural properties of fluid-phase suspensions of ionic microgels in the swollen state. While being of interest in their own right, microstructural properties such as the radial distribution function and static structure factor are also required as input in our calculation of dynamic suspension properties, including generalized sedimentation and collective diffusion coefficients, and the high-frequency and zero-frequency viscosities.

The calculation of the structural suspension properties is done in the framework of OZ integral equations using the hypernetted chain (HNC) and thermodynamically self-consistent Rogers-Young (RY) closures [19].

The resulting macroion pair distribution function is then used as input to our calculations of dynamic suspension properties, such as the hydrodynamic function. For the calculation of short-time dynamic properties, we employ as semi-analytic methods the pairwise-additivity (PA) approximation of HIs and the Beenakker-Mazur (BM) mean-field method. The good performance of these methods has been established earlier, by comparison with elaborate dynamic computer simulations, for a variety of colloidal model systems describing globular proteins, impermeable charge-stabilized colloids, and non-ionic spherical microgels [20–24]. The methods account for the salient hydrodynamic particle interactions mediated by the intervening solvent flow. To obtain long-time dynamic properties such as the zero-frequency viscosity, we implement a simplified mode-coupling theory (MCT) method for computing memory (stress relaxation) contributions.

The thesis is organized as follows. In chapter 2, we explain how the effective one-component Hamiltonian and the effective colloidal interaction potential are derived from mapping the original multi-component system onto an effective one-component system of pseudo-macroions. We present different mean-field methods for the derivation of the electrostatic part of the effective macroion pair potential for both ion- and solvent-permeable, and impermeable charged macroions. These methods are based on three different formulations: first, a density functional theory, second a linear response theory, and third a (linear) multi-species Ornstein-Zernike (OZ) integral equation scheme. All three methods start from a PM-type description, where the microions are treated as pointlike and the solvent is described as a structureless dielectric Newtonian fluid characterized by a uniform dielectric constant $\varepsilon$ and shear viscosity $\eta_0$. The three methods are modified and used also in our derivation of the effective pair potential of ion-permeable macroions.

In chapter 3, we introduce the employed charge-renormalization schemes, namely: single-colloid-center cell-models and renormalized jellium models; and multi-colloid-center renormalized linear response theory (RLRT) and shifted Debye-Hückel approximation (SDHA).

In chapter 4, we describe how mechanical features of microgels are modeled and introduce the methods for modeling the concentration-dependent deswelling of ionic microgels. We briefly describe the Hertz potential and Flory-Rehner theory for modeling the polymeric nature of the ionic microgels. Moreover, we introduce both the Poisson-Boltzmann cell model (PBCM) method and the thermodynamic perturbation theory (TPT) method for the calculation of the microgel equilibrium size.

Chapter 5 summarizes the methods used for the calculation of structural, thermodynamic and dynamic properties. We define the structural properties, namely colloidal pair distribution function and structure factor, and thermodynamic properties such as the suspension pressure and osmotic compressibility, together with their calculation methods based on the effective macroion pair potential. In particular, we discuss hypernetted chain (HNC), Perkus-Yevick (PY) and Rogers-Young (RY) integral equation schemes. We further discuss short-time dynamic properties including the hydrodynamic function, concentration-dependent diffusion function, sedimentation velocity, collective diffusion coefficient and high-frequency viscosity, in conjunction with the corresponding calculation methods that involve the pairwise-additivity (PA) approximation and the Beenakker-Mazur (BM) methods. Regarding long-time dynamic properties, we discuss the zero-frequency suspension viscosity and present a simplified MCT method for its calculation.

In chapter 6, we report our comprehensive theoretical study of concentration-dependent deswelling effects on thermodynamic, structural, and dynamic properties of weakly cross-linked ionic microgels dispersed in a good solvent. We scrutinize PBCM and TPT methods for determining the equilibrium microgel size. They are used in a second step to analyze the effect of microgel deswelling on the effective microgel interactions. By comparison with a (fictitious) reference suspension of constant-size microgels, we assess the impact that deswelling has on structural as well as on diffusion and rheological suspension properties.

In chapter 7, we finally assess the performance of charge renormalization schemes. To this end, we compare first the different predictions of the effective interaction parameters to assess the pros and cons of each considered method. We analyze next the performance of the different renormalization schemes by comparing the resulting predictions for the pair structure and thermodynamic suspension properties with those from earlier PM-based Monte Carlo (MC) simulations. In particular, a detailed analysis of the suspension pressure is provided, wherein we discuss the importance of the different pressure contributions arising from the renormalized, concentration-dependent effective macroion pair potential.

We conclude the thesis with chapter 8, where we summarize and value the main results of the thesis, and discuss possible future extensions.

In the appendixes A and B, we give salient details about PA and BM methods, respectively, for calculating dynamic suspension properties. Moreover, in appendix C, we explain how the suspension pressure is calculated in RLRT using a general virial equation.

# Chapter Two

# EFFECTIVE INTERACTIONS OF IMPERMEABLE AND PERMEABLE COLLOIDS

In this chapter, we present the general framework for deriving the effective interaction potential of dressed, (pseudo-)colloidal particles. In this framework, the microionic degrees of freedom are integrated out, resulting in an effective one-component suspension of microion-dressed colloidal particles interacting by an effective potential, where the electrostatic screening by the microions is accounted for. We start with a brief description of the primitive model, where all ionic species are treated on equal footing as isotropically charged hard spheres, immersed in a structureless dielectric solvent. We later focus on a mean-field, analytic derivation of the effective colloid-colloid interaction potential and volume (grand-free) energy both for hard ion-impermeable and soft ion-permeable charge-stabilized colloids. In addition to employing density functional theory and linear response theory methods, we derive an effective colloid interaction potential using an Ornstein-Zernike (OZ) integral equation scheme applied to soft, ion-permeable colloids.

## 2.1 Effective one-component models

Charge-stabilized (monodisperse) colloidal suspensions consist of different ionic species, which significantly differ in terms of their charges and sizes from one another, i.e., large multivalent colloidal macroions and small (hydrated) counter- and coions, the latter collectively addressed as microions. The ion species are typically suspended/dissolved in a low-molecular, polar solvent such as water.

In many theoretical investigations of charged-stabilized colloidal systems, the solvent is treated as a structureless continuum, statically characterized by its macroscopic dielectric constant $\epsilon$ and hydrodynamically modeled as a Newtonian fluid with shear viscosity $\eta_0$. This is commonly amended by a generalized Primitive Model (PM) level of description, where the different ionic species are described on equal level as isotropically-charged (hard) spheres, interacting by Coulombic forces [6]. In the PM, the dielectric mismatch between solvent-impermeable (macro-)ions and solvent is disregarded, namely there are no induced polarization charges [25], and it is assumed that the internal charge distribution of a spherical microion follows rigidly the sphere motion. This is likewise assumed in case of solvent- and microion permeable colloidal spheres, i.e. intra-particle effects and external electrokinetic are disregarded. Without external electric fields or strong imposed flow, electrokinetic effects are typically quite small. While interesting from a theoretical viewpoint, electrokinetic effects are not considered in this thesis.

The PM has been widely applied for quantifying ionic correlations in charge-stabilized systems using elaborate computer simulations, in particular for charge and diameter asymmetries up to about 1:100 [8, 26–28], corresponding to micellar and protein systems, and, furthermore, for charge and diameter ratios up to 1:250 and 1:500 respectively, describing colloidal suspensions of moderately-charged and sized macroions [29]. Numerical solutions of specific OZ integral equation schemes, such as the hypernetted chain scheme, have allowed to treat asymmetries in size and charge as large as 1:1000 [29]. The analysis of larger asymmetries, and a detailed exploration of salt-variation effects, where at least three ionic species are involved, is still a challenging task using numerical methods. However, largely-asymmetric systems admit a great simplification by tracing out the degrees of freedom associated with the small microions in the suspension, resulting in an effective one-component system of dressed macroions, which is governed by an effective Hamiltonian that describes the effective interactions between the remaining (large) particles. The resulting effective interactions account not only for the direct interactions between the macroions but also for the induced effects of the solvent, counterions, salt ions and cross-linked polymer chains in case of ionic microgels [1]. Even when all direct interactions among the original species are strictly pairwise additive (as in the PM), the effective interactions can still include many-body contributions and depend on the thermodynamic state of the system [30]. The density dependence of the effective pair potentials is analyzed in detail in this thesis.

The advantage of working with effective interactions lies not only in the theoretical simplifications that allows for using well-developed theoretical tools adapted from the theory of simple liquids. Effective colloidal interactions are especially valuable in calculating materials properties of soft matter systems, such as viscosity and diffusion properties, and in studying their thermodynamic behaviour. They constitute the essential input to molecular simulation studies and statistical mechanical theories [30]. The effective one-component description also allows to make direct contact with experiments probing static and dynamical properties of the large colloidal particles only. Having the effective interactions between the (dressed) colloids at disposal permits the computation of structural properties such as the colloid-colloid static structure factor, which is obtained from light scattering, small-angle neutron or x-ray scattering, depending on the colloidal sizes [3].

Another important quantity arising from mapping a multi-component system onto an effective one-component one is the so-called volume (grand-free) energy term. This contribution to the effective Hamiltonian is independent of the colloidal coordinates (and momenta). The expectation value of any operator depending on these coordinates only, such as the static structure factor, is unaffected by the volume energy [1]. In suspensions of neutral colloidal particles such as PMM spheres in an organic solvent, the volume energy does in general not affect the phase behavior [31]. However, in the case of charge-stabilized systems at low salinity, the volume term depends significantly on the concentration of the colloids due to the overall electroneutrality constraint, rendering it relevant when studying the suspension thermodynamics and phase behaviour [1, 32, 33].

In the following, we introduce the generalized PM and present the derivation of the effective colloid pair interaction and volume energy term, using linearized Poisson-Boltzmann-type mean-field approximations both for ion-permeable and ion-impermeable colloids. We focus hereby on the following methods: density functional theory, linear response theory and a multi-ion species OZ integral equation scheme with linear (mean-spherical approximation) closure relations. To obtain explicit analytic results, the microions are treated for simplicity as pointlike and monovalent. The assumed monovalency allows for neglecting inter-microion correlation effects. Under appropriated conditions, the latter can trigger microion-pairing and macroion charge reversal in case of non-monovalente microions [34–36].

## 2.2 Generalized primitive model of ionic mixtures

Systems like dispersions of charge-stabilized spherical colloids, globular protein solutions and electrolyte solutions can be described by the so-called generalized Primitive Model (PM). In this simplified model, all ions are treated on equal footing as isotropically-charged (Brownian) spheres, interacting by Coulomb plus excluded volume or, in case of ionic microgels, elastic forces. All ions are immersed in a structureless dielectric and Newtonian solvent. Specific properties of the solvent are neglected except for its static dielectric constant $\epsilon$ and its shear viscosity $\eta_0$. As already stated above, we neglect image-charge effects that can give rise to many-body dielectric interactions, caused by differences in the dielectric properties of the ions/colloids and the solvent.

Consider a PM system consisting of three different ion species, with each species formed by $N_\alpha$ monodisperse spherical particles of radius $a_\alpha$, mass $m_\alpha$ and valence $z_\alpha$ immersed in a macroscopic suspension of volume $V$, with $\alpha = 0, 1, 2$. The system Hamiltonian can be expressed in the general form,

$$\mathcal{H} = H_{00} + H_{11} + H_{22} + H_{01} + H_{02} + H_{12} + H_{\mathrm{m}}, \tag{2.1}$$

where $H_{\alpha\alpha}$ is the Hamiltonian of the individual ion species $\alpha$, i.e.

$$H_{\alpha\alpha}(\{\mathbf{r}_\alpha^{N_\alpha}\}) = K_\alpha + \sum_{i<j}^{N_\alpha} u_{\alpha\alpha}(\mathbf{r}_{ij}). \tag{2.2}$$

Here, species $\alpha = 0$ is identified with the large colloidal macroions. The first term on the right-hand side of Eq. (2.2) is the kinetic energy,

$$K_\alpha = \frac{1}{2} \sum_{i=1}^{N_\alpha} m_\alpha \, \mathbf{p}_{\alpha\, i}^2, \tag{2.3}$$

where $\mathbf{p}_{\alpha\, i}$ is the momentum of the $\alpha$-type ion $i$. The second term is the potential energy due to the interaction between particles of the same species $\alpha$ described by the bare pair potential $u_{\alpha\alpha}(\mathbf{r}_{ij})$, with $\mathbf{r}_{ij} = \mathbf{r}_i - \mathbf{r}_j$, and $\mathbf{r}_i$ denoting the center position of the $i$th $\alpha$-type particle. $H_{01}$, $H_{02}$ and $H_{12}$ in Eq. (2.1) correspond to the potential energies due to the bare interactions between particles of different species $\alpha \neq \beta$, i.e.

$$H_{\alpha\beta} = \sum_{i=1}^{N_\alpha} \sum_{i<j}^{N_\beta} u_{\alpha\beta}(\mathbf{r}_{ij}). \tag{2.4}$$

For soft colloidal macroions, which are penetrated by solvent and microions, such as weakly cross-linked ionic microgels, there is an additional contribution, $H_{\mathrm{m}}$, arising from the self-energy of the macroions, which can affect their equilibrium size and hence their effective interactions. More specifically, the (total) system Hamiltonian accounts for the electric and steric pair interactions between all dispersed ions. The pair-interaction potential between two impermeable, hard PM ions of species $\alpha$ and $\beta$, with hard-core radii $a_\alpha$ and $a_\beta$, respectively, whose center distance is $r$, is of the form $u_{\alpha\beta}(r) = u_{\alpha\beta}^{\mathrm{hs}}(r) + u_{\alpha\beta}^{\mathrm{C}}(r)$. Here, $u_{\alpha\beta}^{\mathrm{hs}}(r)$ is the excluded volume (hard-sphere) pair potential,

$$u^{\mathrm{hs}}_{\alpha\beta}(r) = \begin{cases} \infty\,, & r < a_\alpha + a_\beta \\ 0\,, & \text{otherwise} \end{cases} \tag{2.5}$$

and $u^{\mathrm{C}}_{\alpha\beta}(r)$ is the Coulomb pair potential,

$$\frac{u^{\mathrm{C}}_{\alpha\beta}}{k_B T}(r) = \lambda_{\mathrm{B}} \frac{z_\alpha z_\beta}{r}, \;\; r > a_\alpha + a_\beta, \tag{2.6}$$

where $\lambda_{\mathrm{B}} = e^2/k_{\mathrm{B}}T\epsilon$ is the Bjerrum length of the solvent, with $T$ the system temperature, $k_{\mathrm{B}}$ the Boltzmann constant and $e > 0$ the elementary proton charge. The Bjerrum length is a length scale for which the thermal energy is equal to the Coulombic energy between two unit charges . For water at room temperature, $\lambda_{\mathrm{B}} \approx 7.1$ Å. For ion-permeable colloidal particles, $u^{\mathrm{HS}}_{00}(r)$ is replaced, e.g., by the Hertz pair potential mimicking their elastic repulsion for small overlap. In equilibrium, the PM obeys the global electroneutrality condition

$$\sum_{\alpha=0}^{2} n_\alpha z_\alpha = 0 \tag{2.7}$$

where $n_\alpha = N_\alpha/V$ is the mean number density of species $\alpha$. The local electroneutrality condition in equilibrium reads

$$\sum_{\alpha=1}^{2} n_\alpha \, z_\alpha \int d\mathbf{r} \;\; [h_{0\alpha}(r) + 1] = -z_0 \tag{2.8}$$

for the macroion species 0, where $h_{0\alpha}(r)$ is the total pair correlation function for two ions of species 0 and $\alpha$. Here,

$$h_{\alpha\beta}(r) = g_{\alpha\beta}(r) - 1, \tag{2.9}$$

and $g_{\alpha\beta}(r)$ are the partial total and partial pair correlation functions of two ions of species $\alpha$ and $\beta$, respectively. Notice that $g_{\alpha\beta}(r)$ is the conditional probability of finding a $\beta$-type particle at distance $r$ from a given $\alpha$-type particle. The functions $h_{\alpha\beta}(r)$ and $g_{\alpha\beta}(r)$ are determined by the partial pair interaction potentials $u_{\alpha\beta}(r)$, which are symmetric, i.e. $u_{\alpha\beta}(r) = u_{\beta\alpha}(r)$. This symmetry is inherited by the partial static and dynamic pair correlation functions.

The PM is in the following our starting point for contracting out the microion degrees of freedom.

## 2.3 Effective Hamiltonian and effective pair potential

Consider a typical PM system consisting of a macroion species 0 and two microion species 1 and 2 where $a_0 \gg a_1, a_2$ and $z_0 \gg z_1, z_2$. By taking advantage of the large asymmetries, we can integrate out the degrees of freedom associated with microion species 1 and 2. Assuming that the PM system is in Donnan equilibrium with a large electrolyte reservoir of microions having (constant) electro-chemical potential $\mu_1$ and $\mu_2$, the total semi-grand free energy $\Omega$ is given by

$$\beta\Omega = -\ln \mathrm{Tr}_0\, \mathrm{Tr}_1\, \mathrm{Tr}_2\, e^{-\beta\mathcal{H}}, \tag{2.10}$$

with canonical trace over the colloidal macroions defined by

$$\mathrm{Tr}_0(\,\dots) := \int_V d\mathbf{p}^{N_0}\, d\mathbf{r}^{N_0}\,(\,\dots) \equiv \langle\,(\,\dots)\,\rangle_0 \tag{2.11}$$

and microion grand canonical trace

$$\mathrm{Tr}_\alpha(\,\dots) := \sum_{N_\alpha=0}^{\infty} \frac{\zeta_\alpha^{N_\alpha}}{N_\alpha!} \int_V d\mathbf{p}^{N_\alpha}\, d\mathbf{r}^{N_\alpha}\,(\,\dots) \equiv \langle\,(\,\dots)\,\rangle_\alpha \tag{2.12}$$

for $\alpha = 1, 2$. Here, $\zeta_\alpha = e^{\beta\mu_\alpha}/\Lambda_\alpha^3$ is the activity of $\alpha$-type microions with thermal de Broglie wavelength $\Lambda_\alpha = h/\sqrt{2\pi m_\alpha k_\mathrm{B} T}$, where $m_\alpha$ is the ion mass and $h$ the Planck constant. Separating the traces, one has

$$\beta\Omega = -\ln \mathrm{Tr}_0 \left[e^{-\beta(H_{00}+H_\mathrm{m})}\, \mathrm{Tr}_1 \mathrm{Tr}_2 \left[e^{-\beta(H_{11}+H_{22}+H_{01}+H_{02}+H_{12})}\right]\right] \equiv -\ln \mathrm{Tr}_0 \left[e^{-\beta H_\mathrm{eff}}\right]. \tag{2.13}$$

The effective Hamiltonian, $H_\mathrm{eff}$, of microion dressed colloids is defined here by

$$H_\mathrm{eff} = H_{00} + H_\mathrm{m} - k_\mathrm{B}T\, \ln \mathrm{Tr}_1 \mathrm{Tr}_2 \left[e^{-\beta(H_{11}+H_{22}+H_{01}+H_{02}+H_{12})}\right] \equiv H_{00} + H_\mathrm{m} + \Omega_\mu, \tag{2.14}$$

where $\Omega_\mu$ is the exact grand-free energy of microions in the external field of macroions at fixed positions $\mathbf{X} = \{\mathbf{R}_1, ..., \mathbf{R}_{N_0}\}$ of their centers. Capital letters are used henceforth for macroion position vectors. The effective Hamiltonian can be re-expressed as

$$H_\mathrm{eff} = E_\mathrm{vol} + \sum_{i<j}^{N_1} u_\mathrm{eff}(|\mathbf{R}_i - \mathbf{R}_j|; n_0) + ... \tag{2.15}$$

where $n_0$ is the colloid concentration. The first term, $E_{\mathrm{vol}}$, on the right-hand side is the volume energy, which is independent of the location $\mathbf{X}$ of the macroions. It can be interpreted as a cohesion energy of the system due to the presence of the microions. It does not affect the micro-structure of the suspension; however, it contributes to the suspension thermodynamics. The second term is the sum of effective pair interactions among the macroions. In principle, there are higher-order $n$-body effective interaction terms, which can be significant for strongly charged macroions at low salt content [37, 38]. The effective $n$-particle interaction potentials represent the interactions among the different $n$-tuples of macroions mediated by the microions.

Practical applications of Eq. (2.14) require approximating $\Omega_\mu$. We present two different methods of calculating $\Omega_\mu$ related to the Poisson-Boltzmann (PB) theory, which is a powerful mean-field approach for dealing with charge-stabilized suspensions having monovalent counterions only.

## 2.4 Mean-field Poisson-Boltzmann-type approximations

To obtain an explicit pairwise additive expression for the effective Hamiltonian, $H_{\mathrm{eff}}$, we focus on the particular case of negatively-charged multivalent macroions, in osmotic contact with a reservoir of monovalent cations and anions. Explicitly, species 0 consists of negatively-charged macroions, relabeled from now on as $0 \to \mathrm{m}$, and species 1 and 2 are microion species, relabeled $1 \to +$ and $2 \to -$ respectively, for notational convenience. The suspension including the $N_{\mathrm{m}}$ spherical microions of negative charge $-Ze$ is taken with water as the solvent in a volume $V$ at room temperature $T$. The strong 1:1 electrolyte reservoir, in Donnan equilibrium with the suspension, has the (fixed) microion concentration $2n_{\mathrm{res}}$ and microion chemical potential $\mu_{\mathrm{res}}$ for both species ($\pm$). It can be regarded to be linked to the suspension via an ideal membrane permeable to the microions and solvent only. The microion chemical potential in the reservoir is well approximated by the ideal form $\mu_{\mathrm{res}} = k_{\mathrm{B}}T \ln(\Lambda_0^3 n_{\mathrm{res}})$, assuming equal thermal de Broglie wavelength $\Lambda_0$ of the ± microions. The macroion concentration (number density), $n_\mathrm{m} = N_\mathrm{m}/V$, determines the volume fraction $\phi = 4\pi a n_\mathrm{m}/3$ of macroions of radius $a$. The suspension must fulfill the equilibrium electroneutrality constraint

$$ZN_\mathrm{m} = \langle N_+\rangle - \langle N_-\rangle, \tag{2.16}$$

where $N_\mathrm{s} = \langle N_-\rangle$ is the equilibrium number of monodisperse (salt) coions in the system, equal to the mean number $N_\mathrm{s}$ of salt ion pairs, and $\langle N_+\rangle$ is the equilibrium mean number of monovalent counterions, with $\langle ...\rangle$ denoting a grand-canonical average. The concentration (number density) $n_\mathrm{s} = N_\mathrm{s}/V$ of salt ion pairs in the suspension is determined by the equality, $\mu_\pm = \mu_\mathrm{res}$, of the microion chemical potentials of cations and anions, $\mu_\pm$, in the suspension with the microion chemical potential, $\mu_\mathrm{res}$, in the reservoir. In the considered Donnan equilibrium, the salt pair concentration $n_\mathrm{s}$ in the suspension is thus determined by the given reservoir salt pair concentration (number density) $n_\mathrm{res}$. Since suspension and reservoir are each electroneutral, $n_\mathrm{s}$ is smaller than $n_\mathrm{res}$ at low reservoir salinity. This is known as the Donnan salt expulsion effect. A closed suspension of given salt content $n_\mathrm{s}$ can be straightforwardly mapped to an equivalent Donnan equilibrium system using an accordingly selected salt concentration $n_\mathrm{res} \geq n_\mathrm{s}$.

We perform the calculation of the effective Hamiltonian and effective pair interactions in the framework of the mean-field PB theory, where the ± microions are taken as pointlike [39] and their correlations are neglected. The Coulombic interaction between pointlike microions is accounted for in a mean-field way. The calculations invoke the (nonlinear) PB (integro-)differential equation obtainable in an ad-hoc way from combining the exact macroscopic Poisson equation with Boltzmann-type microion distribution. More fundamentally, the PB equation follows from the minimization of the system semi-grand free-energy functional for disregarded microion correlation contributions. The PB equation is a mean-field equation, which can be also deduced using a field theoretical approach from a zeroth-order systematic expansion of the semi-grand-partition function.

For the specified system, in the literature, one can find different formulations to map the multi-component system onto an effective one-component model of (dressed) colloids by deriving an approximate effective Hamiltonian, effective pair potentials and volume energy [31, 40]. Here, we are going to focus on three particular ways, which provide us with the basis for the subsequent computation of structural, thermodynamic, and dynamic properties of charge-stabilized colloidal suspensions. The first way is a density functional theory method, based on minimizing the mean-field approach of the microion grand-free energy functional. The second way consists of a perturbative expansion of the microion grand-free energy, where the microion density distributions are calculated within linear response approximation. These two formulations provide us with effective pair potentials and volume energy terms. In the third way, we use a linear mean-spherical-approximation closure relation in the multi-component OZ equation to derive an effective macroion pair potential. In all cases, we consider a mean-field approach where microion correlations are disregarded.

### 2.4.1 Density functional theory (DFT) approach

In a given external potential created by the $N_\mathrm{m}$ macroions at fixed positions $\mathbf{X} = \{\mathbf{R}_1, ..., \mathbf{R}_{N_\mathrm{m}}\}$, the microion grand free energy functional is formally given by

$$\hat{\Omega}_\mu[n_\pm(\mathbf{r})] = \hat{\Omega}_\mathrm{id}[n_\pm(\mathbf{r})] + \hat{U}_\mathrm{el}[n_\pm(\mathbf{r})] + \hat{U}_\mathrm{ext}[n_\pm(\mathbf{r})] + \hat{\Omega}_\mathrm{corr}[n_\pm(\mathbf{r})], \tag{2.17}$$

where the nonlinear ideal-gas grand free energy functional has the form

$$\beta\hat{\Omega}_\mathrm{id}[n_\pm(\mathbf{r})] = \sum_{i=\pm} \int_V d\mathbf{r}\, n_i(\mathbf{r}) \left[ \ln\left(\frac{n_i(\mathbf{r})}{n_\mathrm{res}}\right) - 1 \right]. \tag{2.18}$$

The electrostatic mean-field energy functional of the microions is given by the quadratic form

$$\beta\hat{U}_\mathrm{el}[n_\pm(\mathbf{r})] = \frac{\lambda_\mathrm{B}}{2} \int_{V'} d\mathbf{r} \int_{V'} d\mathbf{r}' \frac{[n_+(\mathbf{r}) - n_-(\mathbf{r})][n_+(\mathbf{r}') - n_-(\mathbf{r}')]}{|\mathbf{r} - \mathbf{r}'|}, \tag{2.19}$$

where $V'$ is the volume available to the microions. In case of impermeable macroions, $V'$ is a Swiss-cheese-like volume consisting of $V$ minus the volume occupied by the $N_\mathrm{m}$ macroions with centers $\mathbf{X} = \{\mathbf{R}_1, ..., \mathbf{R}_{N_\mathrm{m}}\}$. For permeable macroions, $V' = V$. The free energy contribution due to the interaction between the microions and the spatially-fixed macroions is the linear (in $n_\pm(\mathbf{r})$) functional

$$\hat{U}_\mathrm{ext}[n_\pm(\mathbf{r})] = \int_V d\mathbf{r}\, e[n_+(\mathbf{r}) - n_-(\mathbf{r})]\Psi(\mathbf{r};\mathbf{X}), \tag{2.20}$$

where $\Psi(\mathbf{r};\mathbf{X})$ is the given external electric potential created by the macroions. The latter has the form

$$\Psi(\mathbf{r};\mathbf{X}) = \lambda_\mathrm{B} \int d\mathbf{r}' \frac{q(\mathbf{r}')}{|\mathbf{r} - \mathbf{r}'|}, \tag{2.21}$$

where $q(\mathbf{r})$ is the sum of the macroion charge distributions in units of $e$. Notice that, for a configuration $\mathbf{X}$ where macroions do not overlap, the integration of $q(\mathbf{r})$ over each macroion volume is equal to $z_0 = Z$. We neglect correlations among the microions, thus the correlation free energy functional vanishes, $\hat{\Omega}_\mathrm{corr} = 0$. Minimizing $\hat{\Omega}_\mu$ with respect to the trial densities $n_\pm(\mathbf{r})$ yields the Boltzmann distribution for the equilibrium microion densities

$$n_\pm(\mathbf{r};\mathbf{X}) = n_\mathrm{res}\, e^{\mp\Phi(\mathbf{r};\mathbf{X})} \tag{2.22}$$

for $\mathbf{r} \in V'(\mathbf{X})$ and Donnan equilibrium with a 1:1 microion reservoir. Here, $\Phi(\mathbf{r};\mathbf{X})$ is the electric potential due to all ions, including the macroions, expressed in units of $e/k_\mathrm{B}T$, given by

$$\Phi(\mathbf{r};\mathbf{X}) = \lambda_\mathrm{B} \int_{V'} d\mathbf{r}' \frac{n_+(\mathbf{r}';\mathbf{X}) - n_-(\mathbf{r}';\mathbf{X})}{|\mathbf{r} - \mathbf{r}'|} + \beta e\, \Psi(\mathbf{r};\mathbf{X}). \tag{2.23}$$

Since $n_\mathrm{res} = \exp(\beta\mu_\mathrm{res}/\Lambda^3_\mathrm{res})$, it follows from Eq. (2.22) that

$$\ln\left[n_\pm(\mathbf{r};\mathbf{X})\Lambda^3_\mathrm{res}\right] \pm \Phi(\mathbf{r};\mathbf{X}) = \beta\mu_\mathrm{res} = \beta\mu_\pm, \tag{2.24}$$

expressing the constancy of the microion electrochemical potentials $\mu_\pm$ in equilibrium.

The mean-field character of the present DFT-PB approximation is reflected in the ideal-gas form of the microion electrochemical potentials for the pointlike microions. Notice that the constant electrostatic potential, $\Phi_\mathrm{res}$, of the microion reservoir is taken to be zero.

Substitution of the equilibrium microion densities into Eq. (2.17) gives the equilibrium microion grand-free energy $\Omega_\mu[n_\pm(\mathbf{r})]$. For brevity, the resulting expressions are not shown here. Applying the Laplace operator to Eq. (2.23) gives the nonlinear PB differential equation,

$$\Delta\Phi(\mathbf{r}) = -4\pi\lambda_\mathrm{B}\left[n_+(\mathbf{r}) - n_-(\mathbf{r}) + q(\mathbf{r};\mathbf{X})\right] = \kappa_\mathrm{res}^2\ \sinh[\Phi(\mathbf{r};\mathbf{X})] - 4\pi\lambda_\mathrm{B}q(\mathbf{r};\mathbf{X}), \quad (2.25)$$

where $q(\mathbf{r};\mathbf{X})$ is zero outside of the $N_\mathrm{m}$ spherical macroions and $\kappa_\mathrm{res}^2 = 8\pi\lambda_\mathrm{B}n_\mathrm{res}$ is the square of the reservoir electrostatic screening constant. For impermeable rigid macroions, the PB equation applies only outside of the particle volumes, but it is augmented by the electrostatic boundary conditions

$$\nabla\Phi(\mathbf{r}).\hat{\mathbf{n}}(\mathbf{r})|_{S_i} = -\lambda_\mathrm{B}\frac{Z}{a^2}; \quad \mathbf{r} \in S_i, \quad (2.26)$$

on the $N_\mathrm{m}$ sphere surfaces $S_i$, where the surface vector $\hat{\mathbf{n}}$ points into the fluid. These boundary conditions properly describe impermeable colloidal macroions for neglected dielectric mismatch with the solvent. This is a complicated nonlinear $N_\mathrm{m}$-sphere boundary value problem that cannot been solved analytically for $N_\mathrm{m} > 2$. However, an analytic solution is straightforwardly obtained assuming pointlike, weakly-charged macroions. This allows for linearizing the PB equation with respect to $\Phi = 0$, resulting in the Debye-Hückel (DH) form

$$\Delta\Phi(\mathbf{r};\mathbf{X}) = \kappa_\mathrm{res}^2\ \Phi(\mathbf{r};\mathbf{X}) - 4\pi\lambda_\mathrm{B}Z\sum_{i=1}^{N}\delta(\mathbf{r}-\mathbf{R}_i), \quad (2.27)$$

valid for $Z\lambda_\mathrm{B}/a \ll 1$ and small volume fractions $\phi \ll 1$. The DH partial differential equation is readily solved by Fourier transformation with the unique result

$$\Phi(\mathbf{r};\mathbf{X}) = \lambda_\mathrm{B}Z\sum_{i=1}^{N}\frac{\exp\{-\kappa_\mathrm{res}|\mathbf{r}-\mathbf{R}_i|\}}{|\mathbf{r}-\mathbf{R}_i|}, \quad (2.28)$$

by requiring that $\Phi \to 0$ for $|\mathbf{r}| \to \infty$. Here, $\kappa_\mathrm{res}^2 = 8\pi\lambda_\mathrm{B}n_\mathrm{res}$ is the reservoir DH electrostatic screening parameter. We notice that the DH total electrostatic potential $\Phi$ is the sum of $N_\mathrm{m}$ screened repulsive Yukawa orbitals centered at the macroion positions [41]. Substitution of these orbitals into $\Omega_\mu$, expanded up to quadratic order in $n_\pm(\mathbf{r})$, leads to the equilibrium grand free energy [41]

$$\Omega_\mu(\mathbf{X}) = E_{\mathrm{vol}}^{\mathrm{DH}} + \frac{1}{2}\sum_{i<j} u_{\mathrm{eff}}(|\mathbf{R}_i - \mathbf{R}_j|), \tag{2.29}$$

with effective macroion pair potential

$$\beta u_{\mathrm{eff}}^{\mathrm{DH}}(r) = \lambda_{\mathrm{B}} Z^2 \frac{\exp(-\kappa_{\mathrm{res}} r)}{r}, \;\; r > 0. \tag{2.30}$$

The first term on the right-hand side of Eq. (2.29) is the DH volume energy contribution, given by the ideal gas form [41]

$$E_{\mathrm{vol}}^{\mathrm{DH}} = -2k_{\mathrm{B}}T n_{\mathrm{res}} V. \tag{2.31}$$

In addition to being independent of the macroion configuration $\mathbf{X}$, the volume energy in DH approximation is also independent of $n_{\mathrm{m}}$. This is due to $\phi \ll 1$, such that the microion concentration in the suspension is dominated by the reservoir-provided salt ions. The salt expulsion effect is accordingly vanishing (i.e. $n_{\mathrm{s}} = n_{\mathrm{res}}$), and the screening is determined by $\kappa_{\mathrm{res}}$.

For finite-sized, impermeable colloids, the excluded-volume radius $a$ can be reintroduced in an *ad hoc* way, by enforcing the local electroneutrality condition [41]. By means of a straightforward calculation, one shows that the condition is fulfilled when replacing $Z \to Z(\exp(\kappa_{\mathrm{res}} a)/(1 + \kappa_{\mathrm{res}} a))$, where a geometric factor is introduced. Then, the effective macroion pair potential of weakly-charged macroions in the salt-dominated regimes reads

$$\beta u_{\mathrm{eff}}(r) = \lambda_{\mathrm{B}} Z^2 \left(\frac{\exp(\kappa_{\mathrm{res}} a)}{1 + \kappa_{\mathrm{res}} a}\right)^2 \frac{\exp(-\kappa_{\mathrm{res}} r)}{r}, \;\; r > \sigma = 2a, \tag{2.32}$$

which is the repulsive electrostatic part of the celebrated Derjaguin-Landau-Verwey-Overbeek (DLVO) potential [2] at high salt concentration, where $\kappa = \kappa_{\mathrm{res}}$. It properly describes the repulsion between impermeable colloids for $Z\lambda_{\mathrm{B}}/a \ll 1$, strong dilution and high salt content, and when the likelihood of two macroions being close to contact is small.

The here presented DFT-PB approach that provides an upper bound to the exact $\Omega_\mu$ will be further evaluated in section 3.4 on charge renormalization of colloidal macroions in the framework of the so-called shifted Debye-Hückel approximation model. This method will be derived from linearizing the total potential $\Phi$ around an appropriately selected value $\tilde{\Phi}$, different from the vanishing reservoir value used in DH theory, in conjunction with a spherical cell model.

### 2.4.2 Linear response theory (LRT)

A different approach to calculate the microion grand-free energy in order to obtain the effective Hamiltonian is perturbation theory. This approach is inspired by the pseudopotential theory of metals, and focuses on effective interactions derived from a perturbative expansion of the microion grand potential about a reference system, taken as a uniform plasma of microions unperturbed by the macroions [42]. By incorporating microion-macroion interactions, this approach can model both thermodynamic and structural properties of colloidal suspensions.

The starting point of the perturbative expansion is the Debye-charging integral [43] expression

$$\Omega_\mu(\mathbf{X}) = \Omega_0 + \int_0^1 d\lambda \left(\langle H_{\mathrm{m}+}\rangle_\lambda + \langle H_{\mathrm{m}-}\rangle_\lambda\right) - E_{\mathrm{b}} \tag{2.33}$$

where the reference system grand potential, $\Omega_0$, is that of a uniform plasma of microions in the absence of the Coulombic potential created by the charged colloidal macroions. Considering that also the reference system is electroneutral, we have added and subtracted the contribution energy, $E_{\mathrm{b}}$, of the charge-neutralizing background. The background energy is explicitly given in [33] for suspensions of ion-impermeable macroions, and can be similarly obtained for ion-permeable macroions [10]. It is possible to see that $E_{\mathrm{b}}$ is formally infinite in the thermodynamic limit. Nevertheless, it is identically canceled by compensating infinite contributions in $H_{\mathrm{m}}$ and $H_{\pm,\pm}$ [33]. The integral term in Eq. (2.33) represents the electrostatic grand free energy change due to the presence of the macroions. More precisely, it expresses the grand-canonical ensemble average of the macroion-microion interaction energy,

$\langle H_{\mathrm{m}+}\rangle_\lambda + \langle H_{\mathrm{m}-}\rangle_\lambda$, in a system where the macroions are "charged" to a fraction $\lambda$ of their full charge $-Ze$ [42] and average denoted by $\langle\ \rangle_\lambda$. Note that when the charge of macroions at $\mathbf{X}$ is gradually increased from zero to its full value, the "Swiss-cheese" plasma (for impermeable macroions) becomes nonuniform due to the electrostatic attraction/repulsion of counterions/coions. Further progress is made by expressing $\langle H_{\mathrm{m}\pm}\rangle_\lambda$ in terms of the macroion-microion pair potentials and the densities of macroions and microions as [42]:

$$\langle H_{\mathrm{m}\pm}\rangle_\lambda = \int d\mathbf{r}' \int d\mathbf{r}\, u_{\mathrm{m}\pm}(|\mathbf{r}-\mathbf{r}'|) n_{\mathrm{m}}(\mathbf{r}) \langle n_\pm(\mathbf{r}')\rangle_\lambda, \tag{2.34}$$

where $n_{\mathrm{m}}(\mathbf{r})$ and $n_\pm(\mathbf{r})$ are the macroion and microion density distributions, respectively, and $u_{\mathrm{m}\pm}(\mathbf{r})$ are the macroion-microion pair potentials, wherein the (im)permeable nature of the macroions is reflected. The integration domain is determined considering that macroions have access to the full volume $V$ and microions are excluded from the interior of the macroions for impermeable macroions. Equivalently, Eq. (2.34) can be expressed in terms of Fourier components as [33]

$$\langle H_{\mathrm{m}\pm}\rangle_\lambda = \frac{1}{V}\sum_{\mathbf{k}\neq 0} \hat{u}_{\mathrm{m}\pm}(k)\hat{n}_{\mathrm{m}}(-\mathbf{k})\langle \hat{n}_\pm(\mathbf{k})\rangle_\lambda + \lim_{k\to 0}\left[\hat{u}_{\mathrm{m}\pm}(k)\hat{n}_{\mathrm{m}}(-\mathbf{k})\langle \hat{n}_\pm(\mathbf{k})\rangle_\lambda\right], \tag{2.35}$$

where we have assumed periodic boundary conditions for a sufficiently large suspension box $V = L^3$ for an isotropic and translationally-invariant suspension. Then, the modulus of the wave vector $\mathbf{k}$ attains the discrete values $k = (2\pi/L)(n_x, n_y, n_z)$ with $n_i \in \mathbb{Z}$. $\hat{f}(\mathbf{k})$ denotes the three dimensional Fourier transformation of the function $f(\mathbf{r})$,

$$\hat{f}(\mathbf{k}) = \int_V d\mathbf{r}\, f(\mathbf{r})\, e^{i\,\mathbf{k}\cdot\mathbf{r}}, \tag{2.36}$$

with the hat labelling a Fourier transformed quantity. Considering the macroions as an external potential and assuming that the microion densities respond linearly to this potential, the Fourier components of the microion densities can be written in terms of the microion "external" potential by introducing the isotropic linear-response functions $\chi_{ij}(k)$ with $k = |\mathbf{k}|$, which describe the linear response of the two-component reference plasma to the macroions.

If we use the obvious symmetry relations $\chi_{+-}(k) = \chi_{-+}(k)$ and $\hat{u}_{\mathrm{m}+}(k) = -\hat{u}_{\mathrm{m}-}(k)$, the Fourier components of the microion densities may be approximated as

$$\langle \hat{n}_+(\mathbf{k})\rangle_\lambda \approx \lambda[\chi_{++}(k) - \chi_{+-}(k)]\hat{u}_{\mathrm{m}+}(k)\hat{n}_{\mathrm{m}}(\mathbf{k}), \qquad k \neq 0 \tag{2.37}$$

and

$$\langle \hat{n}_-(\mathbf{k})\rangle_\lambda \approx \lambda[\chi_{+-}(k) - \chi_{--}(k)]\hat{u}_{\mathrm{m}+}(k)\hat{n}_{\mathrm{m}}(\mathbf{k}), \qquad k \neq 0. \tag{2.38}$$

Note that for $k = 0$ there is no response and $\hat{n}_\pm(0) = \langle N_\pm\rangle/V$, as determined by the grand-canonical mean numbers of microions in the suspension [33]. Further progress is achieved by specifying the linear-response functions $\chi_{ij}(k)$, which are proportional to the corresponding partial static structure factors, $S_{ij}(k)$, according to

$$\chi_{ij}(k) = -\beta(n_+ + n_-)(x_i x_j)^{1/2} S_{ij}(k), \tag{2.39}$$

where $S_{ij}(k) = \delta_{ij} + (x_i x_j)^{1/2}(n_+ + n_-)\hat{h}_{ij}(k)$, with $x_\pm = \langle N_\pm\rangle/(\langle N_+\rangle + \langle N_-\rangle)$ and mean microion densities $n_\pm = \langle N_\pm\rangle/V$ [19]. The monovalent microions are characterized by relatively small electrostatic coupling parameters $\Gamma_\pm = \lambda_{\mathrm{B}}/a_\pm^{\mathrm{is}} \ll 1$, where $a_\pm^{\mathrm{is}} = (4\pi n_\pm/3)^{-1/3}$ is the concentration-dependent ion-sphere radius of the (pointlike assumed) microions. Typically, in a weakly coupled plasma, short-range correlations are weak enough to justify a random phase approximation (RPA) [44]. This amounts to approximating the two-particle direct correlation functions of the microion plasma by its exact asymptotic ($r \to \infty$) limiting form $c_{ij}^{(2)}(r) = -\beta u_{ij}(r)$, taken for all distances $r > 0$. Using the RPA closures in the Fourier-transformed Ornstein-Zernike (OZ) equations (see section 5.3), the Fourier components of the response functions are obtained as [33]

$$\chi_{++}(k) - \chi_{+-}(k) = -\frac{\beta n_+}{1 - n_\mu \hat{c}(k)} = -\frac{\beta n_+}{1 + \kappa^2/k^2}, \tag{2.40}$$

$$\chi_{+-}(k) - \chi_{--}(k) = \frac{\beta n_-}{1 - n_\mu \hat{c}(k)} = \frac{\beta n_-}{1 + \kappa^2/k^2} \tag{2.41}$$

and

$$\chi(k) = -\frac{\beta n_\mu}{1 - n_\mu \hat{c}(k)} = -\frac{\beta n_\mu}{1 + \kappa^2/k^2} \tag{2.42}$$

where $\hat{c}(k) = c^{(2)}_{++}(r) = c^{(2)}_{--}(r) = -c^{(2)}_{+-}(r)$. The screening constant in the suspension is given by

$$\kappa = \sqrt{\frac{4\pi\lambda_{\mathrm{B}} n_\mu}{(1-\phi)}} \tag{2.43}$$

for ion-impermeable macroions, and by

$$\kappa = \sqrt{4\pi\lambda_{\mathrm{B}} n_\mu} \tag{2.44}$$

for ion-permeable macroions, with $n_\mu = n_+ + n_-$ the total concentration of microions.

Substitution of these $\chi_{ij}$ leads to an analytic expression for $\Omega_\mu$ (cf. Eq. (2.33)). When the latter is substituted into Eq (2.14), the effective macroion Hamiltonian of pairwise additive form is obtained,

$$H_{\mathrm{eff}}(\mathbf{X}) = K_{\mathrm{m}} + \frac{1}{2}\sum_{\substack{i,j=1\\ i\neq j}}^{N_{\mathrm{m}}} u_{\mathrm{eff}}(|\mathbf{R}_i - \mathbf{R}_j|) + E_{\mathrm{vol}}, \tag{2.45}$$

where $K_{\mathrm{m}}$ is the kinetic energy of the $N_{\mathrm{m}}$ macroions, and

$$u_{\mathrm{eff}}(r) = u_{\mathrm{mm}}(r) + u_{\mathrm{ind}}(r) \tag{2.46}$$

is the effective macroion electrostatic pair potential. The effective potential is the sum of the bare Coulomb potential, $u_{\mathrm{mm}}(r)$, and the microion-induced potential, $u_{\mathrm{ind}}(r)$, whose Fourier transform reads [33]

$$\hat{u}_{\mathrm{ind}}(k) = \chi(k)[\hat{u}_{\mathrm{m+}}(k)]^2. \tag{2.47}$$

The volume energy in the present linear response approximation is obtained as

$$E_{\mathrm{vol}} = \Omega_0 + \frac{N_{\mathrm{m}}}{2}\lim_{r\to 0} u_{\mathrm{ind}}(r) + N_{\mathrm{m}}(n_+ - n_-) \times \lim_{k\to 0}\left[-\frac{z}{2Z}\hat{u}_{\mathrm{ind}}(k) + \hat{u}_{\mathrm{m+}}(k)\right] - E_{\mathrm{b}}, \tag{2.48}$$

where the grand-free energy, $\Omega_0$, of the unperturbed uniform plasma of microions in Donnan equilibrium is given by the Legendre transformation $\Omega_0 = F_0 - \mu_+ N_+ - \mu_- N_-$, where $F_0$ is the free energy of the two-component reference plasma approximated by the ideal-gas form. Thus

$$\beta\Omega_0 = \sum_{i=\pm} \langle N_i \rangle \left[ \ln\left(\frac{n_\pm}{n_{\mathrm{res}}}\right) - 1 \right]. \tag{2.49}$$

As noted earlier, $E_{\mathrm{vol}}$ is independent of the macroion positions $\mathbf{X}$, but it depends on the mean density of macroions $n_{\mathrm{m}}$, contributing significantly at lower salinity to the total semi-grand free energy $\Omega$ of the suspension [33]. It affects the system thermodynamics and hence the osmotic pressure, as we discuss in detail further down. The suspension salt pair concentration, $n_{\mathrm{s}}$, in the LRT approximation is determined from equating the microion chemical potentials in suspension and reservoir, using additionally that $\langle N_- \rangle = N_{\mathrm{s}}$.

To obtain explicit expressions for $u_{\mathrm{eff}}(r)$ and $E_{\mathrm{vol}}$, still the explicit specifications of the internal macroion structure and the corresponding interactions are required. We consider here the case of impermeable colloids, described by a hard-core spherical volume inaccessible to microions and solvent. The bare macroion-macroion interaction is given by

$$\beta u_{\mathrm{mm}}(r) = \begin{cases} \frac{\lambda_{\mathrm{B}} Z^2}{r}\,, & r > \sigma \\ \\ \infty\,, & r \leq \sigma \end{cases} \tag{2.50}$$

with $\sigma = 2a$ the macroion hard-core diameter, while

$$\beta u_{\mathrm{m}\pm}(r) = \begin{cases} \mp\frac{\lambda_{\mathrm{B}} Z z}{r}\,, & r > a \\ \\ \mp\frac{\lambda_{\mathrm{B}} Z z}{a}\alpha\,, & r \leq a \end{cases} \tag{2.51}$$

holds for macroion-microion bare pair potentials of macroions with charge $-Ze$ and microions with charge $\pm ze$. In order to ensure exclusion of microions from the macroion hard cores and the microion densities to vanish within the core, the macroion-microion pair potentials are extended inside the core, where $\alpha$ is a constant selected such that $n_\pm(r) = 0$ for $r < a$ [33, 40]. The volume accessible to microions and fluid is $V_{\mathrm{fl}} = V(1-\phi)$, where $\phi$ is the volume fraction of impermeable macroions. Using Eqs. (2.50) and (2.51), the corresponding microion densities in LRT are obtained as

$$n_{\pm}(\mathbf{r}) = n_{\mathrm{s}} \pm x_{\pm}\frac{Z}{z}\frac{\kappa^2}{4\pi}\frac{\exp(\kappa a)}{1+\kappa a}\sum_{j=1}^{N_{\mathrm{m}}}\frac{\exp(-\kappa|\mathbf{r}-\mathbf{R_j}|)}{|\mathbf{r}-\mathbf{R_j}|}, \qquad |\mathbf{r}-\mathbf{R_j}| > a, \tag{2.52}$$

i.e. in form of a linear superposition of spherical orbitals centered at the $N_{\mathrm{m}}$ macroion centers $\mathbf{X}$. We have approximated the bulk density of positive and negative microions far from any macroion by the system salt concentration $n_{\mathrm{s}}$, which is a good approximation provided $\phi \ll 1$ [33]. The induced potential in Eq. (2.46) has the explicit form

$$\beta u_{\mathrm{ind}}(r) = \begin{cases} \lambda_{\mathrm{B}} Z^2 \left(\frac{\exp(\kappa a)}{1+\kappa a}\right)^2 \frac{\exp(-\kappa r)}{r} - \frac{\lambda_{\mathrm{B}} Z^2}{r}\,, & r > \sigma \\ -\frac{\lambda_{\mathrm{B}} Z^2}{2r}\left(\frac{1}{1+\kappa a}\right)^2 \left[2(1+\kappa a)\kappa r - \frac{1}{2}(\kappa r)^2\right]\,, & r < \sigma \end{cases}, \tag{2.53}$$

which results in the effective macroion electrostatic pair potential

$$\beta u_{\mathrm{eff}}(r) = \lambda_{\mathrm{B}} Z^2 \left(\frac{\exp(\kappa a)}{1+\kappa a}\right)^2 \frac{\exp(\kappa r)}{r}, \qquad r > \sigma \tag{2.54}$$

with screening parameter

$$\kappa = \sqrt{\frac{4\pi\lambda_{\mathrm{B}}}{(1-\phi)}n_{\mu}} = \sqrt{\frac{4\pi\lambda_{\mathrm{B}}}{(1-\phi)}(Z_{\mathrm{m}}n_{\mathrm{m}} + 2n_{\mathrm{s}})}, \tag{2.55}$$

where total electroneutrality is used in the second equality. Notice that the effective DH pair potential in Eq. (2.32) is recovered in the salt-dominated case, where $\kappa \approx \kappa_{\mathrm{res}}$ and $2n_{\mathrm{s}} \gg n_{\mathrm{m}}Z$ provided $\phi \ll 1$ holds in addition. The factor $(1-\phi)^{-1/2}$ accounts for the exclusion of microions from the macroion cores.

From substituting the induced potential $u_{\mathrm{ind}}(r)$ into Eq. (2.48), the volume energy of a impermeable-macroion suspension with monovalent microions, $z = 1$, follows as [45]

$$\beta E_{\mathrm{vol}} = \beta\Omega_0 - N_{\mathrm{m}}Z^2\frac{\lambda_{\mathrm{B}}}{2a}\frac{\kappa a}{1+\kappa a} - N_{\mathrm{m}}\frac{Z}{2}\frac{n_+ - n_-}{n_+ + n_-}. \tag{2.56}$$

The infinities associated with the $k \to 0$ limit formally cancel one another. The first term on the right-hand side is the ideal-gas plasma grand-free energy. The second term accounts for the electrostatic interaction energy between macroions and microions, and it is equal $N_{\mathrm{m}}$

times the electrostatic interaction energy of a macroion and its screening cloud of microions. Notice that this is equivalent to one half of the interaction energy of a macroion and its cloud, where all the microions are placed at a radial distance $\kappa^{-1}$ from the surface of the macroion. The third term arises from the $k \to 0$ limit term in Eq. (2.48)[33], and it can be interpreted as the Donnan potential energy [42], i.e. the work required to move microions from the reservoir of zero potential to the suspension in order to obtain the mean densities $n_\pm$. The Donnan potential is the mean potential difference between suspension and reservoir, and it is equal to $-Zn_\mathrm{m}/2n_\mathrm{res}$ in units of $k_\mathrm{B}T$ in the linearized case. It vanishes in the salt-dominated case, where $2n_\mathrm{res} \gg Zn_\mathrm{m}$.

LRT also provides a way of analytically computing the effective interaction potential and volume energy term for ion- and solvent-permeable charged colloids. On assuming uniformly-charged spherical colloids of charge $-Ze$ each, the macroion-microion bare potential is given by [10]

$$\beta u_{\mathrm{m}\pm}(r) = \begin{cases} \mp \frac{\lambda_\mathrm{B} Z z}{r}\,, & r > a \\ \mp \frac{\lambda_\mathrm{B} Z z}{2a}\left(3 - \frac{r^2}{a^2}\right)\,, & r \leq a \end{cases}\,, \tag{2.57}$$

where $r$ is the distance from the center of a macroion to a pointlike microion. The potential for $r \leq a$ can be obtained from integrating the electric field of a uniformly charged sphere. Usage of this potential yields in linear-response approximation the microion density profiles $n_\pm(r) = n_\mathrm{s} \mp n_\pm\,\psi(r)$, where $\psi(r)$ as the electrostatic potential (in units of $k_\mathrm{B}T$) inside and around a macroion, given by [13]

$$\psi(r) = \begin{cases} -\frac{3Z\lambda_\mathrm{B}}{(\kappa a)^2\, r}\left(\cosh(\kappa a) - \frac{\sinh(\kappa a)}{(\kappa a)}\right)\exp(-\kappa r)\,, & r > a \\ -\frac{3Z\lambda_\mathrm{B}}{(\kappa a)^2\, r}\left[\frac{r}{a} - \left(1 + \frac{1}{\kappa a}\right)\exp(-\kappa a)\sinh(\kappa r)\right]\,, & r \leq a \end{cases}\,. \tag{2.58}$$

with screening parameter

$$\kappa = \sqrt{4\pi\lambda_\mathrm{B} n_\mu} = \sqrt{4\pi\lambda_\mathrm{B}(Zn_\mathrm{m} + 2n_\mathrm{s})}, \tag{2.59}$$

using electroneutrality in the second equality. Different from Eq. (2.55), the present expression for $\kappa$ excludes the factor $1/(1-\phi)^{1/2}$ that originally accounts for the macroion excluded volume. The effective electrostatic pair potential between the permeable dressed macroions is of the form

$$u_{\mathrm{eff}}(r) = \begin{cases} u_{\mathrm{Y}}(r), & r > \sigma = 2a \\ u_{\mathrm{ov}}(r), & r \leq \sigma \end{cases}, \tag{2.60}$$

which for non-overlapping macroions is a Yukawa (screened-Coulomb) pair potential,

$$\beta u_{\mathrm{Y}}(r) = \lambda_{\mathrm{B}} Z_{\mathrm{net}}^2 \left( \frac{e^{\kappa a}}{(1+\kappa a)} \right)^2 \frac{e^{-\kappa r}}{r} \qquad r > \sigma, \tag{2.61}$$

where the net microgel valence, $Z_{\mathrm{net}}$, is given by

$$Z_{\mathrm{net}} = Z - 4\pi \int_0^a [n_+(r) - n_-(r)] r^2 dr\,, \tag{2.62}$$

i.e. by the bare valence $Z$ minus the total charge of interior microions. From inserting the equilibrium counterion and coion density profiles $n_\pm(r)$, we obtain

$$Z_{\mathrm{net}} = Z \frac{3(1+\kappa a)}{(\kappa a)^2\, e^{\kappa a}} \left( \cosh(\kappa a) - \frac{\sinh(\kappa a)}{\kappa a} \right), \tag{2.63}$$

for the linearized net macroion valence. Overlapping permeable macroions interact in LRT via a soft electrostatic pair potential

$$u_{\mathrm{ov}}(r) = u_{\mathrm{mm}}(r) + u_{\mathrm{ind}}(r), \quad r \leq \sigma, \tag{2.64}$$

where

$$\beta u_{\mathrm{mm}}(r) = Z^2 \frac{\lambda_{\mathrm{B}}}{a} \left( \frac{6}{5} - \frac{1}{2}\tilde{r}^2 + \frac{3}{16}\tilde{r}^3 - \frac{1}{160}\tilde{r}^5 \right) \tag{2.65}$$

is the bare (Coulomb) pair potential between two overlapping, uniformly charged spheres, and

$$\beta u_{\mathrm{ind}}(r) = \left( \frac{3Z}{\tilde{\kappa}^2} \right)^2 \frac{\lambda_{\mathrm{B}}}{2r} \left[ \left( 1 + \frac{1}{\tilde{\kappa}} \right)^2 e^{-2\tilde{\kappa}} \sinh(\kappa r) + \left( 1 - \frac{1}{\tilde{\kappa}^2} \right) \times \right.$$
$$\left. \times \left( 1 - e^{-\kappa r} + \frac{1}{2}\kappa^2 r^2 + \frac{1}{24}\kappa^4 r^4 \right) - \frac{2}{3}\tilde{\kappa}^2 \left( 1 - \frac{2}{5}\tilde{\kappa}^2 \right) \tilde{r} - \frac{1}{9}\tilde{\kappa}^4 \tilde{r}^3 - \frac{1}{720}\tilde{\kappa}^4 \tilde{r}^6 \right] \tag{2.66}$$

is the microion-induced pair potential, with $\tilde{\kappa} = \kappa a$ and $\tilde{r} = r/a$. The volume energy per macroion for monovalent microions, $z = 1$, is given by [13]

$$\frac{\beta E_{\mathrm{vol}}}{N_{\mathrm{m}}} = \frac{\beta \Omega_0}{N_{\mathrm{m}}} - 3Z^2 \frac{\lambda_{\mathrm{B}}}{a} \left\{ \frac{1}{5} - \frac{1}{2\tilde{\kappa}^2} + \frac{3}{4\tilde{\kappa}^3} \left[ 1 - \frac{1}{\tilde{\kappa}^2} + \left( 1 + \frac{2}{\tilde{\kappa}} + \frac{1}{\tilde{\kappa}^2} \right) e^{-2\tilde{\kappa}} \right] \right\} - \frac{Z}{2} \frac{n_+ - n_-}{n_+ + n_-}, \tag{2.67}$$

where the second term on the right-hand side is explicitly noticed to be different from the corresponding term in Eq. (2.56). In closing our discussion of LRT approximation for permeable and impermeable spherical macroion suspensions, we comment in the range of applicability of the method. First, even though LRT assumes weak microion response to the macroion charge perturbation, and thus a weak induced screening by the inhomogeneous microion concentration field, the obtained potential form of a screened-Coulomb potential is supported by Poisson-Boltzmann cell model calculations (see later), ab initio simulations [13, 14], and experiments [14]. Second, the excluded volume correction factor $(1-\phi)^{-1/2}$ in the screening constant $\kappa$ for impermeable colloidal macroions becomes significant, even in the weak-screening regime, for concentrated suspensions. Although LRT neglects fluctuations and correlations in the microion densities, Monte Carlo (MC) simulations and cell model calculations for spherical macroions suggest that such correlations contribute only marginally to the total semi-grand free energy [33]. For zero macroion concentration ($n_\mathrm{s} \to 0$), or high salt concentration ($n_\mu \to \infty$), such that $(n_+ - n_-)/n_\mu \to 0$, the leading-order nonlinear corrections all vanish. This finding partially explains the remarkably broad range of validity of a Yukawa form of the (non-overlapping) effective pair potential [30]. Since LRT is a mean-field method, the assumption of monovalent microions is crucial for this validity.

### 2.4.3 Integral equation scheme: mean spherical approximation (MSA)

Alternatively to DFT-PB and LRT approximations of the microion grand free energy, it is also possible to derive an expression of the effective macroion pair potential with the generalized PM-based multispecies Ornstein-Zernike (OZ) integral equation scheme. Different (one-component) OZ integral equation schemes are addressed in detail in section 5.3. Here, we describe how $u_\mathrm{eff}(r)$ can be derived using a multicomponent OZ description with an explicit analytic result obtained from using the linear MSA closure relations, which are appropriate for weakly-charged macroions. Different from LRT and linearized DFT-PB approaches, the present MSA approach does not directly provide an expression for $E_{\text{vol}}$. The latter can be obtained (not shown here) from a MSA-based free energy expression [46, 47], derived using MSA $h_{ij}(r)$ as input.

Consider a PM suspension composed of $m+1$ different spherical ionic species, where species 0 corresponds to colloidal macroions. Instead of considering the $m+1$ coupled OZ equations relating the Fourier-transformed partial total correlation functions $\hat{h}_{ij}(q)$ to the partial direct correlation functions $\hat{c}_{ij}(q)$, with $q$ the modulus of the wave vector $\mathbf{q}$, we are only interested in the correlations among the macroion species 0. Therefore, we define the Fourier-transformed effective macroion direct correlation function, $\hat{c}_{\text{eff}}(q)$, of an effective one-component macroion system by

$$S(q) = 1 + n_0 \hat{h}_{00}(q) = \frac{1}{1 - n_0 \hat{c}_{\text{eff}}(q)}, \tag{2.68}$$

where $S(q)$ is the structure factor of the effective one-component macroion system and $n_0 = n_{\text{m}}$ is the number density of macroions. We enforce here that the macroion-macroion structure factor $S_{00}(q)$ of the multicomponent PM system to be the same as that of the effective one-component macroion system, i.e. $S_{00}(q) = S(q)$. The effective direct correlation function is then related to the partial direct correlation functions by [9]

$$\hat{c}_{\text{eff}}(q) = \hat{c}_{00}(q) + \hat{\mathbf{c}}_0{}^T(q)(\mathbb{1} - \hat{\mathbb{c}}(q))^{-1}\, \hat{\mathbf{c}}_0(q), \tag{2.69}$$

where the elements of the $m \times 1$ column vector $\hat{\mathbf{c}}_0(q)$ are given by $(\hat{\mathbf{c}}_0)_i = n_i^{1/2} \hat{c}_{0i}(q)$ $(i = 1, ..., m)$ and the elements of the $m \times m$ matrix $\hat{\mathbb{c}}(q)$ are given by $(\hat{\mathbb{c}})_{ij} = (n_i n_j)^{1/2} \hat{c}_{ij}(q)(i, j = 1, ..., m)$, where $\hat{c}_{ij}(q)$ are the inter-species partial direct correlation functions of the multicomponent system. The latter satisfy

$$c_{ij}(r) \to -\beta u_{ij}(r), \tag{2.70}$$

in the long-distance limit, $r \to \infty$, for all $i, j = 0, ..., m$, where $u_{ij}(r)$ are the direct (bare) interaction potentials between ions of species $i$ and $j$. The direct correlation functions can be rewritten as

$$c_{ij}(r) = -\beta u_{ij}(r) + c^{\mathrm{s}}_{ij}(r), \qquad r > 0, \tag{2.71}$$

where $c^{\mathrm{s}}_{ij}(r)$ are the short-range contribution of $c_{ij}(r)$ including, for example, hard-core interactions. On specifying the direct interactions between the different ion species, it is possible to obtain $\hat{c}_{\mathrm{eff}}(q)$ using approximate closure relations relating $c_{ij}(r)$ to $h_{ij}(r)$ and $u_{ij}(r)$. The effective pair potential, $u_{\mathrm{eff}}(r)$, between the macroions is then obtained asymptotically from

$$c_{\mathrm{eff}}(r) \rightarrow -\beta u_{\mathrm{eff}}(r) \tag{2.72}$$

for $r \rightarrow \infty$. While this OZ-based method gives an asymptotic expression of the effective pair potential, it does not provide per se the (grand) free energy of the effective one-component macroion system. The latter can be derived based on the free energy functional associated with the invoked closure relations [46, 47].

For an explicit derivation of the effective pair potential, consider the case of impermeable, hard spherical colloids of radius $a_0 = a$, valence $z_0 = -Z$ and concentration $n_0 = n_{\mathrm{m}}$ coexisting with $m$ different pointlike microion species, $a_i = 0$, of valences $z_i$. The bare interaction potentials are

$$\beta u_{ij}(r) = \begin{cases} \infty\,, & 0 < r \leq a_i + a_j \\ \frac{\lambda_{\mathrm{B}} z_i z_j}{r}\,, & r > a_i + a_j \end{cases}. \tag{2.73}$$

Using the linear MSA closure for the partial direct correlation functions [19]

$$c_{ij}(r) = -\beta u_{ij}(r), \qquad 0 < r, \tag{2.74}$$

$$c_{0j}(r) = -\beta u_{0j}(r), \qquad a < r, \tag{2.75}$$

together with $g_{0j}(r) = 0$, with $0 < r \leq a_i$ and $i, j = 1, ..., m$, i.e. the partial direct correlation functions relative to the microions are approximated by their asymptotic forms at all separations $r$, it is possible to obtain the effective interaction between macroions, as [48, 49]

$$\beta u_{\mathrm{eff}}(r) = \lambda_{\mathrm{B}} Z^2 X^2_{\mathrm{MSA}} \frac{\exp(-\kappa r)}{r}, \;\; r > 2a. \tag{2.76}$$

The effective colloid valence is $Z_{\mathrm{eff}}^{\mathrm{MSA}} = X_{\mathrm{MSA}} Z$, where

$$X_{\mathrm{MSA}} = \cosh(\kappa a) + U\left(\kappa a \cosh(\kappa a) - \sinh(\kappa a)\right), \tag{2.77}$$

and the associated screening constant is given by the DH form

$$\kappa^2 = 4\pi\lambda_{\mathrm{B}} \sum_{i=1}^{m} n_i z_i^2, \tag{2.78}$$

which, differently from the LRT expressions, does not include the excluded-volume factor $1/(1-\phi)^{1/2}$. For monovalent counterions and added 1:1 electrolyte of pair concentration $n_{\mathrm{s}}$, we find

$$(\kappa a)^2 = \frac{\lambda_{\mathrm{B}}}{a}\left(8\pi n_{\mathrm{s}} a^3 + 3\phi\, Z\right), \tag{2.79}$$

or simply

$$(\kappa a)^2 = 3\frac{\lambda_{\mathrm{B}}}{a}\phi\, Z \tag{2.80}$$

in the salt-free case. The parameter $U$ is determined by

$$U = \frac{c}{(\kappa a)^3} - \frac{\gamma}{\kappa a} \tag{2.81}$$

where $c = 3\phi/(1-\phi)$ and

$$\gamma = \frac{c + \Gamma_{\mathrm{MSA}} a}{1 + c + \Gamma_{\mathrm{MSA}} a}. \tag{2.82}$$

The MSA screening parameter $\Gamma_{\mathrm{MSA}}$ is the unique positive solution of the biquadratic equation

$$(\Gamma_{\mathrm{MSA}} a)^2 = (\kappa a)^2 + \frac{(q_0 a)^2}{(1 + c + \Gamma_{\mathrm{MSA}} a)^2} \tag{2.83}$$

fulfilling $\Gamma_{\mathrm{MSA}} > \kappa$, where $(q_0 a)^2 = 3\lambda_{\mathrm{B}}\phi Z^2/a$. In the infinite dilution limit of macroions, $\Gamma_{\mathrm{MSA}} \to \kappa$ and $X_{\mathrm{MSA}} Z \to Z$. In the high temperature limit, $\beta \to 0$, we obtain $\kappa a \ll 1$ and $\Gamma_{\mathrm{MSA}} a \ll 1$, and hence

$$X_{\mathrm{MSA}} Z \to (1+\phi) Z > Z. \tag{2.84}$$

The fact that the effective valence $Z_{\mathrm{eff}}^{\mathrm{MSA}}$ is larger than $Z$ is obtained in the MSA treatment for higher macroion concentrations. This feature can be attributed to the reduced screening ability of the counterions in presence of surrounding macroions restricting the volume accessible to the microions.

Throughout this thesis, we consider a semi-open charge-stabilized suspension in osmotic equilibrium with a microion reservoir, so that the suspension salt concentration, $n_\mathrm{s}$, is a state-dependent parameter. In the shown MSA formalism, a relation between $n_\mathrm{s}$ and the reservoir salt concentration $n_\mathrm{res}$, establishing a link between a semi-open and a close system, has not been accounted for in previous works [26]. This relation follows from the Nernst-Planck relation in Donnan equilibrium

$$\exp[\mp\Phi_\mathrm{D}] = \frac{n_\pm \gamma_\pm}{n_\mathrm{res}\gamma_\mathrm{res}}, \tag{2.85}$$

expressing the equality of microion chemical potentials in suspension and reservoir. $\Phi_\mathrm{D} = \beta e \psi_\mathrm{D}$ is the reduced (Donnan) potential jump across (a mentally-pictured) microion-permeable membrane. Here, $\gamma_\pm$ and $\gamma_\mathrm{res}$ are the activity coefficients of the two monovalent ionic species in the suspension and in the symmetric 1:1 electrolyte reservoir, respectively. Notice that the microion activity coefficient in the reservoir is taken to be equal for counter- and coions, i.e. $\gamma_{+,\mathrm{res}} = \gamma_{-,\mathrm{res}} = \gamma_\mathrm{res}$; whereas, $\gamma_+ \neq \gamma_-$ in the suspension, due to the released counterions. The suspension salt-pair concentration, $n_\mathrm{s}$, is equal the coion concentration in the suspension. Using overall electroneutrality and expressing the microion activity coefficients as $\gamma_\pm = \gamma_\pm^\mathrm{hs}\gamma_\pm^\mathrm{C}$, where $\gamma_\pm^\mathrm{hs} = 1/(1-\phi)$ are the hard-sphere and $\gamma_\pm^\mathrm{C}$ the MSA Coulomb contributions [50, 51], the suspension salt concentration is given by

$$n_\mathrm{s} = -\frac{1}{2}n_\mathrm{m}Z + \sqrt{\frac{n_\mathrm{res}^2}{(1-\phi)^2}\exp[\lambda_\mathrm{B}(2\Gamma_\mathrm{MSA} - \kappa_\mathrm{res})] + \left(\frac{1}{2}n_\mathrm{m}Z\right)^2}. \tag{2.86}$$

Notice that $n_\mathrm{s}$ depends on $\kappa$ via $\Gamma_\mathrm{MSA}(\kappa)$, which in turn depends on $n_\mathrm{s}$. Thus, $n_\mathrm{s}$ is self-consistently determined in conjunction with the biquadratic equation for $\Gamma_\mathrm{MSA}$ in Eq. (2.83). When nonideal MSA contributions to the chemical potentials are neglected, which amounts to $\Gamma_\mathrm{MSA} = \kappa$ and $\phi = 0$, the standard DH Donnan equilibrium expression is recovered from Eq. (2.86).

The MSA method has proven to give a reasonably accurate description of the microstructure of weakly-charged macroion suspensions at high volume fractions, where electrostatic effects are a small perturbation to the uncharged hard-sphere reference mixture [49]. Examples in case where it can be applied are globular protein solutions for valences $Z \lesssim 30$ and $\phi \gtrsim 0.3$ [22]. However, for dilute suspensions of highly charged particles, MSA predicts for the PM unphysical negative contact values for likewise charged ions, for instance $g_{00}(r)$. This deficiency of the MSA can be overcome using a rescaling procedure where macroion hard-core diameter $\sigma$ at fixed concentration $n_{\mathrm{m}}$ is appropriately increased [52], as established in the rescaled mean spherical approximation (RMSA) among others [53].

Having considered the MSA-based $u_{\mathrm{eff}}(r)$ for impermeable colloids, we consider next permeable colloids. For simplicity, we treat a binary salt-free PM composed of spherical macroions (m) of fixed (bare) charge, $-Ze$, uniformly distributed inside the macroion coexisting with the backbone-released pointlike counterions (+) encountered inside and outside of the macroions. The Fourier transform of the effective direct macroion correlation function $c_{\mathrm{eff}}(r)$ reduces here to

$$\hat{c}_{\mathrm{eff}}(q) = \hat{c}_{\mathrm{mm}}(q) + \frac{n_+ \hat{c}_{\mathrm{m}+}(q) \hat{c}_{\mathrm{m}+}(q)}{1 - n_+ \hat{c}_{++}(q)}. \tag{2.87}$$

The Coulombic interactions invoking negatively-charged macroions of valence $Z$ and monovalent microions are [10]

$$\beta u_{++} = \frac{\lambda_{\mathrm{B}}}{r}, \qquad r > 0 \tag{2.88}$$

for the counterion-counterion interaction,

$$\beta u_{\mathrm{m}+}(r) = \begin{cases} -\frac{\lambda_{\mathrm{B}} Z}{r}, & r > a \\ -\frac{\lambda_{\mathrm{B}} Z}{2a}\left(3 - \frac{r^2}{a^2}\right), & 0 < r \leq a \end{cases}, \tag{2.89}$$

for the macroion-counterion interaction, and

$$\beta u_{\mathrm{mm}}(r) = \begin{cases} \frac{\lambda_{\mathrm{B}} Z^2}{r}, & r > \sigma \\ \frac{\lambda_{\mathrm{B}} Z^2}{a}\left(\frac{6}{5} - \frac{1}{2}\left(\frac{r}{a}\right)^2 + \frac{3}{16}\left(\frac{r}{a}\right)^3 - \frac{1}{160}\left(\frac{r}{a}\right)^5\right), & 0 < r \leq \sigma \end{cases}, \tag{2.90}$$

for the macroion-macroion direct interaction with the counterions allowed to penetrate the uniformly-charged macroions of radius $a$. Using MSA closures

$$c_{ij}(r) = -\beta u_{ij}(r), \qquad 0 < r \tag{2.91}$$

with $i, j \in \{0, 1\}$, the Fourier-transformed Eqs. (2.88)-(2.90) and Eq. (2.87) lead to

$$\beta \hat{u}_{\mathrm{eff}}(q) = 36\pi \lambda_{\mathrm{B}} Z^2 \frac{[\sin(qa) - qa\cos(qa)]^2}{(qa)^6} \frac{1}{q^2 + \kappa^2} \tag{2.92}$$

where $\hat{c}_{\mathrm{mm}}(q) = \hat{c}^{\mathrm{s}}_{\mathrm{mm}}(q) - \beta \hat{u}_{\mathrm{mm}}(q)$ was used. Here,

$$\kappa^2 = 4\pi \lambda_{\mathrm{B}} n_+ = 4\pi \lambda_{\mathrm{B}} n_{\mathrm{m}} Z \tag{2.93}$$

is determined by the counterion concentration $n_+$. Noticing that the Fourier backtransform of

$$\hat{f}_1(q) = \frac{[\sin(q) - q\cos(q)]^2}{q^6} \tag{2.94}$$

is

$$f_1(r) = \begin{cases} \frac{(r-2)^2(r+4)}{192\pi}\,, & 0 < r \leq \sigma \\ 0\,, & r > \sigma \end{cases} \tag{2.95}$$

and that $f_2(r) = e^{-\kappa r}/(4\pi r)$ is the backtransform of $\hat{f}_2(q) = 1/(q^2 + \kappa^2)$, the effective macroion pair potential is expressed by the convolution integral

$$\beta u_{\mathrm{eff}}(r) = 36\pi \frac{\lambda_{\mathrm{B}}}{a^3} Z^2 \int f_1(r') f_2(|\mathbf{r} - \mathbf{r}'|)\, d\mathbf{r}'. \tag{2.96}$$

Integrating Eq. (2.96), we finally obtain

$$\beta u_{\mathrm{eff}}(r) = \begin{cases} \lambda_{\mathrm{B}} Z^2 \left[\frac{3}{\tilde{\kappa}^2}\left(\cosh(\tilde{\kappa}) - \frac{\sinh(\tilde{\kappa})}{\tilde{\kappa}}\right)\right]^2 \frac{e^{-\kappa r}}{r}\,, & r > \sigma \\ \frac{3\lambda_{\mathrm{B}} Z^2 (24 + 12\,\tilde{\kappa}^2(\tilde{r}^2 - 2) + \tilde{\kappa}^4 \tilde{r}(\tilde{r}-2)^2(4+\tilde{r}) + 12 e^{-\tilde{\kappa}(2+\tilde{r})}(1+\tilde{\kappa})(1 + 2e^{2\tilde{\kappa}}(\tilde{\kappa}-1) + \tilde{\kappa} - e^{2\tilde{\kappa}\tilde{r}}(1+\tilde{\kappa})))}{16\tilde{\kappa}^6\, r}\,, & 0 < r \leq \sigma \end{cases} \tag{2.97}$$

for the MSA-based effective pair potential without salt, where $\tilde{\kappa} = \kappa a$ and $\tilde{r} = r/a$. The potential smoothly extends into the overlap region $r < \sigma$ with zero slope (i.e. zero repulsive force) at full overlap of two macroions at $r = 0$. This potential has been derived earlier and independently using the LRT method [10], and it is widely used as a simple model for the electrostatic interaction of ionic spherical microgels with uniform backbone charge [11, 14, 15]. In fact, the effective Denton pair potential in Eq. (2.60) reduces to Eq. (2.97) in the salt-free limit $n_- \to 0$.

The assumptions underlying Eqs. (2.91) and (2.74) are that the microion-microion correlations are treated in the linear DH approximation for pointlike microions [9]. Using residual calculus, one can show that, asymptotically, $u_{\text{eff}}(r) \propto e^{\kappa r}/r$, with $\kappa$ given by Eq. (2.78), provided the pointlike microions are treated in DH approximation, without having to specify the microion-macroion and macroion-macroion correlation functions. As shown here, an analytic expression for $u_{\text{eff}}(r)$ is obtained when both (++) and (m+) direct correlations are treated in the linear MSA approximation. As noted earlier, the poor description in MSA of short-range electrostatic correlations can result in non-physical negative values of $g(r) = g_{00}(r)$ near contact [5]. This is improved when instead the nonlinear HNC closures are used for the macroion-microion direct correlation function, i.e.

$$c_{01}(r) = -\beta u_{01}(r) + h_{01}(r) - \ln\{1 + h_{01}(r)\}, \qquad r > 0 \tag{2.98}$$

guaranteeing that $g_{01}(r) \geq 0$. Instead of using HNC closure for $g_{00}(r)$, a great simplification is obtained when the so-called jellium assumption is used. This constitutes the so-called nonlinear jellium approximation (JA), presuming that all the backbone charges of the $(N_{\text{m}} - 1)$ macroions around a central macroion are smeared out as a uniform background, the so-called *jellium*, of charge density $n_{\text{m}} Z e$. Overall electroneutrality is ensured in the nonlinear JA, but macroion-macroion correlations are disregarded [9]. One can show that the JA implies a (nonlinear) PB equation, which in the salt-free case is of the form [9]

$$\Delta\Phi(r) = \begin{cases} -4\pi\lambda_{\text{B}} \left[ n_0 Z + n_1 z\, e^{-z\Phi(r)} - \frac{3Z\lambda_{\text{B}}}{a^3} \right], & 0 < r \leq a \\ -4\pi\lambda_{\text{B}} \left[ n_0 Z + n_1 z\, e^{-z\Phi(r)} \right], & r > a \end{cases} \tag{2.99}$$

with the reduced potential $\Phi(r)$ defined in terms of $h_{01}(r)$ by

$$h_{01}(r) = e^{-z\Phi(r)} - 1. \tag{2.100}$$

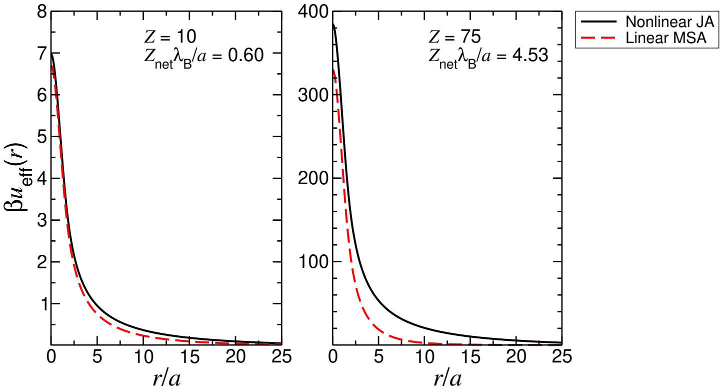

**Figure 2.1** Effective electrostatic macroion pair potential, $u_{\text{eff}}$, for two different coupling parameters $Z_{\text{net}}\lambda_{\text{B}}/a$ for uniformly-charged ion-permeable macroions. Dashed red line corresponds to linear MSA-based result, while solid black line corresponds to numerical nonlinear HNC-JA solution on identifying $u_{\text{eff}}$ with $-k_{\text{B}}Tu_{\text{eff}}$ down to $r = 0$. Other system parameters: $\phi = 0.005$, $a = 12$ nm and $\lambda_{\text{B}} = 0.726$ nm.

The consequential boundary conditions are $\Phi(r \to \infty) = 0$ and $\Phi'(0) = 0$, plus the continuity of $\Phi(r)$ and $\Phi'(r)$ at $r = a$. Using the HNC closure, the numerical solution for $\Phi(r)$ gives $h_{01}(r)$ and hence $c_{01}(r)$. When the latter is substituted into Eq. (2.87), $c_{\text{eff}}(r)$ and hence the long-distance Yukawa form of $u_{\text{eff}}(r)$ are obtained, providing a renormalized effective macroion valence $Z_{\text{eff}}$. For $\Phi(r) \ll 1$, this last formulation leads back to the MSA-based $u_{\text{eff}}(r)$ in Eq. (2.97). This generalizes the findings by Denton to the linear JA model case: in linear treatment of ionic correlations, MSA integral equation scheme and LRT give the same $u_{\text{eff}}$. Such an identity does not necessarily hold for the volume energy.

In Fig. 2.1, we display the effective macroion pair potential, $u_{\text{eff}}$, of uniformly-charged ion-permeable colloids for two representative coupling parameters $Z_{\text{net}}\lambda_{\text{B}}/a$, obtained using the linear MSA and nonlinear HNC-JA approximations, respectively. The first one is computed analytically using Eq. (2.97), while the second one is obtained numerically as explained above. At low macroion coupling, both methods give the same $u_{\text{eff}}(r)$, while for the larger coupling, nonlinear contributions described by the HNC-JA scheme imply a stronger effective pair potential.

# Chapter Three

# CHARGE RENORMALIZATION METHODS

The explicit results for $u_{\mathrm{eff}}$ end $E_{\mathrm{vol}}$ discussed so far are for macroion suspensions where the microion distribution is only weakly perturbed by the macroion charges, i.e. where the coupling parameter $\lambda_{\mathrm{B}} Z_{(\mathrm{net})}/a$ is small. For strongly coupled suspensions where $\lambda_{\mathrm{B}} Z_{(\mathrm{net})}/a$ is not small, it is necessary to renormalize the bare macroion charge, $Z$, and suspension screening constant, $\kappa$, to incorporate the nonlinear response of the microions to the strong electric field of the macroions. Notice that, in the coupling parameter $\lambda_{\mathrm{B}} Z_{(\mathrm{net})}/a$, we use $Z$ for impermeable and $Z_{\mathrm{net}}$ for microion-permeable colloids.

In this chapter, we describe how nonlinear effects can be incorporated into the discussed multi-colloid-center LRT and DFT-PB schemes. We start by considering first simple renormalization schemes in the context of single-macroion PB spherical cell models and jellium models, where inter-macroion correlations are basically disregarded. Cell-model-based charge renormalization is combined later on with a linearized DFT-PB scheme, resulting into the so-called shifted DH approximation. Particular focus is given to an appropriate linearization of the suspension mean-field electrostatic potential $\Phi$. We will mainly deal with charge-renormalization methods for impermeable colloids where nonlinear effects are particularly strong, but we also discuss shortly how these methods can be modified to deal with ion-permeable colloids. As done throughout this thesis, the microions are treated as pointlike and monovalent, and their interactions are described in a mean-field way.

## 3.1 Cell model approximations

Commonly used charge renormalization schemes are based on a simplifying cell model (CM) picture of the suspension. These schemes follow from the observation that for strongly repelling spherical colloids, there is a region around each colloid which is void of further ones [54]. On assuming a crystalline-like structure, a Wigner-Seitz cell tesselation can be applied, where each Wigner-Seitz cell is approximated by a spherical cell containing a single colloid at its center. Each cell is treated identically and independently (no inter-cell correlations) and is considered to be in Donnan equilibrium with a large 1:1 strong electrolyte reservoir of monovalent microions of constant concentration $2n_{\text{res}}$. The only piece of information about the colloid environment is the volume fraction $\phi$ related to the spherical cell by its radius $R = a/\phi^{1/3}$. Considering Boltzmann distributions for the microion concentration fields, the total electrostatic suspension potential in the fluid region, $a < r < R$, of the cell is determined by the nonlinear PB equation

$$\Phi''(r) + \frac{2}{r}\Phi'(r) = \kappa_{\text{res}}^2 \sinh\{\Phi(r)\}, \tag{3.1}$$

where $\Phi(r) = e\beta\psi(r)$ is the reduced total electrostatic potential, and $\kappa_{\text{res}}^2 = 8\pi\lambda_{\text{B}}n_{\text{res}}$ is the square of the reservoir electrostatic screening constant. The inner and outer boundary conditions for ion-impermeable macroions are given by

$$\Phi'(a) = \frac{Z\lambda_{\text{B}}}{a^2}, \quad \Phi'(R) = 0 \tag{3.2}$$

at the colloid surface and cell edge, respectively. The inner boundary condition states that the radial electric field on the colloid surface obeys Coulomb's law, while the outer one assures that the cell is overall electroneutral. The suspension salt pair concentration, $n_{\text{s}}$, is calculated by integrating the coion (anion) concentration profile $n_-(r)$ across the negatively-charged central macroion in the cell, i.e.

$$n_\mathrm{s} = \frac{4\pi}{V_\mathrm{c}(1-\phi)} \int_a^R n_-(r)\, r^2\, dr = \frac{4\pi n_\mathrm{res}}{V_\mathrm{c}^\mathrm{fl}} \int_a^R e^{\Phi(r)}\, r^2\, dr, \tag{3.3}$$

relating $n_\mathrm{s}$ to the given reservoir salt concentration. Here, $V_\mathrm{c} = 4\pi R^3/3$ is the cell volume and $V_\mathrm{c}^\mathrm{fl} = V_\mathrm{c}(1-\phi)$ is the fluid volume in the cell interior. Since $\Phi < 0$ for negatively-charged macroions, one notices that $n_\mathrm{s} \leq n_\mathrm{res}$, which expresses the Donnan salt expulsion effect. The presented CM is also referred as the nonlinear PBCM approximation, hinging on the nonlinear Boltzmann-distributed microion profiles.

For defining effective interaction parameters characterizing the effective macroion pair potential with charge-renormalization effects included, we expand the nonlinear term in Eq. (3.1) up to first order around a yet undetermined potential value $\tilde{\Phi}$, leading to a PB equation for the linearized electrostatic potential $\Phi_l(r)$, i.e.

$$\Phi_l''(r) + \frac{2}{r}\Phi_l'(r) = \kappa_\mathrm{eff}^2(\Phi_l(r) - \tilde{\Phi} + \gamma), \tag{3.4}$$

where $\gamma = \tanh\{\tilde{\Phi}\}$, and

$$\kappa_\mathrm{eff}^2 = \kappa_\mathrm{res}^2 \cosh\{\tilde{\Phi}\} \tag{3.5}$$

is a new renormalized (effective) screening constant. In order to make further progress, we need to specify the linearization value $\tilde{\Phi}$. Two convenient choices are the (nonlinear) electrostatic potential value at the cell edge, i.e. $\tilde{\Phi} = \Phi(R)$, and the volume-average, mean (nonlinear) electrostatic potential, $\tilde{\Phi} = \bar{\Phi} = \frac{4\pi}{V_\mathrm{c}^\mathrm{fl}} \int_a^R r^2 \Phi(r) dr$. The first choice is referred to as potential linearization with respect to the edge potential value, or edge linearization for short, while the second one is called linearization with respect to the mean potential value, or mean linearization for short. The two boundary conditions that $\Phi_l(r)$ has to fulfill to be uniquely determined depend on the chosen linearization value. They read $\Phi_l'(R) = 0$ and $\Phi_l(R) = \Phi(R)$ for edge linearization, stating electroneutrality and equality of linearized and nonlinear potential at the cell edge; and $\Phi_l'(R) = 0$ and $\frac{4\pi}{V_\mathrm{c}^\mathrm{fl}} \int_a^R r^2 \Phi_l(r)\, dr = \bar{\Phi}$ for mean linearization, corresponding to electroneutrality and the equality of the volume-averaged mean values of the linear and nonlinear potentials (both averaged in the fluid volume). The general two-parametric solution of Eq. (3.4) has the form

$$\Phi_l(r) = c_+ \frac{e^{\kappa_{\text{eff}} r}}{r} + c_- \frac{e^{-\kappa_{\text{eff}} r}}{r} + \tilde{\Phi} - \gamma, \tag{3.6}$$

where $c_\pm$ are constants determined by the boundary conditions. Since the cell radius is finite for $\phi > 0$, also the positive exponential has to be considered for $\Phi_l(r)$.

We proceed to provide the renormalized macroion valence, $Z_{\text{eff}}$, which together with the renormalized screening constant, $\kappa_{\text{eff}}$, determine the so-called renormalized effective pair potential

$$\beta u_{\text{eff}}(r) = \lambda_{\text{B}} Z_{\text{eff}}^2 \left( \frac{e^{\kappa_{\text{eff}} a}}{1 + \kappa_{\text{eff}} a} \right)^2 \frac{e^{-\kappa_{\text{eff}} r}}{r}, \qquad r > 2a, \tag{3.7}$$

for impermeable macroions, such that for a weak bare macroion charge, where $Z_{\text{eff}} = Z$, the linear electrostatic part of the DLVO potential is recovered. For a specified linearization value $\tilde{\Phi}$, the according renormalized screening parameter $\kappa_{\text{eff}}$ follows from Eq. (3.5). For specified $\tilde{\Phi}$ and hence $\Phi_l(r)$, the renormalized valence, $Z_{\text{eff}}$, is then consistently defined by the electrostatic boundary (surface charge (SC)) condition,

$$Z_{\text{eff}} := \frac{\Phi_l'(a)\, a^2}{\lambda_{\text{B}}}, \tag{3.8}$$

on the surface of the macroion sphere based on the linearized potential. This definition of $Z_{\text{eff}}$ was firstly introduced in the pioneering work of Alexander *et. al.* using edge linearization [55]. Depending on $\tilde{\Phi}$, different values for $\kappa_{\text{eff}}$ and $Z_{\text{eff}}$ are obtained.

Following Boon *et. al.* [56], an alternative effective valence can be defined from analytically extrapolating $\Phi_l(r)$ to the center of the cell by assuming a pointlike colloid with effective valence $Q_{\text{eff}}$ defined by

$$Q_{\text{eff}} := \lim_{r \to 0} \frac{\Phi_l'(r) r^2}{\lambda_{\text{B}}}. \tag{3.9}$$

The quantity $Q_{\text{eff}}$ is called extrapolated point charge (EPC) and its definition is triggered from noting that $\Phi_l(r \approx 0) = \lambda_{\text{B}} Q_{\text{eff}}/a$, since no screening is operative at $r = 0$. In order to directly compare the two renormalized valence definitions, one needs to account for the geometric factor in the renormalized DLVO potential. Thus, the renormalized valence $Z_{\mathrm{eff}}$ in the EPC scheme is actually defined as

$$Z_{\mathrm{eff}} = \frac{1+\kappa_{\mathrm{eff}}a}{e^{\kappa_{\mathrm{eff}}a}} Q_{\mathrm{eff}}. \tag{3.10}$$

This definition does not agree with the definition of $Z_{\mathrm{eff}}$ in Eq. (3.8), with the latter used for the SC. Depending on the choice of $\tilde{\Phi}$ with according boundary conditions, and on the SC or EPC definitions of $Z_{\mathrm{eff}}$ in Eqs. (3.8) and (3.10), respectively, four different expressions of $Z_{\mathrm{eff}}$ in terms of the independent system variables $\kappa_{\mathrm{res}}a$, $Z\lambda_{\mathrm{B}}/a$ and $\phi$ are obtained, i.e.

$$\frac{Z_{\mathrm{eff}}\lambda_{\mathrm{B}}}{a} = \gamma F_i(\kappa_{\mathrm{eff}}a, \phi^{-1/3}). \tag{3.11}$$

The four functions $F_i$, with $i = 1, ..., 4$, are obtained from $\Phi_l(r)$ in Eq. (3.6) with accordingly determined coefficients $c_{\pm}$. For the SC definition of $Z_{\mathrm{eff}}$ and linearization with respect to the edge potential (SC edge), we obtain [55]

$$F_1(x,y) = \frac{1}{x}[(x^2y-1)\sinh\{x(y-1)\} + x(y-1)\cosh\{x(y-1)\}], \tag{3.12}$$

while for the SC definition of $Z_{\mathrm{eff}}$ with linearization with respect to the mean potential (SC mean) [57], it follows

$$F_2(x,y) = \frac{x^2(y^3-1)}{3}. \tag{3.13}$$

If instead we consider the EPC definition of $Z_{\mathrm{eff}}$ with edge linearization (EPC edge), we obtain [56]

$$F_3(x,y) = (\frac{1}{x}+1)e^{-x}(xy\cosh(xy) - \sinh(xy)); \tag{3.14}$$

and, finally, for the EPC definition of $Z_{\mathrm{eff}}$ in conjunction with linearization with respect to the mean potential (EPC mean), it holds

$$F_4(x,y) = \frac{x^2(y^3-1)\xi}{3} \tag{3.15}$$

with

$$\xi = \frac{1+x}{e^x}\left[\left(e^{-x}(x+1) - \frac{e^x e^{-2yx}(x-1)(xy+1)}{xy-1}\right)^{-1} + \left(\frac{e^{-x}e^{2yx}(xy-1)(x+1)}{xy+1} - e^x(x-1)\right)^{-1}\right]. \tag{3.16}$$

Notice in all four cases that $Z_{\text{eff}} \to Z$ for $Z\lambda_{\text{B}}/a \ll 1$. For larger values of $Z$, nonlinear screening comes into play, triggered by a strong accumulation of counterions near the colloid surface so that $Z_{\text{eff}} < Z$. For large $Z$, $Z_{\text{eff}}$ approaches a plateau value $Z_{\text{eff}}^{\text{sat}}$. This so-called renormalized charge saturation is due to the invoked mean-field PB approximation of pointlike microions allowing for an arbitrarily-high surface concentration of counterions [58, 59]. The approach of $Z_{\text{eff}}$ to an (apparent) plateau value, however, is a genuine physical effect when $Z\lambda_{\text{B}}/a$ is not too large.

Using Eq. (3.1), one can show that $|\Phi(r)|$ is a strictly monotonically decreasing function with increasing radial distance $r$, implying that $|\bar{\Phi}| > |\Phi(R)|$ and consequently that $\kappa_{\text{eff}}(\text{mean}) > \kappa_{\text{eff}}(\text{edge})$. Thus, there is stronger effective screening for mean than for edge linearization.

The pros and cons of the various definition of $Z_{\text{eff}}$ will be discussed in chapter 7, where we also give numerical results.

For given $\Phi_l(\mathrm{r})$, the linear microion profiles inside the cell are given by

$$n_{\pm}^{l}(r) = n_{\text{res}} e^{\mp\tilde{\Phi}}[1 \pm \tilde{\Phi} \mp \Phi_l(r)]. \tag{3.17}$$

Integrating the linear microion charge density, $n_+^l(r) - n_-^l(r)$, and the total microion density, $n_+^l(r) + n_-^l(r)$, over the fluid volume $V_{\text{c}}^{\text{fl}}$ of a cell, and using the definition of $Z_{\text{eff}}$ in Eq. (3.8), we obtain for the effective screening parameter under mean linearization [57]

$$\kappa_{\text{eff}}^2 = \frac{4\pi\lambda_{\text{B}}}{V_{\text{fl}}}\left(Z_{\text{eff}} + 2N_{\text{s}}^{\text{eff}}\right) = \frac{4\pi\lambda_{\text{B}}}{(1-\phi)}\left(Z_{\text{eff}}n_{\text{m}} + 2n_{\text{s}}^{\text{eff}}\right). \tag{3.18}$$

Here, $N_s^{\text{eff}} = \frac{4\pi}{V_{\text{c}}^{\text{fl}}}\int_a^R r^2\, n_-^l(r)\, dr$ is the mean number of the free salt ion pairs in the suspension and $n_{\text{s}}^{\text{eff}} = N_{\text{s}}^{\text{eff}}/V_{\text{c}}$. From Eq. (3.18), we obtain the effective suspension salt concentration,

$n_{\rm s}^{\rm eff}$, related to the free (i.e. uncondensed) macroions as

$$n_{\rm s}^{\rm eff}\,a^3 = \frac{a}{8\pi\lambda_{\rm B}}\left[(1-\phi)(\kappa_{\rm eff}\,a)^2 - 3\phi\frac{Z_{\rm eff}\lambda_{\rm B}}{a}\right]. \tag{3.19}$$

Alternatively, for edge linearization, where $\tilde{\Phi} = \Phi(R)$, it holds

$$\kappa_{\rm eff}^2 = \frac{4\pi\lambda_{\rm B}}{(1-\gamma)V_{\rm fl}}\left(Z_{\rm eff} + \frac{2N_s^{\rm eff}}{1+\gamma}\right) = \frac{4\pi\lambda_{\rm B}}{(1-\phi)(1-\gamma)}\left(Z_{\rm eff}n_{\rm m} + \frac{2n_{\rm s}^{\rm eff}}{1+\gamma}\right), \tag{3.20}$$

with the effective suspension salt concentration given by

$$n_{\rm s}^{\rm eff} = \frac{\kappa_{\rm eff}^2}{8\pi\lambda_{\rm B}}(1-\phi)(1-\gamma^2) - \frac{n_{\rm m}}{2}Z_{\rm eff}(1-\gamma), \tag{3.21}$$

where $\gamma = \tanh\{\Phi(R)\}$. We notice from Eqs. (3.18) and (3.20) that the square of the effective screening constant consists of two additive contributions, namely a contribution proportional to $n_{\rm m}Z_{\rm eff}$ arising from the free (i.e. uncondensed) part of the macroion-surface released counterions, and a contribution due to free salt ion pairs.

In case of implementing EPC method for incorporating nonlinear effects, the corresponding renormalized interaction parameters are used in Eqs. (3.19) and (3.21) in order to obtain approximations of the effective suspension salt concentration for mean and edge linearizations, respectively.

From a physics viewpoint, mean linearization is more consistent than edge linearization, since in the former case the density variations of the nonlinear potential around $\Phi_l$ are of second order only, which is not the case for edge linearization. Only in mean linearization, the Donnan expression for $n_{\rm s}$ is correctly recovered to first order, where $Z_{\rm eff} = Z + \mathcal{O}([\lambda_{\rm B}Z/a]^2)$, and also the correct expression of $\kappa_{\rm eff}^2$ is recovered for $n_{\rm res} \to 0$. Different from Eq. (3.20), which invokes the factors $1/(1\pm\gamma)$, Eq. (3.18) naturally splits into free counterion and salt ion contributions. Using a proper pressure definition, mean linearization guarantees furthermore positive pressure values [60]. Another convenient feature of mean linearization is that $Z_{\rm eff}$ is directly obtained from $\bar{\Phi}$ according to

$$\frac{Z_{\rm eff}\lambda_{\rm B}}{a} = \left(\frac{1-\phi}{3\phi}\right)(\kappa_{\rm res}a)^2\sinh(\bar{\Phi}). \tag{3.22}$$

In the salt-free case, where $n_{\text{res}} = 0$, the suspension is a closed system, since no counterions can leave the cell into the empty reservoir because of electroneutrality. For a system in Donnan equilibrium, it holds that $|\Phi(R, n_{\text{res}})| \to \infty$ for $n_{\text{res}} \to 0$. To recover the salt-free system as a limiting case, one therefore redefines the salt-free system potential by

$$\Phi(r) = \lim_{n_{\text{res}} \to 0} \left[\Phi(r; n_{\text{res}}) - \Phi(R; n_{\text{res}})\right]. \tag{3.23}$$

The salt-free potential fulfills the nonlinear PB-type equation for negatively-charged macroions,

$$\Phi''(r) + \frac{2}{r}\Phi'(r) = -k_0^2 e^{-\Phi(r)}, \qquad a < r \le R, \tag{3.24}$$

where $k_0^2 = 4\pi\lambda_{\text{B}} n_+^0 > 0$ is the new electrostatic screening constant and $n_+(r) = n_+^0 \exp\{-\Phi(r)\}$ is the nonlinear counterion profile. The two boundary conditions in the salt-free system plus an equation for the additional quantity $k_0$ are

$$\Phi'(a) = \frac{Z\lambda_{\text{B}}}{a^2}; \quad \Phi'(R) = 0, \tag{3.25}$$

and

$$k_0^2 = \frac{4\pi\lambda_{\text{B}} Z}{\int_a^R d^3r \exp\{\Phi(r)\}} = \Phi''(R), \tag{3.26}$$

respectively, where the equation $k_0^2$ expresses the electroneutrality of the cell. Notice that $\Phi(R) = 0$. The present nonlinear boundary value problem can be solved self-consistently. Alternatively, it can be mapped onto a boundary value problem invoking a third-order differential equation, following Ref. [61].

Linearization of Eq. (3.24) with respect to an arbitrary value $\tilde{\Phi}$ gives

$$\Phi_l''(r) + \frac{2}{r}\Phi_l'(r) = k_0^2 \exp\{\tilde{\Phi}\}[1 + \Phi_l(r) - \tilde{\Phi}], \qquad a < r \le R, \tag{3.27}$$

with boundary conditions similar to systems with salt, and $k_0$ determined from the nonlinear boundary value problem. The renormalized screening parameter in the salt-free case follows then explicitly as

$$\kappa_{\text{eff}}^2 = k_0^2 \times \begin{cases} e^{-\bar{\Phi}}, & \text{mean} \\ e^{-\Phi(R)}, & \text{edge} \end{cases}. \tag{3.28}$$

Notice that $e^{-\Phi(R)} = 1$ under salt-free conditions. Therefore, as in the Donnan equilibrium case, it holds that $\kappa_{\text{eff}}(\text{mean}) > \kappa_{\text{eff}}(\text{edge})$. The renormalized macroion valence in the four considered cases follows from

$$\frac{Z_{\text{eff}}\lambda_{\text{B}}}{a} = F_i(\kappa_{\text{eff}}a, \phi^{-1/3}). \tag{3.29}$$

with $\gamma = 1$ and for $i \in \{1, ..., 4\}$ with $F_i(x, y)$ still given by Eqs. (3.12)-(3.16). For $Z_{\text{eff}}$ in the SC model, it follows explicitly that

$$\frac{Z_{\text{eff}}\lambda_{\text{B}}}{a}(n_{\text{res}} = 0) = \left(\frac{1-\phi}{3\phi}\right)(\kappa_{\text{res}}a)^2 e^{-\tilde{\Phi}}. \tag{3.30}$$

Since $\tilde{\Phi} = \Phi(R) = 0$ in edge linearization, and $\tilde{\Phi} = \bar{\Phi}$ in mean linearization with $\bar{\Phi} < 0$ for negatively-charged macroions, it follows that $Z_{\text{eff}}(\text{mean}) > Z_{\text{eff}}(\text{edge})$ under salt-free condition. This inequality holds empirically also when systems with salt are considered.

In the salt-free case, we can see that $\Phi(r) = \lambda_{\text{B}}Z/r$, with $Z_{\text{eff}} = Z$ and $\kappa_{\text{eff}} = 0$ for $n_{\text{m}} \to 0$ ($R \to \infty$). This expresses that the entropy of counterions dominates the electric free energy of counterion attraction to the surface in an unbounded three-dimensional space ($a < r < R \to \infty$), i.e. the $Z$ counterions around the central macroion are randomly distributed throughout space, and do not contribute to screening.

We have considered here the CM for an impermeable central macroion only. Similar CM-based charge-renormalization procedures can be also designed for a permeable macroion [62]. In section 6.3, CM renormalization procedure for permeable macroions is employed in our discussion of the concentration-dependent deswelling of weakly cross-linked ionic microgels.

## 3.2 (Non-)Penetrating renormalized jellium model (RJM)

Different from the spherical CM, which is motivated by a crystalline order of the suspension, the renormalized jellium model (RJM) describes fluid-like suspensions. This charge-renormalization scheme, used alternatively to provide renormalized values $Z_{\text{eff}}$ and $\kappa_{\text{eff}}$ as input to the linear electrostatic DLVO potential, is based on the JA [9], described earlier in subsection 2.4.3. In the JA, a spherical macroion of radius $a$ is singled out and positioned at the origin of the coordinate frame. The remaining $(N_\mathrm{m} - 1)$ macroions and their condensed counterions are assumed to form a uniform neutralizing background, called the jellium, smeared out in the infinite fluid space $r > a$, where the uncondensed counterions and coions can freely move [63]. Assuming a Boltzmann distribution for the pointlike, monovalent free microions and a uniform, structureless jellium for the remaining macroions, i.e. $g_\mathrm{mm}(r) = 1$ for $r > a$, the resulting nonlinear PB equation for the total (reduced) electrostatic potential $\Phi$ in Donnan equilibrium has the form [64]

$$\Phi''(r) + \frac{2}{r}\Phi'(r) = \kappa_\mathrm{res}^2 \sinh\{\Phi(r)\} + 3\phi\frac{Z_\mathrm{back}\lambda_\mathrm{B}}{a^3}, \qquad r > a, \tag{3.31}$$

where $\kappa_\mathrm{res}^2 = 8\pi\lambda_\mathrm{B} n_\mathrm{res}$. The first term on the right-hand side is the reduced charge-density contribution by the microions, while the second term is the (reduced) uniform jellium charge density outside the central macroion, with $Z_\mathrm{back}$ denoting the background macroion valence. The latter is taken to be equal to $Z_\mathrm{eff}$, and is self-consistently determined. The boundary conditions guaranteeing a unique solution are $\Phi'(a) = Z\lambda_\mathrm{B}/a^2$, with $Z$ the bare macroion valence, and $\Phi'(r \to \infty) = 0$, accounting for electroneutrality with an asymptotically decaying electric field. Different from the electric field, the electrostatic potential at infinity $r \to \infty$, called Donnan potential, $\Phi_\infty$, is non-zero and given by

$$\Phi_\infty = \operatorname{arsinh}\left[-\frac{3\phi}{(\kappa_\mathrm{res}a)^2}\frac{Z_\mathrm{back}\lambda_\mathrm{B}}{a}\right] \tag{3.32}$$

in terms of $Z_\mathrm{back}$. This boundary value problem can be solved numerically only. Linearizing Eq. (3.31) with respect to $\Phi_\infty$, we obtain the linearized electrostatic potential, $\Phi_l(r)$ satisfying

$$\Phi_l''(r) + \frac{2}{r}\Phi_l'(r) = \kappa_\mathrm{eff}^2(\Phi_l(r) - \Phi_\infty), \qquad r > a, \tag{3.33}$$

with effective screening constant $\kappa_{\text{eff}}^2 = \kappa_{\text{res}}^2 \cosh\{\Phi_\infty\}$, which can be alternatively written as

$$(\kappa_{\text{eff}} a)^4 = (\kappa_{\text{res}} a)^4 + \left(3\phi \frac{Z_{\text{back}} \lambda_{\text{B}}}{a}\right)^4. \tag{3.34}$$

We see that $(\kappa_{\text{eff}} a)^4$ has two clearly distinguishable contributions: the first one due to the salt microions, given by the reservoir salt concentration, and the second one, due to microion-dressed macroions. The boundary conditions determining $\Phi_l$ uniquely are $\Phi_l'(r \to \infty) = 0$, expressing overall electroneutrality of the infinite jellium system, and $\Phi_l(r) \sim \Phi(r)$ for $r \to \infty$, demanding that the linear solution matches the nonlinear one asymptotically. As in the CM, the effective valence, $Z_{\text{eff}}$, is obtained from $\Phi_l$ using [63, 64]

$$Z_{\text{eff}} := \frac{\Phi_l'(a)\, a^2}{\lambda_{\text{B}}}. \tag{3.35}$$

The solution of Eq. (3.33) can be analytically expressed in terms of $Z_{\text{eff}}$ as

$$\Phi_l(r) - \Phi_\infty = \frac{Z_{\text{eff}} \lambda_{\text{B}} e^{\kappa_{\text{eff}} a}}{1 + \kappa_{\text{eff}} a} \frac{e^{-\kappa_{\text{eff}} r}}{r}, \qquad r > a. \tag{3.36}$$

Finally, from comparing Eq. (3.36) against the likewise-exponential asymptotic form of the non-linear solution $\Phi(r)$, we obtain $Z_{\text{eff}}$ in terms of $Z_{\text{back}}$. In order to find $Z_{\text{eff}}$, we demand self consistency by requiring that $Z_{\text{eff}} = Z_{\text{back}}$ [64], from which $Z_{\text{eff}}$ is obtained iteratively using a selected starting value $Z_{\text{back}}$<Z.

Similarly to the CM, we obtain a relation between semi-open and closed systems. This link follows from the mean concentration of the free co- and counterions inside the suspension [63],

$$n_\pm = n_{\text{res}} \exp\{\mp\Phi_\infty\}. \tag{3.37}$$

The effective suspension salt pair concentration, $n_{\text{s}}^{\text{eff}}$, is thus obtained in terms of $n_{\text{res}}$ and $\Phi_\infty$ as

$$n_{\text{s}}^{\text{eff}} = n_- = n_{\text{res}} \exp\{\Phi_\infty\} \leq n_{\text{res}}, \tag{3.38}$$

since $\Phi_\infty < 0$ holds for negatively charged colloids. Just as in the renormalized CM, the renormalized valence, $Z_{\text{eff}}$, in RJM asymptotes to a saturation value when $Z \to \infty$. Likewise, typically $Z_{\text{eff}} < Z$ and it is found that $Z_{\text{eff}} \to Z$ and $\kappa_{\text{eff}} \to \kappa_{\text{res}}$ in the limits $\phi \to 0$ and $n_{\text{res}} \to 0$.

In the salt-free case, suspension electroneutrality requires that $n_+^0 \exp(-\Phi_\infty) = Z_{\text{back}} n_{\text{m}}$ together with $\Phi(r) \to 0$ for $r \to \infty$. Thus, the nonlinear PB equation, Eq. (3.31), acquires the form

$$\Phi''(r) + \frac{2}{r}\Phi'(r) = -3\phi \frac{Z_{\text{back}}\lambda_{\text{B}}}{a^3}(\exp\{-\Phi(r)\} - 1), \qquad r > a, \tag{3.39}$$

with boundary conditions $\Phi'(a) = Z\lambda_{\text{B}}/a^2$ and $\Phi(r \to \infty) = 0$. Linearizing the right-hand side of Eq. (3.39) around $\Phi_\infty = 0$ , one obtains

$$\Phi_l''(r) + \frac{2}{r}\Phi_l'(r) = \kappa_{\text{eff}}^2 \Phi_l(r), \qquad r > a, \tag{3.40}$$

where

$$\kappa_{\text{eff}}^2 = 4\pi\lambda_{\text{B}} Z_{\text{back}}, \tag{3.41}$$

and the boundary conditions are $\Phi_l'(r \to \infty) = 0$ and $\Phi_l(r) \sim \Phi(r)$ for $r \to \infty$. With the effective valence defined by Eq. (3.35), the solution of Eq. (3.40) has the form

$$\Phi_l(r) = \frac{Z_{\text{eff}}\lambda_{\text{B}} e^{\kappa_{\text{eff}} a}}{1 + \kappa_{\text{eff}} a} \frac{e^{-\kappa_{\text{eff}} r}}{r}, \qquad r > a. \tag{3.42}$$

As for a system with added salt, $Z_{\text{eff}}$ is determined from asymptotically matching the linearized potential $\Phi_l(r)$ to the nonlinear one for a selected $Z_{\text{back}}$. Using again the self-consistency assumption $Z_{\text{back}} = Z_{\text{eff}}$, $Z_{\text{eff}}$ is obtained for a salt-free system.

A variant of the discussed non-penetrating RJM is the penetrating RJM, where the neutralizing jellium is not only smeared out across the fluid volume $r > a$, but also penetrates the volume of the central colloid while the microions are still expelled. This leads to the same PB equation Eq. (3.31) for $r > a$, but with boundary conditions

$$\begin{aligned} \Phi'(a) &= \frac{\lambda_{\text{B}}}{a^2}(Z + Z_{\text{back}}\phi), \\ \Phi'(r \to \infty) &= 0. \end{aligned} \tag{3.43}$$

The inner boundary condition states now that the electric field on the surface of the central colloid is due to the bare charge, $-Ze$, of the central colloid plus an additional contribution,

$Z_{\text{back}}\phi$, arising from the penetrating jellium charge inside the volume of the central colloid. Charge renormalization is introduced identically to the non-penetrating jellium case, by linearization with respect to $\Phi_\infty$. The inner boundary condition in Eq. (3.43) involves now the altered self-consistency condition $Z_{\text{eff}} = Z + \phi Z_{\text{back}}$, which implies that $Z_{\text{eff}} = Z(1+\phi) + \mathcal{O}(Z^2)$ for small $Z$. This is the same effective charge obtained from the high-temperature-limiting MSA solution.

## 3.3 Renormalized linear response theory (RLRT)

In this section, we discussed how charge renormalization can be implemented into the LRT multi-colloid-center model for strongly charged macroions. We address here the case of impermeable colloids only. As discussed, assuming a weak perturbation of the (Swiss-cheese-like) uniform microion distribution by the charged colloids, LRT [65] provides an analytic expression of the effective one-component effective Hamiltonian, $H_{\text{eff}} = H_{\text{mm}} + \Omega_\mu$, and, consequently, of the semi-grand free energy $\Omega$. The LRT effective Hamiltonian is stated in Eq. (2.45), the volume energy $E_{\text{vol}}$ in Eq. (2.56), and the effective pair potential between the microion-dressed colloids in Eq. (2.54) for $r > \sigma$. The screening constant is $\kappa^2 = 4\pi\lambda_{\text{B}}(n_+ + n_-)/(1-\phi)$, where the excluded volume of the macroions is accounted for by the factor $1/(1-\phi)$.

The applicability of LRT ceases when, for larger colloid charges $Z\lambda_{\text{B}}/a \gtrsim 1$, nonlinear screening effects due to strengthening of macroion-microion correlations come into play, resulting in a strong accumulation of counterions near the macroion surface [65, 66]. The LRT can be extended to more strongly correlated macroion suspensions by explicitly distinguishing between surface-bounded microions and so-called free microions in the volume (grand-free) energy according to

$$E_{\text{vol}} = \Omega_{\text{free}} + F_{\text{bound}}, \tag{3.44}$$

by analyzing the balance between electric and thermal microion energies [67]. The grand-free energy, $\Omega_{\text{free}}$, of the free microions is treated to quadratic order, providing formally the same effective pair potential for the colloidal particles as in Eq. (2.54), but now characterized by a renormalized effective valence, $Z_{\text{eff}} \leq Z$, and renormalized effective screening constant, $\kappa_{\text{eff}}$, both depending on the state-dependent concentration of free microions. The fraction of strongly-associated, i.e. bound, microions is related to an association shell $(a, a+\delta)$ of thickness $\delta$ surrounding a macroion, which is determined as the distance from the microion surface at which the electrostatic energy of attraction of a counterion is comparable to its thermal energy, i.e.

$$e|\Phi(a+\delta)| = Ck_{\text{B}}T, \tag{3.45}$$

where $\Phi(r)$ is the (LRT-orbital) electrostatic potential at distance $r$ from a colloid center and $C$ is a selected number of order unity. Using LRT combined with this microion-association scheme, the reduced electrostatic potential around a dressed colloid is of the form

$$\Phi(r) = -Z_{\text{eff}}\lambda_{\text{B}} \frac{e^{\kappa_{\text{eff}}(a+\delta)}}{1+\kappa_{\text{eff}}(a+\delta)} \frac{e^{-\kappa_{\text{eff}} r}}{r}, \quad r \geq a+\delta, \tag{3.46}$$

with $\kappa_{\text{eff}}^2 = 4\pi\lambda_{\text{B}}(\tilde{n}_+ + \tilde{n}_-)$ being the effective (renormalized) screening constant. Moreover, $\tilde{n}_\pm = \tilde{N}_\pm/[N_{\text{m}}(1-\tilde{\phi})]$ and $\tilde{N}_\pm$ are the mean number densities and numbers of free microions, respectively, and $\tilde{\phi} = \phi(1+\delta/a)^3$ is the effective volume fraction of the macroions including their macroion-association shells. Notice that $\kappa_{\text{eff}}$ can be rewriten as

$$\kappa_{\text{eff}}^2 = \frac{4\pi\lambda_{\text{B}}}{(1-\phi)} \left( Z_{\text{eff}}\, n_{\text{m}} + 2\tilde{n}_{\text{s}}^{\text{eff}} \right), \tag{3.47}$$

using electroneutrality and $\tilde{n}_- = \tilde{n}_{\text{s}}^{\text{eff}}$, with $\tilde{n}_{\text{s}}^{\text{eff}}$ the renormalized salt concentration of free microion pairs. Substituting Eq. (3.46) into Eq. (3.45), the association shell thickness is determined by

$$\left| \frac{Z_{\text{eff}}\lambda_{\text{B}}}{[1+\kappa_{\text{eff}}(a+\delta)](a+\delta)} + \bar{\Phi} \right| = C, \tag{3.48}$$

for given $Z_{\text{eff}}$, $\phi$, and $C$, on noting that $\kappa_{\text{eff}}$ depends self-consistently on $\delta$. The mean potential value has the form $\bar{\Phi} = -(\tilde{n}_+ - \tilde{n}_-)/(\tilde{n}_+ + \tilde{n}_-)$. Typically, and somewhat arbitrarily, C is taken equal to 1.

The distinction between strongly-associated and freely-moving microions implies a corresponding separation of the total grand free energy $\Omega$. The free microions are only weakly correlated with the macroions, and thus well described by linear-response theory. The volume grand free energy per macroion, $\varepsilon_{\text{vol}} = E_{\text{vol}}/N_{\text{m}}$, has the form

$$\varepsilon_{\text{vol}} = \sum_{i=\pm} \frac{\tilde{N}_i}{N_{\text{m}}} \left[ \ln \left( \frac{\tilde{n}_i}{n_{\text{res}}} \right) - 1 \right] - \frac{Z_{\text{eff}}^2}{2} \frac{\lambda_{\text{B}} \kappa_{\text{eff}}}{1 + \kappa_{\text{eff}}(a + \delta)} - \frac{Z_{\text{eff}}}{2} \frac{\tilde{n}_+ - \tilde{n}_-}{\tilde{n}_+ + \tilde{n}_-} + f_{\text{bound}} \tag{3.49}$$

with the free energy per microion of bound counterions given by

$$f_{\text{bound}} \approx (Z - Z_{\text{eff}}) \left[ \ln \left( \frac{(Z - Z_{\text{eff}})}{v_s} \Lambda_0^3 \right) - 1 \right] + \frac{Z_{\text{eff}}^2 \lambda_{\text{B}}}{2a}. \tag{3.50}$$

The first term on the right side is the ideal-gas free energy of the bound counterions in the association shell of volume $v_{\text{s}} = (4\pi/3)[(a + \delta)^3 - a^3]$, and the second term accounts for the self-energy of a dressed macroion of valence $Z_{\text{eff}}$, assuming the bound counterions to be localized near the macroion surface ($r = a$). Here, $\Lambda_0$ is the microion thermal de Broglie wavelength assumed to be equal for ± ions.

The effective macroion valence, $Z_{\text{eff}}$ and hence the association shell thickness, $\delta$, can be determined then by equating the chemical potentials of microions in the free and bound phases. It can be shown that this is equivalent to minimizing the volume grand-free energy, $\varepsilon_{\text{vol}}$, at fixed temperature and mean microion densities [65]. The effective macroion valence, $Z_{\text{eff}}$ is then obtained, for given bare valence $Z$, by the variational condition,

$$\left( \frac{\partial \varepsilon_{\text{vol}}}{\partial Z_{\text{eff}}} \right)_{T, \tilde{n}_\pm} = 0. \tag{3.51}$$

Notice that $Z_{\text{eff}}$ and $\delta$ are inter-related by Eq. (3.48). The effective valence, $Z_{\text{eff}}$, and corresponding shell thickness, $\delta$, determine in turn the effective screening constant $\kappa_{\text{eff}}$.

## 3.4 Shifted Debye-Hückel approximation (SDHA)

The SDHA method was developed by Boon et. al. in [56]. Like the RLRT, it is a multi-colloid-center method based on DFT-PB-type approximations similar to the ones discussed in subsection 2.4.1. As originally done in [56], we present its essentials for suspensions of impermeable colloids.

Assuming for the moment pointlike macroions, we formally expand the DFT-PB grand-free energy functional $\hat{\Omega}_\mu(\mathbf{X})$ in Eq. (2.17) in the presence of $N_\mathrm{m}$ (pointlike) macroions at positions $\mathbf{X}$ up to quadratic order in the microion trial densities $\rho_\pm(\mathbf{r};\mathbf{X}) - \bar{n}_\pm$, measured relative to yet-unknown constant densities $\bar{n}_\pm$. In the considered Donnan equilibrium, these densities $\bar{n}_\pm$ are not taken independently, but are related by

$$\bar{n}_\pm = n_\mathrm{res} e^{\pm\tilde{\Phi}}, \tag{3.52}$$

for a yet unspecified potential value, $\tilde{\Phi}$, so that $\bar{n}_+\bar{n}_- = n_\mathrm{res}^2$. Minimizing $\hat{\Omega}_\mu(\mathbf{X})$, quadratically expanded with respect to the trial microion densities $\bar{n}_\pm$, the linearized equilibrium microion profiles

$$n_\pm(\mathbf{r};\mathbf{X}) = n_\mathrm{res}\, e^{\mp\tilde{\Phi}} \left[1 \mp \left(\Phi_l(\mathbf{r};\mathbf{X}) - \tilde{\Phi}\right)\right], \qquad \mathbf{r} \in \mathbb{R} \tag{3.53}$$

are obtained, with the linearized suspension potential $\Phi_l(\mathbf{r};\mathbf{X})$. The so-called shifted linearized potential, $\Phi_l^\mathrm{s}(\mathbf{r};\mathbf{X})$, defined by

$$\Phi_l^\mathrm{s}(\mathbf{r};\mathbf{X}) = \Phi_l(\mathbf{r};\mathbf{X}) - \tilde{\Phi} + \gamma, \tag{3.54}$$

for $\gamma = \tanh(\tilde{\Phi})$, fulfills the multi-colloid-center linearized PB equation (shifted DH equation)

$$\Delta\Phi_l^\mathrm{s}(\mathbf{r};\mathbf{X}) = \kappa_\mathrm{eff}^2\, \Phi_l^\mathrm{s}(\mathbf{r};\mathbf{X}) - 4\pi\lambda_\mathrm{B} q(\mathbf{r};\mathbf{X}), \qquad \mathbf{r} \in \mathbb{R}^3. \tag{3.55}$$

Here,

$$q(\mathbf{r};\mathbf{X}) = \sum_{j=1}^{N_\mathrm{m}} \delta(\mathbf{r} - \mathbf{R}_j) Q_\mathrm{eff} \tag{3.56}$$

is the charge density of pointlike macroions at positions $\mathbf{X} = \{\mathbf{R}_1, \dots, \mathbf{R}_{N_\mathrm{m}}\}$, where charge renormalization (discussed further down) is accounted for in the effective macroion valence $Q_\mathrm{eff}$. Moreover, $\kappa_\mathrm{eff}^2 = \kappa_\mathrm{res}^2 \cosh(\tilde{\Phi})$ is taken as the renormalized screening parameter linked to $Q_{\rm eff}$. By means of Fourier transformation, one straightforwardly obtains the solution

$$\Phi^{\rm s}_l(\mathbf{r};\mathbf{X}) = \lambda_{\rm B} Q_{\rm eff} \sum_{j=1}^{N_{\rm m}} \frac{e^{-\kappa_{\rm eff}|\mathbf{r}-\mathbf{R}_j|}}{|\mathbf{r}-\mathbf{R}_j|}, \tag{3.57}$$

for the shifted linearized potential, which is a superposition of $N_{\rm m}$ Yukawa-type orbitals. Substitution of $n_\pm(\mathbf{r};\mathbf{X})$, according to Eq. (3.53), into the quadratic-order expanded microion grand free energy results in

$$\beta\Omega_\mu(\mathbf{X}) = \beta E_{\rm vol} + \lambda_{\rm B} Q^2_{\rm eff} \sum_{i<j}^{N_{\rm m}} \frac{e^{-\kappa_{\rm eff}|\mathbf{R}_i-\mathbf{R}_j|}}{|\mathbf{R}_i-\mathbf{R}_j|} \tag{3.58}$$

with volume energy

$$\beta E_{\rm vol} = -V\frac{\kappa^2_{\rm eff}}{8\pi\lambda_{\rm B}}\left(\frac{\kappa^4_{\rm res}}{\kappa^4_{\rm eff}}+1\right) + N_{\rm m} Q_{\rm eff}(\tilde{\Phi}-\gamma) \tag{3.59}$$

where V is the macroscopic suspension volume.

So far, we have not specified the value of $\tilde{\Phi}$, and hence the resulting value for $\kappa_{\rm eff}$ and $Q_{\rm eff}$. This is done now using, for simplicity, a spherical CM with $\tilde{\Phi}$ identified as $\Phi(R)$ or $\bar{\Phi}$. The first identification, $\tilde{\Phi} = \Phi(R)$, was made in [56]. The macroion effective valence $Q_{\rm eff}$, defined using in Eq. (3.9), is related to the effective valence $Z_{\rm eff}$ by Eq. (3.10), i.e. $Z_{\rm eff}$ is obtained from $Q_{\rm eff}$ by multiplying the latter with a geometric factor due to the actually finite radius of the macroions. The hard-core of the macroions is reintroduced a posteriori in the same way as discussed earlier by enforcing electroneutrality of the individual orbitals, leading to the geometric factor in the relation between $Z^{\rm EPC}_{\rm eff}$ and $Q_{\rm eff}$.

Quite interestingly, and different from the CM with SC definition of the renormalized valence in Eq. (3.8), $Z^{\rm EPC}_{\rm eff}$ in the EPC definition can be to some extent larger than the bare colloid valence $Z$ for high colloid concentration and small coupling $Z\lambda_{\rm B}/a$, where nonlinear charge renormalization effects are negligible.

In the salt-dominated case where $2n_{\rm res} \gg n_{\rm m}Z$, one finds $Z^{\rm EPC}_{\rm eff} \to Z$ and $\kappa_{\rm eff} \to \kappa_{\rm res}$. The volume energy reduces then to the DFT-PB volume energy in Eq. (2.31), and the effective pair potential to the DH one in Eq. (2.30).

# Chapter Four

# MEAN-FIELD THEORY OF SOFT PERMEABLE PARTICLES

In this chapter, we focus on suspensions of soft ion- and solvent permeable spherical charged colloidal particles, with the aim of modeling ionic-microgel suspensions. We begin by presenting the basic theoretical background for describing particles with state-dependent equilibrium size. We briefly introduce the elastic Hertz potential and the Flory-Rehner theory for modeling, in a coarse-grained way, the polymeric nature of the microgels. In combination with the effective electrostatic interaction descriptions of chapter 2, we derive total effective pair potentials for suspensions of stimuli-responsive ionic microgels. Finally, we end the chapter by presenting two mean-field methods for calculating the concentration-dependent equilibrium size of weakly cross-linked ionic microgels. Numerical results by these methods are presented in chapter 6.

## 4.1 Soft Hertz potential

The Hertz potential quantifies changes in the elastic energy of two deformable objects when subjected to an axial compression [68]. It has been derived within linear elasticity theory using geometric considerations [69]. Due to its simple functional form, the Hertz potential for elastic spherical particles has been extensively used to model the elastic repulsive interaction of weakly deformable macromolecules, such as star polymers, globular micelles [68] and spherical microgels [12, 15, 70–72].

For two overlapping, identical elastic spheres of Hertz radius $a_{\mathrm{H}}$ at center-to-center separation $r$, the Hertz potential reads [12]

$$\beta u_{\mathrm{H}}(r) = \begin{cases} \varepsilon_{\mathrm{H}} \left(1 - \frac{r}{2a_{\mathrm{H}}}\right)^{5/2} , & r \leq 2a_{\mathrm{H}} \\ 0\,, & r > 2a_{\mathrm{H}} \end{cases} , \tag{4.1}$$

with softness parameter

$$\varepsilon_{\mathrm{H}} = \frac{16 Y a_{\mathrm{H}}^3}{15(1-\nu^2)}, \tag{4.2}$$

where $\nu$ is Poisson's ratio and $Y$ is Young's modulus of the particle material, related to each other via the bulk modulus $K$ by $Y = 3K(1-2\nu)$ [15]. In the limit $k_{\mathrm{B}}T/\varepsilon_{\mathrm{H}} \to 0$, the hard-sphere potential is recovered, while for $k_{\mathrm{B}}T/\varepsilon_{\mathrm{H}} \to \infty$ the system approaches ideal gas behavior.

In this work, we utilize the Hertz potential for modelling the steric elastic repulsion of two spherical ionic microgel particles at small overlap, and for temperatures smaller than the low critical solution temperature of the corresponding polymer solution. Under such conditions, the Hertz soft particle radius $a_{\mathrm{H}}$ is identified with the equilibrium (swollen) radius $a$. For polymer gels in good solvents, scaling theory [19] predicts that Young's modulus scales linearly with temperature and crosslinker number density according to $Y \propto T N_{\mathrm{ch}}/a^3$, with $N_{\mathrm{ch}}$ the number of chains in between two crosslinkers [15]. Thus, the reduced interaction (softness) parameter $\varepsilon_{\mathrm{H}}$ is determined by the single-particle elastic moduli, independent of temperature and particle volume [12], and it scales linearly with the number of chains $N_{\mathrm{ch}}$ constituting the microgel polymeric network, neglecting any dependence of $\nu$ on the swelling ratio $\alpha = a/a_0$ [15]. Here, $a_0$ is the dry radius of the microgels, namely the radius of the microgels in the collapsed state at temperatures $T > T_{\mathrm{cr}}$, where $T_{\mathrm{cr}}$ is the lower critical solution temperature of the corresponding polymer solution.

When describing spherical microgels suspensions, the Hertz potential is typically implemented under the assumption that the interacting elastic spheres are only slightly deformed. Clearly, this does not hold for very large compression or at high microgel concentrations (well above the overlap concentration)[68]. This important point has been recently assessed by means of simulations of neutral microgels using a sophisticated simulation method [73]. The simulations allowed to calculate all elastic moduli of microgels as functions of the crosslinker concentration and to determine the effective interactions between two microgels, and connect hereby the elastic properties to the effective pair potential. By doing this, in [73] the range of validity of the Hertz potential was assessed, showing that it holds up to nominal packing fractions smaller than $\phi \approx 1$. In another study, based on a combination of numerical calculations and experiments on core-corona microgel suspensions, a multi-Hertzian model was proposed in order to properly describe more complex inter-microgel interactions [74]. Notice further that the Hertz potential is defined in terms of single-particle properties. The definition of the microgel size and the calculation of the elastic moduli of single microgels are ambiguous and challenging tasks. In fact, an important point is that, to validate the Hertz potential description and thus to examine the link between single-particle elasticity and bulk behavior, the simultaneous knowledge of at least two elastic moduli is required [73].

## 4.2 Flory-Rehner theory for microgel polymer backbones

The Flory–Rehner theory provides an approximate expression for the change in free energy upon solvent-induced swelling of a cross-linked polymer network. This expression is obtained by considering, first, the entropy change due to mixing of solvent molecules with chains of the cross-linked network structure; second, the chain configurational entropy change resulting from an expansion of the network; and third, the energy change of mixing. The entropy change due to the mixing of solvent molecules and cross-linked network chains is approximated by the entropy change for mixing disoriented polymers and solvent. Assuming that there is no volume change on mixing, and a microscopically uniform mixture, which is randomly-mixed, the entropy of mixing is that of and ideal gas, i.e. [18]

$$\Delta S_{\text{mix}} = -T\left[N_1 \ln \phi_1 + N_2 \ln \phi_2\right], \tag{4.3}$$

where $N_1$ and $N_2$ are the numbers of solvent and solute (monomer) molecules, respectively, and $\phi_1$ and $\phi_2$ are the volume fractions of solvent and solute. Since $\phi_{1,2} < 0$, the mixing entropy is always positive and hence promotes mixing. This entropic contribution includes translational entropy only and assumes that the conformational entropy of a polymer is identical in the mixed and pure states.

Assuming a lattice model, namely the polymer and solvent molecules constituting the solution are disposed occupying sites in a lattice, and considering that the molecules are placed into the lattice sites randomly, ignoring any correlations, the energy change of mixing *per molecule*, in mean-field approach, is given by [75]

$$\Delta u_{\text{mix}} = \chi \phi_{\text{p}}(1 - \phi_{\text{p}}), \tag{4.4}$$

where $\phi_{\text{p}}$ is the volume fraction of monomers, and $\chi$ is the Flory solvent-polymer interaction parameter. Here, it is also assumed that the mixing takes place at constant volume, and the interactions between the polymer backbone monomers are assumed to be small enough, that interparticle correlations between the monomers along the chain can be ignored. Eq. (4.4) describes the energy change when going from an unmixed two-phases system to a randomly mixed system keeping the system volume constant. The Flory interaction parameter is explicitly defined by

$$\chi = \beta \, \frac{\nu}{2} \, (2u_{12} - u_{11} - u_{22}), \tag{4.5}$$

where $\nu$ is the coordination number of the lattice, and $u_{ij}$ represents the pair energy between adjacent lattice sites occupied by species $i$ and $j$, with $i, j \in \{1, 2\}$ [75]. One can show that

$\chi \propto B\, v_1$, where $B$ represents the interaction energy density characteristic of the solvent-solute pair and $v_1$ is the molar volume of the solvent (species 1) [18]. Depending on the sign of the Flory interaction parameter $\chi$, this energetic contribution can be positive (opposing mixing), e.g. for hydrophobic polymer backbones; zero in case of ideal mixture; or negative (favoring mixing). It is important to notice that, in deriving Eq. (4.4), it is assumed that there is no volume change of the monomers upon mixing. In case of volume change on mixing and local packing effects, the temperature dependence of the Flory interaction parameter is empirically taken as

$$\chi(T) \approx A + \frac{C}{T}, \tag{4.6}$$

where the first term $A$ on the right-hand side is referred to as the entropic part, and the second one as the enthalpic part [75].

Assuming that during swelling the deformation of the polymer network takes place without any appreciable change in the internal energy of the network structure, apart from the mixing with the solvent, the free energy change produced by the network expansion is proportional to the entropy change of the deformation. The latter results from combining the entropy changes due to both the deformation of the chain end-to-end vector distribution and the crosslinking of the chains to form the final network. Considering a network composed of $N_{\mathrm{ch}}$ randomly crosslinked chains, whose end-to-end displacements are adequately described by a Gaussian probability distribution, the elastic free-energy contribution of the swelling for isotropic deformation is of the form [18]

$$\beta \Delta F_{\mathrm{el}} = \frac{3}{2} N_{\mathrm{ch}} (\alpha_d^2 - \ln \alpha_d - 1), \tag{4.7}$$

with $\alpha_d$ denoting the linear deformation factor.

Combining Eqs. (4.3), (4.4) and (4.7), one obtains an expression for the free energy change due to the isotropic (de)swelling of spherical microgels. Bearing in mind that the number of polymer monomers remains constant upon swelling, the resulting mean-field free energy change per microgel is of the form [15, 72]

$$\beta f_{\mathrm{p}}(a) = N_{\mathrm{mon}}[(\alpha^3 - 1)\ln(1-\alpha^{-3}) + \chi(1-\alpha^{-3})] + \frac{3}{2}N_{\mathrm{ch}}(\alpha^2 - \ln\,\alpha - 1)\,. \tag{4.8}$$

Here, $N_{\mathrm{mon}}$ is the total number of polymer monomers in a microgel, and the number of solvent molecules and the solvent volume fraction are written in terms of the swelling ratio $\alpha = v_{\mathrm{swo}}/v_{\mathrm{dry}}$, with $v_{\mathrm{swo}}$ and $v_{\mathrm{dry}}$ the volume of the swollen and dry microgel, respectively. The dry state of microgels is the state where microgels collapse draining out the solvent content. This corresponds to temperatures $T > T_{\mathrm{cr}}$, where $T_{\mathrm{cr}}$ is the lower critical solution temperature of the according polymer solution. The first term on the right-hand side of Eq. (4.8) is the ideal mixing entropy of microgel monomers and solvent molecules; the second term, proportional to $\chi$, accounts for polymer-solvent interactions; and the last term accounts for the elastic free energy. As argued in [15, 72], the approximations employed here for the microgel backbone self-energies are reasonable for loosely cross-linked, uniformly structured microgels.

The Gaussian model is reasonable for chain end-to-end displacements much shorter than the polymer contour length, which implies swelling ratios $\alpha \ll \sqrt{N_{\mathrm{mon}}/N_{\mathrm{ch}}}$ [15]. Although the presented Flory-Rehner theory was originally developed for macroscopic gels, it yields a reasonable description of the elastic properties of loosely cross-linked microgel suspensions, despite of overestimating the solvency parameter [15]. An extension to more-crosslinked networks is achieved by accounting for the crosslinking effects on the structural entropy of the network and on the entropy change under derformation, as it was done in Refs. [16, 17] for a randomly cross-linked network with tetrafunctional cross-linkers.

## 4.3 Stimuli-responsive particles: Equilibrium size determination

Ion- and solvent-penetrable, charged colloidal particles might experience an intrinsic (osmotic) pressure, due to the heterogeneous distribution of ionic species inside and outside of the colloidal particles. Changes in the system conditions, such as temperature and colloidal concentration, produce consequential changes in the osmotic pressure difference between the inside and outside of the particles away from zero. To recover equilibrium, where the intrinsic pressure is again zero, the equilibrium size of the microgels is readjusted accordingly.

Ionic microgel paticles are typically globular particles consisting of a cross-linked network of polyelectrolyte chains. When dispersed in a polar solvent under good solvent conditions, an ionic microgel particle becomes charged due to the dissociation of counterions from ionizable groups on its polymer backbone. For weak cross-linking, the forces exerted by the intrinsic osmotic pressure variations are comparable to the elastic and entropic forces in the network. Therefore, the soft particles (de)swell to an equilibrium size, characterized by an equilibrium radius $a$ that can be substantially larger than the one in the dry state $a_0$, in response to variations in the environmental conditions.

To study ionic microgel suspensions, we implement an effective one-component suspension description, similar to that for charge-stabilized colloids (see chapter 2), but now accounting for the polymeric degrees of freedom in a coarse-grained way. We describe here the employed microgel model, and the essential steps of tracing out the microion and polymer-backbone monomeric degrees of freedom, leading to an effective one-component microgel suspension description of pseudo-microgels interacting via a state-dependent effective pair potential [14, 15, 72].

For simplicity, we assume that the ionic microgels have a uniform distribution of backbone polyelectrolyte monomers, cross-linkers, and backbone charges [15]. The charged microgel backbone polymers and cross-linkers coexist with polymer-released counterions and salt ions dissolved in the solvent. For temperatures $T > T_{\mathrm{cr}}$ higher than the lower critical solution temperature (LCST) $T_{\mathrm{cr}}$ of the corresponding polymer solution, the microgels are collapsed into a dry state, characterized by a dry radius $a_0 < a$, where $a$ is the microgel equilibrium radius of a swollen microgel particle at a temperature $T$ lower than the LCST. The swollen microgel radius $a$ depends, in addition to temperature and solvent quality, on the elastic properties of the backbone network and the backbone charge, and furthermore on the microgel concentration and background (reservoir) ionic strength. Assuming that a single microgel consists of a uniform polymer network with $N_{\mathrm{mon}}$ monomers, the dry microgel radius $a_0$ is well approximated by $a_0 \approx (N_{\mathrm{mon}}/\phi_{\mathrm{rcp}})^{1/3} a_{\mathrm{mon}}$, where $\phi_{\mathrm{rcp}} = 0.64$ is the volume fraction for random close-packing of spherical monomers and $a_{\mathrm{mon}}$ is the monomer radius. It is assumed here that random close-packing is the unstressed polymer backbone structure in the collapsed state [16–18, 62].

Identifying the whole microgel as an ion-permeable macroion, a similar treatment to the one in section 2.4 regarding the electrostatic part of the interactions can be made. Consider a monodisperse microgel suspension formed by $N_{\mathrm{m}}$ spherical microgels, each of negative backbone charge $-Ze$, with $e$ the proton charge, dispersed in water at temperature $T$ and for (suspension) volume $V$. The suspension is taken in (Donnan) osmotic equilibrium with a strong 1:1 electrolyte reservoir of ion concentration $2n_{\mathrm{res}}$. The counterions dissociated from the polymer backbones are likewise taken as monodisperse. The microgel concentration (number density), $n_{\mathrm{m}} = N_{\mathrm{m}}/V$, determines the volume fraction $\phi_0 = 4\pi a_0^3 n_{\mathrm{m}}/3$ of dry microgels and the volume fraction $\phi = 4\pi a^3 n_{\mathrm{m}}/3$ of the swollen microgels. The dry volume fraction should be thought of as a non-dimensionalized microgel concentration. For simplicity, the backbone valence $Z > 0$ is assumed to be constant, independent of concentration, ionic strength, and equilibrium radius, thus disregarding possible chemical charge regulation effects. Here, $Z$ should be viewed as a net backbone valence, already accounting for the possibility of Manning counterion condensation at polymer sites. Global electroneutrality implies $ZN = \langle N_+ \rangle - \langle N_- \rangle$, where $N_{\mathrm{s}} = \langle N_- \rangle$ is the equilibrium number of monodisperse coions in the suspension, equal to the number, $N_{\rm s}$, of salt ion pairs, and $\langle N_+ \rangle$ is the equilibrium number of monovalent counterions. As mentioned, the concentration (number density) $n_{\rm s} = N_{\rm s}/V$ of salt ion pairs in the suspension is determined by the equality of the microion chemical potentials of cations and anions, $\mu_{\pm}$, in the suspension and the microion chemical potential in the reservoir, $\mu_{\rm res}$. In Donnan equilibrium, the salt pair concentration $n_{\rm s}$ in the suspension is state-dependent and determined by the given reservoir salt pair concentration (number density) $n_{\rm res}$.

As explained before, our starting point in deriving the one-component model of pseudo-microgels is a semi-grand canonical description of uniform-backbone spherical microgels plus hydrated microions, with the solvent degrees of freedom already integrated out. This amounts to describing the solvent statically as a dielectric continuum of dielectric constant $\epsilon$ and Bjerrum length $\lambda_B = e^2/(\epsilon k_{\rm B}T)$, and dynamically as a Newtonian solvent of shear viscosity $\eta_0$. In this McMillan-Mayer implicit solvent picture, the semi-grand canonical partition function of the suspension reads

$$\Xi = \langle \langle \langle {\rm e}^{-\beta(K+U_{\rm m}+U_{\rm mm}+U_{{\rm m}\mu}+U_{\mu\mu})} \rangle_{\rm p} \rangle_{\mu} \rangle_{\rm m} \,. \tag{4.9}$$

Here, $\beta = 1/(k_{\rm B}T)$, $K$ is the total kinetic energy of all polymeric and ionic suspension constituents, and the angular brackets denote canonical traces over polymer (p) and center-of-mass microgel (m) coordinates and grand-canonical traces over the microion ($\mu$) coordinates. The polymer coordinates are particle-internal degrees of freedom related to the motion of segments and associated fixed-charges constituting the cross-linked polymer chains. In the Boltzmann factor, $U_{\rm m}$ denotes the single-microgel energy, comprising both polymeric and electrostatic self energies, $U_{\rm mm}$ incorporates polymeric and electrostatic energies of interaction between the microgels, and $U_{{\rm m}\mu}$ and $U_{\mu\mu}$ account, respectively, for microgel–microion and microion–microion interactions.

Performing the trace over polymer coordinates, and exploiting the decoupling of electrostatic and polymeric contributions to the free energy resulting from the assumption of a uniform distribution of backbone charges, one obtains

$$\Xi = \mathrm{e}^{-\beta(U_\mathrm{e}+F_\mathrm{p})}\langle\langle e^{-\beta(K_{\mathrm{m},\mu}+U_\mathrm{mm}+U_{\mathrm{m}\mu}+U_{\mu\mu})}\rangle_\mu\rangle_\mathrm{m}, \tag{4.10}$$

where $U_\mathrm{e}$ is the sum of the electrostatic self energies of the $N_\mathrm{m}$ microgels, which for uniformly distributed backbone charges is

$$U_\mathrm{e}(a) = \sum_{i=1}^{N_\mathrm{m}} u_\mathrm{e}(a) = N_\mathrm{m}\left(\frac{3}{5}\frac{Z^2e^2}{\epsilon a}\right), \tag{4.11}$$

with the equilibrium radius $a$ of swollen microgels. Furthermore, $K_{\mathrm{m},\mu}$ is the translational kinetic energy associated with the center-of-mass microgel (m) and microion ($\mu$) coordinates.

The free energy associated with the non-electrostatic polymeric degrees of freedom of the $N_\mathrm{m}$ microgels is

$$F_\mathrm{p}(a) = \sum_{i=1}^{N_\mathrm{m}} f_\mathrm{p}(a)\,. \tag{4.12}$$

where the polymer free energy per microgel, $f_\mathrm{p}(a)$, is obtained using Flory-Rehner theory [16–18] and given by Eq. (4.8).

Tracing out in a second step the microion degrees of freedom for fixed configuration $\mathbf{X}$ of microgels leads to the expression [15]

$$\Xi = \langle \mathrm{e}^{-\beta H_\mathrm{eff}}\rangle_\mathrm{m}\,, \tag{4.13}$$

with the effective Hamiltonian of pseudo-microgels,

$$H_\mathrm{eff} = K_\mathrm{m} + U_\mathrm{e} + F_\mathrm{p} + E_\mathrm{vol}(n_\mathrm{m}) + U_\mathrm{eff}(n_\mathrm{m})\,, \tag{4.14}$$

where $K_\mathrm{m}$ accounts for the translational kinetic energy of the microgels. Moreover, $E_\mathrm{vol}(n_\mathrm{m})$ is the microgel configuration-independent volume energy, and for ion-permeable charged colloids it is given by Eq. (2.67). Furthermore, $U_\mathrm{eff}(n_\mathrm{m})$ is the configuration-dependent effective $N_\mathrm{m}$-particle interaction energy of pseudo-microgels. The latter incorporates electrostatic screening by the traced-out microions and consists of the bare interaction energy, $U_\mathrm{mm}$, comprising the concentration-independent Coulomb and elastic inter-microgel interactions, and a concentration- and temperature-dependent contribution, related to the grand-free energy, $\Omega_\mu$, of microions in the presence of the microgels. Note that the effective Hamiltonian $H_{\rm eff}$ depends on the microgel particle size, since each contribution on the right side of Eq. (4.14), except for the kinetic energy $K_{\rm m}$, implicitly depends on the particle radius $a$.

In a suspension of weakly-crosslinked spherical ionic microgels, the microgel radius $a$ is a state-dependent thermodynamic variable, whose equilibrium mean value for temperatures $T < T_{\rm cr}$ in the swollen state is determined from the minimization of the semi-grand free energy $\Omega(a_{\rm t}) = -k_{\rm B}T\ln(\Xi(a_{\rm t}))$ of the suspension with respect to trial radius values $a_{\rm t}$. The necessary condition for determining the equilibrium radius $a$ is thus

$$\left.\frac{\partial\Omega}{\partial a_{\rm t}}\right|_{N_{\rm m},Z,{\rm res}} = 0 \tag{4.15}$$

at $a_{\rm t} = a$. In addition to the dry radius $a_0$ and the parameters $Z$ and $n_{\rm res}$, the elasticity-related Flory-Rehner and Hertz potential parameters, $\chi$, $N_{\rm m}$, $N_{\rm ch}$, and $\varepsilon_{\rm H}$, are kept constant in taking the size derivative for fixed reservoir properties. In this way, $a$ is determined as a function of the control parameters $n_{\rm m}$, $Z$, and $n_{\rm res}$ for fixed temperature and microgel elastic properties.

The minimization of $\Omega$ with respect to $a_{\rm t}$ is equivalent to the mechanical requirement that the intrinsic (osmotic) pressure difference [14, 62],

$$\Pi(a_{\rm t}) = \Pi_{\rm g}(a_{\rm t}) + \Pi_{\rm e}(a_{\rm t})\,, \tag{4.16}$$

between the interior and exterior of a single microgel is zero at thermodynamic equilibrium, where $a_{\rm t} = a$. Upon swelling of a microgel, the intrinsic electrostatic pressure, which is nonzero both inside and outside the particle, must adjust to any variation of the intrinsic gel pressure to ensure, in equilibrium, continuity of the total intrinsic pressure $\Pi$ across the particle periphery.

The polymer-gel intrinsic pressure contribution, $\Pi_{\rm g}$, due to solvency, elasticity, and mixing entropy of individual microgel networks and the elastic inter-microgel repulsive interaction, the latter modelled by the Hertz elastic pair interactions (cf. Eq. (4.1)), is given in the present microgel model by

$$\Pi_{\rm g}(a_{\rm t}) = -\frac{\partial}{\partial v_{\rm t}}\left[f_p(a_{\rm t}) + \frac{n}{2}\Big\langle u_{\rm H}(r;a_{\rm t})\Big\rangle_{\rm eff}\right] , \tag{4.17}$$

where $v_{\rm t} = 4\pi a_{\rm t}^3/3$ is the microgel trial volume. The electrostatic pressure contribution to $\Pi(a_{\rm t})$ is

$$\Pi_{\rm e}(a_{\rm t}) = -\frac{\partial}{\partial v_{\rm t}}\left[u_e(a_{\rm t}) + \varepsilon_{\rm vol}(a_{\rm t}) + \frac{n}{2}\Big\langle u_{\rm eff}(r;a_{\rm t})\Big\rangle_{\rm eff}\right] , \tag{4.18}$$

where $u_e(a_{\rm t})$ is the electrostatic self energy of the uniform backbone microgel charge, and $u_{\rm eff}(r;a_{\rm t})$ is the effective electrostatic pair potential (cf. Eq. (2.60)). For conditions where overlap distances are very unlikely, the Hertz potential energy does not contribute to $\Pi(a_{\rm t})$ and the canonical average $\langle\cdots\rangle_{\rm eff}$ over the center positions of pseudo-microgels of radius $a_{\rm t}$ is determined solely by the Flory-Rehner and electrostatic parameters. The equilibrium microgel radius is determined by the competition between $\Pi_{\rm g}$, which is negative for $a_{\rm t}$ sufficiently larger than $a_0$ favoring deswelling, and the positive-valued $\Pi_e(a_{\rm t})$ favoring swelling. Physically speaking, the microion distribution in the microgel interior and the self-repulsion of the charged sites of the polymer backbone network generate an outward electrostatic pressure that swells the macroion. This swelling is limited by the inward elastic restoring forces due to the cross-linked polymer gel. In equilibrium, the balance between these opposing pressures determines the microgel size. In principle, an additional contribution to the pressure difference across the periphery of a microgel may arise from the Laplace pressure, $2\gamma/a$, associated with the interfacial tension, $\gamma$, at the interface between the microgel and the solution. We assume, however, that the water-swollen polymer gel is sufficiently dilute, weakly cross-linked, and hydrophilic that this interfacial contribution is negligible compared with the electrostatic and gel contributions to the total intrinsic pressure.

The microgel surface plays here the role of a *mobile* semi-permeable membrane, permeable to microions and solvent only, where the outer and inner pressures on this fictitious membrane balance to $\Pi(a) = 0$ at mechanical equilibrium. This single-particle intrinsic osmotic pressure should be distinguished from the non-zero suspension osmotic pressure, $\pi_{\rm os} = p - p_{\rm res}$, acting across a (mentally pictured) *fixed* semi-permeable membrane separating the suspension from the microion reservoir.

In the following, we present two methods for calculating the state-dependent equilibrium radius $a$ as a function of microgel concentration $n_{\mathrm{m}}$, backbone valence $Z$, and reservoir salt concentration $n_{\mathrm{res}}$. For practical reasons, the results are presented in terms of the swelling ratio

$$\alpha = \frac{a}{a_0}, \tag{4.19}$$

which measures the swelling of the microgels relative to the microgel dry size at $T > T_{\mathrm{cr}}$.

The first method makes direct use of Eq. (4.15) and of the one-component multi-center picture of pseudo-macroions interacting electrostatically by the linear-response effective pair potential $u_{\mathrm{eff}}(r)$ in Eq. (2.60) in combination with the Hertz potential $u_{\mathrm{H}}(r)$ for describing the elastic repulsion between overlapping polymer networks. In this method, the semi-grand free energy is approximated using a thermodynamic perturbation theory (TPT) [15]. The second method invokes a spherical cell model (CM) approximation for the semi-grand free energy of a single macroion with nonlinear PB distributions of microions, referred to accordingly as the PBCM method. The two methods differ in the manner in which they treat inter-microgel electrostatic interactions and correlations.

### 4.3.1 Thermodynamic perturbation theory (TPT)

In the thermodynamic perturbation theory (TPT) method, the equilibrium radius $a$ is obtained by minimizing the semi-grand free energy per microgel [15],

$$\frac{\Omega(a_{\mathrm{t}}, n_{\mathrm{m}})}{N_{\mathrm{m}}} = u_{\mathrm{e}}(a_{\mathrm{t}}) + \varepsilon_{\mathrm{vol}}(a_{\mathrm{t}}) + f_{\mathrm{p}}(a_{\mathrm{t}}) + f_{\mathrm{ex}}(a_{\mathrm{t}}, n_{\mathrm{m}})\,, \tag{4.20}$$

with respect to trial radius $a_{\mathrm{t}}$. We have disregarded here the kinetic (ideal gas) free energy contribution, $\ln(\Lambda_{\mathrm{m}}^3 n_{\mathrm{m}}) - 1$, to $\Omega/N_{\mathrm{m}}$, where $\Lambda_{\mathrm{m}}$ denotes the thermal de Broglie wavelength of microgels, since it is independent of $a_{\mathrm{t}}$. The excess semi-grand free energy per microgel, $f_{\mathrm{ex}}(a_{\mathrm{t}}, n_{\mathrm{m}})$, is due to the effective interactions between the pseudo-microgels. Provided $U_{\mathrm{eff}}(\mathbf{X}; n_{\mathrm{m}})$ is pairwise additive, $f_{\mathrm{ex}}(a_{\mathrm{t}}, n_{\mathrm{m}})$ is exactly given by the charging-process ($\lambda$-integration) expression [19, 76]

$$f_{\mathrm{ex}}(a_{\mathrm{t}}, n_{\mathrm{m}}) = \frac{n_{\mathrm{m}}}{2} \int d^3 r \, v_{\mathrm{eff}}(r) \times \int_0^1 d\lambda \, g_{\lambda}(r; a_{\mathrm{t}}, n_{\mathrm{m}}), \tag{4.21}$$

irrespective of whether the pair potential is state-dependent or not. Here, $g_{\lambda}(r; a_{\mathrm{t}}, n_{\mathrm{m}})$ is the radial distribution function corresponding to the pair potential $\lambda v_{\mathrm{eff}}(r)$ at charging fraction $\lambda$, which ranges from $g_{\lambda}(r) = 1$ for $\lambda = 0$ to the radial distribution function of the actual suspension for $\lambda = 1$. The effective pair potential

$$v_{\mathrm{eff}}(r) = u_{\mathrm{eff}}(r) + u_{\mathrm{H}}(r), \tag{4.22}$$

combines the steric effective repulsion, due to the polymer network, with the effective electrostatic repulsion for ion-permeable charged particles. In principle, the above two-step integral expression can be used in Eq. (4.20) to determine $a$ by minimization of $\Omega(a_{\mathrm{t}}, n_{\mathrm{m}})$. Moreover, it provides a route to determine the suspension pressure, $p$, and the osmotic compressibility from the first and second volume derivatives of $\Omega(a, n_{\mathrm{m}})$. We are going to address the calculation of suspension pressure and the osmotic compressibility in detail in the next chapter.

To avoid the cumbersome double integration involving the calculation of a large number of radial distribution functions for different values of $\lambda$, we approximate $f_{\mathrm{ex}}(a_{\mathrm{t}}, n_{\mathrm{m}})$ instead using a first-order perturbation expression [19], given by the right-hand side of

$$f_{\mathrm{ex}}(a_{\mathrm{t}}, n_{\mathrm{m}}) \leq \min_{(d)} \left\{ f_{\mathrm{EHS}}(d, n_{\mathrm{m}}) + 2\pi n_{\mathrm{m}} \int_d^{\infty} dr r^2 \, g_{\mathrm{EHS}}(r; d, n_{\mathrm{m}}) \, v_{\mathrm{eff}}(r; a_{\mathrm{t}}, n_{\mathrm{m}}) \right\}, \tag{4.23}$$

which invokes a reference system of effective hard spheres (EHS) of diameter $d$, radial distribution function $g_{\mathrm{EHS}}(r; d, n_{\mathrm{m}})$, and free energy per particle $f_{\mathrm{EHS}}(d, n_{\mathrm{m}})$. The excess EHS free energy per particle, $f_{\mathrm{EHS}}$, is accurately described by the analytic Carnahan-Starling free energy expression, and the EHS radial distribution function by the semi-analytic Percus-Yevick result [77] with Verlet-Weis correction [19]. The above perturbation expression provides an upper bound to the actual excess free energy per particle, $f_{\rm ex}(a_{\rm t}, n_{\rm m})$, for all values of the effective diameter $d$, as it is seen from the Gibbs-Bogoliubov inequality [19]. The equilibrium radius $a$ results from the (double) minimization of $\Omega(a_{\rm t}, n_{\rm m})/N_{\rm m}$ in Eq. (4.20) with respect to $a_{\rm t}$, after substitution of the right-hand side of Eq. (4.23) for the excess free energy minimized with respect to $d > 0$. For $v_{\rm eff} = u_{\rm eff}(r) + u_{\rm H}(r)$, we use the analytic linear-response expressions from Eqs. (2.60) and (4.1), respectively; and $\varepsilon_{\rm vol} = E_{\rm vol}/N_{\rm m}$ is given by Eq. (2.67). For $f_{\rm p}(a_{\rm t})$, we employ the Flory-Rehner expression in Eq. (4.8).

The suspension salt pair concentration $n_{\rm s}$, which affects $\kappa(n_{\rm m}, n_{\rm s})$, and hence the range of the effective pair potential in the TPT expression for $f_{\rm ex}(a, n_{\rm m})$ in Eq. (4.23), is determined, in turn, from equating the microion chemical potentials in suspension and reservoir, using $\langle N_- \rangle = N_{\rm s}$, according to

$$\frac{\partial}{\partial n_{\rm s}} \Big[ n_{\rm m} \left( \varepsilon_{\rm vol}(a) + f_{\rm ex}(a, n_{\rm m}) \right) \Big]_{n_{\rm m}} = k_{\rm B} T \ln \left( \Lambda_{\rm s}^3 n_{\rm res} \right) . \tag{4.24}$$

The TPT method was successfully tested in earlier works for deswelling ionic microgels [15], incompressible ionic microgels [13], and impermeable charged colloids [44]. The method self-consistently incorporates effective microgel pair interactions for low to moderately high $Z$ values, where linear-response theory can be used.

### 4.3.2 PBCM-based method

The Denton-Tang PBCM-based method, or PBCM (Poisson-Boltzmann Cell Model) method for short, was developed by Denton and Tang [14]. It combines the implementation of the PB theory for the description of a multi-component system with spherical CM approximation of the suspension, in order to provide a way for calculating the microgel equilibrium size. As explained before in section 3.1, the CM applies to suspensions of ionic microgels, where, on average, around each microgel there is a region void of others [54]. This condition requires a sufficiently strong and long-ranged electrostatic repulsion between the microgels and concentrations small enough that particle overlap is unlikely. Then, a Wigner-Seitz cell tessellation can be used, with each WS cell approximated by an overall electroneutral spherical cell of radius $R = (3/4\pi)^{1/3}\, n_\mathrm{m}^{-1/3}$, containing a single spherical microgel of trial radius $a_\mathrm{t}$ at its center. In Donnan equilibrium, the cell is in osmotic contact with a 1:1 electrolyte reservoir of salt pair concentration $2\,n_\mathrm{res}$. In the PBCM, the radially symmetric concentration profiles $n_\pm(r)$ of the pointlike monovalent ions are described in a mean-field way by the Boltzmann distributions, $n_\pm(r) = n_\mathrm{res} e^{\mp\Phi(r)}$, where $\Phi(r) = \psi(r)e/(k_\mathrm{B}T)$ is the reduced form of the total electrostatic potential $\psi(r)$ due to all charges in the cell. As for the TPT method, polarization and image charge effects are disregarded, which can be justified by the high solvent content of weakly cross-linked swollen microgels. While the cell model focuses on a single microgel only, with the semi-grand suspension free energy being $N_\mathrm{m}$ times that of a single cell, the presence of other microgels is implicitly accounted for through the cell radius $R$ and the associated (trial) volume fraction $\phi_\mathrm{t} = (a_\mathrm{t}/R)^3$.

Assuming, as in TPT, a uniform backbone charge distribution inside each microgel, the electrostatic potential in the cell region $0 < r < R$ is obtained from solving the nonlinear PB equations,

$$\Phi''(r) + \frac{2}{r}\Phi'(r) = \begin{cases} \kappa_\mathrm{res}^2 \sinh\Phi(r) + \dfrac{3Z\lambda_\mathrm{B}}{a_\mathrm{t}^3}\,, & 0 < r \le a_\mathrm{t} \\ \kappa_\mathrm{res}^2 \sinh\Phi(r)\,, & a_\mathrm{t} < r \le R \end{cases}\,, \tag{4.25}$$

where $\kappa_\mathrm{res}^2 = 8\pi\lambda_\mathrm{B} n_\mathrm{res}$ is the square of the reservoir Debye screening constant. The solution for $\Phi(r)$ is uniquely determined by the boundary conditions $\Phi'(0) = 0 = \Phi'(R)$, for the electric field at the cell center and edge, respectivaly, and by the continuity conditions, $\Phi(a_\mathrm{t}^-) = \Phi(a_\mathrm{t}^+)$ and $\Phi'(a_\mathrm{t}^-) = \Phi'(a_\mathrm{t}^+)$, at the microgel surface. Once $\Phi(r)$, and hence the microion concentration distributions, are determined by numerically solving Eq. (4.25) for given boundary conditions and microgel trial radius $a_\mathrm{t}$, the intrinsic osmotic pressure $\Pi(a_\mathrm{t})$ in the PBCM follows from Eqs. (4.17) and (4.18), taken for $\langle u_\mathrm{H}\rangle_\mathrm{eff} = 0 = \langle u_\mathrm{eff}\rangle_\mathrm{eff}$, and for $\varepsilon_\mathrm{vol}$ replaced by $\langle u_{\mathrm{m}\mu}(r)\rangle_\mu$, i.e., by the electrostatic interaction energy between the uniform central microgel backbone charge and pointlike microions, weighted by the microion number density profiles $V_\mathrm{R} n_\pm(r)$ and averaged over the cell volume $V_\mathrm{R} = (4\pi/3)R^3$. Consideration of the variation of the electrostatic component of the free energy with respect to the microgel radius leads to an exact statistical mechanical expression for the electrostatic pressure [14],

$$\beta\Pi_\mathrm{e}(a_\mathrm{t})v_\mathrm{t} = \frac{Z\lambda_\mathrm{B}}{2a_\mathrm{t}}\left(\frac{2}{5}Z - \langle N_+\rangle + \langle N_-\rangle + \frac{\langle r^2\rangle_+ - \langle r^2\rangle_-}{a_\mathrm{t}^2}\right) , \tag{4.26}$$

where

$$\langle N_\pm\rangle = 4\pi\int_0^{a_\mathrm{t}} n_\pm(r)r^2 dr \tag{4.27}$$

and

$$\langle r^2\rangle_\pm = 4\pi\int_0^{a_\mathrm{t}} n_\pm(r)r^4 dr \tag{4.28}$$

are the mean numbers of internal microions and the second moments of the interior microion number density profiles, respectively.

Using Eq. (4.8), the polymer gel contribution to the intrinsic osmotic pressure for trial radius $a_\mathrm{t}$ is [14]

$$\beta\Pi_g(a_\mathrm{t})v_\mathrm{t} = -N_\mathrm{m}[\alpha^3\ln(1-\alpha^{-3}) + \chi\alpha^{-3} + 1] - N_\mathrm{ch}(\alpha^2 - 1/2) \, . \tag{4.29}$$

According to Eq. (4.16), the equilibrium microgel radius is obtained from setting the sum of the intrinsic pressure contributions in Eqs. (4.26) and (4.29) equal to zero.

In the cell model, the net microgel valence $Z_\mathrm{net}$ is calculated by means of Eq. (2.62) using the microion number density profiles, $n_\pm(r; a)$, and the suspension salt pair concentration $n_\mathrm{s}$, by integrating the coion (anion) profile over the cell volume according to

$$n_\mathrm{s} = \frac{4\pi}{V_\mathrm{R}}\int_0^R n_-(r; a)\, r^2\, dr \, , \tag{4.30}$$

where $V_R = 4\pi R^3/3$. While TPT is self-consistently linked to the effective pair potential between microgels, $v_\mathrm{eff}(r)$, such a direct link does not exist in the single-microgel PBCM, which does, however, incorporate the nonlinear electrostatic response of the microions that is neglected in TPT. However, an *ad hoc* link between PBCM and the linear-response $u_\mathrm{eff}(r)$

is readily established, for given $Z$, by identifying the net microgel valence $Z_{\rm net}$ and $\kappa a$ in the no-overlap Yukawa potential in Eq. (2.61) with the PBCM-calculated values $Z^*_{\rm net}$ and $\kappa^* a^*$, respectively, where

$$(\kappa^*)^2 = 4\pi\lambda_{\rm B}(n_{\rm m}Z^* + 2n^*_{\rm s}). \tag{4.31}$$

The asterisk labels PBCM-calculated properties. An apparent backbone valence, $Z^*$, is defined here as a function of $Z^*_{\rm net}$ and $\kappa^* a^*$ by

$$Z^*_{\rm net} = Z^* \frac{3\,(1+\kappa^* a^*)}{(\kappa^* a^*)^2\, e^{\kappa^* a^*}} \left[\cosh(\kappa^* a^*) - \frac{\sinh(\kappa^* a^*)}{\kappa^* a^*}\right], \tag{4.32}$$

which when used in the expression for the overlap electrostatic potential $u_{\rm ov}(r)$, according to the substitution $\{Z, a, \kappa\} \to \{Z^*, a^*, \kappa^*\}$, maintains the continuity of the effective potential and its first derivative at $r = 2a$. Substitution of $Z^*$ into Eq. (4.31) gives an implicit equation for $\kappa^*$, which can be solved iteratively. For lower backbone valences $Z \leq 200$, $Z^*$ is close to $Z$, so that the latter can be used instead as input in Eq. (4.31).

For ionic microgel systems with electrostatic coupling strengths $\Gamma_{\rm el} \equiv Z_{\rm net}\lambda_{\rm B}/a \lesssim 5$, the nonlinear electrostatic effects by the microions are negligible or small, so that both TPT and PBCM can be directly used in conjunction with the linear-theory effective pair potential in Eq. (2.61). For stronger electrostatic couplings, experience gained with rigid charged colloids suggests that the Yukawa form of the effective potential in Eq. (2.61) is still applicable, but now for renormalized values of $Z$ and $\kappa$, which can be obtained, e.g., from linearization of the potential $\Phi(r)$ in the cell model with respect to its value at the cell boundary [62] or with respect to the cell volume averaged potential value. Such charge-renormalization approaches to obtain renormalized $Z_{\rm eff}$ and $\kappa_{\rm eff}$ have been discussed before in chapter 3.

# Chapter Five

# MICROSTRUCTURE, THERMODYNAMICS AND DYNAMICS

We explain here various analytical tools for calculating thermodynamic, structural and dynamic properties of charged-stabilized suspensions. We discuss the underlying concepts, and the corresponding calculation methods of various structural and dynamical properties, which characterize the suspension. For characterizing the static microstructure on the pair level, the macroion pair distribution function, $g(r)$, and the associated macroion static structure factor, $S(q)$, are introduced together with the methods for their calculation. Regarding thermodynamic properties, we explain different methods for obtaining pressure and osmotic compressibility of the suspension. Finally, as dynamic properties, we calculate and study high- and low-frequency viscocities, and self-diffusion and collective diffusion coefficients with the salient hydrodynamic interactions between colloids accounted for.

In this chapter, the calculation tools for determining (equilibrium) structural and dynamic suspension properties are based on the one-component model of (dressed) pseudo-macroions interacting by a state-dependent effective macroion pair potential $v_{\text{eff}}(r; n_{\text{m}})$, with the exception of the suspension (osmotic) pressure, which requires accountance of the volume energy $E_{\mathrm{vol}}$ and the $n_{\mathrm{m}}$-dependence of $u_{\mathrm{eff}}(r;n_{\mathrm{m}})$. The employed methods for calculating dynamic properties depend on $v_{\mathrm{eff}}$ only implicitly via $g(r)$ and $S(q)$. For simplicity, the hydrodynamic macroion radius is identified with $a(\phi_0)$. As always in this thesis, we take the suspension to be in (Donnan) osmotic equilibrium with a 1:1 electrolyte reservoir.

## 5.1 Static pair distribution and structure functions

The concept of reduced particle distribution functions has proven to be very useful in the theory of simple liquids, since it provides a convenient description of the fluid micro-structure and its thermodynamic properties. Among these reduced distribution functions, the pair distribution functions are of greatest importance, since for a simple fluid whose potential energy is pairwise additive with a state-independent pair potential $u(r)$, all structural and thermodynamic properties can be expressed in terms of $g(r)$, $S(q)$ and $u(r)$. Hereafter, we discuss the pair distribution functions first for a simple one-component fluid, and proceed then to a suspension of monodisperse macroions.

Consider a one-component fluid of $N$ spherical particles at center positions $\mathbf{X} = \{\mathbf{r}_1, ..., \mathbf{r}_N\}$ in a volume $V$ at temperature $T$. The $m$-particle distribution function, $g_N^{(m)}(\mathbf{r}_1, ..., \mathbf{r}_m)$, for $m \leq N$, is defined in a canonical ensemble description by

$$g_N^{(m)}(\mathbf{r}_1, ..., \mathbf{r}_m) := \frac{\rho_N^{(m)}(\mathbf{r}_1, ..., \mathbf{r}_m)}{\Pi_{i=1}^{m} \rho_N^{(1)}(\mathbf{r}_i)}, \tag{5.1}$$

where $\rho_N^{(m)}(\mathbf{r}_1, ..., \mathbf{r}_m)$ is the equilibrium $m$-particles density

$$\rho_N^{(m)}(\mathbf{r}_1, ..., \mathbf{r}_m) = \frac{N!}{(N-m)!} \int_{V^{N_{\mathrm{m}}}} d\mathbf{r}^{(N-m)}\, P_N(\mathbf{r}^N), \tag{5.2}$$

for given probability distribution $P_N(\mathbf{r}^N) = e^{-\beta U(\mathbf{r}^N)}/Z_N$, with potential energy $U(\mathbf{r}^N) = \sum_{i<j}^{N} u(|\mathbf{r}_1 - \mathbf{r}_2|)$ and partition function $Z_N = \int d\mathbf{r}^N\, e^{-\beta U(\mathbf{r}^N)}$. We assume that the fluid potential energy, $U(\mathbf{r}^N)$, is purely pairwise-additive with isotropic pair potential $u(r)$. Note that $\rho_N^{(m)}(\mathbf{r}_1, ..., \mathbf{r}_m)$ is the density distribution function of finding any set of $m$ particles at

a specified configuration of center positions $\mathbf{X}$, irrespective of the positions of the remaining particles and the momenta of all particles, and regardless of how they are labeled [19, 78]. One can also see that the single particle density of a uniform fluid is equal to the average number density, i.e. $\rho_N^{(1)}(\mathbf{r}) = n = N/V$. The $m$-particle distribution functions, $g_N^{(m)}$, in Eq. (5.1) measure the $m$-particle correlations in the fluid relative to a classical ideal gas under the same conditions [78], i.e. they quantify to what extent the micro-structure of the fluid deviates from the corresponding random structure of an ideal gas [19].

For pairwise additive $U(\mathbf{r}^N)$, the knowledge of $g_N^{(2)}$ is sufficient to describe the equation of state and other thermodynamic properties. In a homogeneous and isotropic simple fluid, the pair distribution function only depends on the distance between the particles, i.e. $g_N^{(2)}(\mathbf{r}_1, \mathbf{r}_2) = g_N^{(2)}(r)$, with $r = |\mathbf{r}_1 - \mathbf{r}_2|$, and it is called radial distribution function (rdf) [78]. By taking the thermodynamic limit, i.e. $N, V \to \infty$ keeping $n = N/V$ fixed, one obtains the ensemble-independent rdf, $g(r)$, of a macroscopic system

$$g(r) = \lim_{N,V\to\infty} g_N^{(2)}(r). \tag{5.3}$$

By its very definition, $g(r) \geq 0$ and $g(r \to \infty) = 1$ in the fluid state. Moreover, one can show that $g(r) = e^{-\beta u(r)} + \mathcal{O}(n)$.

As noted above, the radial distribution function plays a key role in liquid state theory for various reasons. Experimentally, $g(r)$ is indirectly measurable by radiation scattering experiments and, for large colloidal particles, also directly determined by confocal microscopy. Theoretically, $g(r)$ is proportional to the average number $4\pi r^2 n\, g(r)\, \Delta r$ of particles lying within the shell $(r, r + \Delta r)$ around a reference particle. Thus, in simulations, $g(r)$ is obtained by counting the number of particles, $N(r)$, in a shell of thickness $\Delta r$ and volume $4\pi r^2 \Delta r$ at distance $r$ from the central particle, i.e. $g(r) \approx \langle N(r)\rangle/(4\pi n r^2 \Delta r)$. The shape of $g(r)$ provides considerable insight into the structure of a liquid at the level of pair correlations [19]. The peaks in $g(r)$ represent *shells* of neighbors around a reference particle, and integrating $4\pi r^2 n\, g(r)\, dr$ from zero up to the position of the first minimum gives an estimate of the nearest-neighbour *coordination number*. For strictly pairwise-additive interaction forces, the thermodynamic properties can be expressed in terms of integrals over $g(r)$ [19], as it is demonstrated in the coming section.

The three-dimensional Fourier transform of $g(r)$, or more precisely that of the total correlation function $h(r) = g(r) - 1$ with $h(r \to \infty) = 0$ in the fluid state, is basically the static structure factor $S(q)$. The latter is directly measurable in static scattering experiments and it is defined by

$$S(q) = \lim_{\substack{N,V\to\infty \\ n \text{ fixed}}} \left\langle \frac{1}{N} \sum_{l,j=1}^{N} e^{i\mathbf{q}\cdot(\mathbf{r}_l - \mathbf{r}_j)} \right\rangle , \tag{5.4}$$

where $q$ is the scattering wavevector of modulus $q = |\mathbf{q}|$ and $\langle ... \rangle$ denotes an equilibrium ensemble average. For given $q$, the static structure factor is the thermodynamic limit of the autocorrelation function of the $\mathbf{q}$-th Fourier component of microscopic density fluctuations [79], characterizing the inter-particle correlations.

By splitting the double sum in Eq. (5.4) into self, $l = j$, and distinct parts, $l \neq j$, one shows that [5, 79]

$$S(q) = 1 + n \int d\mathbf{r}\, e^{i\mathbf{q}\cdot\mathbf{r}} \left[g(r) - 1\right] = 1 + 4\pi n \int_0^\infty dr\, r^2 \left[g(r) - 1\right] \frac{\sin(qr)}{qr} \tag{5.5}$$

obtaining that $S(q \to \infty) = 1$. Since Fourier transforms are one-to-one maps, $S(q)$ can be Fourier-inverted to determine $h(r)$ and $g(r)$, but this requires to know $S(q)$ for all wave numbers $q$ where $S(q)$ exhibits significant oscillations. In static light scattering experiments on colloidal suspensions, this is usually not feasible since the largest $q$ value accessible is limited by $q_{\max} = 4\pi/\lambda$, which corresponds to backward scattering [79].

The concepts of radial distribution function and associated structure factor are easily extended to fluid systems with more than a single component. Considering a multi-component simple fluid constituted by $m$ different spherical species, one can introduce $m(m+1)/2$ partial pair correlation functions $g_{\alpha\beta}(r)$, which provide the conditional probability of finding a $\beta$-type particle at center-to-center distance $r$ from a given $\alpha$-type particle relative to the corresponding ideal gas mixture under same conditions. The according $m(m+1)/2$ partial total pair correlation functions, $h_{\alpha\beta}(r) = h_{\beta\alpha}(r)$, are given by $h_{\alpha\beta}(r) = g_{\alpha\beta}(r) - 1$. The associate partial static structure factors, $S_{\alpha\beta}(q)$, in a homogeneous and isotropic fluid are related to the total pair correlation functions by [5, 80]

$$S_{\alpha\beta}(q) = \delta_{\alpha\beta} + (n_\alpha\, n_\beta)^{1/2} \int_V d\mathbf{r}\, h_{\alpha\beta}(r) e^{i\mathbf{q}.\mathbf{r}}, \qquad \alpha \in \{1, ..., m\} \tag{5.6}$$

with $\delta_{\alpha\beta}$ denoting the Kronecker delta and $n_\alpha = N_\alpha/V$. It holds then that $S_{\alpha\beta}(q \to \infty) = \delta_{\alpha\beta}$ in a fluid.

While introduced here for a simple fluid with state-independent particle interactions, $g(r)$ and $S(q)$ are accordingly defined for an effective one-component system of (dressed) macroions (in a McMillan-Mayer picture), with state-dependent (screened) macroion interactions. The electrostatic screening guarantees that thermodynamic (virial) integrals are finite, allowing for the application of thermodynamic concepts to the effective one-component suspension.

## 5.2 Thermodynamic properties

In this section, we present our methods for calculating thermodynamic properties of charge-stabilized suspensions of monodispersed macroions in Donnan equilibrium, notably the suspension pressure and osmotic compressibility in a fluid-state system. We analyze and compare the approximations invoked in the different methods.

### 5.2.1 Suspension pressure

The first property that we analyze is the equilibrium suspension pressure $p$. Provided the radial distribution function, $g(r)$, of an homogeneous isotropic system is constituted only by a single species interacting with the pairwise potential $u(r)$, the system pressure can be expressed in terms of the pressure virial equation [19]

$$p = p_{\mathrm{id}} + p_{\mathrm{ex}} = n\, k_{\mathrm{B}}T - \frac{2\pi}{3} n^2 \int_0^\infty dr r^3 g(r) \frac{\partial u}{\partial r}. \tag{5.7}$$

The first pressure contribution on the right-hand side is the kinetic ideal gas pressure, $p_{\mathrm{id}} = nk_{\mathrm{B}}T$, while the second one, $p_{\mathrm{ex}}$, is the excess part due to pair interactions. Notice that $p_{\mathrm{ex}} > 0$ for purely repulsive systems, where $u'(r) < 0$. Eq. (5.7) relates a thermodynamic property of the system to an integral involving microscopic structural and interaction properties such as $g(r)$ and $u(r)$. There exist several routes to determine the pressure from $g(r)$ and $u(r)$. The one in Eq. (5.7) is addressed as the pressure route.

As detailed in chapter 2, we reduce a multi-component charge-stabilized suspension to a one-component system of dressed macroions with effective interactions accounting summarily for the influence of the integrated-out microion and solvent components. Provided the full effective Hamiltonian, $H_{\mathrm{eff}}$, one can obtain the semi-grand suspension free energy, $\Omega = -k_{\mathrm{B}}T \ln \Xi$, with partition function $\Xi = \langle \exp\{-\beta H_{\mathrm{eff}}\} \rangle_{\mathrm{m}}$ and $\langle ... \rangle_{\mathrm{m}}$ denoting the canonical trace over macroion center positions and momenta. The pressure of the multi-component suspension is then determined by

$$p = -\left(\frac{\partial \Omega}{\partial V}\right)_{\mathrm{res}} = n_{\mathrm{m}}^2 \left(\frac{\partial f}{\partial n_{\mathrm{m}}}\right)_{\mathrm{res}}, \tag{5.8}$$

for constant reservoir conditions, i.e. for fixed reservoir ion chemical potentials and hence fixed $n_{\mathrm{res}}$. Here, $f = \Omega/N_{\mathrm{m}}$ is the semi-grand free energy per macroion. In taking the macroion concentration derivative, the electroneutrality condition $n_{\mathrm{s}} = \langle N_+ \rangle / V - n_{\mathrm{m}} Z$ needs to be maintained for given $Z$. As noted earlier, the effective Hamiltonian can be expressed as $H_{\mathrm{eff}} = K_{\mathrm{m}} + U_{\mathrm{e}} + F_{\mathrm{p}} + E_{\mathrm{vol}}(n_{\mathrm{m}}) + U_{\mathrm{eff}}(n_{\mathrm{m}})$. To account for microgel suspensions with state-dependent particle size, we have included the terms $U_{\mathrm{e}}$ and $F_{\mathrm{p}}$, denoting the electrostatic self-energies of the microgels and the free energy associated with the nonelectrostatic polymeric degrees of freedom of the microgels, respectively. For incompressible impermeable particles, $U_{\mathrm{e}}$ does not contribute to $p$ and can be skipped, and $F_{\mathrm{p}} = 0$. From the first equality in Eq. (5.8), the suspension pressure is given by the exact, generalized one-component virial equation [81]

$$p = p_{\mathrm{vol}} + p_{\mathrm{se}} + n_{\mathrm{m}} k_{\mathrm{B}} T - \frac{1}{3V} \Big\langle \sum_{i=1}^{N_{\mathrm{m}}} \mathbf{R}_i \cdot \frac{\partial U_{\mathrm{eff}}}{\partial \mathbf{R}_i} \Big\rangle_{\mathrm{eff}} - \Big\langle \frac{\partial U_{\mathrm{eff}}}{\partial V} \Big\rangle_{\mathrm{eff}} \tag{5.9}$$

invoking in particular the configuration-dependent effective $N_\mathrm{m}$-particle interaction energy, $U_\mathrm{eff}(\mathbf{X}; n_\mathrm{m})$, and its volume derivative originated from its concentration dependence. Here, $\mathbf{X} = \{\mathbf{R}_1, \cdots, \mathbf{R}_{N_\mathrm{m}}\}$ are the positions of the spherical macroions and $p_\mathrm{vol}$ is the pressure contribution due to the volume energy, $p_\mathrm{vol} = -(\partial E_\mathrm{vol}/\partial V)_{T,N_\mathrm{m},n_\mathrm{res}}$. Regarding the pressure of microgel suspensions, there is an additional pressure contribution,

$$p_\mathrm{se} = n_\mathrm{m}^2 \frac{\partial [u_e(a) + f_\mathrm{p}(a)]}{\partial n_\mathrm{m}}, \tag{5.10}$$

originating from the electrostatic and polymeric self-energies (se) per macroion, owing to their implicit concentration dependence via the equilibrium radius $a(n_\mathrm{m})$. This contribution is absent for incompressible particles. The angular brackets $\langle \cdots \rangle_\mathrm{eff}$ denote the canonical average with respect to the equilibrium distribution function, $P_\mathrm{eq}(\mathbf{X}) \propto \exp[-\beta U_\mathrm{eff}(\mathbf{X})]$, of pseudo-microgels, not to be confused with the canonical macroion trace $\langle \cdots \rangle_\mathrm{m}$. The volume derivative of $\Omega$ in Eq. (5.9) is for fixed reservoir ion chemical potentials and hence fixed $n_\mathrm{res}$. The generalized virial equation, Eq. (5.9), does not suffer from ambiguities introduced when state-dependent pair potentials are combined in an *ad hoc* manner with the compressibility and virial equation of state expressions for a one-component simple fluid [76, 82].

In general, $U_\mathrm{eff}(\mathbf{X})$ can contain higher-order effective interaction terms. For sufficiently dilute systems with non-overlapping double layers, $U_\mathrm{eff}(n_\mathrm{m})$ is well approximated just by the pairwise additive contribution invoking $u_\mathrm{eff}$ only, as for both the DFT-PB approximation and LRT. In such a case, the generalized virial equation of the suspension pressure under isothermal conditions reduces to [19]

$$\beta p = n_\mathrm{m} - \frac{2\pi}{3} n_\mathrm{m}^2 \int_0^\infty dr r^3 g(r) \frac{\partial \beta u_\mathrm{eff}(r)}{\partial r} + 2\pi n_\mathrm{m}^3 \int_0^\infty dr r^2 g(r) \frac{\partial \beta u_\mathrm{eff}(r)}{\partial n_\mathrm{m}} + \beta p_\mathrm{vol} + \beta p_\mathrm{se}, \tag{5.11}$$

where we have introduced the radial distribution function, $g(r)$, of the effective (one-component) particles determined by the effective pair interaction $u_\mathrm{eff}(r; n_\mathrm{m})$. For strongly interacting macroions, $u_\mathrm{eff}(r; n_\mathrm{m})$ with charge-renormalized parameters can be used so that Eq. (5.11) is still applicable.

This new pressure expression provides a generic way to compute the pressure in an effective one-component system, without $p_{\rm se}$ contribution for rigid particles, and with $p_{\rm se}$ contribution for ionic microgels.

In this thesis, we also implemented different models, such as the cell model and jellium model, that provide alternative expressions for the pressure, which are also decent approximations of the suspension pressure under certain conditions.

The pressure $p_\mu$ in the spherical cell model due to the mobile microions follows from the contact theorem [83]

$$\beta p_\mu = n_+(R) + n_-(R)\,, \tag{5.12}$$

stating that $p_\mu$ is determined in an ideal-gas-like way by the microion concentrations at the cell edge, where the electric field vanishes due to overall electroneutrality. Since the suspension is mentally pictured as superposition of $N_{\rm m}$ identical spherical noninteracting cells, the suspension pressure in the CM can be approximated as

$$p \approx p_{\rm CM} = k_B T\ [n_+(R) + n_-(R)] + k_{\rm B} T n_{\rm m}, \tag{5.13}$$

where we have added the ideal-gas contribution of the $N_{\rm m}$ macroions. When approximating the thermodynamics of a charge-stabilized colloidal suspension using the CM, in addition to the kinetic macroion pressure part $n_{\rm m} k_{\rm B} T$, there are macroion-correlation-induced pressure contributions to $p$ that are not accounted for in the CM. Thus, for non-small $n_{\rm m}$, $p_\mu$ and $p_{\rm CM}$ can differ significantly from $p$, except for low reservoir salt concentrations, where the dominant number of backbone-released counterions ($Z N_{\rm m} \gg N_{\rm s}$) contributes most to $p$ [84]. We are going to analyze the various pressure parts in details in chapter 7.

Similarly to the cell model, within the jellium models the suspension pressure is derived using the contact theorem, and the vanishing of the electric field at $r \to \infty$ [64] according to

$$\beta p_{\rm jell} = n_{\rm m} + n_+(\infty) + n_-(\infty)\,, \tag{5.14}$$

where the ideal gas pressure contribution of the macroions is added. Here, $n_\pm(\infty)$ are the microion concentrations far distant from the central macroion. Notice that in the limit of strong macroion dilution, $n_\mathrm{m} \to 0$, where $R \to \infty$ in the cell model, it holds that $p_\mu \to p_\mathrm{jell}$.

### 5.2.2 Osmotic compressibility

The isothermal compressibility in a one-component simple fluid is defined as

$$\chi_T = -\frac{1}{V}\left(\frac{\partial V}{\partial p}\right)_T = \frac{1}{n}\left(\frac{\partial n}{\partial p}\right)_T . \tag{5.15}$$

In case of an ideal one-component gas of concentration $n$, $\chi_T^\mathrm{id} = (nk_\mathrm{B}T)^{-1}$. Calculation of the isothermal compressibility also establishes a route that relates structural to thermodynamic properties of a system. For an isotropic and homogeneous fluid, the compressibility equation is

$$\frac{\chi_T}{\chi_T^\mathrm{id}} = 1 + n\int d\mathbf{r}\,[g(r) - 1] = \lim_{q\to 0} S(q), \tag{5.16}$$

linking the isothermal compressibility, $\chi_T$, to an integral over $h(r)$ or, equivalently, to the long-wavelength limit of the structure factor according to Eq. (5.5). Thus, $\chi_T$ can be determined experimentally from measuring/extrapolating the structure factor for $q \to 0$. Very notably, the compressibility equation holds even for particles with nonpairwise additive interactions.

We address now how, for a suspension of macroions plus dissolved microions, the osmotic isothermal suspension compressibility is obtained. Assuming a semi-open system of macroions in Donnan (osmotic) equilibrium with a microion reservoir, the osmotic compressibility, $\chi_\mathrm{osm}$, is given by [39]

$$\chi_\mathrm{osm} = \frac{1}{n_\mathrm{m}}\left(\frac{\partial n_\mathrm{m}}{\partial \pi_\mathrm{osm}}\right)_\mathrm{res} , \tag{5.17}$$

with $n_\mathrm{m}$ the macroion number density and

$$\pi_\mathrm{osm} = p - p_\mathrm{res} \tag{5.18}$$

the osmotic pressure of the suspension, measured relative to the reservoir pressure $p_{\mathrm{res}} = 2k_{\mathrm{B}}Tn_{\mathrm{res}}$. The leading non-ideal (limiting-law) contribution to the reservoir pressure grows in proportion with the power 3/2 of the reservoir salt concentration according to $k_{\mathrm{B}}T\kappa_{\mathrm{res}}^3/(24\pi)$ [85]. Therefore, non-ideality contributions to the reservoir pressure are negligible for the considered reservoir ionic strengths of monovalent electrolyte ions, which is consistent with the PB description of microions implemented in this thesis.

The system volume and macroion concentration derivatives in Eqs. (5.9) and (5.17) are for fixed reservoir properties, i.e., for fixed $n_{\mathrm{res}}$, or, equivalently, fixed $\mu_{\mathrm{res}}$, and fixed $T$, so that [84]

$$\left(\frac{\partial p}{\partial n_{\mathrm{m}}}\right)_{\mathrm{res},T} = \left(\frac{\partial \pi_{\mathrm{osm}}}{\partial n_{\mathrm{m}}}\right)_{\mathrm{res},T}. \tag{5.19}$$

Quite remarkably, in Donnan equilibrium, the osmotic compressibility can be expressed via the so-called Kirkwood-Buff (KB) relation [84, 86],

$$\frac{\chi_{\mathrm{osm}}}{\chi_{\mathrm{osm}}^{\mathrm{id}}} = k_{\mathrm{B}}T\left(\frac{\partial n_{\mathrm{m}}}{\partial p}\right)_{\mathrm{res},T} = 1 + n_{\mathrm{m}}\int d^3r\,[g_{\mathrm{mm}}(r) - 1] = \lim_{q\to 0} S_{\mathrm{mm}}(q), \tag{5.20}$$

solely in terms of the solvent-averaged macroion-macroion radial distribution function $g_{\mathrm{mm}}(r)$. The KB relation follows from the isothermal differential Gibbs-Duhem relation in Donnan equilibrium, $dp = n_{\mathrm{m}}\,d\mu_{\mathrm{m}}$, where $\mu_{\mathrm{m}}$ is the macroion chemical potential, in conjunction with the relation $\beta S_{\mathrm{mm}}(0; n_{\mathrm{m}}) = (\partial \ln n_{\mathrm{m}}/\partial \mu_{\mathrm{m}})_{T,\mu_{\pm}}$ for the zero-wavenumber structure factor of the macroions confined to the suspension [86].

Notice that, differently from the full compressibility of the multi-component suspension $\chi = (\partial n_{\mathrm{t}})/(\partial p)/n_{\mathrm{t}}$, with $n_{\mathrm{t}}$ the total density [39], $\chi_{\mathrm{osm}}$ depends only on the macroion-macroion pair correlation function $g_{\mathrm{mm}}(r)$, while $\chi$ requires for its calculation the knowledge both of the microion–microion and microion–macroion correlation functions [39].

Considering the mapping of the multi-component system onto an effective one-component macroion system, the suspension osmotic compressibility is also given by the zero-wavenumber limit of $S(q)$, which is uniquely determined by the effective macroion pair interaction $u_{\mathrm{eff}}(r; n_{\mathrm{m}})$. Recall that the effective pair potential in the one-component system is defined such that it reproduces the same macoion-macroion pair correlation functions as obtained in the multi-component PM system, $g_{\mathrm{mm}}(r) = g(r)$ and $S_{\mathrm{mm}}(q) = S(q)$ [39].

Like Eq. (5.9) for $p$, the KB relation in Eq. (5.20) is valid also for a non-pairwise additive effective potential energy $U_{\mathrm{eff}}(\mathbf{X})$.

In calculations of the osmotic compressibility, one can take advantage of a theorem by Henderson [87], asserting that for a one-component system with only pairwise interactions, for each considered thermodynamic state (concentration $n_{\mathrm{m}}$ and temperature $T$) there is a one-to-one correspondence between $g(r; n_{\mathrm{m}})$ and the underlying pair potential, up to an irrelevant additive constant for the latter. As thoroughly discussed in [76, 84], at given concentration $n$ and temperature $T$, the osmotic compressibility is thus obtained also from the concentration derivative of the suspension pressure, $p^{\mathrm{OCM}}$, for a fictitious system with state-independent pair potential $u(r) = u_{\mathrm{eff}}(r; n_{\mathrm{m}}, T)$. Explicitly,

$$\left(\frac{\partial p}{\partial n_{\mathrm{m}}}\right)_{\mathrm{res},T} = \left(\frac{\partial p^{\mathrm{OCM}}}{\partial n_{\mathrm{m}}}\right)_{u_{\mathrm{eff}},T}, \tag{5.21}$$

where $p^{\mathrm{OCM}}$ is the one-component model (OCM) pressure of the fictitious system, given by the right-hand side of Eq. (5.11) without volume pressure $p_{\mathrm{vol}}$, and without the integral invoking the concentration derivative of $u_{\mathrm{eff}}(r)$. The concentration derivative on the right-hand side of Eq. (5.21) is taken for fixed $u_{\mathrm{eff}}$, by discarding any concentration dependence of the effective pair potential. This amounts to keeping $\kappa a$ and $Z_{\mathrm{net}}$ fixed to their values at the considered concentration and temperature. A consistency test of the approximations used in calculating $u_{\mathrm{eff}}(r)$, the equilibrium radius $a$, and $g(r)$ follows from comparing numerical values for the reduced osmotic compressibility identified by $S(q \to 0)$ with its values obtained from Eq. (5.21).

## 5.3 Ornstein-Zernike integral equation schemes

The Ornstein-Zernike (OZ) integral equation is a theoretical concept allowing for the calculation of pair correlation functions $g(r)$ and $S(q)$ from the knowledge of $u(r)$. Firstly introduced by Ornstein and Zernike in their study of critical opalescence [88], it can be viewed as an equation that defines the direct correlation function $c(r)$ in terms of $h(r)$. For a homogeneous and isotropic one-component fluid system, the Ornstein–Zernike equation has the form

$$h(r) = c(r) + n \int d\mathbf{r}'\, c(|\mathbf{r} - \mathbf{r}'|)h(r'). \tag{5.22}$$

The second term on the right-hand side is a convolution integral. The total correlation function, $h(r)$, between two particles is thus expressed as the sum of a direct correlation part, $c(r)$, plus an indirect correlation part (convolution integral) mediated by other particles with weight $n$ [78]. From this physical interpretation of the OZ equation, one infers that the range of $c(r)$ is comparable with that of the pair potential $u(r)$, while $h(r)$ can be longer ranged than $u(r)$, due to the effect of indirect correlation part [19]. On taking the Fourier transform of both sides of Eq. (5.22), we obtain an algebraic expression for $S(q) = 1 + n\hat{h}(q)$:

$$S(q) = \frac{1}{1 - n\,\hat{c}(q)} \tag{5.23}$$

where $\hat{c}(q)$ and $\hat{h}(q)$ are the three-dimensional Fourier transforms of $c(r)$ and $h(r)$, respectively.

The OZ equation can be also derived in the context of density functional theory, with the introduction of density correlation functions and defining the direct correlation function as a functional derivative with respect to the single-particle density profile of the excess part of the free energy functional [19].

In order to calculate $h(r)$ using the OZ equation, a second equation is required to obtain a closed integral equation. This second equation is called *closure* and relates $c(r)$ to $h(r)$ and $u(r)$. There are various ways to derive different closures for specific purposes, that relate $c(r)$ in some physically appealing approximation to $g(r)$ and $u(r)$. Hereafter, we introduce various closure relations used in this work, and we discuss their respective merits and shortcomings. A deeper understanding of these closures and the physical meaning of $c(r)$ can be obtained using diagramatic and density functional theory methods. Following Ref. [78], we establish the employed closures simply using plausibility arguments. For the studied systems, some general properties that the closures must fulfill are the following. All considered closures account for the non-overlap condition $h(r < \sigma) = -1$, i.e. $g(r < \sigma) = 0$, in case of a pair potential $u(r)$ including a hard-core excluded volume part with particle diameter $\sigma$. Furthermore, they need to fulfill the asymptotic condition $c(r) = -\beta u(r)$ for $r \to \infty$, valid for a wide class of pair potentials [78].

Before proceeding, we briefly extend the OZ equation to multi-component systems. In a multi-component mixture constituted by $m$ different species, the $m(m+1)/2$ total correlation functions $h_{\alpha\beta}(r)$, that fully characterize the micro-structure of the system, are related by a set of $m(m+1)/2$ coupled OZ equations. In case of a homogeneous and isotropic fluid mixture, these OZ equations are given by

$$h_{\alpha\beta}(r) = c_{\alpha\beta}(r) + \sum_{\gamma=1}^{m} n_\gamma \int d\mathbf{r}' c_{\alpha\gamma}(|\mathbf{r} - \mathbf{r}'|) h_{\gamma\beta}(r'), \tag{5.24}$$

where $c_{\alpha\beta}(r)$ are the partial direct correlation functions for two particles belonging to components $\alpha$ and $\beta$, respectively, with $\alpha, \beta, \gamma \in \{1, ..., m\}$, and $n_\alpha$ denoting the concentration of $\alpha$-component particles. Fourier-transforming these equations leads to

$$h_{\alpha\beta}(q) = c_{\alpha\beta}(q) + \sum_{\gamma=1}^{m} n_\gamma \, c_{\alpha\gamma}(q) h_{\gamma\beta}(q). \tag{5.25}$$

To obtain a complete set of integral equations that determine the (partial) total correlation functions $h_{\alpha\beta}$(r), $m(m+1)/2$ closure relations are needed. Similarly to the one-component case, we also observe that the total correlation functions, $h_{\alpha\beta}(r)$, between two particles of components $\alpha$ and $\beta$ are written as the sum of a direct correlation part, $c_{\alpha\beta}(r)$, plus an indirect correlation part mediated through all the other particles of components $\gamma = 1, ..., m$ with relative weight $n_\gamma$ (see Eq. (5.24)).

### 5.3.1 Hypernetted chain (HNC) scheme

The approximate hypernetted chain (HNC) closure for the direct correlation function of a one-component fluid system has the from [19]

$$c(r) \approx -\beta u(r) + h(r) - \ln\left[1 + h(r)\right]. \tag{5.26}$$

Exponentiating, we obtain

$$g(r) \approx e^{-\beta u(r) + h(r) - c(r)}, \tag{5.27}$$

showing that the positive definiteness of the exact $g(r)$ is preserved at any density. Since $h(r \to \infty) = 0$ in a fluid, the HNC closure guarantees the correct asymptotic behavior of $c(r)$ for arbitrary concentration $n$. Combining Eq. (5.26) with the OZ equation produces the nonlinear HNC integral equation for $g(r)$ [79]

$$\ln g(r) + \beta u(r) = \rho \int \left[g(|\mathbf{r} - \mathbf{r}'|) - 1\right]\left[g(r') - 1 - \ln g(r') - \beta u(r')\right] d\mathbf{r}'. \tag{5.28}$$

This equation can be solved only numerically for given pair potential.

The HNC approximation predicts $g(r)$ exactly to first order in $n$ [79]. While being of poor performance for neutral hard spheres [19, 78], the HNC satisfactorily accounts for the effects of soft cores and long-range repulsive potential tails, which makes it relevant for the study of ionic fluids and dispersions of Yukawa particles.

### 5.3.2 Percus-Yevick (PY) scheme

The Percus-Yevick closure has the form [89]

$$c(r) \approx g(r)\left[1 - e^{\beta u(r)}\right], \tag{5.29}$$

predicting $c(r)$ to vanish wherever the potential is zero. The implementation of the Perkus-Yevick closure into the OZ equation results in the nonlinear integral equation [19]

$$y(r) = 1 + \rho \int d\mathbf{r}' \left[e^{-\beta u(|\mathbf{r} - \mathbf{r}'|)} y(|\mathbf{r} - \mathbf{r}'|) - 1\right]\left[e^{-\beta u(r')} - 1\right] y(r'), \tag{5.30}$$

for the continuous cavity function $y(r) := e^{\beta u(r)} g(r)$. For the three-dimensional hard-sphere fluid case, this equation can be solved analytically, but a numerical solution is required for other pair potentials [79]. The PY scheme has proved to be more accurate than the HNC approximation when the potential is short-ranged and strongly repulsive [78]. In this sense, HNC and PY methods are complementary closures.

As already mentioned, the PY integral equation is of special interest in the theory of simple liquids, because it is solvable analytically in the case of a hard-sphere fluid, which, when combined with the so-called Verlet-Weis correction, produces highly-accurate predictions of $g_(r)$ and $S(q)$ in good agreement with computer simulation results even up to the freezing volume fraction $\phi_{\mathrm{f}} = 0.494$ [78]. For a monodisperse hard-sphere system of particles with diameter $\sigma = 2a$ and volume fraction $\phi$, the Verlet-Weis corrected radial distribution function, $g_{\mathrm{HS}}^{\mathrm{VW}}(r)$, is given by [19, 78, 90]

$$g_{\mathrm{HS}}^{\mathrm{VW}}(x;\sigma) = g_{\mathrm{HS}}^{\mathrm{PY}}(x;\sigma') + A\frac{e^{-(\mu-1)x}}{x}\cos[\mu(x-1)] \tag{5.31}$$

where $x = r/\sigma > 1$. The rescaled volume fraction $\phi'$ is of the form $\phi' = \phi(1-\phi/16)$, corresponding to a rescaled diameter $\sigma' = (\phi'/\phi)^{1/3}\sigma$. The constant $A$ is fixed by demanding that the contact value predicted by Eq. (5.31) matches the one obtained from the Carnahan-Starling equation of state [19], i.e. $g_{\mathrm{HS}}^{\mathrm{VW}}(\sigma^+;\phi) = g_{\mathrm{HS}}^{\mathrm{CS}}(\sigma^+;\phi)$. The exponent $\mu$ is determined from enforcing equal isothermal compressibility between Verlet-Weis and Carnahan-Starling expressions, i.e. $S_{\mathrm{HS}}^{\mathrm{VW}}(q=0;\phi) = S_{\mathrm{HS}}^{\mathrm{CS}}(q=0;\phi)$. The Verlet-Weis corrected PY-scheme gives in practise an accurate estimation of the principal-peak height $S(q_{\mathrm{m}})$ of the hard-sphere structure factor up to the freezing concentration.

Different from the HNC approximation, the PY approximation does allow for unphysical negative values of $g(r)$. Although the PY-$g(r)$ of mondisperse hard-sphere fluids is non-negative at all distances $r$, negative values of PY partial radial distribution functions of strongly size-asymmetric hard-sphere mixtures are found at certain intermediate distances. However, the PY predicted contact values in these asymmetric systems remain positive valued [79].

### 5.3.3 Rogers-Young (RY) scheme

As noted earlier, there are different routes to compute thermodynamic properties directly from the pair correlation functions. We have discussed the virial route, Eq. (5.7), and the compressibility route, Eq. (5.16), but additionally there exist the energy route and the chemical potential route [91]. Due to the approximate nature of the different closures, the results for a thermodynamic property, such as $p$, obtained via different routes are in general different. This lack of thermodynamic consistency is a common feature of many OZ integral equation schemes.

In order to overcome part of the thermodynamic inconsistencies of the HNC and PY closures, Rogers and Young have combined them in a hybrid integral equation scheme that produces a consistent estimation of the compressibility and improved results for $g(r)$ [92]. The Rogers-Young (RY) closure is given by [78, 92]

$$g(r) \approx e^{-\beta u(r)} \left\{ 1 + \frac{1}{f(r)} \left[ e^{f(r)[h(r)-c(r)]} - 1 \right] \right\} \tag{5.32}$$

with the mixing function

$$f(r) = 1 - e^{-\alpha r} \tag{5.33}$$

including a mixing parameter $\alpha \in [0, \infty)$. From comparison with Eqs. (5.27) and (5.29), it is noticed that the RY closure reduces to the PY closure when $\alpha = 0$ and to the HNC case when $\alpha = \infty$ [89]. The mixing parameter $\alpha$ determines thus the proportion in which HNC and PY solutions are mixed. It is determined from enforcing equality of the compressibilities derived from the virial and compressibility routes, i.e. $\chi_T^{\mathrm{v}} = \chi_T^{\mathrm{c}}$, commonly done by assuming $\alpha$ to be density independent. In our application of the RY method to the effective one-component macroion system, we enforce the osmotic compressibility equality, $\chi_{\mathrm{osm}}^{\mathrm{v}} = \chi_{\mathrm{osm}}^{\mathrm{c}}$.

The RY closure has been found to perform quite well for fluids with purely repulsive potentials, when compared against computer simulation results, but it underestimates $g(r)$

and $S(q)$ oscillations for Yukawa systems close to the freezing transition [78].

## 5.4 Dynamic properties

In charge-stabilized colloidal suspensions, different (macroion) diffusion coefficients and rheological properties needs to be distinguished. Colloidal self-diffusion relates to the Brownian motion of the spherical colloidal macroions in a uniform suspension, and it is characterized by the colloidal mean-square displacement, with its short-time and long-time slopes referred to as translational short-time and long-time self-diffusion coefficients $d_\mathrm{s}$ and $d_\mathrm{s}^\mathrm{L}$, respectively. For arbitrary effective interactions between the (dressed) colloidal particles, it holds that $d_\mathrm{s}^\mathrm{L} < d_\mathrm{s} \leq d_0$, where $d_0 = k_\mathrm{B}T/(6\pi\eta_0 a_\mathrm{h})$ is the Stokes-Einstein-Sutherland translational diffusion coefficient of an isolated spherical colloid with hydrodynamic radius $a_\mathrm{h}$. For directly and hydrodynamical interacting colloids, there are dynamic cages of neighboring particles formed around each colloid which slow their self-diffusion motion. This is the reason for the inequalities noted above. The long-time coefficient, $d_\mathrm{s}^\mathrm{L}$, can be substantially smaller than $d_\mathrm{s}$ for strongly correlated particles, e.g. $d_\mathrm{s}^\mathrm{L} \approx 0.1 \times d_\mathrm{s}$ under freezing transition conditions [93, 94].

Different from self-diffusion, collective diffusion is a collective transport mechanism where colloidal particles diffuse collectively along a thermally induced local concentration gradient. The associated diffusion coefficient is called collective diffusion coefficient $d_\mathrm{c}$. In principle, one needs to distinguish, as in self-diffusion, the short-time collective diffusion from the long-time one. However, the latter is only slightly smaller than the first one, even for concentrated suspensions. Depending on the effective colloid interactions, $d_\mathrm{c}$ is larger than $d_0$, and substantially so at low salinity and intermediate concentrations where the osmotic compressibility of the suspension is low. Experimentally, $d_\mathrm{c}$ can be inferred from the so-called dynamic structure factor, $S(q, t)$, obtained in dynamic scattering experiment. This structure factor is an extension of $S(q)$ to finite correlation times $t$.

Two rheological properties, addressed in this section in addition to diffusion, are the short-time (high-frequency) and long-time (zero-frequency) suspension viscosities $\eta_\infty$ and $\eta > \eta_0$, respectively. These properties linearly relate the average suspension shear stress to the rate-of-strain applied to the suspension in a low-amplitude oscillatory shear experiment at high and low (zero) frequencies, respectively.

The employed methods for calculating dynamic suspension properties are all based on the one-component model of pseudo macroions interacting via an (equilibrium) state-dependent effective pair potential $u_{\mathrm{eff}}(r; n_{\mathrm{m}})$. By this, we ignore electrokinetic effects arising from the non-instantaneous response of the microioins to the colloid dynamics. Without external electric fields, electrokinetic effects are typically small and hence of secondary importance.

In our calculations, we identify for simplicity the hydrodynamic radius, $a_{\mathrm{h}}$, with the hard-core radius $a$ in case of rigid, impermeable colloids, and with the equilibrium particle radius $a(n_{\mathrm{m}})$ in case of size-variable, ionic microgels. While on first sight this identification seems to be a severe approximation for weakly-crosslinked solvent permeable microgels, calculations show that the Darcy permeability of microgels is actually quite small, i.e. the water inside a microgel moves actually quite rigidly along with the particle [24].

### 5.4.1 General expressions

We are interested in charge-stabilized colloidal suspensions consisting of mesoscopic impermeable solid or soft permeable (dressed) spherical particles of radius $a$, dispersed in a polar solvent, whose molecules are orders of magnitude smaller. Consequently, we treat the solvent as a structureless dielectric continuum on the relevant time and length scales of the colloidal particles. Particularly, the solvent is hydrodynamically described as a Newtonian fluid, characterized by the constant shear viscosity $\eta_0$. The incompressible fluid around colloidal particles, which are suspended in the fluid without experiencing significant sedimentation, flows under low Reynolds number conditions. Therefore, the solvent flow can be described by the quasi-steady linearized Navier-Stokes equation for incompressible flow, referred to as Stokes or creeping flow equations. The Stokes equation describes an instantaneous, inertia-free force balance between viscous, pressure and external forces acting on each fluid element [95]. On this level of description, the quasi-stationary flow follows instantaneously the likewise inertia-free motion of the suspended colloidal particles. Any perturbation that the colloidal particles exert on the fluid flow is quasi-instantaneously transmitted, affecting the motion of neighboring particles in the suspension, which are, in turn, sources of additional flow perturbations which instantaneously react back on the motion of the original particle which readjusts its motion accordingly. This long-range coupling of the motion of individual colloids by the intervening solvent flow is referred to as Hydrodynamic Interactions (HIs) [95], which are typically long-ranged and of many-body character [19]. Different from the direct (effective) interaction forces such as embodied in $u_{\text{eff}}(r; n_{\text{m}})$, HIs are dissipative and hence not derivable from a potential energy. These features make the theoretical treatment of HIs a demanding task.

The colloidal particles are furthermore affected by the thermal bombardment by the solvent molecules, giving rise to stochastic forces on the colloids that drive their Brownian motion. There is a characteristic time, $\tau_{\text{B}}$, that quantifies the momentum relaxation of a colloidal Brownian particle in a suspending fluid. It is given by $\tau_{\text{B}} = m/\zeta_0$, where $m$ is the mass of the colloidal particle and $\zeta_0 = 6\pi\eta_0 a_{\text{h}}$ is its friction coefficient. For correlation times $t \gg \tau_{\text{B}}$, the velocities of the colloidal spheres have relaxed to Maxwellian equilibrium, so that only the slow relaxation of their positions (and orientations) is resolved. Therefore, one can describe the dynamics of the interacting Brownian spheres in terms of the many-particles probability density function, $P(\mathbf{X}, t)$, for the configurational space of positional degrees of freedoms only [78]. For a quiescent suspension of spherical colloidal particles with orientation-independent direct pair forces, $P(\mathbf{X}, t)$, with $\mathbf{X} = \{\mathbf{R}_1, ..., \mathbf{R}_N\}$, is given by the translational generalized Smoluchowski equation (GSE) [78, 96],

$$\frac{\partial}{\partial t}P(\mathbf{X},t) = \hat{O}(\mathbf{X})P(\mathbf{X},t), \tag{5.34}$$

where

$$\hat{O}(\mathbf{X}) = \sum_{i,j=1}^{N} \nabla_i \cdot \boldsymbol{\mu}_{ij}(\mathbf{X}) \cdot \left[k_{\mathrm{B}}T\nabla_j - \mathbf{F}_j^{\mathrm{int}}(\mathbf{X})\right] \tag{5.35}$$

is the second-order Smoluchowski differential operator. Eq. (5.34) is also addressed as the $N$-particle diffusion equation. Here, $\mathbf{F}_j^{\mathrm{int}}(\mathbf{X}) = -\nabla_j U^{\mathrm{eff}}(\mathbf{X})$ is the force owing to the $N$-particle interaction potential $U^{\mathrm{eff}}(\mathbf{X})$ and $\boldsymbol{\mu}_{ij}$ are the translational hydrodynamic mobility tensors arising from the HIs. These tensors linearly relate the hydrodynamic force exerted by the surrounding fluid on a particle $j$, $\mathbf{F}_j^{\mathrm{h}}$, to the translational velocity, $\mathbf{v}_i$, of a particle $i$ [96, 97], i.e.

$$\mathbf{v}_i = -\sum_{i,j=1}^{N} \boldsymbol{\mu}_{ij}(\mathbf{X}) \cdot \mathbf{F}_j^{\mathrm{h}}. \tag{5.36}$$

Eq. (5.36) states that the velocity of a colloidal particle is influenced quasi-instantaneously by the hydrodynamic forces exerted on all other particles. The tensor $\boldsymbol{\mu}_{ij}$ depends on the instantaneous particle configuration $\mathbf{X}$ and on the hydrodynamic boundary conditions on the particle surfaces. In our study, we only consider the case of stick surface hydrodynamic boundary conditions. The mobility tensors can be combined to form the $3N \times 3N$ translational mobility matrix $\mu$, which is symmetric, positive definite and proportional to the diffusivity tensor $D$, $D = k_{\mathrm{B}}T\mu$ [78]. The calculation of the mobility tensors requires, in principle, the solution of the Stokes equation by accounting for the boundary conditions imposed on the surfaces of all colloidal particles [19]. This is a complex many-spheres boundary value problem that can be analytically solved only on the pair level, applicable in the high-dilution regime only.

In equilibrium, $(\partial/\partial t)P = 0$, and the GSE is satisfied by the equilibrium density function $P_{\mathrm{eq}}(\mathbf{X}) \propto \exp\{-\beta U^{\mathrm{eff}}(\mathbf{X})\}$. The latter is independent of the mobility tensors, showing explicitly that the HIs are dynamic viscous forces with no influence on the static equilibrium properties [78].

Diffusion of the colloidal particles can be experimentally determined by the dynamic structure factor

$$S(q,t) = \lim_{N,V\to\infty} \left\langle \frac{1}{N} \sum_{j,k=1}^{N} \exp\{i\mathbf{q}\cdot[\mathbf{r}_j(0) - \mathbf{r}_k(t)]\} \right\rangle , \tag{5.37}$$

in a dynamic light, x-ray or neutron scattering experiment. Here, $N$ is the number of colloidal particles in the scattering volume, $\mathbf{q}$ the scattering wave vector, and $\mathbf{r}_j(t)$ the position of the $j$-th particle at time $t$. The brackets, $\langle ... \rangle$, denote an equilibrium ensemble or time average for an ergodic system. The thermodynamic limit, $N \to \infty$ and system volume $V \to \infty$ with $n = N/V$ fixed guarantees that $S(q,t)$ is ensemble independent.

Using the GSE, Eq. (5.34), $S(q,t)$ can be in principle calculated from [78]

$$S(q,t) = \lim_{N,V\to\infty} \left\langle \frac{1}{N} \sum_{j,k=1}^{N} e^{i\mathbf{q}\cdot\mathbf{r}_j} \left( e^{\hat{\mathcal{O}}_B t} e^{-i\mathbf{q}\cdot\mathbf{r}_k} \right) \right\rangle_{\text{eff}} , \tag{5.38}$$

where $\hat{\mathcal{O}}_B$ is the formal adjoint of the Smoluchowski operator (cf. Eq (5.35)), also called backward Smoluchowski operator. The script "eff" in the average $\langle ... \rangle_{\text{eff}}$ and in $U^{\text{eff}}$ reminds that an effective one-component colloidal system of dressed colloidal spheres with direct interactions encoded in $u_{\text{eff}}(r)$ is considered. The operator $\hat{\mathcal{O}}_B$ is negative-semi definite, so that $S(q,t)$ is a positive valued and strictly monotonic decaying function of time in the fluid-phase regime [98].

For analyzing the information on diffusion embodied in $S(q,t)$ based on Eq. (5.38), it is appropriate to consider different time scales. We focus on times $t \gg \tau_{\text{B}}$, where inertial effects are not resolved anymore and the GSE applies [78]. Under these conditions, there are two well-defined regimes: first, the colloidal short-time regime, characterized by correlation times $t$ such that $\tau_{\text{B}} \ll t \ll \tau_{\text{I}}$; and second, the colloidal long-time regime where $\tau_{\text{I}} \ll t$. Here, $\tau_{\text{I}} = a^2/d_0$ is the structural relaxation time over which noticeable changes in the particle positions over distances of the order of $a$ take place.

For $t \ll \tau_I$, particle displacements by Brownian motion are minuscule compared to the particle radius. Hence, the short-time dynamic properties are influenced solely by the inter-particle HIs, which are quasi-instantaneously transmitted. These transport properties can thus be calculated as genuine equilibrium averages invoking the configuration-dependent hydrodynamic mobilities. The non-dynamic direct interactions embodied in the inter-particle potential are only indirectly influential through their effect on the equilibrium colloidal microstructure encoded in $g(r)$ and $S(q) = S(q, t = 0)$. Long-time transport properties, such as the zero-frequency suspension viscosity $\eta$, and the long-time self-diffusion coefficient $d_{\mathrm{s}}^{\mathrm{L}}$, are influenced additionally by the inter-particle interactions via non-instantaneous caging (i.e., memory) effects. In the following two subsections, we are going to address short- and long-time dynamics separately.

### 5.4.2 Short-time dynamics

The short-time regime corresponds to correlation times $\tau_{\mathrm{B}} \ll t \ll \tau_{\mathrm{I}}$ well above the momentum-relaxation characteristic time $\tau_{\mathrm{B}}$, and shorter than the structural relaxation time $\tau_{\mathrm{I}}$. Within this range, $S(q, t)$ in Eq. (5.38) can be expanded in a series of cummulants. The leading cummulant describes an exponential decay of $S(q, t)$ according to [5, 99, 100]

$$S(q, \tau_{\mathrm{B}} \ll t \ll \tau_{\mathrm{I}}) \approx S(q) \exp\{-q^2 D(q) t\} , \tag{5.39}$$

where $D(q)$ is a wavenumber-dependent, short-time diffusion function characterizing the short-time decay of concentration fluctuations of wavelength $2\pi/q$. Comparing Eq. (5.39) with the first cummulant of $S(q, t)$ obtained from the expression in Eq. (5.38), one identifies that $D(q)$ is given by the ratio [5, 99, 100]

$$D(q) = d_0 \frac{H(q)}{S(q)} , \tag{5.40}$$

where $H(q)$ is the so-called hydrodynamic function given by the equilibrium average [5]

$$H(q) = \left\langle \frac{1}{N \mu_0 q^2} \sum_{l,j=1}^{N} \mathbf{q} \cdot \boldsymbol{\mu}_{lj}(\mathbf{X}) \cdot \mathbf{q} \, e^{i\mathbf{q}\cdot(\mathbf{r}_l - \mathbf{r}_j)} \right\rangle_{\mathrm{eff}} , \tag{5.41}$$

over the configurations $\mathbf{X}$ of the colloidal particles. Here, $k_{\mathrm{B}} T \mu_0 = d_0$ and $\boldsymbol{\mu}_{lj}(\mathbf{X})$ are the translational $N$-spheres mobility tensors from Eq. (5.36).

The positive-valued function $H(q)$ is a measure of the influence of HIs on short-time translational diffusion over the length scale $\sim 1/q$. In the (hypothetical) case of hydrodynamically non-interacting particles, $H(q) \equiv 1$, independent of $q$ and particle concentration. Deviations of $H(q)$ from the infinite dilution value of one thus hallmark the influence of HIs.

Eq. (5.41) can be split according to

$$H(q) = \frac{d_{\rm s}}{d_0} + H_{\rm d}(q)\,, \tag{5.42}$$

into the sum of a self-part equal to the short-time self-diffusion coefficient $d_{\rm s}$ (in units of $d_0$), quantifying the initial slope of the particle mean-square displacement, and a wavenumber-dependent distinct part, $H_{\rm d}(q)$, accounting for hydrodynamic cross correlations between the particles. The latter part decays to zero at large $q$. Thus, for large $qa_{\rm h} \gg 1$, the hydrodynamic function becomes equal to $d_{\rm s}/d_0$, while for small wavenumbers $qa_{\rm h} \ll 1$ it reduces to the (short-time) sedimentation coefficient, $K$, of an homogeneous suspension subjected to a weak constant (gravitational) force field, given by

$$K = \frac{V_{\rm sed}}{V_0} = \lim_{q\to 0} H(q), \tag{5.43}$$

with $V_{\rm sed}$ being the short-time average sedimentation velocity of hydrodynamically interacting monodisperse particles, and $V_0$ the isolated particle sedimentation velocity in the same constant force field.

Two additional diffusion coefficients arising from $D(q)$ in Eq. (5.40) are the (short-time) collective diffusion coefficient, $d_{\rm c}$, and the (short-time) cage diffusion coefficient, $d_{\rm cge}$. The collective diffusion coefficient is related to the sedimentation coefficient by

$$d_{\rm c} = d_0 \frac{K}{S(q\to 0)} = \frac{d_0\,K}{k_{\rm B}T\,(\partial n/\partial \pi_{\rm osm})_{\rm res}}\,, \tag{5.44}$$

and it characterizes the decay rate of thermally-induced concentration fluctuations of macroscopic wavelengths. The cage diffusion coefficient $d_{\rm cge} = D(q_{\rm m})$, with $q_{\rm m}$ indicating the principal peak position of the hydrodynamic function, characterizes the decay rate of thermally induced concentration fluctuations of a wavelength related to the extension, $2\pi/q_{\mathrm{m}}$, of the dynamic nearest-neighbor cage formed around a colloidal particle [97]. Like any cooperative diffusion coefficient, $d_{\mathrm{c}}$ is the ratio of a kinetic coefficient (here, $K$) and a thermodynamic property, which in the present case is the isothermal (osmotic) compressibility factor.

A non-diffusional, rheological short-time property characterizing the suspension as a whole is the high-frequency viscosity, $\eta_\infty$, at low shear rates. This property linearly relates the average deviatoric suspension shear stress to the applied rate of strain in a low-amplitude, oscillatory shear experiment at frequencies $\omega \gg 1/\tau_{\mathrm{I}}$, where shear-induced perturbations of the microstructure away from the equilibrium spherical symmetry are negligible. Experimentally, $\eta_\infty$ can be determined using a torsional rheometer operated at high frequencies and low amplitudes. The high-frequency viscosity is a purely hydrodynamic property, whose statistical physics expression is given, owing to isotropy, by (see, e.g., [101])

$$\eta_\infty = \eta_0 + \lim_{q\to 0} \sum_{\alpha,\beta=1}^{3} \left\langle \frac{1}{10V} \sum_{l,j=1}^{N} \mu^{dd}_{lj,\alpha\beta\beta\alpha}(\mathbf{X})\, e^{i\mathbf{q}\cdot(\mathbf{r}_l-\mathbf{r}_j)} \right\rangle_{\mathrm{eff}}, \tag{5.45}$$

where $\mu^{dd}_{lj,\alpha\beta\beta\alpha}$ are the Cartesian components of the fourth-rank dipole-dipole hydrodynamic tensor $\boldsymbol{\mu}^{dd}_{lj}$, relating the symmetric hydrodynamic force dipole moment tensor of microgel sphere $l$ to the rate of strain tensor evaluated at the center of a sphere $j$. Other parameters are the suspension volume $V$ and the fluid viscosity $\eta_0$. In Eq. (5.45), the zero-wavenumber limit is taken after the ensemble averaging over a macroscopic system, guaranteeing in this way convergence of the integrals following from the averaging over the spatially slowly decaying hydrodynamic tensors [102].

### 5.4.3 Long-time dynamics

As noted before, the long-time regime corresponds to correlation times $t \gg \tau_I$, during which the particle configuration has changed significantly. Different from short-time properties, in the long-time regime the suspension properties are additionally influenced by thermally-driven microstructural relaxation processes depending not only on the hydrodynamic interactions, but also on the direct inter-particle interactions. The joint influence of these interactions renders the calculation of long-time transport properties demanding. The dynamic caging effect noted before leads to a weak distortion of the dynamic next-neighboring cage formed around each particle at longer times, so that long-time properties are not equilibrium averages anymore, as it is the case for short-time properties [78].

In this thesis, we analyze the (long-time) collective diffusion coefficient, $d_\mathrm{c}$, and the zero-frequency viscosity, $\eta$. The long-time collective diffusion coefficient appears in Fick's law, $\mathbf{j} = -d_\mathrm{c}^\mathrm{L}\nabla n_\mathrm{m}$, linearly relating a macroscopic concentration gradient, $\nabla n_\mathrm{m}$, to the collective diffusion current $\mathbf{j}$. As discussed earlier, the long-time collective diffusion coefficient is only slightly smaller than the short-time one given in Eq. (5.44) (by at most 6% for concentrated suspensions of no-slip colloidal hard spheres) [103]. The difference can be expected to be even smaller for particles with electrostatic repulsion [99]. Therefore, we use the short-time collective diffusion coefficient as a good approximation of the long-time collective diffusion coefficient.

The second considered colloidal long-time property is the low-shear-rate, zero-frequency viscosity as measured in a suspension subjected to steady-state weak shear flow. This viscosity is the sum [98],

$$\eta = \eta_\infty + \Delta\eta\,, \tag{5.46}$$

of $\eta_\infty$ and a positive shear-stress relaxation contribution denoted as $\Delta\eta$. The latter is related to the additional dissipation in the suspension originating from stress relaxations of the shear-perturbed next-neighbor particle cages formed around each particle, and it is influenced both by direct and hydrodynamic interactions. The viscosity part, $\Delta\eta$, can be calculated based on an exact Green-Kubo relation for the time integral of the equilibrium stress auto-correlation function where HIs are included [98].

### 5.4.4 Methods of calculation

We describe here the different analytic methods used in this thesis for calculating the considered short-time and long-time dynamic properties on basis of the effective one-component colloidal model.

For the calculation of $H(q)$, we use the well-established analytic BM-PA scheme [97]. This scheme is a hybrid of the second-order Beenakker-Mazur method (BM), used here for the wavenumber-dependent distinct part $H_\mathrm{d}(q)$, and the hydrodynamic pairwise-additivity (PA) approximation used for the $q$-independent self part $d_\mathrm{s}/d_0$. The BM-PA scheme combines the advantages of the BM and PA methods. It requires the (dressed) colloidal macroion structure factor and radial distribution function, $S(q)$ and $g(r)$, respectively, as its only input, for which the RY scheme based on the effective pair interaction $u_\mathrm{eff}(r)$ is used. In case of microion-permeable soft colloids with concentration-dependent radius $a(n_\mathrm{m})$, the latter is determined using the TPT/PBCM methods in section 4.3 for the according effective pair potential. The overall good accuracy of the BM-PA scheme was assessed by comparison with elaborate dynamic simulation results, where many-particles HIs are accounted for, and with experimental $H(q)$ data, for a variety of colloidal model systems including solvent-permeable hard spheres (as a model of non-ionic microgels), charge-stabilized rigid spherical particles, and globular proteins exhibiting short-range attraction and long-range repulsion [21, 97, 99, 104]. PA and BM methods are described in Appendix A and Appendix B, respectively.

The high-frequency viscosity, $\eta_\infty$, is calculated using a modified Beenakker-Mazur mean-field method. In this semi-analytic method invoking one-dimensional integrals only, many-particles HIs are approximately accounted for, but lubrication is disregarded. Lubrication is rather irrelevant, however, for the charge-stabilized suspensions explored in this work. Like the BM-PA scheme for $H(q)$, the modified BM method for $\eta_\infty$ has $S(q)$ as its only input. The modified BM expression for $\eta_\infty$ reads [97]

$$\frac{\eta_\infty}{\eta_0} = 1 + \frac{5}{2}\phi(1+\phi) - \frac{1}{\lambda_0} + \frac{1}{\lambda_0 + \lambda_2}\,, \tag{5.47}$$

with the so-called zeroth and second-order BM viscosity contributions, $\lambda_0(\phi)$ and $\lambda_2(\phi)$, respectively, whose explicit forms are given in Appendix B. The invoked modification of the standard BM expression for $\eta_\infty/\eta_0$ is the subtraction of the structure-independent BM part, $1/\lambda_0$, and its replacement by the structure-independent pairwise additive viscosity contribution, $1 + 2.5\phi(1 + \phi)$, which is known to give the dominant contribution at low salinity and small volume fractions. The modified BM expression is in very good agreement with Stokesian Dynamics simulation data for the high-frequency viscosity of low-salinity charge-stabilized suspensions, even up to the freezing transition concentration [97].

As noted above, the calculation of the shear relaxation contribution, $\Delta\eta$, to the zero-frequency viscosity, $\eta = \eta_\infty + \Delta\eta$, is more demanding since it is explicitly influenced by direct and hydrodynamic interactions. Starting from an exact but formal Green-Kubo relation for $\Delta\eta$, mode-coupling theory (MCT) integro-differential equations with HIs included have been derived for its approximate calculation, whose numerical solution is quite involved. We use therefore a simplified MCT theory expression for $\Delta\eta$, constituting the first-iteration step in the self-consistent numerical solution of the MCT equations. This simplified MCT expression is [98]

$$\frac{\Delta\eta}{\eta_0} = \frac{1}{40\pi}\int_0^\infty dy\, y^2\, \frac{(S'(y))^2}{S(y)}\frac{1}{H(y)}\,, \tag{5.48}$$

where $y = 2qa$ and $S'(y) = dS(y)/dy$. HIs enter here only through the dynamic structure factor $S(q,t)$, which in turn is approximated by its short-time form given by the right-hand side of Eq. (5.39) involving $H(q)$. Since for correlated particles $S(q,t)$ decays more slowly than exponentially at longer times, $\Delta\eta$ is somewhat underestimated by Eq. (5.48), as compared to the fully self-consistent MCT viscosity solution. This underestimation becomes more pronounced at higher $\phi$.

# Chapter Six

# SIZE-VARYING IONIC MICROGELS: NUMERICAL RESULTS

In this chapter, we explore theoretically suspensions of soft weakly-crosslinked spherical ionic microgels. We present a comprehensive treatment of dynamic and static equilibrium microstructural properties of these suspensions in the swollen state accounting for counterion-regulated deswelling effects. For this purpose, the ionic microgels are modeled in a coarse-grained way as microion- and solvent-permeable, monodisperse elastic colloidal spheres, with the charged sites of the crosslinked polymer gel backbone simply described by a uniform charge distribution. This description is reasonable, under the proviso that the cross-linker density does not vary strongly along the particle radius. Within this description, we employ the PBCM and TPT mean-field methods from section 4.3 for describing the concentration-dependent deswelling of microgels and calculating their equilibrium mean size. In combination with an effective pair potential expression of ionic microgels derived within the multi-center approach in sections 2.1 and 4.1, we determine the pressure and osmotic compressibility of ionic microgel suspensions as well as the microgel pair distribution function and static structure factor using the HNC and thermodynamically self-consistent RY integral-equation methods, presented in section 5.3. Finally, the microgel pair distribution function is used as input to our calculations of dynamic suspension properties. Semi-analytic methods, based on the one-component effective microgel picture presented in section 5.4, are used to calculate dynamic properties. In our assessment of deswelling effects, the results obtained for various static and dynamic suspension properties are compared with the ones for a (fictitious) reference suspension of constant-size microgels.

In order to analyze the influence of counterion-induced deswelling on thermodynamic, structural and dynamic properties, and to make contact with a study by Weyer *et. al.* [15], in which TPT results for the mean microgel radius were compared against computer simulations for salt-free systems, we use the following system parameters, corresponding to aqueous suspensions at lower salinity: solvent Bjerrum length $\lambda_B = 0.714\,\text{nm}$ (i.e., water as solvent at temperature $T = 293\,K$), backbone microgel bare valences $Z = 100$, 200, and 500, dry microgel radius $a_0 = 10$ nm, backbone monomer number per microgel $N_{\text{mon}} = 2 \times 10^5$, polymer chain number per microgel $N_{\text{ch}} = 100$, solvency parameter $\chi = 0.5$, and Hertz softness parameter $\epsilon_H = 1.5 \times 10^4$. For the 1:1 electrolyte reservoir concentration in the considered Donnan equilibrium, we use $c_{\text{res}} = 100\ \mu$M, if not stated otherwise, so that $n_{\text{res}} = c_{\text{res}}\, N_A$, where $N_A$ is the Avogradro number. Values of the dry volume fraction, $\phi_0 = (4\pi/3) n_m a_0^3$, in the range from $2 \times 10^{-4} - 5 \times 10^{-2}$ are considered. Here, $n_m$ is the microgel (macroion) number density. Thus, $\phi_0 \propto n_m$ has the meaning of a dimensionless microgel concentration. The Debye screening length, $1/\kappa$, introduced in Eq. (2.59), attains values from $40 - 4.4$ nm, for (reduced) concentration values $\phi_0$ varied from $0.001 - 0.05$. It is noteworthy that, for most of the considered suspensions, $\kappa$ is determined by the mean concentration, $Zn_m$, of monovalent counterions released from the microgel polymer backbone, which is significantly higher than the salt pair concentration $n_s$ in the suspension.

The electrostatic repulsion between the microgels is quantified by the reduced electrostatic coupling strength $\Gamma_{\text{el}} \equiv Z_{\text{net}} \lambda_B / a$, which in the present study is in the range of 1 - 9, comparable to values for typical ionic microgel systems [7, 105, 106]. The electrostatic repulsion between the microgels is here strong enough that configurations of microgels that are in contact or overlapping are very unlikely, such that $g(r \leq 2a) \approx 0$ holds for the microgel radial distribution function. On the other hand, nonlinear screening effects are in most cases weak enough that the linear TPT method can be used for determining the mean microgel equilibrium radius $a$, in addition to the PBCM method.

## 6.1 Equilibrium radius predictions

For computing the microgel equilibrium radius $a$, we follow the stability criterion presented in Eq. (4.15) or, equivalently, in Eq. (4.16). We describe the elastic and solvent-interaction free energy contributions of a microgel using Flory-Rehner theory [16–18] for uniform cross-linker distribution. For calculating the electrostatic semi-grand free energy contribution of microgels in a concentrated suspension, in Donnan equilibrium with a 1:1 strong electrolyte reservoir, we use two different mean-field methods, namely the spherical Poisson-Boltzmann cell model (PBCM) approach of Denton and Tang [14], presented in subsection 4.3.2, and a first-order thermodynamic perturbation theory (TPT) method of Weyer and Denton [15], introduced in subsection 4.3.1. The equilibrium microgel radius is obtained from minimizing the total suspension free energy, equivalent to enforcing the balance of total (intrinsic) pressure inside and outside a microgel particle.

In the following, we analyze TPT and PBCM predictions for the concentration-dependent microgel swelling ratio, $\alpha(\phi_0) = a(\phi_0)/a_0$, the suspension salt concentration $n_{\mathrm{s}}(\phi_0)$, and the electrostatic coupling strength $\Gamma_{\mathrm{el}}(\phi_0)$, where $\phi_0 \propto n_{\mathrm{m}}$ is the non-dimensional microgel concentration.

The physical mechanism leading to counterion-induced deswelling with increasing concentration can be reasoned on the basis of Fig. 6.1, which shows PBCM results at two different concentrations for the radial dependence of the (reduced) total microion charge density, $\rho^{\mathrm{el}}(r) = [n_+(r) - n_-(r)]\, e$, and of the coion concentration $n_-(r)$ (displayed in the

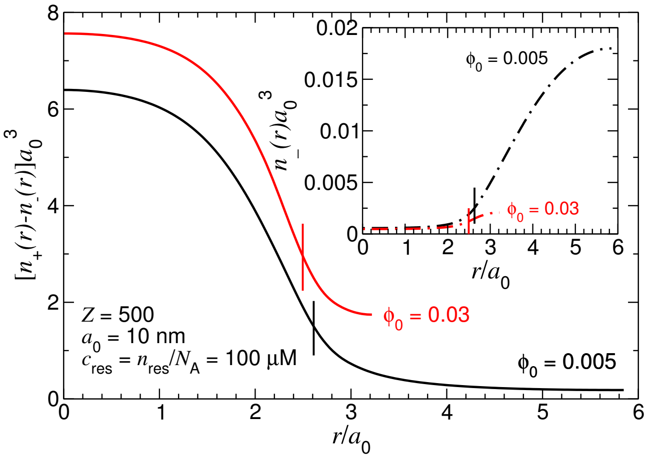

**Figure 6.1** PBCM predictions for radial profile of microion charge density $\rho^{\text{el}}(r)$ in units of $1/(a_0^3\,e)$, versus radial distance $r$ from center of cell (units of dry radius $a_0$) for microgel valence $Z = 500$, dry radius $a_0 = 10$ nm, reservoir salt concentration $c_{\text{res}} = n_{\text{res}}/N_{\text{A}} = 100\,\mu$M, and dry volume fractions $\phi_0 = 0.03$ and 0.005 (red and black solid curves). Inset: Reduced coion number density $n_-(r)a_0^3$ (dashed-dotted curves). All curves terminate at the cell radius $r = R = a_0/\phi_0^{1/3}$. Vertical line segments indicate the equilibrium swelling ratio, $\alpha = a/a_0$, computed from zero balance of intra-particle pressure contributions in Eqs. (4.26) and (4.29), respectively.

inset) inside and outside of a negatively charged microgel centered at $r = 0$. For both considered concentrations $\phi_0$, the counterions constitute the dominant microion species where $n_+(r) \gg n_-(r)$, and hence $\rho^{\text{el}}(r) \approx n_+(r)e$ holds for the total microgel charge concentration inside the cell up to its boundary at radius $R = a_0/\phi_0^{1/3}$, where the curves in Fig. 6.1 terminate.

One clearly notices that both the equilibrium microgel radius $a$, marked by the vertical line segments in the figure, and the radius $R$ of the spherical cell in PBCM decrease with increasing concentration. The counterion concentration profile rises with increasing system concentration, while the coion concentration profile falls. With increasing concentration, the volume exterior to the microgels is reduced, making it (entropically) less favorable for counterions to reside outside the oppositely charged microgel backbone region. Consequently, a fraction of the outside counterions permeates into the backbone region, thereby lowering the expansive intrinsic PBCM pressure contribution $\Pi_{\text{e}}$ (Eq. (4.26)). In response, the microgel deswells until a new equilibrium with the contractile polymer gel pressure contribution $\Pi_{\mathrm{g}}$, in Eq. (4.18), is established at a smaller equilibrium radius. The enhanced counterion permeation of microgels with increasing concentration is reflected in the lowering of the net microgel valence $Z_{\mathrm{net}}$, defined in Eq. (2.62), which for the backbone valence $Z = 500$ is given by $Z_{\mathrm{net}} = 223$ at $\phi_0 = 0.005$ and by $Z_{\mathrm{net}} = 154$ at $\phi_0 = 0.03$. The counterion-induced deswelling becomes weaker with increasing salt concentration, which causes a flattening of the microion concentration profiles across the microgel surface.

In the PBCM method, the mean salt concentration, $n_{\mathrm{s}}$, in the suspension is obtained by integrating the coion concentration profile over the cell volume according to Eq. (4.30). In the TPT method, $n_{\mathrm{s}}$ is computed using the equality of the chemical potentials of the microions in the suspension and reservoir. We reemphasize that in Donnan equilibrium, $n_{\mathrm{s}}$ is a state-dependent quantity. The TPT and PBCM predictions for the concentration dependence of $n_{\mathrm{s}}$ are depicted in Fig. 6.2 (red and black curves, respectively), for reservoir microion concentration $c_{\mathrm{res}} = 100\,\mu$M and backbone valences $Z = 100$, 200, and 500. The monotonic decrease of $n_{\mathrm{s}}$ with increasing $\phi_0$, and hence with increasing number of backbone-released counterions, is due to an increasing expulsion of salt ion pairs into the reservoir, necessitated to maintain global electroneutrality in the suspension.

At high dilution, $\phi_0 \to 0$, where the concentration of salt counterions greatly exceeds the concentration of backbone-released counterions, the exact limit $n_{\mathrm{s}} \to n_{\mathrm{res}}$ is recovered by both methods. For the moderately high valences $Z = 100$ and $Z = 200$ considered here, the TPT and PBCM curves for $n_{\mathrm{s}}(\phi_0)$ in Fig. 6.2 lie close to each other, but with a slightly stronger salt expulsion predicted in the PBCM. Pronounced differences are observed for the high valence $Z = 500$ and intermediate $\phi_0$, where the concentration, $Zn_{\mathrm{m}}$, of backbone-released counterions is comparable to the salt-counterion concentration. While the PBCM predicts a decreasing $n_{\mathrm{s}}$ with increasing $Z$, in accord with physical expectation, this trend is reversed for $\phi_0 \lesssim 0.005$ by the TPT curve for $Z = 500$. We attribute this reversal to the disregard in the linear TPT of nonlinear electrostatic effects, which come into play at high valences and low $\phi_0$. The PBCM is based on the nonlinear PB-type equation Eq. (4.25) and accounts for nonlinear electrostatic effects, but not for inter-microgel correlations. The latter are accounted for in TPT, but on linear level only.

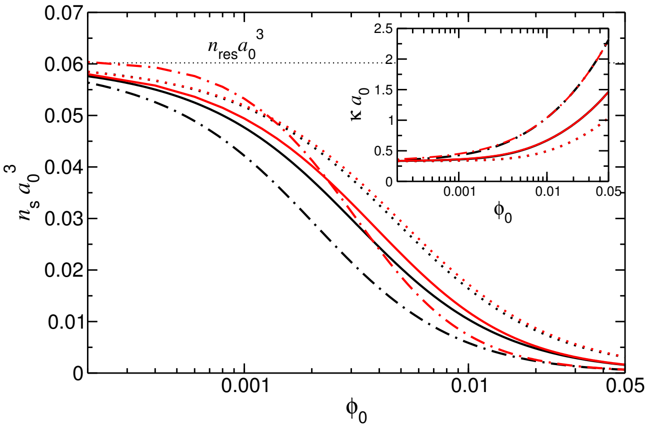

**Figure 6.2** Reduced suspension salt concentration, $n_{\mathrm{s}}a_0^3$, versus microgel concentration $\phi_0$. Inset: Reduced Debye screening constant $\kappa a_0$. TPT predictions are in red, and PBCM predictions in black, for backbone valence $Z = 100$ (dotted), 200 (solid), and 500 (dash-dotted). Reservoir salt concentration is $c_{\mathrm{res}} = n_{\mathrm{res}}/N_{\mathrm{A}} = 100\,\mu$M.

The inset of Fig. 6.2 displays TPT and PBCM predictions for the Debye screening constant $\kappa$ based on Eq. (2.59), but using different predictions for $n_{\mathrm{s}}$ depending on the method. We notice that these predictions for $\kappa$ are practically equal on the scale of the inset. In dimensionless form, the screening constant is

$$(\kappa a_0)^2 = (\kappa_{\mathrm{c}}a_0)^2 + (\kappa_{\mathrm{s}}a_0)^2 = 3\phi_0\frac{Z\lambda_{\mathrm{B}}}{a_0} + 8\pi\lambda_{\mathrm{B}}n_{\mathrm{s}}a_0^2\,. \tag{6.1}$$

The first term on the right-hand side is the contribution by the backbone-released counterions (subscript c). The second term, proportional to $n_{\mathrm{s}}$, is the salt-ion contribution (subscript s). This splitting of $\kappa^2$ into released-counterion and salt-ion contributions allows to identify the counterion-dominated regime by the condition $\kappa_{\mathrm{c}} \gg \kappa_{\mathrm{s}}$ and the salt-dominated regime by $\kappa_{\mathrm{c}} \ll \kappa_{\mathrm{s}}$. At very low microgel concentrations, i.e., in the salt-dominated regime where $\kappa \approx \kappa_{\mathrm{s}}$, the TPT and PBCM predictions for $\kappa$ differ due to differing values for $n_{\mathrm{s}}$. However, these differences are not visible in the inset. At higher concentrations in the counterion-dominated regime where $\kappa \approx \kappa_{\mathrm{c}}$, both methods predict practically the same $\kappa \approx \kappa_{\mathrm{c}}$, de-

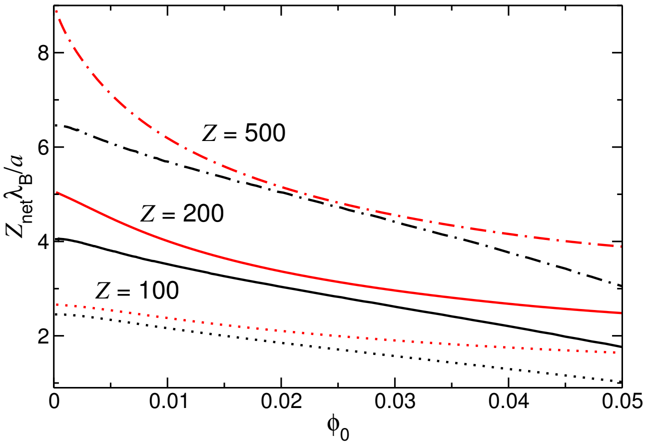

**Figure 6.3** Electrostatic coupling parameter, $\Gamma_{\mathrm{el}} = Z_{\mathrm{net}}\lambda_{\mathrm{B}}/a$, versus microgel concentration $\phi_0$, where $Z_{\mathrm{net}}$ is the net microgel valence. System parameters, colors, and linetypes are the same as in Fig. 6.2.

termined by $Z$ and $\phi_0$. With increasing backbone valence, $\kappa_{\mathrm{c}}$ increases while $\kappa_{\mathrm{s}}$ decreases, owing to increased salt expulsion. The total screening constant $\kappa$ increases monotonically with increasing concentration, more steeply so for higher $Z$.

Figure 6.3 shows the electrostatic coupling strength, $\Gamma_{\mathrm{el}}$, as a function of $\phi_0$. Notice that $\Gamma_{\mathrm{el}}$ depends on the equilibrium radius $a$ and net microgel valence $Z_{\mathrm{net}}$, both of which are monotonically decreasing with increasing $\phi_0$. The decrease of $Z_{\mathrm{net}}$ due to inside-permeated counterions is more pronounced than the decrease of $a$ with increasing concentration, which explains the monotonic decrease of $\Gamma_{\mathrm{el}}$. The overall behavior of the coupling strength as function of concentration and backbone valence is similar in the TPT and PBCM, but the TPT consistently predicts a stronger electrostatic coupling than PBCM. The greatest differences are visible for low concentrations and for the highest considered backbone valence $Z = 500$ where $\Gamma_{\mathrm{el}} > 5$, such that nonlinear electrostatic effects, not accounted for in the linear TPT, come into play, as we are going to see in chapter 7. We stress here that, in contrast to suspensions of impermeable, solid particles, a reduction in the concentration of permeable, compressible particles results in a strengthening of the electrostatic interparticle repulsion.

Figure 6.4 depicts the concentration dependence of the equilibrium microgel swelling ra-

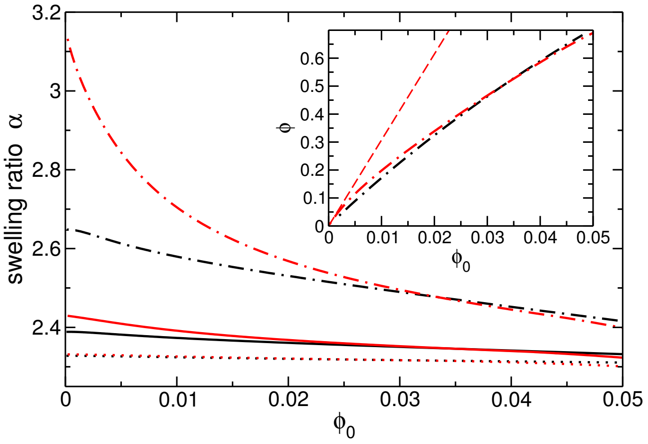

**Figure 6.4** Swelling ratio, $\alpha = a/a_0$, versus reduced concentration, $\phi_0$, for backbone valence $Z = 500$ (dashed-dotted), 200 (solid), and 100 (dotted) at $c_{\rm res} = 100\,\mu$M. Inset: Swollen microgel volume fraction $\phi = \phi_0\,\alpha^3$ versus $\phi_0$. The straight dashed line in the inset depicts $\phi = \phi_0\,\alpha(\phi_0^*)^3$ for a fixed TPT microgel radius taken at $\phi_0^* = 2.0 \times 10^{-4}$ and backbone valence $Z = 500$. Other system parameters are the same as in Fig. 6.2.

tio, $\alpha = a/a_0$, for three different backbone valences. At a given $\phi_0$, the swelling ratio increases with increasing $Z$, owing to an enhanced electrostatic repulsion between the $Z$ monovalently charged backbone sites for a constant reservoir salt concentration $c_{\rm res} = 100\ \mu$M. Deswelling in the counterion-dominated regime displayed in the figure is most pronounced at smaller $\phi_0$, where $a$ decreases more strongly for higher $Z$. For $Z = 500$, the TPT predicts distinctly higher swelling ratios than the PBCM, and a distinctly steeper decay of $\alpha = a/a_0$ with increasing $\phi_0$.

An important quantity characterizing the swollen microgels is the volume fraction $\phi = \phi_0\,\alpha^3$, whose concentration dependence is shown in the inset for $Z = 500$. Due to deswelling, $\phi$ increases sublinearly with increasing $\phi_0$. Differences between the TPT and PBCM predictions for $\phi$ are small except for small concentrations, where nonlinear electrostatic coupling is significant.

To assess quantitatively the effect of deswelling on structural and dynamic properties, it is useful to compare findings for the actual suspension of deswelling microgels with those for a fictitious reference suspension of non-swelling particles. We select the system parameters of the reference system to be the same as in the actual one, except for the microgel radius $a_{\rm ref}$, which is fixed to the equilibrium value of the deswelling system at the lowest considered concentration, $\phi_0^{\rm ref}$, where nonlinear screening by the microions can still be disregarded. Explicitly, we set $a_{\rm ref} = a(\phi_0^{\rm ref})$ using $\phi_0^{\rm ref} = 0.005$, a reservoir concentration fixed to $c_{\rm res} = 100\ \mu$M, and backbone valences restricted to values $Z \leq 200$.

Figure 6.5 shows the swelling ratio, $\alpha$, predicted by the two methods, compared with the respective constant value $\alpha(\phi_0 = 0.005)$ (dashed horizontal lines) for the reference system. Note that the reference-system microgel radius is different for the two methods, namely, $a_{\rm ref} \approx 24.1$ nm in TPT and $a_{\rm ref} \approx 23.8$ nm in PBCM. The transition from salt-ion to counterion domination occurs at very small concentrations, resolved in the inset of Fig. 6.5. The vertical line segments mark here the microgel concentration where $Zn_{\rm m} = 2n_{\rm s}$ and hence $\kappa_{\rm c} = \kappa_{\rm s}$. At very small concentrations where $\kappa_{\rm c} < \kappa_s$, $\alpha$ changes only little with concentration.

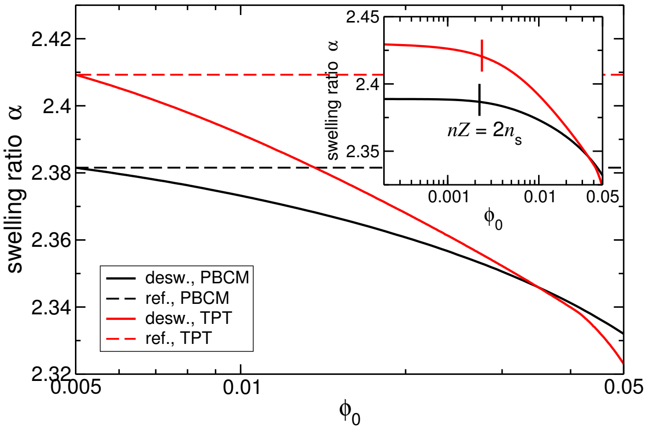

**Figure 6.5** Predictions of TPT and PBCM for swelling ratio $\alpha = a/a_0$ versus microgel concentration $\phi_0$ compared with corresponding reference system results (dashed lines). Inset: Swelling ratio $\alpha$ for low concentrations where the salt-dominated regime is resolved. System parameters: $Z = 200$ and $c_{\rm res} = 100\,\mu$M.

It was shown in [54, 56, 57, 63, 65, 67] and will be presented in chapter 7, that nonlinear electrostatic coupling, which comes into play for $\Gamma_{\rm el} \gtrsim 5$, can be incorporated into linear Yukawa-type effective pair potentials, such as in Eq. (2.61), by using renormalized values, $Z_{\text{eff}}$ and $\kappa_{\text{eff}}$, of the particle (backbone) valence and of the Debye screening constant, respectively. Different renormalization schemes were developed for this purpose for charge-stabilized suspensions of impermeable particles, as discussed in chapter 3, but considerably less applications to ionic microgels were reported so far [62, 105–108].

In the remainder of this chapter, we study fluid-phase suspensions mostly for conditions $\Gamma_{\text{el}} < 5$ where the TPT and PBCM results can be directly compared without the need to invoke microgel charge renormalization. For higher values of $Z_{\text{net}}$, this condition limits us to concentrations $\phi_0 > \phi_0^{\text{ref}} = 0.005$ in the counterion-dominated regime where deswelling is most pronounced.

## 6.2 Potential parameters and pressure contributions

Having introduced the reference system of constant-size microgels, we analyze next the parameters characterizing the effective pair potential of deswelling ionic microgels, in comparison with the reference system values. For the considered system parameters, the likelihood of particle overlap is small. The effective microgel interaction is thus determined by the non-overlapping (Yukawa) part of the effective pair potential, $u_{\text{Y}}(r; n)$, in Eq. (2.61). The Yukawa potential, which is characterized by $Z_{\text{net}}$ and $\kappa$, can be expressed in the form

$$\beta u_{\text{Y}}(r; n_{\text{m}}) = 2a_0 A_{\text{Y}} \frac{e^{-\kappa r}}{r}\,, \tag{6.2}$$

where $A_{\text{Y}} = \beta u_{\text{Y}}(2a_0; n_{\text{m}}) \exp(2\kappa a_0)$ is an interaction strength parameter.

In Fig. 6.6, the concentration dependence of the net microgel valence $Z_{\text{net}}$ and the Debye screening constant $\kappa$ of deswelling particles are compared with the reference system predictions. While $Z_{\text{net}}$ decreases with increasing concentration, $\kappa$ monotonically increases. This trend can be attributed to the associated increase in the number of counterions inside the microgels. Deswelling slightly increases $Z_{\text{net}}$, but has almost no effect on $\kappa$, which in the counterion-dominated regime is determined solely by $Z$ and $\phi_0$, independent of $n_{\text{s}}$ (see

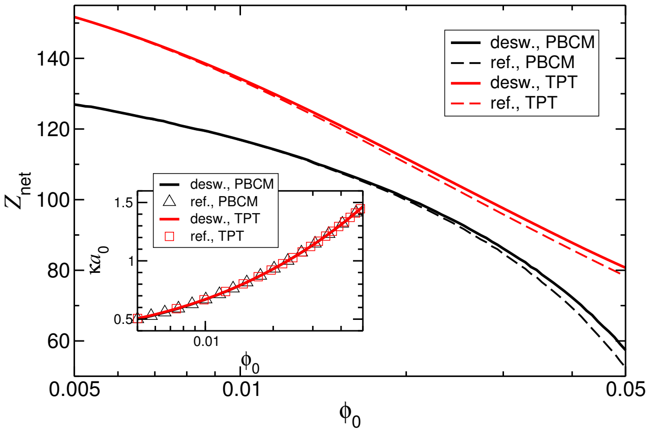

**Figure 6.6** Concentration dependence of net microgel valence $Z_{\rm net}$. Inset: Reduced Debye screening constant versus $\phi_0$. Predictions of TPT and PBCM for deswelling systems (solid red and black lines, respectively) are compared with constant-size reference system predictions (dashed lines). System parameters: $Z = 200$ and $c_{\rm res} = 100$ $\mu$M.

Eq. (6.1)). At low $\phi_0$, the $Z_{\rm net}$ curves merge with those of the reference system, since $a_{\rm ref}$ at $\phi_0 = 0.005$ becomes equal to the radius $a$ of the deswelling microgels. Deswelling enlarges the volume available to the microions outside the microgels by a factor $V(\phi_{\rm ref} - \phi)$, where $\phi_{\rm ref} = \phi_0 \left(a_{\rm ref}/a_0\right)^3$ is the volume fraction of the reference system. The resulting gain in entropy for counterions leaving the deswelling microgels is nearly compensated by the larger work required to expel these ions, as the backbone charge density of opposite sign is increased by a factor $\left(a_{\rm ref}/a\right)^3$. The net effect is an only slightly increased $Z_{\rm net}$ for the deswelling microgel system. Both TPT and PBCM predict such a slight enhancement of $Z_{\rm net}$ at higher $\phi_0$, but with consistently higher values in case of TPT.

According to Figs. 6.7(a) and (b), $A_{\rm Y}$ grows with increasing concentration, while $\beta u_{\rm Y}(2a)$ decreases. The order relation $Z_{\rm net}(\phi_0) \geq Z_{\rm net}^{\rm ref}(\phi_0)$ is valid, which implies the order relation $\beta u_{\rm Y}(2a) \geq \beta u_{\rm Y}^{\rm ref}(2a)$ for the effective potential at contact distance $2a$. The opposite order $A_{\rm Y} \leq A_{\rm Y}^{\rm ref}$ holds for the interaction parameter $A_{\rm Y}$ in Eq. (6.2). To understand these relations, recall with Eq. (2.63) that $A_{\rm Y}$ is proportional, in addition to $Z_{\rm net}^2$, to a geometric factor depending on $\kappa a$, and this factor is higher for the reference system. Fig. 6.7(b) quantifies the aforementioned peculiarity of ionic microgel systems that, with decreasing concentration,

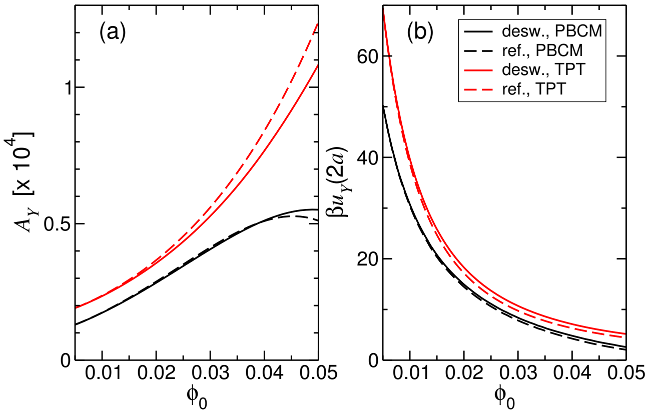

**Figure 6.7** Influence of deswelling on interaction strength parameters (a) $A_{\rm Y} = \beta u_{\rm Y}(2a; n_{\rm m}) \exp(2\kappa a_0)$ and (b) $\beta u_{\rm Y}(2a; n_{\rm m})$ for an effective Yukawa pair potential describing non-overlapping microgels, as predicted by TPT. System parameters: $Z = 200$ and $c_{\rm res} = 100\ \mu$M.

the electrostatic coupling strength measured at contact distance is increased.

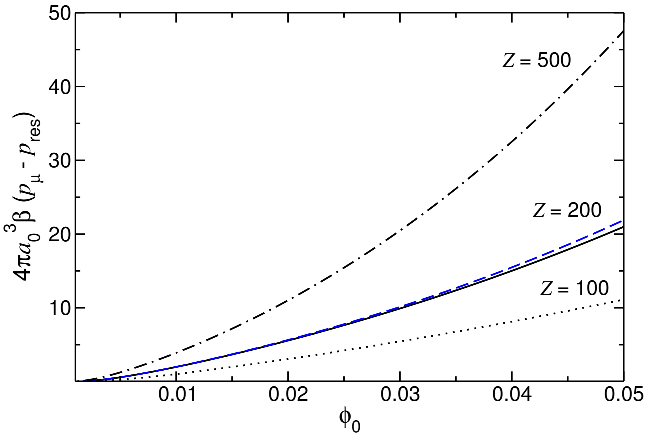

**Figure 6.8** PBCM prediction for microion osmotic pressure $p_\mu - p_{\rm res}$ (in reduced units) versus $\phi_0$ for backbone valences $Z$ as indicated and reservoir pressure $p_{\rm res} = 2n_{\rm res}k_{\rm B}T$. For $Z = 200$, the microion osmotic pressure of reference system is also shown (blue dashed line). Other parameters as in Fig. 6.2.

Having assessed how the effective pair potential is affected by deswelling, we address next various pressure contributions. Figure 6.8 displays PBCM results for the microion pressure $p_\mu$, calculated using the contact theorem in Eq. (5.12). As expected, for given $\phi_0$, $p_\mu$ grows rapidly with increasing backbone valence. For $Z = 200$, the microion pressure of the reference system slightly exceeds the pressure for deswelling particles, essentially due to the higher volume fraction, $\phi_{\mathrm{ref}} > \phi$, of the reference system.

It is instructive to compare the PB cell model pressure, $p_\mu$, defined in Eq. (5.12), with the total suspension pressure $p$ from TPT and the volume energy-derived contribution $p_{\mathrm{vol}}$. In TPT, the suspension pressure can be computed from $f(a, n_{\mathrm{m}}) = F(a, n_{\mathrm{m}})/N_{\mathrm{m}}$, in Eq. (4.20), using the thermodynamic relation in Eq. (5.8), where the concentration dependence of $a(n_{\mathrm{m}})$ must be accounted for, giving rise, in particular, to the extra pressure contribution $p_{\mathrm{se}}$ in Eq. (5.10). In taking the concentration derivative of $f$, the electroneutrality condition $n_{\mathrm{s}} = \langle N_+\rangle/V - n_{\mathrm{m}}Z$ must be maintained for given $Z$. Using Eq. (2.67) for the volume energy of ion-permeable particles, the volume pressure contribution, $p_{\mathrm{vol}}$ in LRT and used in the TPT method, takes the form [13]

$$\begin{aligned}\beta p_{\mathrm{vol}} = n_{\mathrm{m}}^2 \left(\frac{\partial \beta \varepsilon_{\mathrm{vol}}}{\partial n_{\mathrm{m}}}\right)_{\mathrm{res}} &= Z n_{\mathrm{m}} + 2n_{\mathrm{s}} + \frac{3Z^2}{2}\frac{\lambda_{\mathrm{B}}}{a} n_{\mathrm{m}} \left[-\frac{1}{\tilde{\kappa}^2} + \frac{9}{4\tilde{\kappa}^3} - \frac{15}{4\tilde{\kappa}^5}\right. \\ &+ \left.\left(\frac{3}{2\tilde{\kappa}^2} + \frac{21}{4\tilde{\kappa}^3} + \frac{15}{2\tilde{\kappa}^4} + \frac{15}{4\tilde{\kappa}^5}\right) e^{-2\tilde{\kappa}}\right], \qquad (6.3)\end{aligned}$$

where $\tilde{\kappa} = \kappa a$. Note that the (reduced) kinetic pressure of the microions, equal to $Zn_{\mathrm{m}}+2n_{\mathrm{s}}$, is included in $p_{\mathrm{vol}}$.

The comparison among the pressure predictions of the different methods is shown in Fig. 6.9 for a system with $Z = 200$ and $c_{\mathrm{res}} = 100$ $\mu$M. All pressures are measured relative to the reservoir osmotic pressure $p_{\mathrm{res}}$. Together with these predictions, also shown is the kinetic microion pressure, $p_{\mathrm{kin}} = (Zn + 2n_{\mathrm{s}})\, k_{\mathrm{B}}T$, with $n_{\mathrm{s}}$ calculated from TPT. In the dilute limit ($\phi_0 \to 0$), all pressure terms converge to $p_{\mathrm{res}}$, and the system salt concentration $n_{\mathrm{s}}$ tends to $n_{\mathrm{res}}$. The dry volume fraction at which $Zn_{\mathrm{m}} = 2n_{\mathrm{s}}$ is $\phi_0 \approx 0.002$. The displayed pressure curves hence represent the counterion-dominated regime.

As seen from comparing $p$ to $p_{\mathrm{vol}}$, inter-microgel correlation contributions to $p$ become significant for $\phi_0 \gtrsim 0.04$, where $p$ becomes distinctly larger than $p_{\mathrm{vol}}$. This comparison shows further that the pressure contribution $p_{\mathrm{se}}$ in Eq. (5.9), generated by the concentration dependence of $a(n_{\mathrm{m}})$ in the single-particle energies $u_{\mathrm{e}}(a)$ and $f_{\mathrm{p}}(a)$ in Eq. (4.20), is negligible at lower concentrations. The PBCM pressure $p_\mu$ exceeds $p_{\mathrm{vol}}$ for non-zero concentrations and is overall close to $p$, except at high $\phi_0$. At this relatively low salt concentration, the kinetic microion pressure difference $p_{\mathrm{kin}} - p_{\mathrm{res}}$ (dotted curve) is practically equal to the reduced ideal gas pressure of counterions, $Zn_{\mathrm{m}}k_{\mathrm{B}}T$ (or $3Z\phi_0$ in reduced units), up to a small negative correction proportional to $2\,(n_{\mathrm{s}} - n_{\mathrm{res}})$, owing to the salt expulsion (Donnan) effect (cf. Fig. 6.2). While in the concentration range of Fig. 6.9 the counterions contribute most strongly to the suspension osmotic pressure, due to the electrostatic attraction of the fixed backbone charge they behave distinctly non-ideal, which is reflected in the non-constant, radially decaying counterion concentration profile $n_+(r)$ (see Fig. 6.1). This is why $p_{\mathrm{kin}}$ is higher than $p$.

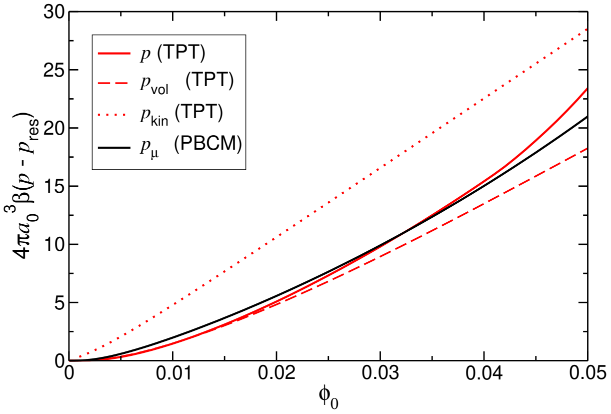

**Figure 6.9** Reduced pressure, $p$, of microgel suspension from TPT (Eqs. (5.8) and (4.20)), volume energy contribution $p_{\mathrm{vol}}$ (Eq. (6.3)), and PBCM pressure, $p_\mu$ (Eq. (5.12)), versus microgel concentration $\phi_0$. All pressures are relative to the reservoir pressure $p_{\mathrm{res}}$. System parameters are $Z = 200$ and $c_{\mathrm{res}} = 100$ $\mu$M. Also shown is the TPT prediction for the kinetic (ideal gas) pressure, $p_{\mathrm{kin}} = Zn_{\mathrm{m}} + 2n_{\mathrm{s}}$, where $n_{\mathrm{s}}$ is system salt density (nearly identical to PBCM prediction).

## 6.3 Structural properties and charge renormalization

For studying the structural properties of the microgel suspension, we use the (density-dependent) total effective pair potential $v_{\mathrm{eff}}(r; n_{\mathrm{m}}) = u_{\mathrm{eff}}(r; n_{\mathrm{m}}) + u_{\mathrm{H}}(r)$, from Eq. (4.22), for describing the effective pair interactions between the pseudo-microgels particles in the effective one-component suspension, but additionally coupling the concentration-dependent microgel size $a(n_\mathrm{m})$. The effective potential combines the steric effective repulsion, $u_\mathrm{H}(r)$ described by Eq. (4.1), due to the polymer network, with the effective electrostatic repulsion, $u_\mathrm{eff}(r; n_\mathrm{m})$, presented in Eq. (2.60). For non-overlapping particles, the effective pair potential is of a screened-Coulomb form, akin to the potential for ion-impermeable charge-stabilized colloidal particles, but with a coupling strength that decreases with increasing concentration and ionic strength of the suspension, as demonstrated in the foregoing section. For overlapping microgels, the effective electrostatic potential remains finite, and is augmented in our model by a soft Hertz potential accounting for elastic repulsion at modest overlap [69, 73]. Van der Waals attraction between the weakly cross-linked microgels can be neglected due to their high solvent content.

Notice that the potential $v_\mathrm{eff}(r; n_\mathrm{m})$ was used already in the TPT method, where it was accounted for in computing the equilibrium microgel size. The electrostatic part $u_\mathrm{eff}$ of $v_\mathrm{eff}$ is derived within LRT and it is self-consistently linked to the TPT method. Whereas for PBCM, we established the link to $u_\mathrm{eff}$ in an *ad hoc* way, by demanding that $Z_\mathrm{net}$ and $\kappa a$ in the nonlinear PBCM method match those used in the LRT-based $u_\mathrm{eff}$ part. This matching procedure was described in detail in subsection 4.3.2.

As explained in section 5.3, using $v_\mathrm{eff}(r; n_\mathrm{m})$ with associated values for the equilibrium radius $a$, net valence $Z_\mathrm{net}$, and screening constant $\kappa$, one can calculate the microgel radial distribution function (rdf) $g(r)$ and static structure factor $S(q)$ characterizing pair correlations in real and Fourier space, respectively. For this purpose, we use the Rogers-Young (RY) integral-equation scheme, described in subsection 5.3.3. This thermodynamically self-consistent scheme is known, from the comparison with a vast body of computer simulation results, to be overall very accurate for the fluid-phase $g(r)$'s and $S(q)$'s of charge-stabilized particles interacting via a repulsive Yukawa-type pair potential [99, 109, 110].

To illustrate the accuracy of the RY method for ionic microgel particles, in Fig. 6.10 the RY results for $g(r)$ and $S(q)$ are compared with Monte-Carlo (MC) simulation data obtained using the method in [15] for a salt-free suspension with $Z = 100$. The RY predictions are also compared with results from the numerically faster, but thermodynamically not self-consistent, HNC integral-equation scheme. There is overall good agreement between the RY and MC data, while the real-space pair correlations are underestimated by the HNC scheme. For the considered specific system, however, the RY prediction for the structure factor principal peak $S(q_m)$ shown in the inset is less accurate than the HNC prediction.

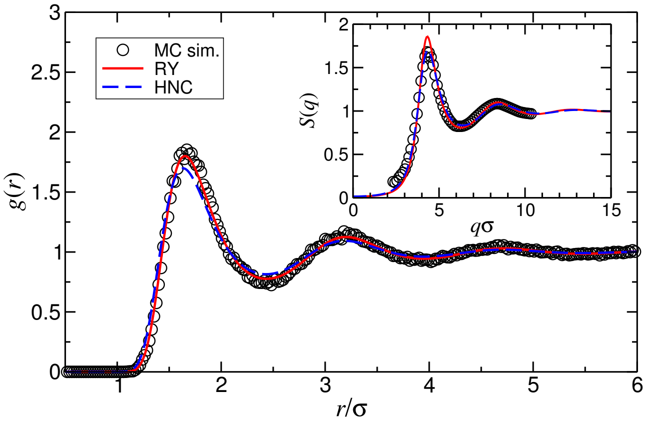

**Figure 6.10** Results of RY, HNC, and MC for the radial distribution function, $g(r)$, and static structure factor, $S(q)$ (inset), of a salt-free microgel suspension with $\phi_0 = 0.01$, $Z = 100$, $\alpha = 2.327$, and $\kappa a_0 = 0.463$. Swelling ratio $\alpha$ is computed using TPT. Length unit is the microgel diameter $\sigma = 2a$.

Rogers-Young results for the concentration dependence of the structure factor peak height $S(q_{\mathrm{m}})$, contact value $g(\sigma)$ and the osmotic compressibility factor $S(0)$ are displayed in Fig. 6.11(a), inset of Fig. 6.11(a) and Fig. 6.11(b) respectively. The contact value, $g(\sigma)$, of the associated rdf remains small in the considered concentration range, showing that the no-overlap potential part, $u_{\mathrm{Y}}(r)$, essentially determines the microstructure of the microgels. The total overlap potential, $u_{\mathrm{ov}}(r) + u_{\mathrm{H}}(r)$, comes into play only at high concentrations. From comparison with the reference system peak height predictions, one notices that $S(q_{\mathrm{m}})$ is reduced when deswelling is accounted for, though only slightly, since for $Z = 200$ the decrease in the microgel radius relative to the reference value remains small even at larger concentrations (cf. Fig. 6.5).

For a given concentration, TPT predicts a more structured system than PBCM, as reflected by the larger values of $S(q_{\mathrm{m}})$. This difference originates from the higher net charge and larger microgel radius in the TPT, as discussed already in relation to Figs. 6.3 and 6.4.

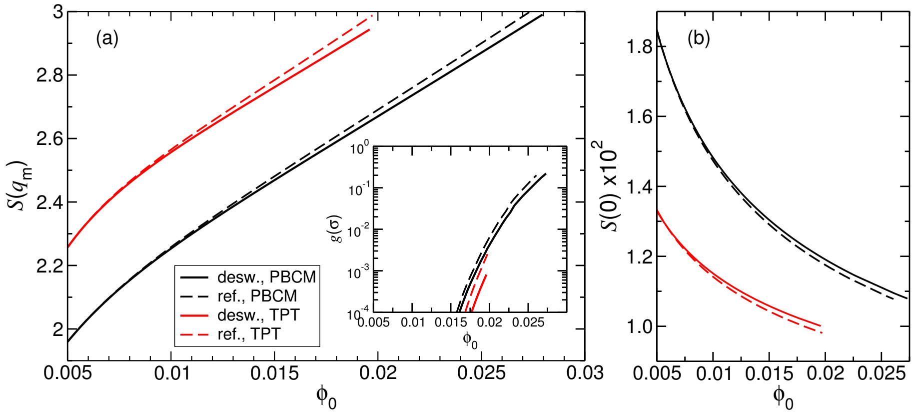

**Figure 6.11** RY results for (a) structure factor peak height, $S(q_{\rm m})$, contact value, $g(\sigma)$ (inset), and (b) osmotic compressibility factor, $S(q \to 0)$, versus $\phi_0$ for $Z = 200$ and $c_{\rm res} = 100$ $\mu$M. Results are presented for deswelling microgels with radius $a$ computed in TPT and PBCM and compared with corresponding results for the reference system (dashed curves). Other parameters as in Fig. 6.5.

In discussing the Kirkwood-Buff relation (Eq. (5.20)), we noted that, for a monodisperse suspension in osmotic equilibrium with a salt reservoir, $S(0) = S(q \to 0)$ equals the osmotic compressibility factor. Rogers-Young predictions for the concentration dependence of $S(0)$ (Fig. 6.11(b)) show that deswelling slightly increases the osmotic compressibility. The increase of $S(0)$ predicted by both methods follows from the reduced volume fraction of deswelling particles, which is lower by the factor $(a/a_{\rm ref})^3$ than that of the reference system. In its effect on $S(0)$, this reduction in volume fraction overcompensates the small deswelling-induced increase of $Z_{\rm net}$ (see Fig. 6.6). The PBCM yields distinctly higher compressibilities than the TPT, since it predicts smaller equilibrium radii and net charges.

The peak value of the structure factor, $S(q_{\rm m})$, can be used as an indicator for the proximity of a fluid suspension to a freezing transition. The frequently cited empirical Hansen-Verlet criterion, $S(q_{\rm m}) = 2.85$, applies only to the freezing of a hard-sphere fluid. It does not apply to suspensions with longer-range, soft inter-particle repulsion. As shown in detail in [110], a somewhat higher freezing indicator value, $S(q_{\rm m}) = 3.1$, should be used for suspensions with long-range Yukawa-type repulsion, where overlap configurations are unlikely. An alternative indicator of freezing in these systems, applicable for very low salinity only, where $\kappa n_{\mathrm{m}}^{-1/3} \lesssim 7$ and freezing into a bcc lattice takes place, is the value $g(r_{\mathrm{m}}) \approx 2.6$ for the principal-peak height of the radial distribution function at radial distance $r_{\mathrm{m}}$ [110].

To illustrate how the freezing transition concentration is determined using the citerion $S(q_{\mathrm{m}}) = 3.1$, we consider a strongly charged microgel suspension with $Z = 500$ and $c_{\mathrm{res}} = 50\ \mu\mathrm{M}$, for which $g(2a) \approx 0$ holds to excellent accuracy up to the freezing transition concentration. For such a strongly coupled system, it is necessary to renormalize the (net) microgel charge and suspension screening constant, so as to incorporate nonlinear response of the microions to the strong electric field of the microgel backbone. To determine these renormalized parameters in the framework of PBCM, we follow Colla *et al.* [62] in linearizing the PB equation (Eq. (4.25)) around the nonlinear potential value $\Phi_{\mathrm{R}} = \Phi(R)$ at the cell boundary. This procedure leads to a linearized PB equation, (see also section 3.1)

$$\Delta\Phi_{\mathrm{l}}(r) = \kappa_{\mathrm{eff}}^2 \left[\Phi_{\mathrm{l}}(r) - \Phi_{\mathrm{R}} + \gamma_{\mathrm{R}}\right] + \frac{3\lambda_{\mathrm{B}} Z^{\mathrm{ren}}}{a^3}\,\Theta(a-r)\,, \tag{6.4}$$

for $r \leq R$, where $\kappa_{\mathrm{eff}}^2 = \kappa_{\mathrm{res}}^2 \cosh(\Phi_{\mathrm{R}})$, and $\gamma_{\mathrm{R}} = \tanh(\Phi_{\mathrm{R}})$, with the latter quantity being negative due to the negative backbone charge. Here, $Z^{\mathrm{ren}}$ is the yet unknown renormalized backbone valence, and $\Theta(r)$ is the unit step function.

The unique solution for the linearized potential, $\Phi_{\mathrm{l}}(r)$, inside and outside the microgel sphere can be obtained analytically using the boundary conditions $\Phi_{\mathrm{l}}(R) = \Phi_{\mathrm{R}}$, $\Phi_{\mathrm{l}}'(R) = 0$, and $\Phi_{\mathrm{l}}'(0) = 0$, in conjunction with the continuity of $\Phi_{\mathrm{l}}(r)$ and its first derivative at $r = a$. These five conditions determine $Z^{\mathrm{ren}}$, together with the four integration constants arising from the integration of the linearized PB equation (Eq. (6.4)) inside and outside a microgel sphere. Input parameters are here $\Phi_{\mathrm{R}}$ and the equilibrium radius $a$, determined independently. Note that the linearized potential $\Phi_{\mathrm{l}}(r)$ gives rise to the same potential and electric field values at the cell boundary as the nonlinear PBCM potential. We refrain from quoting the somewhat lengthy analytic expressions for $\Phi_{\mathrm{l}}(r)$ and $Z^{\mathrm{ren}}$ given in [62]. As discussed in [62] (see also [111]), due to the monotonic increase of the microgel radius with increasing bare backbone valence $Z$, the renormalized valence $Z^{\mathrm{ren}} \leq Z$ does not reach a saturation value beyond the linear regime, as it does for non-permeable rigid colloids [55, 57]. Instead, $Z^{\mathrm{ren}}$ grows monotonically with increasing $Z$, showing only a slight indication of a plateau behavior in the regime of intermediately high $Z$ and low suspension salinity.

In Donnan equilibrium, the renormalized *net* microgel charge number, $Z^{\mathrm{ren}}_{\mathrm{net}}$, is obtained in the PBCM as

$$\begin{aligned} Z^{\mathrm{ren}}_{\mathrm{net}} = -\frac{a^2\Phi_{\mathrm{l}}'(a)}{\lambda_{\mathrm{B}}} &= \frac{\tanh(\Phi_{\mathrm{R}})}{\kappa_{\mathrm{eff}}\lambda_{\mathrm{B}}}\Big[\kappa_{\mathrm{eff}}(a-R)\cosh(\kappa_{\mathrm{eff}}(a-R)) \\ &+ (\kappa_{\mathrm{eff}}^2 aR-1)\sinh(\kappa_{\mathrm{eff}}(a-R))\Big], \end{aligned} \tag{6.5}$$

which follows alternatively from Eq. (2.62), wherein $Z$ and $n_{\pm}(r)$ on the right-hand side are replaced, respectively, by $Z^{\mathrm{ren}}$ and the linearized microion profiles

$$n_{\mathrm{l},\pm}(r) = n_{\mathrm{res}} e^{\mp\Phi_{\mathrm{R}}}\left[1 \mp (\Phi_{\mathrm{l}}(r) - \Phi_{\mathrm{R}})\right] , \tag{6.6}$$

whose values at the cell boundary match the non-linearized ones.

To implicitly account for nonlinear effects, we use $Z^{\mathrm{ren}}_{\mathrm{net}}$ given by Eq. (6.5) as the input for the net valence in the linear-response, non-overlap Yukawa potential $u_{\mathrm{Y}}(r)$ in Eq. (2.61). In addition, $\kappa_{\mathrm{eff}}$ might be identified as the renormalized input for the screening constant in $u_{\mathrm{Y}}(r)$, as done based on the original description by Alexander *et al.* [55] for the case of non-permeable rigid spheres [56, 57]. However, to recover the PBCM screening constant in Eq. (4.31) in the limiting case of low backbone charges, where charge renormalization is not operative, we determine the renormalized screening constant, $\kappa^{\mathrm{ren}}$, to be substituted into $u_{\mathrm{eff}}(r)$, in a manner that maintains the smoothness of the effective potential at $r = a$ for the nonlinear case. Explicitly, we determine $\kappa^{\mathrm{ren}}$ as

$$(\kappa^{\mathrm{ren}})^2 = 4\pi\lambda_{\mathrm{B}}\left(nZ^{\mathrm{ren}}_{\mathrm{app}} + 2\,n^{\mathrm{ren}}_{\mathrm{s}}\right) , \tag{6.7}$$

where

$$n^{\mathrm{ren}}_{\mathrm{s}} = \frac{4\pi}{V_{\mathrm{R}}}\int_0^R n_{\mathrm{l,\text{-}}}(r)\, r^2\, dr\, . \tag{6.8}$$

The apparent renormalized backbone valence, $Z_{\text{app}}^{\text{ren}}$, is defined by Eq. (4.32) using the substitutions $Z^* \rightarrow Z_{\text{app}}^{\text{ren}}$, $\kappa^* \rightarrow \kappa^{\text{ren}}$, and $Z_{\text{net}}^* \rightarrow Z_{\text{net}}^{\text{ren}}$. Notice that $\kappa^{\text{ren}}$ is given here only implicitly, so that an iteration procedure with starting seed $\kappa_{\text{eff}}$ is used for its calculation. For $\kappa_{\text{eff}}$, we obtain the expression

$$(\kappa_{\text{eff}})^2 = \frac{4\pi\lambda_{\text{B}}}{1-\gamma_R}\left[n_{\text{m}} Z^{\text{ren}} + \frac{2\,n_{\text{s}}^{\text{ren}}}{1+\gamma_R}\right] , \tag{6.9}$$

similar to the one for impermeable charged colloids [57] (cf. Eq. (3.20)). The screening constants $\kappa_{\text{eff}}$, $\kappa^{\text{ren}}$, and $\kappa$ mutually differ, except in the limit $Z \rightarrow 0$, where $\gamma_{\text{R}} \rightarrow 0$ and $\{n_{\text{s}}, n_{\text{s}}^{\text{ren}}\} \rightarrow n_{\text{res}}$, in which case all three quantities are equal to the reservoir screening constant, $\kappa_{\text{res}}$.

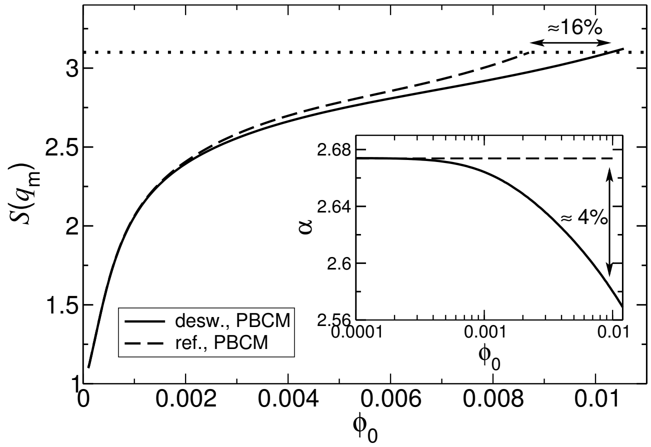

**Figure 6.12** RY peak height, $S(q_{\text{m}})$, for strongly repelling microgels with $Z = 500$ and $c_{\text{res}} = 50$ $\mu$M. Results are presented for deswelling (solid curve) and reference system constant-size microgels (dashed curve), based on the charge-renormalized PBCM. The dotted horizontal line marks the freezing criterion $S(q_{\text{m}}) = 3.1$. Inset: Swelling ratio $\alpha = a/a_0$ in charge-renormalized PBCM.

Rogers-Young results for the concentration dependence of $S(q_{\text{m}})$ of strongly charged microgels are displayed in Fig. 6.12. The effective pair potential parameters are determined here using the PBCM charge-renormalization method described above. The inset shows the size ratio, $a(\phi_0)/a_{\text{ref}}$, with $a_{\text{ref}} = a(\phi_0 = 0.005)$, as predicted by the nonlinear PBCM method. The RY values for $g(2a)$ are practically zero (i.e. $g(2a) < 0.001$) for all considered $\phi_0$, so that $S(q_{\text{m}}) = 3.1$ qualifies as a freezing indicator. Figure 6.12 illustrates that, for strongly charged microgels, deswelling significantly increases the freezing transition concentration by about 16 %, corresponding to a 4 % decrease in the swelling ratio $\alpha$ (see inset).

For deswelling microgels, the freezing transition concentration determined by $S(q_{\mathrm{m}}) = 3.1$ is $\phi_0 \approx 0.01$. The RY rdf peak height is here $g(r_{\mathrm{m}}) = 2.7$, which is close to the freezing transition value 2.6 holding for suspensions of colloids interacting by a repulsive hard-core-Yukawa pair potential, whose state points in the phase diagram are located on the fluid-bcc part of the freezing transition line, characterized by $\kappa_{\mathrm{coll}} n_{\mathrm{m}}^{-1/3} \lesssim 7$ [110]. If we identify $\kappa_{\mathrm{coll}}$ by $\kappa^{\mathrm{ren}}$, where $(\kappa^{\mathrm{ren}})^2 = 4\pi\lambda_{\mathrm{B}} n_{\mathrm{m}} Z_{\mathrm{app}}^{\mathrm{ren}}$ holds for the present counterion-dominated microgel system, we obtain $\kappa_{\mathrm{coll}} n_{\mathrm{m}}^{-1/3} \approx 6.3$, consistent with a fluid-bcc freezing transition close to the fluid-bcc-fcc triple point [110].

## 6.4 Diffusion and rheological properties

We explore next dynamic properties of ionic microgel suspensions, using the one-component picture of pseudo-microgels interacting via the state-dependent total effective pair potential $v_{\mathrm{eff}}(r; n_{\mathrm{m}})$ (see Eq. (4.22)). For a single microgel swollen by the solvent, the solvent inside is nearly immobilized, moving quasi-instantaneously with the microgel backbone [112]. In fact, it has been shown that the microgels behave hydrodynamically as permeable spheres with a reduced penetration length of about 3% of their interaction radius $a$ [24]. Since we are not interested in the effect of the concentration-dependent deswelling on the hydrodynamic radius, we can then identify for simplicity the hydrodynamic radius $a_{\mathrm{h}}$ of the microgels with the equilibrium radius $a$.

The deswelling ratio $\alpha(\phi_0)$, net valence $Z_{\mathrm{net}}(\phi_0)$, and Debye screening constant $\kappa(\phi_0)$ are determined here using TPT and PBCM methods. As explained in subsection 5.4.4, the employed methods for calculating dynamic properties depend on $v_{\mathrm{eff}}(r; n_{\mathrm{m}})$ only implicitly via the radial distribution function $g(r)$ and static structure factor $S(q)$.

Figure 6.13(a) displays our results for the positive definite hydrodynamic function $H(q)$

at concentration $\phi_0 = 0.005$, calculated using the BM-PA hybrid scheme described in subsection 5.4.4, which requires $S(q)$ as the only input. This input is calculated using the RY scheme, which gives somewhat different results in TPT and PBCM, respectively, owing to their different predictions for $a$ and $Z_{\mathrm{net}}$. For example, at $\phi_0 = 0.005$, we find $\phi = 0.067$ in PBCM and $\phi = 0.073$ in TPT. The differences in $S(q)$ cause less pronounced differences in $H(q)$, since the latter depends on $S(q)$ only in a global (functional) way [24, 97]. The differences in $H(q)$ are greatest at the peak position, which is located at practically the same wavenumber $q_{\mathrm{m}}$ as the principal peak of $S(q)$. There are pronounced undulations in $H(q)$ due to strong HIs between the microgels. Recall that in the absence of HIs, $H(q) = 1$ independent of $q$. The peak height $H(q_{\mathrm{m}})$ exceeds unity for $\phi_0 = 0.005$, a feature characteristic for general charge-stabilized suspensions at low salinity and low volume fractions $\phi$, where the hard core of the colloidal particles is masked by the strong and long-range electrostatic repulsion [23, 99].

Also displayed in Fig. 6.13(a) is the hydrodynamic function (with TPT input for $a$) of a more concentrated suspension at $\phi_0 = 0.02$, which corresponds in the TPT case to the volume fraction $\phi = 0.26$. The principal peak of $H(q)$ at $q_{\mathrm{m}}$ is here significantly below one. The reduced short-time self-diffusion coefficient, $d_{\mathrm{s}}/d_0(a) = H(q\sigma \gg 1)$, is accordingly significantly lower than its value for $\phi_0 = 0.005$, which can be attributed to the enhanced hydrodynamic hindrance of self-diffusion for higher concentrations (cf. Eq. (5.42)).

The differences in the $H(q)$'s of deswelling and reference microgels (solid and dashed curves, respectively, in Figs. 6.13(a) and 6.13(b)) are small, and basically due to the higher volume fraction of the reference system. This is also the reason for the slight downshift of the reference-system $H(q)$ relative to the one of the deswelling system. The microgel $H(q)$ bears a qualitative similarity to the one of colloidal hard spheres (hs) at the same volume fraction $\phi = 0.26$, in particular regarding its peak value and location. The hydrodynamic function of hard spheres, $H^{\mathrm{hs}}(q)$, is likewise characterized by a peak height below one, and the peak is located at $q_{\mathrm{m}}\sigma \approx 2\pi$. TPT based explicit values are $H(q_{\mathrm{m}}) = 0.81$ (0.65) for the peak height,

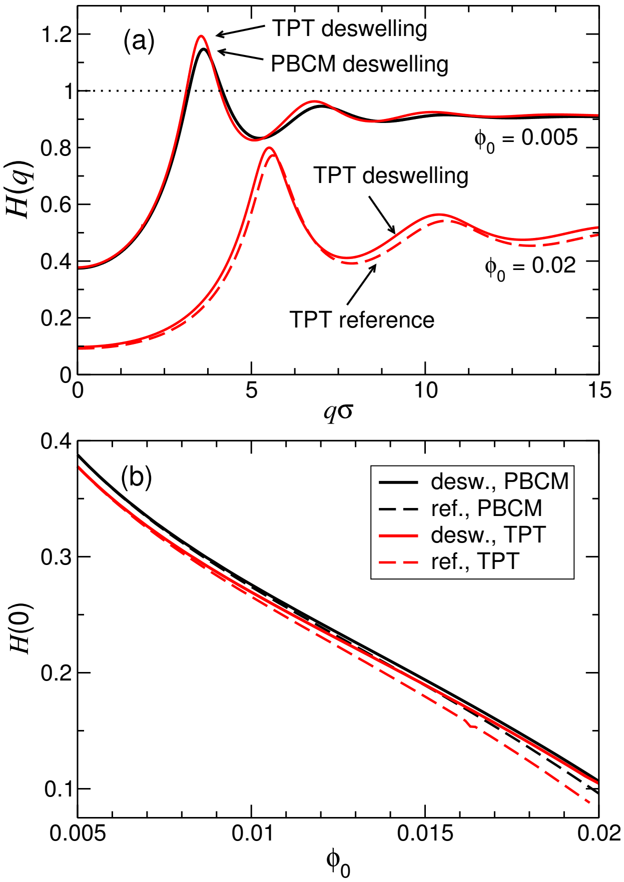

**Figure 6.13** (a) BM-PA results for the hydrodynamic function $H(q)$ as function of reduced wavenumber, $q\sigma$, for two concentrations $\phi_0$ as indicated. The lower one, $\phi_0 \approx 0.005$, is the concentration where the collective diffusion coefficient attains its maximum. At $\phi_0 = 0.02$, the $H(q)$ of deswelling particles with TPT-calculated radius is compared with that of the reference system. (b) Concentration dependence of sedimentation coefficient $K = H(q \to 0)$. Solid curves: deswelling particles in the TPT (red) and PBCM (black). System parameters: $Z = 200$ and $c_{\mathrm{res}} = 100\ \mu$M.

$d_{\mathrm{s}}/d_0 = 0.52$ (0.51) for the short-time self-diffusion coefficient, and $K = H(q \to 0) = 0.11$ (0.18) for the sedimentation coefficient, where the values given in brackets are the respective values for colloidal hard spheres, obtained using the analytic expressions [24, 100]

$$H^{\mathrm{hs}}(q_{\mathrm{m}}) = 1 - \phi/\phi_{\mathrm{cp}} = 1 - 1.35\,\phi$$

$$d_{\mathrm{s}}^{\mathrm{hs}}/d_0 = 1 - 1.8315\,\phi\left(1 + 0.12\,\phi - 0.70\,\phi^2\right)$$

$$K^{\mathrm{hs}} = 1 - 6.5464\,\phi\left(1 - 3.348\phi + 7.426\phi^2 - 10.034\phi^3 + 5.882\phi^4\right)$$

$$g^{\mathrm{hs}}(r_{\mathrm{m}} = 2a^{+}) = \frac{1 - 0.5\,\phi}{(1-\phi)^{3}}\,, \tag{6.10}$$

which are accurate for volume fractions up to the hard-sphere freezing transition value $\phi = 0.494$. Notice the strictly linear decline of $H^{\mathrm{hs}}(q_{\mathrm{m}})$ with increasing volume fraction, which holds to high accuracy for the complete liquid-phase concentration range. In the above expression for $H^{\mathrm{hs}}(q_{\mathrm{m}})$, $\phi_{\mathrm{cp}} = \pi/\left(3\sqrt{2}\right) \approx 0.74$ is the highest possible volume fraction, attained for monodisperse hard spheres in close-packed fcc and hcp crystalline structures.

Equation (6.10) quotes also the accurate Carnahan-Starling expression for the height, $g^{\mathrm{hs}}(2a^{+})$, of the principal peak of the hard-sphere rdf, located at the contact distance $r_{\mathrm{m}} = 2a^{+}$. The BM-PA values of $H(q)$ at $q = q_{\mathrm{m}}$ and in the $q \to \infty$ limit are somewhat higher than the corresponding hard-sphere values. There are also differences between the microgel $g(r)$ and the hard-sphere $g^{\mathrm{hs}}(r)$ (not shown here). The microgel rdf for $\phi_0 = 0.02$ has the peak height $g(r_{\mathrm{m}}) = 2.50$ at pair distance $r_{\mathrm{m}} = 1.32\sigma$, whereas $g^{\mathrm{hs}}(\sigma^{+}) = 2.15$. The differences from the hard-sphere values are due to the electrostatic repulsion between the microgels, which is here of shorter range $1/\kappa = 0.4a$. The pair potential contact value, $\beta u_{\mathrm{Y}}(2a) \approx 18$, is still significantly higher, however, than the thermal energy $k_{\mathrm{B}}T$ (see Fig. 6.7(b)), reflected in a nearly zero probability, $g(2a) < 10^{-3}$, of finding two microgels in contact.

Owing to HIs, two microparticles in contact sediment faster than at larger separations. This underlies the fact that the sedimentation coefficient, $K = V_{\mathrm{sed}}/V_0 = H(q \to 0)$, for a homogeneous ionic microgel suspension is lower than that for hard spheres at the same $\phi$. The monotonic decline of $K$ with increasing concentration is shown in Fig. 6.13(b). Owing to stronger solvent backflow, the sedimentation velocity, $V_{\mathrm{sed}}(\phi)$, is lower in a more concentrated suspension than in a less concentrated one. The maximal sedimentation velocity, $V_{\mathrm{sed}}(\phi = 0) = V_0$, is thus attained at infinite dilution, where $K = 1$. Since the major effect of deswelling is to lower $\phi$, $K$ is higher for deswelling microgels than for the constant-size reference particles, which explains the slightly higher values of $K$ in PBCM, since $a_{\mathrm{PBCM}} < a_{\mathrm{TPT}}$.

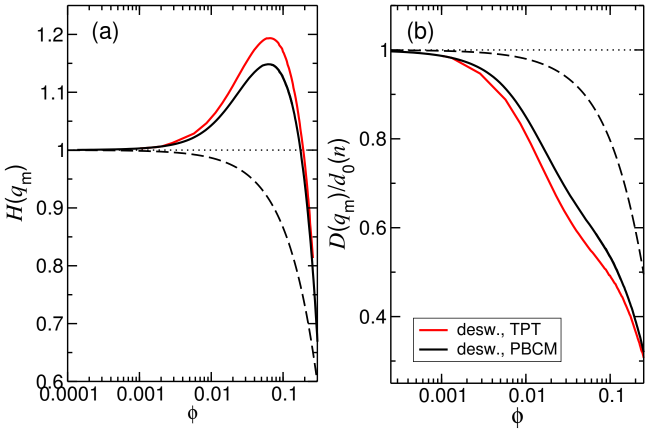

**Figure 6.14** BM-PA results for (a) hydrodynamic function peak height, $H(q_\mathrm{m})$, and (b) reduced cage diffusion coefficient, $D(q_\mathrm{m})/d_0(n_\mathrm{m})$, as functions of volume fraction $\phi = \phi_0\,\alpha(n_\mathrm{m})^3$ using TPT (solid red curve) and PBCM (sold black curve) for $\alpha(n_\mathrm{m})$ and compared with hard-sphere results (dashed curves). System parameters: $Z = 200$ and $c_\mathrm{res} = 100$ $\mu$M.

As seen in Fig. 6.14(a), the $H(q_\mathrm{m})$ of ionic microgels has a nonmonotonic volume fraction dependence. Starting from a value of one at infinite dilution, with increasing $\phi$, $H(q_\mathrm{m})$ increases towards its maximal value $\sim 1.2$ at $\phi \approx 0.07$ corresponding to $\phi_0 \approx 0.005$, but it thereafter declines monotonically, reaching values below one for $\phi \gtrsim 0.2$. This behavior should be contrasted with the strictly linear decrease of $H(q_\mathrm{m})$ for hard spheres (curved, dashed line on the employed lin-log scale). In contrast to the nonmonotonic $H(q_\mathrm{m})$, both $K$ and $d_\mathrm{s}/d_0$ (latter not shown here) decrease monotonically with increasing $\phi$. Furthermore, unlike the swollen radius $a$, which decreases with increasing $\phi_0$, the reduced Debye screening constant $\kappa a$ increases monotonically from $\kappa a \approx 1.24$ at $\phi_0 = 0.005$ to $\kappa a \approx 3.4$ at $\phi_0 = 0.05$.

For rigid charged particles interacting via a repulsive Yukawa-type potential, the order relations $H(q_\mathrm{m};\phi) > H^\mathrm{hs}(q_\mathrm{m};\phi)$, $d_\mathrm{s}(\phi) > d_\mathrm{s}^\mathrm{hs}(\phi)$, and $K(\phi) < K^\mathrm{hs}(\phi)$ were previously demonstrated [113, 114]. These relations hold also for ionic microgels provided particle overlap is very unlikely, i.e., provided $g(2a) \approx 0$.

At low $Z$ or high salt content, overlap of microgels is likely and their softness matters. To illustrate this, we briefly consider a weakly charged system, $Z = 5$, with soft Hertz repulsion

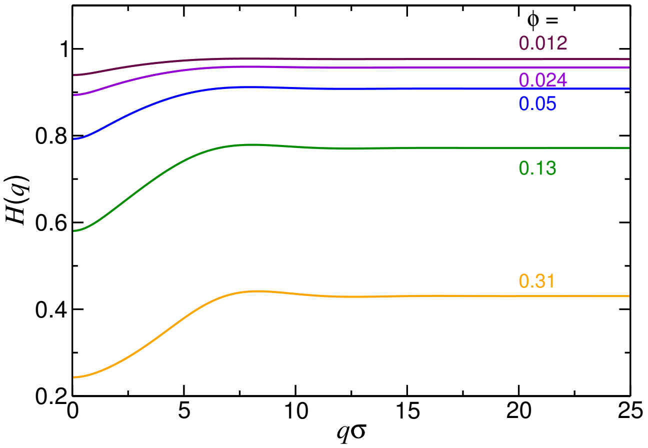

**Figure 6.15** BM-PA results for hydrodynamic function, $H(q)$, of soft low-charge microgels for different volume fraction $\phi$ as indicated. We employ PBCM equilibrium-size calculations and PY closure. System parameters: $\epsilon_{\mathrm{H}} = 10$, $a = 23$ nm, $Z = 5$ and $c_{\mathrm{res}} = 100\ \mu$M.

of strength $\epsilon_{\mathrm{H}} = 100$. We use here PBCM method for calculating the microgel equilibrium size, which does not significantly vary in the range of studied concentrations, due to the weak electrostatic effects. For the static pair correlation functions, we use PY closure, which is applicable owing to the short-range effective pair interaction (cf. subsection 5.3.2). Here, we find that the contact value of the soft particles is approximately equal to the unity, $g(\sigma) \approx 1$, in the range of considered concentrations. In Fig. 6.15, we observe a flattening of the oscillations of $H(q)$ at larger $q$, implying $H(q_{\mathrm{m}}) \approx d_{\mathrm{s}}/d_0$. Moreover, the particle softness tends to enhance $K$, while $H(q_{\mathrm{m}})$ is lowered, as noticed in Fig. 6.16 for a comparison against hard-sphere results. This behavior of $H(q)$ is also observed for model system of particles interacting by pure Hertz potential [24]. The conditions under which softness effects matter in nonionic and weakly charged microgel systems are not further explored in this work. This will be the subject of a forthcoming study.

An important feature distinguishing (ionic) microgels from impermeable solid particles is that $d_0(n_{\mathrm{m}}) = k_{\mathrm{B}}T/(6\pi\eta_0 a(n_{\mathrm{m}})) = d_0^{\mathrm{dry}}/\alpha(n_{\mathrm{m}})$ depends on concentration. Here, $d_0^{\mathrm{dry}}$ is the Stokes-Einstein diffusion coefficient of collapsed (dry) microgels, and $\alpha(n_{\mathrm{m}}) = a(n_{\mathrm{m}})/a_0$ the swelling ratio at microgel concentration $n_{\mathrm{m}}$.

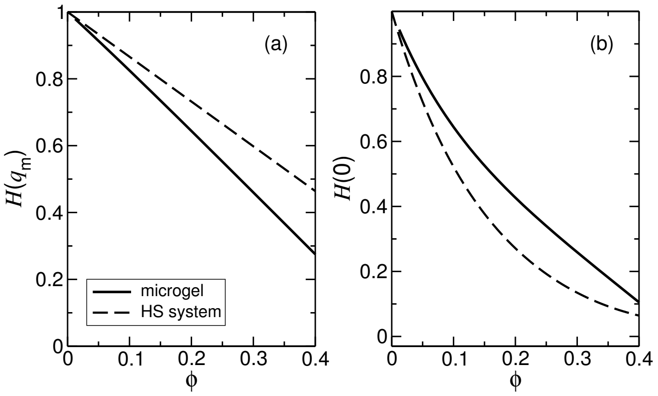

**Figure 6.16** BM-PA results for (a) hydrodynamic function peak height, $H(q_\mathrm{m})$, and (b) sedimentation coefficient, $K = H(q \to 0)$, versus swollen volume fraction $\phi$ for weakly-charged microgel and hard-sphere systems. Eq. (6.10) has been used to compute hard-sphere quantities. Other parameters as in Fig. 6.15.

The wavenumber-dependent short-time diffusion function, $D(q)$, measured in units of $d_0(n_\mathrm{m})$, is determined according to Eq. (5.40) by the ratio of the kinetic factor $H(q)$ and $S(q)$, the latter being independent of HIs. The principal minimum of $D(q)$ is located, for repulsive interactions, at practically the same wavenumber $q_\mathrm{m}$ at which $S(q)$ and $H(q)$ attain their respective maxima, with $S(q_\mathrm{m})$ being in general distinctly higher than $H(q_\mathrm{m})$. The so-called cage diffusion coefficient, $D(q_\mathrm{m})$, quantifies the slow relaxation of concentration fluctuations of wavelength $2\pi/q_\mathrm{m}$ comparable with the diameter of the dynamic cage formed around each particle by its neighbors. For hard spheres, $D(q_\mathrm{m})/d_0$ decreases monotonically with increasing $\phi$, which reflects a dynamic stiffening of the next-neighbor cage. The cage diffusion coefficient of hard spheres is quantitatively described, within 2% accuracy up to the freezing volume fraction, by the polynomial

$$\frac{D^\mathrm{hs}(q_\mathrm{m})}{d_0} = 1 - 2\,\phi - 0.566\,\phi^2 + 2\,\phi^3\,, \tag{6.11}$$

according to which $D^\mathrm{hs}(q_\mathrm{m})$ follows closely a linear decline with slope $-2$ for volume fractions up to $\phi \sim 0.3$. At freezing, where $H^\mathrm{hs}(q_\mathrm{m}) \approx 0.33$ and $S^\mathrm{hs}(q_\mathrm{m}) \approx 2.85$, $D^\mathrm{hs}(q_\mathrm{m}) \approx 0.12 \times d_0$.

The cage diffusion coefficient of ionic microgels is plotted in Fig. 6.14(b) as a function of $\phi$, where $D(q_\mathrm{m})$ is normalized by the concentration-dependent single-microgel diffusion coefficient $d_0(n_\mathrm{m})$, allowing direct comparison with the reduced cage diffusion coefficient of hard spheres (Eq. (6.11)). Unlike $H(q_\mathrm{m})$, the reduced cage diffusion coefficient monotonically decreases with increasing $\phi$. The only remnant of the peak in $H(q_\mathrm{m})$ is a shallow inflection point in $D(q_\mathrm{m})/d_0(n_\mathrm{m})$ at $\phi \approx 0.07$. Owing to the electrostatic repulsion, the next-neighbor cage of microgels is more structured than that of hard spheres at the same $\phi$, reflected in an accordingly higher structure factor peak and lower cage diffusion coefficient. The distinctly higher values of $S(q_\mathrm{m})$ in TPT, in comparison to PBCM, lead to lower values of $D(q_\mathrm{m})/d_0(n_\mathrm{m})$ in TPT, which explains the reverse order in the curves of $H(q_\mathrm{m})$ and $D(q_\mathrm{m})/d_0(n_\mathrm{m})$ in Figs. 6.14(a) and (b), respectively.

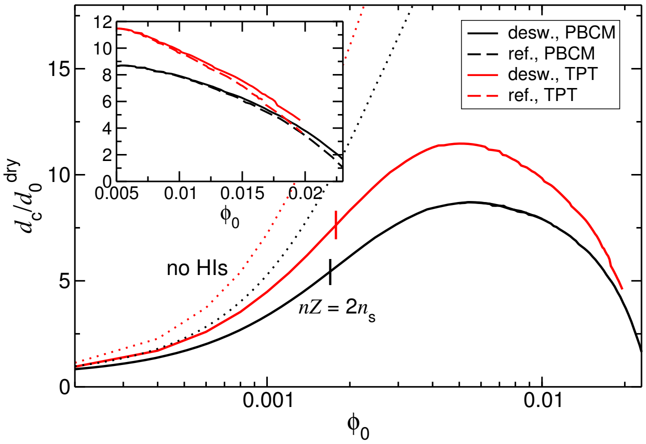

**Figure 6.17** BM-PA results for the reduced collective diffusion coefficient of deswelling microgels, $d_\mathrm{c}/d_0^\mathrm{dry}$, versus $\phi_0$ (solid curves) for swollen radius $a$ calculated using TPT (red) and PBCM (black). Dotted curves are results without HIs where $H(0) = 1$. Vertical line segments mark concentrations at which $\kappa_\mathrm{c} = \kappa_\mathrm{s}$ (cf. Eq. (6.1)). System parameters: $Z = 200$ and $c_\mathrm{res} = 100$ $\mu$M. Inset: Comparison with reference system results (dashed lines) for concentrations exceeding the peak position value $\phi_0 \approx 0.005$.

While $D(q)$ is minimal at $q_\mathrm{m}$, it attains its maximum at $q = 0$ where, according to Eq. (5.44), it has the physical meaning of a collective diffusion coefficient, denoted as $d_\mathrm{c} = D(q \to 0)$. The maximum reflects the fast relaxation of long-wavelength concentration fluctuations by a collective diffusive motion of particles. In this context, recall that $H(q)$ and $S(q)$ are both minimal at $q = 0$. At a given $\phi_0$, however, $S(0)$ appearing in the denominator of $d_\mathrm{c} = d_0(n_\mathrm{m})K/S(0)$ is clearly smaller than $K = H(0)$, as noticed from Figs. 6.11 and 6.13(b), leading to a consequentially large value of $d_\mathrm{c}$.

Figure 6.17 displays $d_\mathrm{c}$ for deswelling ionic microgels, obtained using the BM-PA method with respective TPT and PBCM input for $a$. To uncover its genuine concentration dependence, $d_\mathrm{c}$ is divided, *in lieu* of $d_0(n_\mathrm{m})$, by the concentration independent single particle diffusion coefficient, $d_0^\mathrm{dry}$, of collapsed microgels, implying that $d_\mathrm{c}/d_0^\mathrm{dry} \to a_0/a$ for $\phi_0 \to 0$.

Akin to low-salinity suspensions of impermeable charge-stabilized particles, a nonmonotonic concentration dependence of $d_\mathrm{c}$ is observed, with a pronounced maximum of $d_\mathrm{c}$ at $\phi_0 \approx 0.005$, i.e., at about the same concentration where $H(q_\mathrm{m})$ is largest. The nonmonotonic concentration dependence of $d_\mathrm{c}$ is explained on noting first that $K$ and $S(0)$ are both monotonically decreasing with increasing $\phi_0$. At low $\phi_0$, the decrease of $S(0)$ with increasing $\phi_0$ is stronger than that of $K$, giving rise to a growing $d_\mathrm{c}$. At higher concentrations, the slowing influence of HIs on $K$ is strong enough that the increase of $d_\mathrm{c}$ is turned into a monotonic decline. To show explicitly that the maximum of $d_\mathrm{c}$, and its decline at higher $\phi_0$, are due to HIs, results for $d_\mathrm{c}$ without HIs are included in the figure for comparison. Without HIs, $K = 1$ holds independent of concentration. The curves for $d_\mathrm{c}(\phi_0)$ without HIs are monotonically increasing, and they converge to the ones with HIs at very low concentrations only. It is further noticed that the larger values of $d_\mathrm{c}$ in TPT are due to the lower osmotic compressibility values predicted by this method, and this even though $d_0(n) \propto 1/a$ in TPT is lower than in PBCM. Quite interestingly, the concentration in Fig. 6.17 where the number of backbone-released counterions equals the number of salt counterions marks an inflection point, where the shape of the curve of $d_\mathrm{c}(\phi_0)$ changes from convex to concave.

The influence of deswelling on $d_\mathrm{c}$ at higher $\phi_0$ is assessed in the inset of Fig. 6.17, in comparison with the reference system predictions (dashed lines). Deswelling slightly enhances collective diffusion, as predicted by both TPT and PBCM. This enhancement can be attributed to weaker HIs between deswelling microgels, with a corresponding increase in $K$ overcompensating the increase in $S(0)$.

A short discussion is in order regarding the BM-PA scheme results for $H(q)$ at wavenumbers $q \ll q_{\rm m}$, where its accuracy is known to worsen with increasing concentration, up to a degree where non-physical negative values for $K$ are predicted [97, 113]. This is mainly due to the self-diffusion contribution to $H(q) = H_{\rm d}(q) + d_{\rm s}/d_0$, which in the hybrid scheme is calculated using the pairwise additivity (PA) approximation. The PA method fully accounts for two-body HIs but neglects three-body and higher-order contributions. These complicated higher-order contributions account for the reduction in the strength of the HIs between two particles, due to a hydrodynamic shielding by intervening particles. The disregard of this hydrodynamic shielding effect by the PA scheme leads at higher concentrations to an underestimation of $d_{\rm s}$. The latter contributes to $H(q)$ most significantly at $q = 0$ where the distinct part, $H_{\rm d}(0)$, is negative. For this reason, we show BM-PA results for $K = H(0)$ and $d_{\rm c} \propto K$ for concentrations up to $\phi_0 = 0.02$ only, where the small-$q$ BM-PA predictions are trustworthy.

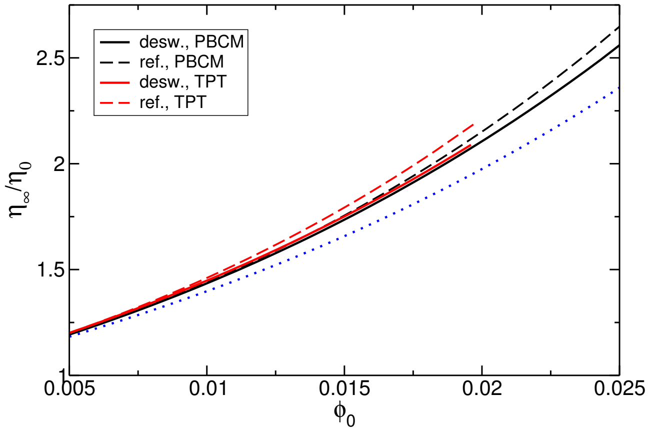

**Figure 6.18** Modified BM theory results for the reduced high-frequency viscosity, $\eta_\infty/\eta_0$, as function of $\phi_0$, for interaction parameters and $a$ calculated using TPT and PBCM. Solid curves are for deswelling microgels, while dashed curves are for the reference system. Dotted curve is the prediction by Eq. (6.12) using $\phi = \phi_0\alpha^3(\phi_0)$, with $\alpha(\phi_0)$ calculated in PBCM. System parameters: $Z = 200$ and $c_{\rm res} = 100\ \mu$M.

Having discussed (short-time) diffusion properties of ionic microgel suspensions, we finally consider rheological properties, namely the high-frequency (short-time) viscosity $\eta_\infty$ and the zero-frequency viscosity $\eta$ introduced in Eqs. (5.45) and (5.46), respectively. Our analysis is limited here to weakly sheared suspensions, where nonlinear phenomena such as shear thinning and the buildup of normal stress differences are negligible. Just as for the diffusion properties, we identify the hydrodynamic particle radius with $a$. As described in subsection 5.4.4, $\eta_\infty$ is calculated using the modified Beenakker-Mazur (BM) expression in Eq. (5.47). The shear stress relaxation contribution, $\Delta\eta$, in $\eta = \eta_\infty + \Delta\eta$ is calculated using the simplified mode-coupling theory (MCT) expression in Eq. (5.48). The only input to these methods is $S(q)$, which is calculated in RY approximation based on $v_{\text{eff}}(r; n_{\text{m}})$, with $a$ obtained in the TPT and PBCM, respectively. HIs are incorporated into the simplified MCT expression via $H(q)$, determined using the BM-PA method.

Figure 6.18 presents results for $\eta_\infty$ (in units of the solvent viscosity $\eta_0$) as a function of $\phi_0$. With increasing concentration, $\eta_\infty$ grows gradually to a value at $\phi_0 = 0.03$ only three times larger than the solvent viscosity. Such a modest growth with increasing concentration is a characteristic feature of $\eta_\infty$. In addition, $\eta_\infty$ is known to be rather insensitive to the form of the pair potential [21, 97] and hence to changes in the equilibrium radius $a$, as reflected in the nearly coincident curves for $\eta_\infty$ with $a$ obtained from TPT and PBCM methods. At a given concentration, the reference microgel suspension has a larger volume fraction than the deswelling microgels system, which explains the mildly higher viscosity values.

For comparison, we show the prediction for $\eta_\infty$ from the polynomial expression,

$$\frac{\eta_\infty}{\eta_0} \approx 1 + \frac{5}{2}\phi(1+\phi) + 7.9\phi^3 \,, \tag{6.12}$$

derived in [21]. This expression is a good viscosity approximation for dilute suspensions of strongly repelling charge-stabilized spheres with prevailing two-body HIs and low values of $S(0)$. As shown in Fig. 6.18, Eq. (6.12) is in qualitative accord with the modified BM results, but underestimates $\eta_\infty$ at higher concentrations. Note that Eq. (6.12), although not a virial expansion to third order in $\phi$, reduces to the linear Einstein viscosity formula for very low volume fractions where the particles are uncorrelated, and thus $\Delta\eta = 0$. For the hypothetical case of vanishing HIs, the particles remain uncorrelated on short time scales for all fluid-phase volume fractions. In this case, $\eta_\infty/\eta_0 = 1 + [\eta]\,\phi$ holds for all $\phi$, with $[\eta] = 5/2$ for no-slip spheres.

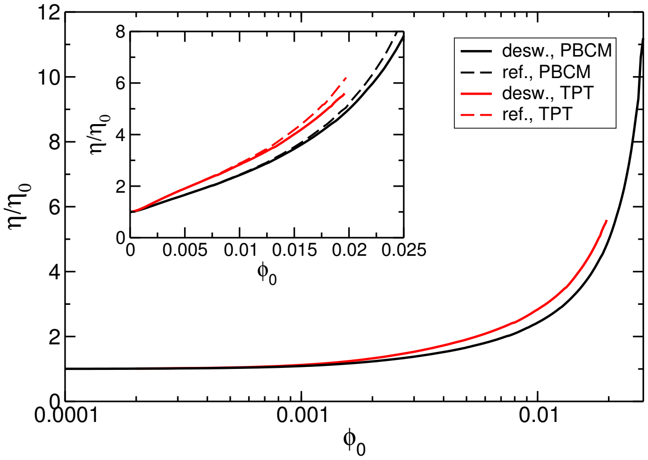

**Figure 6.19** Reduced zero-frequency viscosity, $\eta/\eta_0$, versus $\phi_0$ for system parameters $Z = 200$ and $c_{\mathrm{res}} = 100\ \mu$M. The viscosity contribution $\eta_\infty$ is calculated using modified BM theory, and the shear stress relaxation contribution $\Delta\eta$ using simplified MCT. Inset: Comparison with reference system viscosity (dashed curves).

The reduced zero-frequency viscosity, $\eta/\eta_0$, of deswelling microgels is plotted in Fig. 6.19 (solid curves). The viscosity curves terminate at the concentration where $S(q_{\mathrm{m}}) \approx 3$, which is of different value in PBCM and TPT, respectively. The pronounced increase of $\eta$ at higher $\phi_0$ is mainly due to the shear stress relaxation part $\Delta\eta$, which we calculated using the simplified MCT expression in Eq. (5.48). The latter is more sensitive to changes in the pair potential than $\eta_\infty$, as reflected in visibly higher values of $\eta$ for $\phi_0 \gtrsim 0.03$, when the TPT radius input is used. The higher volume fractions of the reference system in comparison to the system of deswelling microgels imply a lower zero-frequency viscosity for the deswelling particles, visible in the inset at higher concentrations.

In closing this section, we notice that for the employed model of ionic pseudo-microgels electro-kinetic effects, which arise due to the non-instantaneous dynamic response of the microion clouds formed inside and outside the microgels, have been disregarded. These effects tend to lower $d_{\mathrm{c}}$ and $d_{\mathrm{l}}$, and to increase $\eta$, but in general by small amounts only. Electrokinetic effects on diffusion and rheology are of secondary importance, in particular, when non-dilute suspensions are considered and when the microions are small compared to the microgels, which is commonly the case.

# Chapter Seven

# CHARGE RENORMALIZATION: NUMERICAL RESULTS

As noted in chapter 3, in the current literature one encounters different colloid charge-renormalization methods, which allow to extend the effective pair potential concept in the one-component picture of diluted suspensions of weakly-charged colloids to highly-charged colloids and more concentrated suspensions. For the here considered systems of ion- and solvent-impermeable colloidal macroion spheres of fixed size and in osmotic equilibrium with a 1:1 electrolyte microion reservoir, the effective one-component description is based on three reduced parameters that uniquely determine the system: the colloid concentration, expressed by the colloid volume fraction $\phi$; the reduced reservoir screening parameter $\kappa_{\mathrm{res}}a$, related to the microion reservoir concentration; and the coupling parameter $Z\lambda_{\mathrm{B}}/a$, with $Z$ denoting the bare colloidal valence. Here, $a$ and $\lambda_{\mathrm{B}}$ are the colloidal (hard-sphere) radius and the solvent Bjerrum length, respectively. We consider impermeable, rigid colloidal particles only, where charge renormalization effects are caused by the quasi-condensation of microions at the surface of the colloidal macroions, leading to renormalized valence values, $Z_{\mathrm{eff}}$, smaller than $Z$.

The renormalization methods map a highly-charged macroion system, with significant nonlinear electrostatic effects, onto an equivalent linearly-behaving system characterized by renormalized effective interaction parameters, namely the renormalized screening constant $\kappa_{\text{eff}}$ and the renormalized valence $Z_{\text{eff}}$. These renormalized interaction parameters are used in the effective DLVO-type electrostatic pair potential $u_{\text{eff}}(r)$ in Eq.(2.32), in order to summarily account for nonlinear effects in the macroion-macroion interactions. The accuracy of each method for describing nonlinear electrostatic effects depends on the addressed region of the parameter space. A drawback of most of these approaches is that they rely on (uncontrolled) approximations which to date are not fully tested [64].

In this chapter, we quantitatively evaluate the performance of the most prominently used charge-renormalization methods by assessing their resulting predictions of structural and thermodynamic properties of colloidal suspensions. We focus on the PB mean-field renormalization methods presented in chapter 3: Surface Charge (SC) and Extrapolated Point Charge (EPC) methods, based on the spherical cell model approximation with edge and mean potential linearizations; the Renormalized Jellium Model (RJM) and the Renormalized Linear Response Theory (RLRT). These methods provide the renormalized effective interaction parameters, $\kappa_{\text{eff}}$ and $Z_{\text{eff}}$, which we use as input to the effective macroion pair potential for computing pair correlation functions characterizing the colloidal structure. We explore the different renormalization predictions for ($\kappa_{\text{eff}}$,$Z_{\text{eff}}$) also in their respective effects on thermodynamic quantities including the suspension pressure, $p$, and the osmotic suspension compressibility, $\chi_{\text{osm}}$.

To assess the performance of the considered renormalization methods and to compare the calculated structural and thermodynamic properties with earlier computer simulation results, we use the following system parameters: solvent Bjerrum length $\lambda_{\text{B}} = 0.714\,\text{nm}$ (i.e., water at $T = 293\,K$), bare colloid valence $Z = 40$, colloid (macroion) radius selected such that $\lambda_{\text{B}}/a = 0.0222\,,\ 0.0445\,,\ 0.0889\,,\ 0.1779\,,\ 0.3558$ and 0.7115, with according coupling parameter $Z\lambda_{\text{B}}/a = 0.89\,,\ 1.78\,,\ 3.56\,,\ 7.12\,,\ 14.23$ and, 28.5. Regarding the 1:1 electrolyte reservoir concentration, $n_{\text{res}}$ is chosen such that $\kappa_{\text{res}}a$ is in the range of $0-18$, which connects the counterion-dominated regime at low $\kappa_{\text{res}}$ with the salt-dominated regime at large $\kappa_{\text{res}}$.

The selected values of the volume fraction $\phi = (4\pi/3)\, n_{\mathrm{m}}\, a^3$ are in the range of $1 \times 10^{-4}$ – $3.75 \times 10^{-1}$.

## 7.1 Renormalized interaction parameters

We utilize the mean-field charge renormalization methods discussed in chapter 3 to compute the renormalized (effective) parameters $\kappa_{\mathrm{eff}}$ and $Z_{\mathrm{eff}}$, going into the effective macroion pair potential $u_{\mathrm{eff}}(r)$, e.g. in Eq. (2.32). A connection between the calculated renormalized parameters and $u_{\mathrm{eff}}(r)$ can be directly established in the RJM and RLRT schemes, while it is only established in an *ad hoc* way in the CM-based renormalization schemes, such as the SDHA scheme by Boon *et. al.* [56].

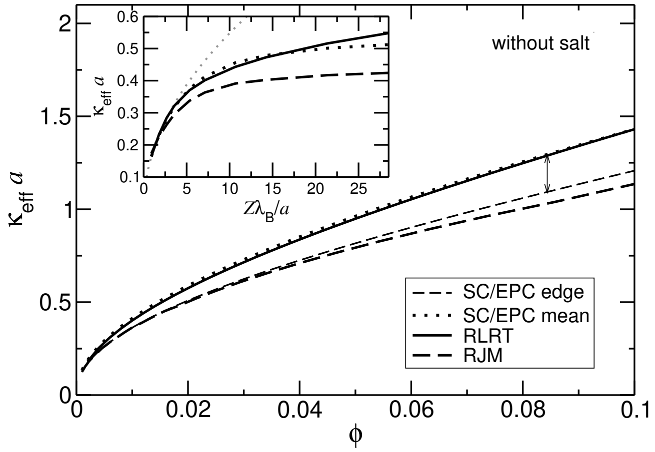

**Figure 7.1** Reduced renormalized screening constant, $\kappa_{\mathrm{eff}}a$, versus colloid volume fraction, $\phi$, for different renormalization methods as indicated. A salt-free suspension ($n_{\mathrm{res}} = 0$) is considered with bare macroion valence $Z = 40$ and $Z\lambda_{\mathrm{B}}/a = 7.12$ for $\lambda_{\mathrm{B}} = 0.714\,\mathrm{nm}$. Inset: $\kappa_{\mathrm{eff}}a$ versus coupling parameter, $Z\lambda_{\mathrm{B}}/a$, for the different methods at $\phi = 0.01$. In the inset, the SC/EPC results with edge linearization are indistinguishable from the RJM result on the scale of the figure. Dotted grey line corresponds to the screening constant $\kappa a = \sqrt{3\phi Z\lambda_{\mathrm{B}}/a}$ without accounting for charge renormalization.

To explore numerically the effective interaction parameter predictions, we first focus on the salt-free case, where a system in Donnan osmotic equilibrium and a closed (canonical) system become identical, since microions cannot leave the suspension into the reservoir due to the electroneutrality constraint. In the salt-free limit, the parameter space is two-dimensional and spanned by $\phi$ and $Z\lambda_{\mathrm{B}}/a$.

The predictions by the various renormalization schemes for $\kappa_{\mathrm{eff}}$ as a function of $\phi$ and $Z\lambda_{\mathrm{B}}/a$, respectively, are shown in Fig. 7.1 for the salt-free case. For all considered methods, one observes an increase of $\kappa_{\mathrm{eff}}$ with increasing $\phi$ and $Z\lambda_{\mathrm{B}}/a$ (inset). Notice that for the CM-based methods SC and EPC, $\kappa_{\mathrm{eff}}$ only differs by the invoked linearization. Within the underlying mean-field approximation, $\kappa_{\mathrm{eff}}$ is only determined by the free (uncondensed) microions for all methods. Therefore, it increases when the number of (surface-released) free counterions is increased, as done by increasing the colloid volume fraction $\phi$ or the colloid bare valence $Z$. This is noticed directly from Eqs. (3.18) and (3.20) for the CM-based methods with edge and mean linearization, respectively, and in Eq. (3.47) for RLRT and Eq. (3.41) for RJM. The potential linearization in RLRT is equivalent to the potential linearization with respect to the (volume-averaged) mean electrostatic potential. There is thus a clear distinction visible in Fig. 7.1 between the curves by the methods invoking linearization with respect to the mean electrostatic potential and the curves by the methods with linearization with respect to the minimum absolute value of the electric potential at the cell edge. This distinction is more pronounced at larger $\phi$ and larger $Z\lambda_{\mathrm{B}}/a$. Methods invoking mean potential linearization predict thus larger renormalized screening parameter.

Fig. 7.2 shows the different predictions for $Z_{\mathrm{eff}}$ and its dependence on $\phi$ and $Z\lambda_{\mathrm{B}}/a$ (in inset). The renormalized valence $Z_{\mathrm{eff}} < Z$ arises from the interaction of the strongly-charged colloid surfaces with their associated counterions. The strongly associated microions can be considered as quasi-condensed [36, 55, 115], which is a nonlinear electrostatic effect. The renormalized valence $Z_{\mathrm{eff}}$ is determined by the competition between the electric interaction energy reduction, via (counterion) quasi-condensation, and the gain in entropy of the microions by spreading out across the system volume. For small but increasing colloid concentration, the number of microions available for surface-condensation is increased, which

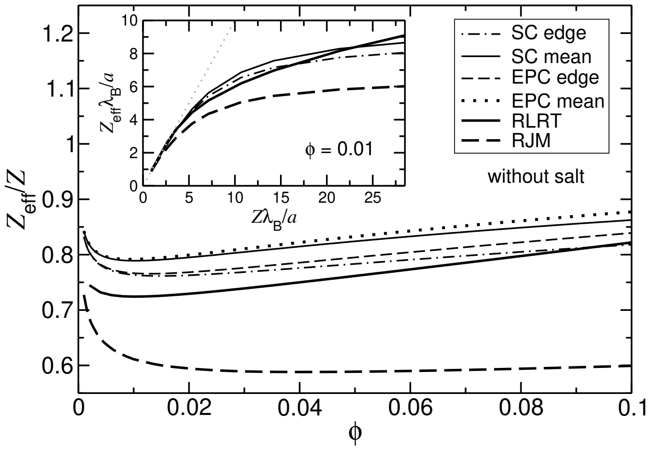

**Figure 7.2** Reduced renormalized valence, $Z_{\mathrm{eff}}/Z$, versus $\phi$ for the indicated renormalization methods and a salt-free suspension ($n_{\mathrm{res}} = 0$) with bare macroion valence $Z = 40$ and $Z\lambda_{\mathrm{B}}/a = 7.12$ for $\lambda_{\mathrm{B}} = 0.714\,\mathrm{nm}$. Inset: $Z_{\mathrm{eff}}\lambda_{\mathrm{B}}/a$ versus coupling parameter, $Z\lambda_{\mathrm{B}}/a$, at $\phi = 0.01$. In the inset, EPC edge and SC edge curves overlap, and likewise EPC mean and SC mean curves.

leads to a decrease of the renormalized charge as observed in the figure. However, this reduction of $Z_{\mathrm{eff}}$ ceases eventually with increasing $\phi$, since the quasi-condensation reduces the electric potential difference between a colloidal surface and the bulk volume (distant from the colloids) disfavoring the condensation of microions. This leads to a minimum of $Z_{\mathrm{eff}}$ at $\phi \approx 0.01$ with a subsequantial increase of $Z_{\mathrm{eff}}$ with further concentration growing. All considered renormalization methods share qualitatively the same behavior, except for RJM where $Z_{\mathrm{eff}}$ increases only very weakly for large volume fractions. The effect on $Z_{\mathrm{eff}}$ by varying the bare valence $Z$ is shown in the inset of Fig. 7.2. For low bare valence $Z$, the potential difference between a colloidal surface and the bulk of the suspension is small so that $Z \approx Z_{\mathrm{eff}}$ without noticeable counterion condensation. As $Z$ is increased, quasi-condensation appears leading to $Z_{\mathrm{eff}} < Z$. For high values of $Z$, $Z_{\mathrm{eff}}$ tends to a saturation value, which is different for each method.

All considered methods make comparable predictions for $Z_{\mathrm{eff}}$ and $\kappa_{\mathrm{eff}}$, except for RJM that predicts distinctly stronger microion condensation in comparison to the other ones with accordingly smaller $Z_{\mathrm{eff}}$ values. From comparing the CM-based methods only, one notices that the effective valence is larger for mean than for edge linearization. The fact that $Z_{\text{eff}}(\text{mean}) > Z_{\text{eff}}(\text{edge})$ was noted already in relation to Eq. (3.30).

We study next the effect of varying the salt concentration. Since we assume Donnan equilibrium with a microion reservoir, our results are presented as functions of the reservoir screening constant, $\kappa_{\text{res}} \propto \sqrt{n_{\text{res}}}$, which is proportional to the square root of the reservoir salt concentration. We analyze how salt variation affects the renormalized interaction parameters. Figure 7.3 depicts how $Z_{\text{eff}}$ and $\kappa_{\text{eff}}$ (the latter in inset) vary with increasing reservoir salt concentration, i.e. increasing $\kappa_{\text{res}} \propto \sqrt{n_{\text{res}}}$. At low salt content, all considered renormalization methods predict $Z_{\text{eff}}$ to be constant and equal to the renormalized valence of a salt-free system. With increasing salt concentration, all predictions of $Z_{\text{eff}}$, except for RLRT, start to grow monotonically and tend to match in the high-salt concentration regime, where $Z_{\text{eff}} \to Z$. RLRT, however, has a peculiar behavior. It shows the correct limiting behavior for low and high salt concentrations, but it is nonmonotonic for intermediate concentrations and with constant value $Z_{\text{eff}} = Z$ above a critical high-salt value $\kappa_{\text{eff}}$. According to the RLRT renormalization scheme described in section 3.3, quasi-condensation is taken to

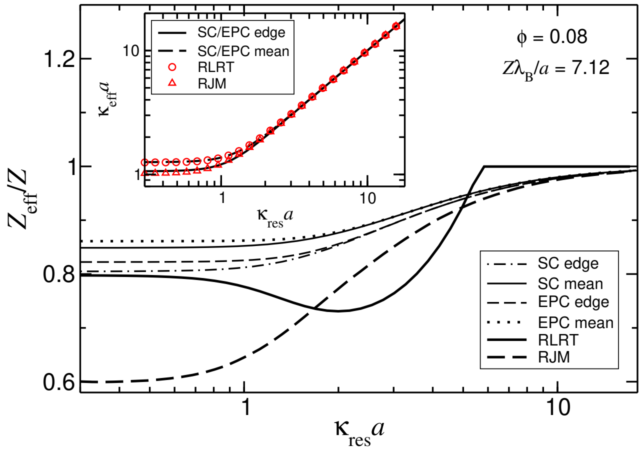

**Figure 7.3** Reduced renormalized valence, $Z_{\text{eff}}/Z$, versus reduced reservoir screening constant $\kappa_{\text{res}}a$ ($\kappa_{\text{res}}^2 \sim n_{\text{res}}$) for $\phi = 0.08$ and different renormalization methods as indicated. Inset: Reduced renormalized screening constant, $\kappa_{\text{eff}}a$, versus reduced reservoir screening constant $\kappa_{\text{res}}a$. Other system parameters: $Z = 40$, $Z\lambda_B/a = 7.12$ and $\lambda_B = 0.714$ nm.

cease abruptly. Similarly to $Z_{\text{eff}}$, the renormalized screening constant $\kappa_{\text{eff}}$ is constant and equal to the salt-free renormalized screening constant at low salt concentrations (see inset of Fig. 7.3). With increasing salt content, $\kappa_{\text{eff}}$ monotonically grows and becomes equal to the reservoir screening constant $\kappa_{\text{res}}$ for high concentrations.

In systems with added salt and for the employed mean-field models, $\kappa_{\text{eff}}^2$ has two additive contributions: one arising from the linearly-behaving salt ions, $(\kappa_{\text{s}}^{\text{eff}})^2$, and a second one, $(\kappa_{\text{c}}^{\text{eff}})^2$, from the free, noncondensed microions, i.e.

$$\kappa_{\text{eff}}^2 = (\kappa_{\text{c}}^{\text{eff}})^2 + (\kappa_{\text{s}}^{\text{eff}})^2. \tag{7.1}$$

In chapter 3, we showed that $\kappa_{\text{c}}^{\text{eff}} \propto \sqrt{\phi Z_{\text{eff}}}$ for the CM-based methods, RLRT and RJM; whereas $\kappa_{\text{s}}^{\text{eff}} \propto \sqrt{n_{\text{res}}}$ in RJM. These dependencies follow readily from Eqs. (3.18), (3.20), (3.34) and (3.47). Equation (7.1) allows to specify two regimes: a counterion-dominated regime for $\kappa_{\text{c}}^{\text{eff}} \gg \kappa_{\text{s}}^{\text{eff}}$ so that $\kappa_{\text{eff}} \approx \kappa_{\text{c}}^{\text{eff}}$; and a salt-dominated regime, for $\kappa_{\text{c}}^{\text{eff}} \ll \kappa_{\text{s}}^{\text{eff}}$ so that $\kappa_{\text{eff}} \approx \kappa_{\text{s}}^{\text{eff}}$. The major differences between the renormalization predictions for $Z_{\text{eff}}$ and $\kappa_{\text{eff}}$ are observed in the counterion-dominated regime, where these parameters are insensitive to salinity variations. In contrast, in the salt-dominated regime, all renormalization methods converge to $\kappa_{\text{eff}} \to \kappa_{\text{res}}$ and $Z_{\text{eff}} \to Z$. Therefore, in analyzing differences between the different renormalization schemes, one should focus on the salt-free limit.

An important quantity that provides a connection between the semi-grand canonical and canonical description in systems with added salt is the suspension salt pair concentration. This quantity also expresses the salt expulsion effect in Donnan equilibrium with increase of the colloid concentration. The suspension salt pair concentration, $n_{\text{s}}$, is (formally) determined from equating the microion chemical potentials in the reservoir and the suspension, within the semi-open description. In case of nonlinear CM approximation, this leads to the result for $n_{\text{s}}$ stated in Eq. (3.3). When charge renormalization is operative, the renormalized suspension salt pair concentration, $n_{\text{s}}^{\text{eff}}$, can be obtained from the renormalized interaction parameters. This quantity would measure the effectively linearly-behaving salt microion

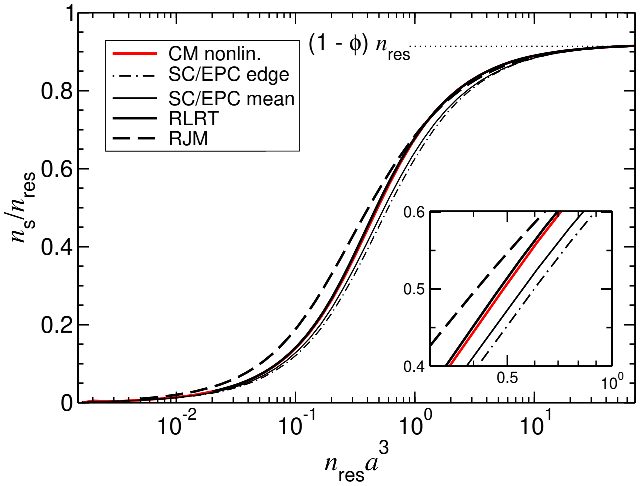

**Figure 7.4** Reduced renormalized suspension salt concentration, $n_{\text{s}}^{\text{eff}}/n_{\text{res}}$, versus reduced reservoir salt concentration, $n_{\text{res}}a^3$, for $\phi = 0.08$ and for the indicated renormalization schemes. Inset: magnification of the counterion- to salt-dominated transition region. Red: nonlinear $n_{\text{s}}$ from CM. Other system parameters: $Z = 40$, $Z\lambda_{\text{B}}/a = 7.12$ with $\lambda_{\text{B}} = 0.71$ nm.

pairs. Explicit expressions for $n_{\text{s}}^{\text{eff}}$ by the various methods are given in Eqs. (3.21) and (3.19) for SC with edge and mean linearization, respectively; Eq. (3.47) for RLRT; and Eq. (3.38) for RJM. For the EPC method, Eqs. (3.21) and (3.19) have been also used as approximations for edge and mean linearization, respectively. The respective results are plotted in Fig. 7.4, where we observe how $n_{\text{s}}^{(\text{eff})}$ varies with increasing reservoir salt concentration $n_{\text{res}}$. Two limiting plateau regions are observed: one in the counterion-dominated regime at low reservoir salt concentration, where $n_{\text{s}}^{\text{eff}} \approx 0$; and one in the salt-dominated regime at high reservoir salt concentration, where $n_{\text{s}}^{\text{eff}} \to (1-\phi)n_{\text{res}}$. The predictions for $n_{\text{s}}^{\text{eff}}$ by the different methods tend to overlap in these limits. In the transition regime for intermediate salt concentrations, the relative differences amount to 20% at most. It is interesting to compare the various predictions for $n_{\text{s}}^{\text{eff}}$ with $n_{\text{s}}$ (red curve), the latter obtained from integrating the nonlinear coion profile in nonlinear CM approximation in Eq. (3.3). As it is seen, $n_{\text{s}}$ is approximately equal to the RLRT prediction of $n_{\text{s}}^{\text{eff}}$.

Recall that salt ions are expelled from the suspension into the reservoir at low- to intermediate reservoir salt concentrations leading to $n_{\text{s}}^{\text{eff}} < (1-\phi)n_{\text{res}}$, since the counterions make here the largest contribution to the suspension chemical potentials. According to Fig. 7.4, RJM predicts the weakest salt-expulsion effect, while the expulsion predicted by the CM-based methods is the strongest.

### 7.1.1 Effective valence larger than bare one

On exploring the predictions by the various charge-renormalization methods in the $(\phi, n_{\mathrm{res}}a^3)$ parameter space, we observed that the EPC methods can predict an effective valence $Z_{\mathrm{eff}}$ that is larger than the bare valence $Z$, for high colloid concentrations and small values of $Z$. Since quasi-condensation of counterions for larger $Z$ always results in renormalized values $Z_{\mathrm{eff}} < Z$, this observation is not a nonlinear renormalization effect. Instead, it is due to a reduction in the linear microion screening of a macroion caused by other nearby macroions.

In Fig. 7.5, $Z_{\mathrm{eff}}$ and $\kappa_{\mathrm{eff}}$ are plotted for an exemplary, weakly-coupled system with $Z\lambda_{\mathrm{B}}/a = 1.52$. Note that $Z_{\mathrm{eff}} > Z$ in EPC for $\phi \geq 0.075$, with no noticeable differences for edge and mean linearizations. There is a remnant of quasi-condensation of counterions visible for $\phi \leq 0.075$, where $Z_{\mathrm{eff}} < Z$. The inset shows the expected monotonic growth of $\kappa_{\mathrm{eff}}$, being the results for the different linearizations approximately similar.

The EPC method is not the only method to predict $Z_{\mathrm{eff}} > Z$ for concentrated suspensions of weakly charged colloids. Another method is the penetrating RJM (see section 3.2), where, different from the nonpenetrating RJM, the homogeneous neutralizing jellium also occupies the colloid interior. As noted before in section 3.2, the RJM is based on the jellium approximation JA, widely used in solid state physics and applied to charge-stabilized suspensions by Beresford-Smith *et. al.* [9]. The JA assumes for the microion radial distribution function that $g_{\mathrm{mm}}(r) = 1$ for all $r > 0$. By combining this approximation with the linear MSA closures for the microion-microion direct correlation functions of pointlike microions, and the MSA closure for the macroion-microion direct correlation functions at $r > a$, the effective macroion pair potential for weak macroion coupling and high dilution is obtained

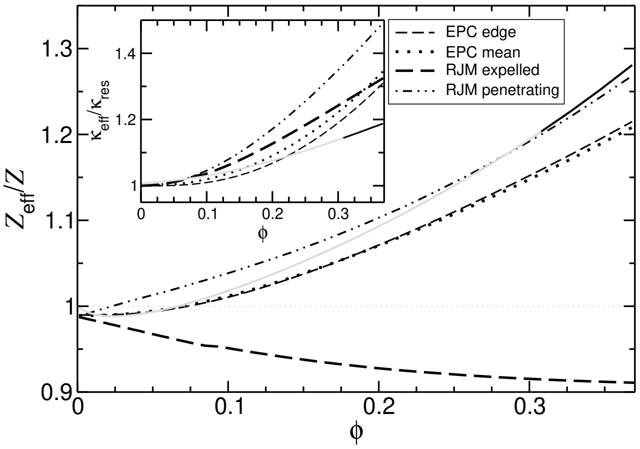

**Figure 7.5** Reduced renormalized valence, $Z_{\text{eff}}/Z$, versus $\phi$ for the indicated charge renormalization schemes. Inset: Reduced renormalized screening constant $\kappa_{\text{eff}}/\kappa_{\text{res}}$ versus $\phi$ for different methods. The solid black part of the MSA curves corresponds to positive contact value, which is the physically relevant part. Other system parameters: $Z = 80$, $Z\lambda_{\text{B}}/a = 1.52$, $\lambda_{\text{B}} = 0.71349$ nm and $\kappa_{\text{res}}a = 1.327$.

in the linear penetrating JA as [9]

$$\beta u_{\text{eff}}(r) = \lambda_{\text{B}} Z^2 (1+\phi)^2 \left( \frac{e^{\kappa a}}{1+\kappa a} \right)^2 \frac{e^{-\kappa r}}{r}, \tag{7.2}$$

with $\kappa^2 = 4\pi\lambda_{\text{B}}(n_+ + n_-)$ for monovalent microions. Contrasting this pair potential with the ones for impermeable colloids derived in section 2.1 by means of DFT and LRT, one notices that they are identical apart from the factor $(1+\phi)^2$, which is due to the macroion core penetration by the jellium. By combining the (penetrating) JA with the nonlinear HNC closure for the macroion-microion direct correlation functions, nonlinear effects might be included. This leads to a description equivalent to the nonlinear PB equation in Eq. (3.31) with associated boundary conditions for the penetrating jellium in Eq. (3.43). Thus, one can apply a charge-renormalization procedure, similar to the one for the nonpenentrating case, resulting in renormalized valence and screening parameter used as inputs to Eq. (7.2) in order to incorporate nonlinear screening effects. The effective pair potential derived within nonlinear penetrating JA approximation by Beresford-Smith *et. al.* [9] has proven to accurately describe the pair structure of a highly-coupled systems with $Z\lambda_{\text{B}}/a \approx 13$, up to macroion concentrations of $\phi = 0.13$ [9].

The second method predicting $Z_{\text{eff}} > Z$ at high concentration and small $Z\lambda_{\text{B}}/a$ is the PM-MSA scheme (see subsection 2.4.3), which gives rise to $u_{\text{eff}}(r)$ shown in Eq. (2.76). This resulting MSA-based effective pair potential is of DLVO-type with $Z_{\text{eff}} = X_{\text{MSA}}Z$, where $X_{\text{MSA}}$ is given by Eq. (2.77), and $\kappa_{\text{eff}} = \kappa$, with $\kappa$ of the DH form in Eq. (2.78) [48]. In the infinite dilution limit $n_{\text{m}} \to 0$, one obtains $X_{\text{MSA}} \to e^{\kappa a}/(1+\kappa a)$, recovering hereby the standard DLVO potential. In the high temperature limit $\beta \to 0$, where $\kappa a \ll 1$, it follows

$$Z_{\text{eff}}^{\text{MSA}} = Z\,X_{\text{MSA}} \to \frac{Z}{1-\phi} \approx (1+\phi)Z + \mathcal{O}(\kappa^2). \tag{7.3}$$

Note that $Z_{\text{eff}}^{\text{MSA}}$ differs from the linear effective valence $Z_{\text{eff}} = Z(1+\phi)$ in the pair potential of Eq. (7.2), the latter derived using linear penetrating JA, only by small correction terms of quadratic order in $\phi$ and $\kappa$. Explicit calculation shows indeed that $Z_{\text{eff}}^{\text{MSA}} > Z$.

Figure 7.5 depicts $Z_{\text{eff}}$ and $\kappa_{\text{eff}}$ predicted by the EPC methods, and by the penetrating- and nonpenetrating RJM for weakly coupled macroion suspensions with $Z\lambda_{\text{B}}/a = 1.52$. The system parameters have been selected in a region where the EPC-based $g(r)$ calculated using RY is of better accuracy than the one based on the SC methods [56]. The curves of $\kappa_{\text{eff}}$, depicted in the inset, present the expected monotonic increase with increasing $\phi$ for all cases, however it is only in the EPC and penetrating RJM methods that $Z_{\text{eff}} > Z$ is found for $\phi \gtrsim 0.1$. The nonpenetrating RJM predicts $Z_{\text{eff}} \leq Z$ for all concentrations.

The solid lines in Fig. 7.5 corresponds to $Z_{\text{eff}}^{\text{MSA}}$ and $\kappa$ as obtained from the linear MSA solution in Eqs. (2.76) and (2.78). Explicitly,

$$\frac{Z_{\text{eff}}^{\text{MSA}}}{Z} = \frac{1+\kappa a}{e^{\kappa a}}[\cosh(\kappa a) + U\,(\kappa a\cosh(\kappa a) - \sinh(\kappa a))], \tag{7.4}$$

with $U$ given in Eq. (2.81). The MSA results for $Z_{\text{eff}}^{\text{MSA}}$ and $\kappa$ are depicted only for $\phi > 0.3$, where the MSA contact value $g(\sigma^{+})$ is nonnegative. As noted already in the context of Eq. (2.84), $Z_{\text{eff}}^{\text{MSA}}$ is lager than $Z$ and approximately equal to $Z_{\text{eff}}$ predicted by the penetrating RJM. According to Ref. [48], the MSA prediction $Z_{\text{eff}}^{\text{MSA}} > Z$ or, equivalently, $X_{\text{MSA}} > e^{\kappa a}/(1+\kappa a)$, can be attributed to a decreased screening ability of the microions around given macroion owing to neighboring macroions, leading to a stronger effective macroion-macroion repulsion. This reduced screening arises in the high concentration region and it might be understood as a consequence of the overlap of the double layers predicted by the standard DLVO potential.

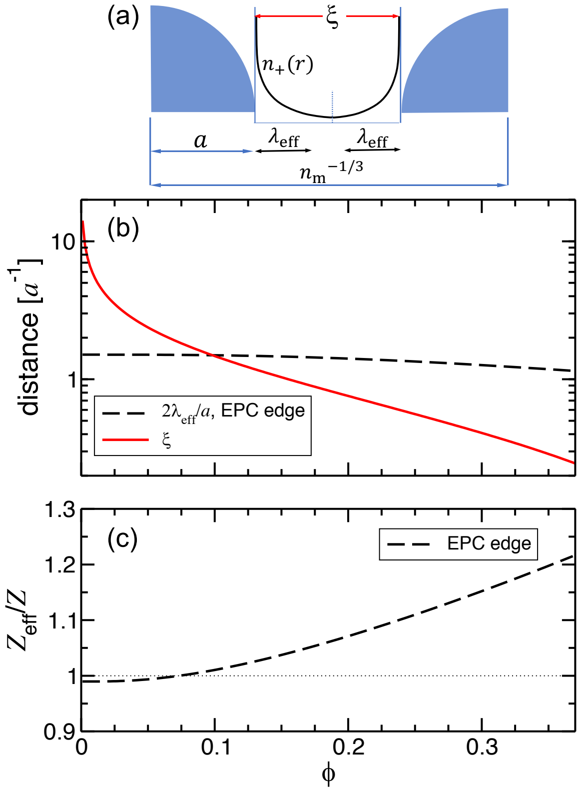

**Figure 7.6** (a) Sketch of the geometry indicating all relevant quantities. (b) Reduced effective screening length, $\lambda_{\rm eff}/a$, and reduced mean distance between two colloid surfaces $\xi = n_{\rm m}^{-1/3}/a - 2$ versus $\phi$ for EPC edge method. (c) Reduced effective valence, $Z_{\rm eff}\lambda_{\rm B}/a$, versus $\phi$. System parameters as in Fig. 7.5.

In order to examine how the double layer overlap is related to the predictions from EPC method, the effective screening lengths resulting from EPC-$\kappa_{\rm eff}$ are plotted in Fig. 7.6. Figure 7.6(a) shows a sketch of the analyzed geometry. In Fig. 7.6(b), we compare twice the effective screening length, $\lambda_{\rm eff} = \kappa_{\rm eff}^{-1}$, with the (reduced) mean surface-to-surface distance, $\xi = n_{\rm m}^{-1/3} - 2a$, of two neighboring macroions. By contrasting this with Fig. 7.6(c), one notices that $Z_{\rm eff}$ becomes larger than $Z$ roughly at the same concentration $\phi$, where the two (diffuse) electric double layers begin to overlap. This illustrates that the finding $Z_{\rm eff} > Z$

is not a single-macroion effect. We point out that the linear screening effect $Z_{\text{eff}} > Z$ for overlapping macroion electric double layers at large $\phi$ is masked by microion condensation (charge-renormalization) for larger coupling, so that $Z_{\text{eff}} < Z$ is observed even at large $\phi$. However, the here discussed linear screening effect with $Z_{\text{eff}} > Z$ can play a role in concentrated solutions of proteins.

## 7.2 Pair structure

Once the renormalized parameters $\kappa_{\text{eff}}$ and $Z_{\text{eff}}$ entering in $u_{\text{eff}}(r)$ are determined, the macroion-macroion $g(r)$ and $S(q)$ can be calculated using the thermodynamically consistent RY scheme described in subsection 5.3.3. The RY scheme provides accurate results for dispersions with Yukawa-type repulsive interactions [99, 109, 110]. This allows for comparing the considered renormalization schemes for $\kappa_{\text{eff}}$ and $Z_{\text{eff}}$ in terms of their predictions for $g(r)$ and $S(q)$.

We focus first on salt-free systems, where the largest differences in the renormalized interaction parameters are observed (cf. Fig. 7.3), and for which PM-based Monte Carlo (MC) simulation results of $g(r)$ are available [8].

In Fig. 7.7, the $g(r)$ for $\kappa_{\text{eff}}$ and $Z_{\text{eff}}$ obtained using SC scheme with mean linearization is compared with PM-MC simulation results by Linse *et. al.* [8], for six different coupling parameter values $Z\lambda_{\text{B}}/a$ as indicated. The depicted curves based on the SC mean method are representative for all considered renormalization schemes. Qualitatively, all schemes give good results for $g(r)$ in the explored parameter range. With increasing $Z\lambda_{\text{B}}/a$ at fixed $\phi = 0.01$, there is an initial build-up of the macroion pair structure progressing from $Z\lambda_{\text{B}}/a = 0.89$ to 7.12. In this coupling range, the principal peak of $g(r)$ at $r_{\text{m}}$ increases with increasing coupling and $r_{\text{m}}$ is decreasing. One further observes an increasing distance range, wherein $g(r) \approx 0$, reflecting stronger electric repulsion. Notice that in the considered coupling range, there is perfect agreement between the $g(r)$ curves with SC mean input for $Z_{\text{eff}}$ and $\kappa_{\text{eff}}$ and the PM-MC simulation data. Small differences between the simulation data for $g(r)$ and the RY-$g(r)$ are visible for the two largest coupling values, but even there the observed trends are the same, i.e. a gradual decrease in $g(r_\mathrm{m})$ in increasing $Z\lambda_\mathrm{B}/a$ from 7.12 to 28.46, with the correlation-hole range $g(r) \approx 0$ decreasing accordingly and $r_\mathrm{m}$ increasing. In the simulation study in Ref. [8], it is shown that for further increasing coupling macroion aggregation occurs.

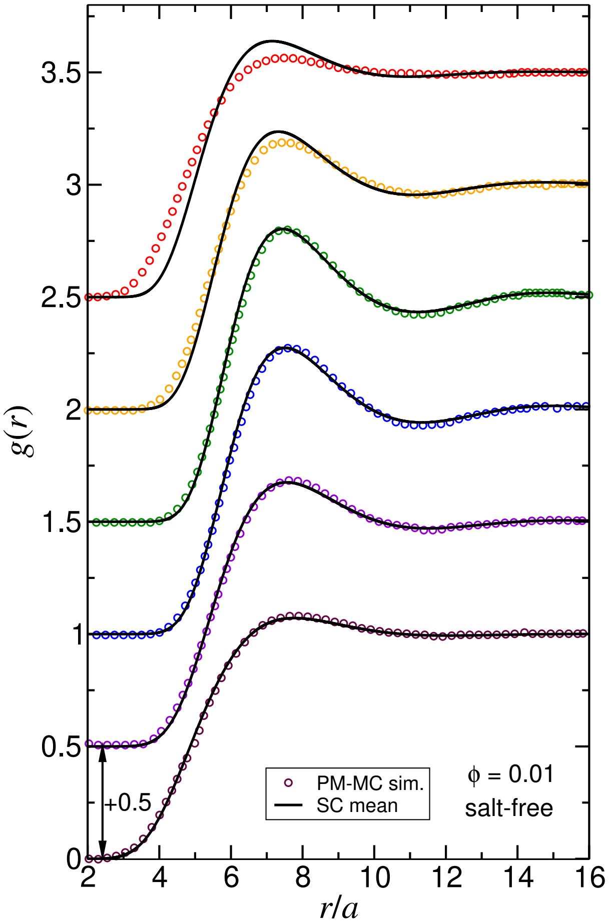

**Figure 7.7** Macroion pair correlation function, $g(r)$, for different coupling parameters, $Z\lambda_\mathrm{B}/a$, of a salt-free suspension ($n_\mathrm{res} = 0$) at $\phi = 0.01$. The solid curves are obtained using RY scheme with SC mean charge-renormalization input for $Z_\mathrm{eff}$ and $\kappa_\mathrm{eff}$ in $u_\mathrm{eff}(r)$, while open circles are PM-MC simulation data [8]. From bottom to top, $Z\lambda_\mathrm{B}/a = 0.89, 1.78, 3.56, 7.12, 14.23, 28.46$. The curves are vertically shifted for better visualization. Other system parameters: $Z = 40$ and $\lambda_\mathrm{B} = 0.71$ nm

The peak height of $g(r)$ is plotted in Fig. 7.8(a) in dependence of $Z\lambda_\mathrm{B}/a$, for renormalized interaction parameters by all considered renormalization schemes. Quite interestingly, the initial increase of $g(r_\mathrm{m})$ at low coupling as seen in the PM-MC simulation data is accurately reproduced by all considered schemes, due to the fact that they agree with the RY-$g(r_\mathrm{m})$ without charge renormalization (dotted curve in panel (a)). The observed agreement expresses thus simply the good accuracy of the RY-scheme for particle systems with repulsive Yukawa-type interactions. Notice that $Z_\mathrm{eff} \approx Z$ and $\kappa_\mathrm{eff} \approx \kappa_0$, with $\kappa_0^2 = 4\pi\lambda_\mathrm{B} n_+$, are predicted by all charge renormalization schemes for $Z\lambda_\mathrm{B}/a \lesssim 5$ (cf. insets of Figs. 7.1 and 7.2). For $Z\lambda_\mathrm{B}/a \gtrsim 5$, charge renormalization becomes relevant and the predictions for $\kappa_\mathrm{eff}$ and $Z_\mathrm{eff}$ by the considered methods become progressively different from each other with further increasing coupling. The dotted curve Fig. 7.8(a) shows that $g(r_\mathrm{m})$ is largely overestimated at stronger coupling for neglected charge renormalization. With charge renormalization accounted for, the nonmonotonic behaviour of the MC data in panel (a) are well described qualitatively by all the renormalization methods. Consistent with its stronger renormalization prediction for $Z_\mathrm{eff}$ (cf. Fig. 7.2), the RJM strongly underestimates $g(r_\mathrm{m})$. RLRT is more accurate, with the simulated $g(r_\mathrm{m})$ overestimated for very high coupling only. The CM-based methods for both linearizations reproduce the PM-MC $g(r_\mathrm{m})$ most accurately, being slightly better than RLRT. We also notice that the CM-based methods with mean linearization perform slightly better than those with edge linearization. Except for RJM, all methods overestimate $g(r_\mathrm{m})$ at very high coupling. There is hardly any difference between EPC and SC curves for $g(r_\mathrm{m})$ when edge or mean linearization is used, respectively.

For salt-free suspensions, $g(r_\mathrm{m})$ is closely associated with the contact value, $u_\mathrm{eff}(\sigma^+)$, of the effective pair potential. This can be noticed from Fig. 7.8 (b), where $\beta u_\mathrm{eff}(\sigma^+)$ is plotted as function of $Z\lambda_\mathrm{B}/a$. The curves for the contact value of the effective pair potential by the different renormalization schemes qualitatively reflect the curves for $g(r_\mathrm{m})$ in panel (a), with peaks at the same respective coupling values. Notice that $\beta u_\mathrm{eff}(\sigma^+) \propto Z_\mathrm{eff}^2 (1+\kappa_\mathrm{eff} a)^{-2}$, where the geometric factor $(1+\kappa_\mathrm{eff} a)^{-2}$ arises from the finite radius $a = \sigma/2$ of the impermeable macroions.

Figure 7.9 displays the concentration dependence of the $g(r)$ and $g(r_\mathrm{m})$ compared with

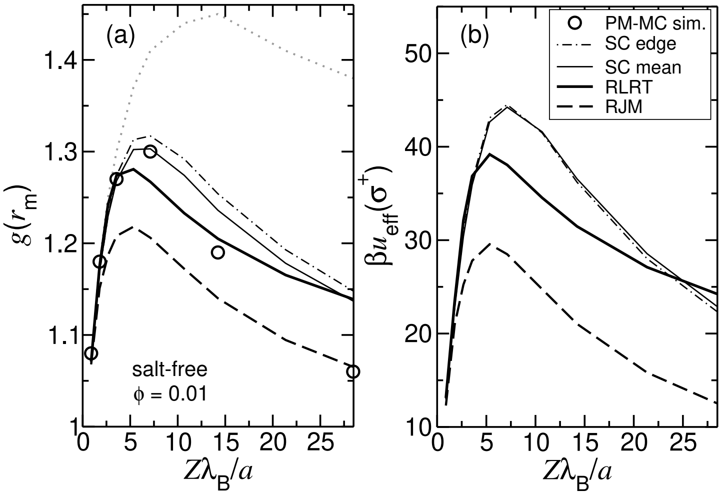

**Figure 7.8** (a) Principal peak height, $g(r_\mathrm{m})$, of the macroion pair correlation function and (b) reduced effective pair potential at contact, $\beta u_\mathrm{eff}(\sigma^+)$, versus bare coupling, $Z\lambda_\mathrm{B}/a$, for the indicated charge-renormalization schemes describing a salt-free suspension ($n_\mathrm{res} = 0$) with bare macroion valence $Z = 40$ at $\phi = 0.01$ for $\lambda_\mathrm{B} = 0.714$ nm. SC edge and SC mean results are very close to EPC edge and EPC mean results, respectively (the latter not shown here). Dotted grey line in (a) corresponds to results without charge renormalization. Curves in (a) are RY-based results, while symbols are PM-MC data from [8].

PM-MC simulation results (open circles) for a salt-free suspension with fixed coupling value $Z\lambda_\mathrm{B}/a = 7.12$, corresponding to the most structured $g(r)$ in Fig. 7.8 having $\phi = 0.01$. For the smallest concentration, $\phi = 0.00125$, the suspension is only weakly structured with a low and flat peak $g(r_\mathrm{m})$ at $r/a \approx 15$. However, the electric repulsion between macroions is still strong enough that $g(r < 7a) \approx 0$. With increasing $\phi$, the fluid-ordered suspension becomes more structured, which is reflected in the sharpening of the principal peak of $g(r)$, with its position $r_\mathrm{m}$ shifting to small inter-particle distances. Moreover, the secondary peak becomes more pronounced, reflecting the build-up of a second next-neighbour shell. The position of the principal peak is approximately equal to the macroion next-neighbour distance, i.e. $r_\mathrm{m} \approx n_\mathrm{m}^{-1/3} = (3\phi/(4\pi a^3))^{-1/3}$. This is typical of suspensions whose structure is determined by long-range repulsive interactions [8], for which $g(\sigma^+) = 0$. All the considered charge-renormalization methods provide $g(r)$'s in good agreement with the PM-MC simulation data. Therefore, only $g(r)$'s with SC-mean input for the renormalized interaction parameters are

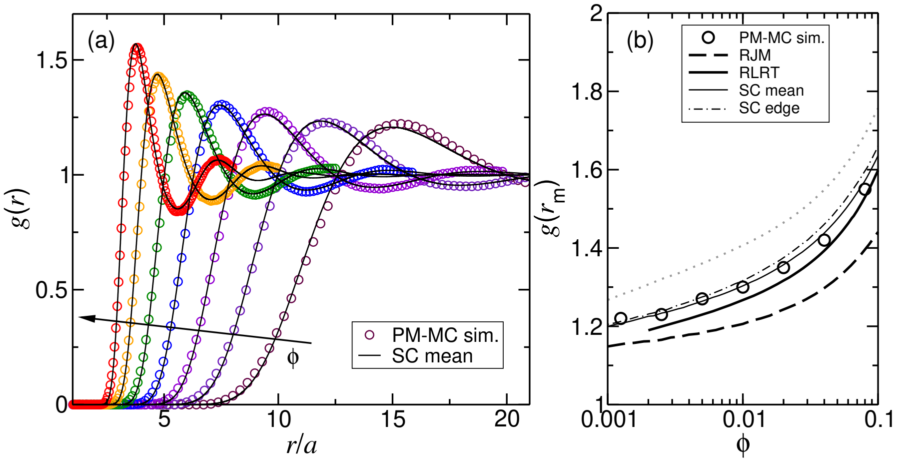

**Figure 7.9** (a) Macroion pair correlation function, $g(r)$, for $\phi = 0.00125$, 0.0025, 0.005, 0.01, 0.02, 0.04, 0.08, (b) Principal peak height, $g(r_\mathrm{m})$, versus $\phi$. Salt-free suspensions ($n_\mathrm{res} = 0$) are considered with $Z\lambda_\mathrm{B}/a = 7.12$. The solid curves in (a) are obtained using RY and renormalized interaction parameters from the indicated schemes. Open circles are PM-MC simulation data from [8]. In (b), SC edge and SC mean results for $g(r_\mathrm{m})$ are very close to the ones for EPC edge and EPC mean, respectively (the latter not shown). Dotted grey line in (b) corresponds to results without charge renormalization. Other system parameters: $Z = 40$ and $\lambda_\mathrm{B} = 0.714$ nm.

shown in panel (a).

In Fig. 7.9(b), $g(r_\mathrm{m})$ is plotted as function of $\phi$ for the different methods. As seen, $g(r_\mathrm{m})$ is underestimated by RJM and, to a lower degree, also by RLRT method, while CM-based methods give quite accurate results in the full concentration range.

As discussed in section 5.1, the static structure factor, $S(q)$, related to $g(r)$ by Eq. (5.5) characterizes pair correlations in Fourier space. Its peak value $S(q_\mathrm{m})$ at $q_\mathrm{m} \approx 2\pi/r_\mathrm{m}$ allows to roughly identify the freezing transition of suspensions of spherical particles with Yukawa-type repulsion, while $S(0)$ provides the osmotic compressibility factor of a monodisperse suspension in osmotic equilibrium with a salt reservoir. We use here $S(q)$ to study the effect of added salt on the pair structure as predicted by the different renormalization methods. Figure 7.10 shows the RY-generated principal peak, $S(q_\mathrm{m})$, as function of the concentration $n_\mathrm{res}$ nondimensionalized in form of the reduced reservoir screening constant $\kappa_\mathrm{res}a = 8\pi\lambda_\mathrm{B}a^2 n_\mathrm{res}$, for the indicated charge-renormalization inputs. The different salinity

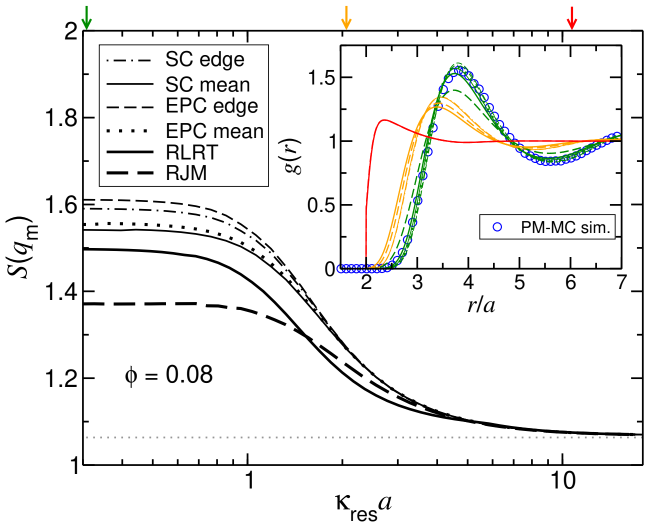

**Figure 7.10** Static structure factor peak, $S(q_\mathrm{m})$, versus reduced reservoir screening constant $\kappa_\mathrm{res}a$ ($\kappa_\mathrm{res}^2 \sim n_\mathrm{res}$) for different renormalization methods as indicated with $\phi = 0.08$ and $Z\lambda_\mathrm{B}/a = 7.12$. Inset: Macroion pair correlation function, $g(r)$, for the different methods and three reservoir salt concentrations representative, respectively, of the counterion-dominated regime ($\kappa_\mathrm{res}a = 0.3$, green), transition regime ($\kappa_\mathrm{res}a = 2.06$, yellow), and salt-dominated regime ($\kappa_\mathrm{res}a = 10.68$, red). The blue circles in the inset are PM-MC simulation results for the salt-free case. The horizontal dotted line in the main figure is the $S(q_\mathrm{m})$ of a HS system, obtained in Carnahan-Starling approximation according to Eq. (7.5). Other system parameters: $Z = 40$ and $\lambda_\mathrm{B} = 0.714$ nm.

values in the counterion-dominated, salt-dominated, and transition regime are selected as indicated in the figure. The suspension with the largest concentration, $\phi = 0.08$, is considered so that the structural differences in $S(q)$, predicted by the different renormalization schemes, are clearly visible. Two plateaus regimes of $S(q_\mathrm{m})$ are distinguishable at low and high salt concentrations, corresponding to the counterion-dominated and salt-dominated regimes, respectively. The strongest differences in $S(q_\mathrm{m})$ obtained from the different charge-renormalization methods are visible in the counterion-dominated regime, consistent with the finding for the renormalized parameters in Fig. 7.3. In line with its most-pronounced charge renormalization prediction (cf. Fig. 7.3), the RJM-based $S(q_\mathrm{m})$ is the smallest one for low salt content, followed by the RLRT and CM-based results. Regarding the CM-based methods, namely SC and EPC, $S(q_\mathrm{m})$ with mean linearization is smaller than with edge linearization. The differences between edge and mean linearization are more pronounced for $S(q_\mathrm{m})$ than for $g(r_\mathrm{m})$. This is relevant for estimating the freezing transition by means of the empirical Hansen-Verlet rule, which states that $S(q_\mathrm{m}) \approx 3.1$ at the freezing point of charge-stabilized systems with $g(\sigma^+) \approx 0$ [85], as in the case of salt-free systems. According to Figs. 7.8 and 7.9, the interaction parameters $Z_\mathrm{eff}$ and $\kappa_\mathrm{eff}$ obtained from SC mean lead to the most accurate freezing concentration prediction based on the Hansen-Verlet criterion.

In the transition regime between counterion-dominated and salt-dominated regimes, $S(q_\mathrm{m})$ decreases with increasing $n_\mathrm{res}$, reflecting a loss in structure. The differences in the predictions of $S(q_\mathrm{m})$ by the different renormalization methods cease in the salt-dominated regime, where $S(q_\mathrm{m})$ approaches the hard-sphere value $S^\mathrm{HS}(q_\mathrm{m})$ at the considered $\phi$. The horizontal, dotted line in Fig. 7.10 indicates the hard-sphere peak value $S^\mathrm{HS}(q_\mathrm{m}) \approx 1.06$ obtained from the parametrization

$$S^\mathrm{HS}(q_\mathrm{m}) = 1 + 0.644\,\phi \frac{1-\phi/2}{(1-\phi)^3} \tag{7.5}$$

given by Banchio *et. al.* in [116], which reproduces quantitatively the simulation data and the Verlet-Weiss corrected PY peak height for hard spheres in the fluid phase.

The inset of Fig. 7.10 shows $g(r)$ for the different renormalization schemes for three considered reservoir salt concentrations, $n_\mathrm{res}$. At low $n_\mathrm{res}$ (green curves), the $g(r)$'s by all methods, except those for RJM, are close to each other and to the zero-salt PM-MC $g(r)$ shown in Fig. 7.9(a) for $\phi = 0.08$.

## 7.3 Pressure and osmotic compressibility

Having discussed the indirect implications of the charge renormalization schemes on $g(r)$ and $S(q)$ through their effect on the interaction parameters entering $u_\mathrm{eff}(r)$, we address now their implications on various suspension pressure contributions and the osmotic compressibility. For instance, the suspension pressure $p$ can be determined by Eq. (5.8), provided the semi-grand suspension free energy per macroion, $f = \Omega/N_\mathrm{m}$, is known including its volume energy contribution. Recall from subsection 2.4.2 that in LRT, $f$ is obtained for impermeable, rigid macroions as

$$f = \varepsilon_{\mathrm{vol}} + f_{\mathrm{m}}, \tag{7.6}$$

where $\varepsilon_{\mathrm{vol}} = E_{\mathrm{vol}}/n_{\mathrm{m}}$ is volume energy per macroion given in Eq. (2.56), and $f_{\mathrm{m}}$ is the macroion free energy per macroion. Charge renormalization is introduced into the LRT scheme, according to section 3.3, by accounting for the thickness $\delta$ of the shell of surface-associated (bound) microions. The pressure in RLRT follows thus from Eq. (5.8) as

$$p = n_{\mathrm{m}}^2 \left( \frac{\partial \omega}{\partial n_{\mathrm{m}}} \right)_{\mathrm{res}} = p_{\mathrm{free}} + p_{\mathrm{m}}. \tag{7.7}$$

According to Eq. (2.56) with renormalized input $\kappa_{\mathrm{eff}}$ and $Z_{\mathrm{eff}}$ as explained in section 3.3,

$$\beta p_{\mathrm{free}} = \tilde{n}_+ + \tilde{n}_- - \frac{Z_{\mathrm{eff}}(\tilde{n}_+ - \tilde{n}_-)\kappa_{\mathrm{eff}}\lambda_{\mathrm{B}}}{4[1 + \kappa_{\mathrm{eff}}(a+\delta)]^2} \tag{7.8}$$

is the pressure contribution arising from the renormalized volume energy. Here, the tilde indicates a free volume correction for the concentrations of free (unbound) microions. In taking the macroion concentration derivative in Eq. (7.7), temperature and reservoir salt concentration, $n_{\mathrm{res}}$, are held constant, and the system electroneutrality is maintained for given $Z$. There is no direct pressure contribution due to bound microions, since the effective interaction parameters are kept fixed in the concentration derivative. The pressure contribution, $p_{\mathrm{m}}$, arising from the microion-dressed macroions follows from [67]

$$\beta p_{\mathrm{m}} = n_{\mathrm{m}} + n_{\mathrm{m}}^2 \beta \left( \frac{\partial f_{\mathrm{m}}^{\mathrm{ex}}}{\partial n_{\mathrm{m}}} \right)_{\mathrm{res}}. \tag{7.9}$$

As explained in subsection 4.3.1 in relation to Eq. (4.23), the excess macroion free energy per macroion, $f_{\mathrm{m}}^{\mathrm{ex}}$, can be approximated by [19]

$$f_{\mathrm{m}}^{\mathrm{ex}}(n_{\mathrm{m}}) \leq \min_{(d)} \left\{ f_{\mathrm{EHS}}(d, n_{\mathrm{m}}) + 2\pi n_{\mathrm{m}} \int_d^\infty dr r^2 g_{\mathrm{EHS}}(r; d, n_{\mathrm{m}})\, u_{\mathrm{eff}}(r; n_{\mathrm{m}}) \right\}, \tag{7.10}$$

which invokes a reference system of effective hard spheres (EHS) of diameter $d$, radial distribution function $g_{\mathrm{EHS}}(r; d, n_{\mathrm{m}})$, and excess free energy per particle $f_{\mathrm{EHS}}(d, n_{\mathrm{m}})$. The latter is described by the Carnahan-Starling free energy expression, and the EHS radial distribution function by the Percus-Yevick expression [77] with Verlet-Weis correction [19]. In practice, the renormalized interaction parameters ($Z_{\mathrm{eff}}$, $\delta$, $\kappa_{\mathrm{eff}}$) are held constant in the variational minimization and in taking thermodynamic derivatives [67].

Alternatively, the suspension pressure $p$ can be computed from the generalized virial equation in Eq. (5.11), since for the considered mean-field methods there are no third- or higher-order effective potential contributions. There is also no pressure contribution, $p_{\mathrm{se}}$, arising from polymeric degrees of freedom because only impermeable, rigid macroions are considered in this section. The suspension pressure results then from

$$\beta p = n_{\mathrm{m}} - \frac{2\pi}{3} n_{\mathrm{m}}^2 \int_0^\infty dr r^3 g(r) \frac{\partial \beta u_{\mathrm{eff}}(r)}{\partial r} + 2\pi n_{\mathrm{m}}^3 \int_0^\infty dr r^2 g(r) \frac{\partial \beta u_{\mathrm{eff}}(r)}{\partial n_{\mathrm{m}}} + \beta p_{\mathrm{free}} \tag{7.11}$$

where $p_{\mathrm{free}}$ is the contribution from the renormalized volume energy. Regarding the pressure contribution invoking the concentration derivative of the effective pair potential in Eq. (7.11), the following points are important to observe. In taking the derivative $\partial u_{\mathrm{eff}}/\partial n_{\mathrm{m}}$, only the concentration dependencies of $u_{\mathrm{eff}}(r; n_{\mathrm{m}})$ arising from the tracing-out of the microions should be considered, and not the additional ones due to the extra imposed charge renormalization. Only the first ones are thermodynamically relevant. An example is given by the volume energy from SDHA, Eq. (3.59), with renormalized $Z_{\mathrm{eff}}$ and $\kappa_{\mathrm{eff}}$ taken for the salt-free case. Here, the correct ideal gas limit $p_{\mathrm{vol}} = k_{\mathrm{B}}T(1+Z)n_{\mathrm{m}} + \mathcal{O}(n_{\mathrm{m}}^2, Z^2)$ is recovered from $p_{\mathrm{vol}} = n_{\mathrm{m}}^2 \partial E_{\mathrm{vol}}/\partial n_{\mathrm{m}}$ only when $Z_{\mathrm{eff}}$ and $\kappa_{\mathrm{eff}}$ are kept constant.

As discussed in section 5.2, in a nonlinear CM description of a suspension, macroion correlations are neglected and $p$ is approximated according to Eq. (5.13) by $p \approx p_{\mathrm{CT}}$, where

$$\beta p_{\mathrm{CT}} = n_{\mathrm{m}} + 2 n_{\mathrm{res}} \cosh[\Phi(R)]. \tag{7.12}$$

Recall that $\Phi(R)$ is the nonlinear total electrostatic potential value at the cell edge, and $k_{\mathrm{B}}T n_{\mathrm{m}}$ is the ideal-gas pressure contribution by the macroions.

In the RJM, the suspension pressure is approximated as $p \approx p_{\mathrm{jell}}$, where

$$\beta p_{\mathrm{jell}} = n_{\mathrm{m}} + \sqrt{(2n_{\mathrm{res}})^2 + (n_{\mathrm{m}} Z_{\mathrm{eff}})^2}, \tag{7.13}$$

for a suspension in Donnan equilibrium (cf. Eq. (5.14). The first term on the right-hand side is the ideal-gas macroion contribution. The second term is the microion contribution, resulting from salt ions of concentration $n_{\mathrm{res}}$ and non-condensed surface-released counterions, respectively. In the salt-free case, Eq. (7.13) reduces to

$$\beta p_{\mathrm{jell}} = n_{\mathrm{m}} + n_{\mathrm{m}} Z_{\mathrm{eff}} = n_{\mathrm{m}}(1 + Z_{\mathrm{eff}}), \tag{7.14}$$

which is of the same form as the ideal gas pressure, $p_{\mathrm{id}}$, of macro- and counterions,

$$\beta p_{\mathrm{id}} = n_{\mathrm{m}}(1 + Z), \tag{7.15}$$

but with $Z$ replaced by $Z_{\mathrm{eff}} < Z$.

To analyze the different approximations for the suspension pressure noted above, we consider first the salt-free case. In Fig. 7.11(a), we compare the different approximations of $p$ as a function of $\phi$, for coupling values $Z\lambda_{\mathrm{B}}/a$ as indicated, in comparison with PM-MC simulation results for $p$ [8]. For calculating the suspension pressure in RLRT, we have used Eqs. (7.7)-(7.9) that provide the same numerical results as Eq. (7.11) up to small numerical errors. Details of the RLRT calculation of $p$ can be found in Appendix C. The suspension pressure resulting from combining SDHA (see section 3.4) with the EPC charge-renormalization scheme is computed using the generalized virial equation in Eq. (7.11). The volume contribution, $p_{\mathrm{vol}}$, is obtained analytically in SDHA from the volume derivative of Eq. (3.59) by keeping the effective interaction parameters $Z_{\mathrm{eff}}$ and $\kappa_{\mathrm{eff}}$ and the linearization points, $\tilde{\rho}_{\pm}$, constant. This results in [56]

$$\beta p_{\mathrm{vol}} = \left(\frac{\partial \beta E_{\mathrm{vol}}}{\partial V}\right)_{N,T,\tilde{\rho}_{\pm}} = \frac{\kappa_{\mathrm{eff}}^2}{8\pi\lambda_{\mathrm{B}}}\left[\left(\frac{\kappa_{\mathrm{res}}}{\kappa_{\mathrm{eff}}}\right)^4 + 1\right], \tag{7.16}$$

for a suspension in osmotic equilibrium with a reservoir of microion pair concentration $2n_{\mathrm{res}}$. In the salt-free case where $\kappa_{\mathrm{res}} = 0$, this reduces to

$$\beta p_{\mathrm{vol}} = \frac{\kappa_{\mathrm{eff}}^2}{8\pi\lambda_{\mathrm{B}}}. \tag{7.17}$$

We have followed here [56] in holding the effective pair potential and the linearization point fixed when taking the volume derivative in Eq. (7.16). A thorough theoretical study [60] based on the linearized cell model came to the conclusion, that while treating the linearization points of the microion concentrations as volume-dependent in calculating $p$ is an admissible procedure, there are advantages in treating them as independent variables. In particular, in linear approximation $p$ remains always positive for a proper choice of the linearization point. It should be stressed that, when $p$ is determined in this way using the SDHA with EPC charge renormalization, the correct Debye-Hückel limiting law for $p$ is recovered to first order in $n_\mathrm{m}$ [117]. Notice that this procedure is equivalent to computing the suspension pressure using an equivalent pointlike macroion system by keeping the charge, $Q_\mathrm{eff}$ (see Eq. (3.9)), of pointlike macroions fixed and neglecting the density-dependence of $\kappa_\mathrm{eff}$ in $u_\mathrm{eff}(r)$.

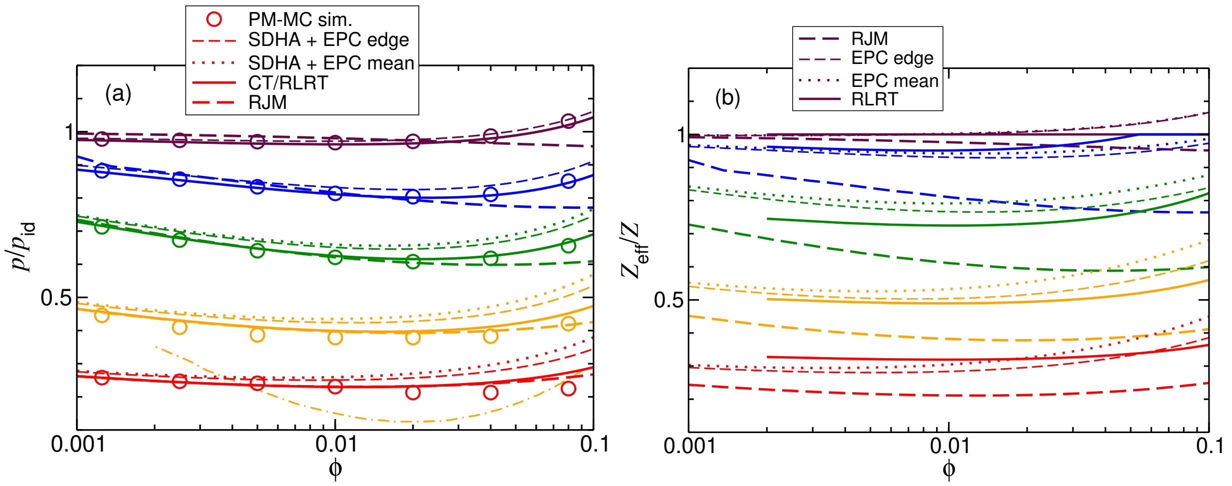

**Figure 7.11** (a) Reduced suspension pressure, $p/p_\mathrm{id}$, with $p_\mathrm{id} = n_\mathrm{m} k_\mathrm{B} T(1 + Z)$ and (b) reduced renormalized valence, $Z_\mathrm{eff}/Z$, versus $\phi$ for a salt-free system ($n_\mathrm{res} = 0$) and different couplings. Different colors label different couplings. From top to bottom: $Z\lambda_\mathrm{B}/a = 0.89$; 3.56; 7.12; 14.23; 28.46. The lines corresponds to different charge-renormalization schemes as indicated, while the circles are PM-MC simulation data [8]. In (a): For $Z\lambda_\mathrm{B}/a = 0.89$ and 3.56, EPC edge and EPC mean values practically overlap, thus only one curve is shown; the nonlinear CT pressure, $p_\mathrm{CT}$, is practically indistinguishable from RLRT; orange dashed-dotted line corresponds to (unrenormalized) LRT result for $Z\lambda_\mathrm{B}/a = 14.23$. Other system parameters: $Z = 40$, $\lambda_\mathrm{B} = 0.714$nm.

In Fig. 7.11, $p$ is normalized by $p_\mathrm{id}$, so that deviations from $p_\mathrm{id}$ due to pair interactions are revealed. Notice that $p$ is smaller than $p_{\mathrm{id}}$, except for low coupling values and large volume fractions, where charge renormalization ceases and the excluded-volume interaction begins to play a role. At given non-small coupling $Z\lambda_{\mathrm{B}}/a$, the reduced suspension pressure has a weakly non-monotonic $\phi$-dependence with a shallow minimum. At constant $\phi$, $p$ decreases with increasing $Z\lambda_{\mathrm{B}}/a$. From an analysis of the PM-MC results for $p$ in [8], it was found that the deviations of $p$ from $p_{\mathrm{id}}$ and its decrease with increasing coupling are related to the sctrong accumulation of counterions near the macroion surfaces. This reduces the number of free counterions making a full pressure contribution. As seen, $p/p_{\mathrm{id}}$ displays a minimum at $\phi \approx 0.03$, where the decrease in the reduced pressure due to enlarged electrostatic interaction with increasing $\phi$ is balanced by an increase in the excluded-volume contribution [8].

All considered effective one-component methods in Fig. 7.11 capture the PM-MC data for $p/p_{\mathrm{id}}$ quite well, except for $p_{\mathrm{jell}}$ (from RJM) at larger $\phi$. The similarity between the pressure and effective valence curves in Fig. 7.11(b) shows that, without salt, $p/p_{\mathrm{id}} \approx Z_{\mathrm{eff}}/Z$ holds for not too large values of $\phi$, as suggested by Eq. (7.14). In particular, note that the concentration value at the minimum of $p/p_{\mathrm{id}}$ roughly coincides with that of the minimum of $Z_{\mathrm{eff}}/Z$.

We recall here that the effective one-component macroion and charge-renormalization methods discussed in the thesis are all of mean-field type. The overall good agreement of these methods with the PM-MC pressure calculations suggests that the microion finite size and other correlation effects are thermodynamically negligible for the considered suspensions of monovalent microions. That charge renormalization has a significant influence on $p$ is seen from the comparison with calculations without an account for charge renormalization (cf. orange dash-dotted line in Fig. 7.11(a)). From comparing the different methods in more detail, one notices from Fig. 7.11 that the contact theorem and RLRT provide overall good approximations of the suspension pressure predicting nearly identical curves on the scale of Fig. 7.11(a). SDHA with EPC methods (edge and mean linearization) tend to overestimate $p$, particularly at large $\phi$ and for strong coupling. Since in SDHA-EPC the generalized virial expression, Eq. (7.11), for computing $p$ is used, for which the according $g(r)$ overestimates the pair structure for strong coupling (cf. Fig. 7.8(a)), it is apparent that the predicted $p$ is less accurate. On contrasting the different linearizations within SDHA-EPC, one notices that in mean linearization $p$ is larger than in edge linearization. This is understood from the effective valence predictions in Fig. 7.11(b), showing that $Z_{\text{eff}}^{\text{mean}} > Z_{\text{eff}}^{\text{edge}}$, expressing that counterion condensation is less pronounced for mean linearization. The strong effective coupling predicted in mean linearization implies that $p^{\text{mean}} > p^{\text{edge}}$. Even though RJM performs rather poorly in structure prediction, it predicts $p$ accurately at high coupling and mildly underestimates $p$ at low coupling and high concentrations. According to Eq. (7.14), this is due to the stronger condensation predictions.

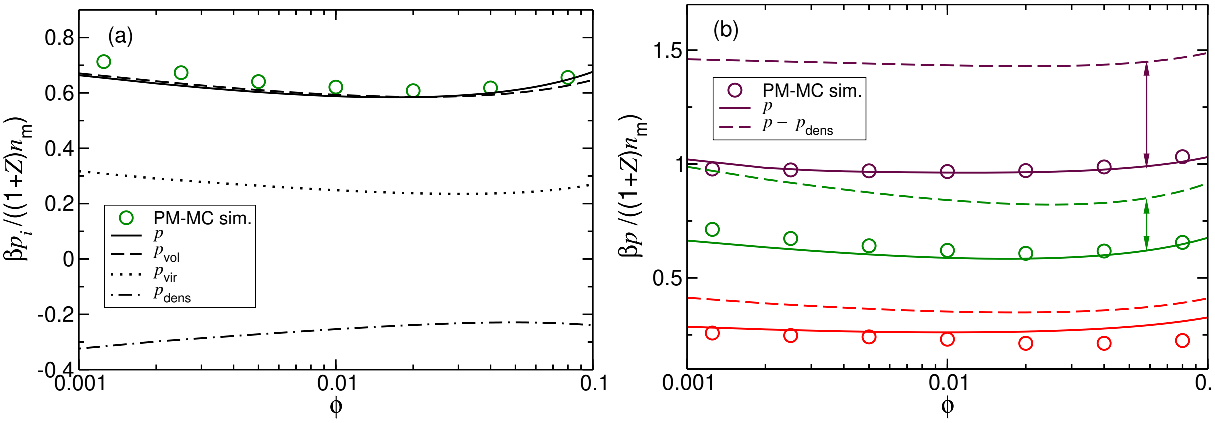

**Figure 7.12** (a) Reduced suspension pressure, $p/p_{\text{id}}$, and its additive constituents versus $\phi$ for $Z\lambda_{\text{B}}/a = 7.12$. (b) Reduced suspension pressure, $p$, and pressure difference $p - p_{\text{dens}}$, versus $\phi$ for different couplings; different colors correspond to different couplings: From top to bottom $Z\lambda_{\text{B}}/a = 0.89$, 7.12 and 28.46. In both (a) and (b), we consider a salt-free system, and the generalized virial theorem in Eq. (7.11) is used in combination with the RLRT charge renormalization scheme. Open circles correspond to PM-MC simulations [8]. Other system parameters are as in Fig. 7.11.

It is interesting to analyze how the different pressure contributions $p_i$ in the generalized virial equation, Eq. (7.11), contribute to the total suspension pressure $p$. We exemplify this for the RLRT, focusing in particular on the importance of the pressure contribution

$$\beta p_{\text{dens}} = 2\pi n_{\text{m}}^3 \int_0^\infty dr r^2 g(r) \frac{\partial \beta u_{\text{eff}}(r)}{\partial n_{\text{m}}}, \tag{7.18}$$

due to the macroion density derivative of $u_{\mathrm{eff}}$. Recall that this term is absent in the calculation of $p$ when implementing SDHA method. For this reason, we split $p$ accordingly to

$$p = p_{\mathrm{free}} + p_{\mathrm{OCM}} + p_{\mathrm{dens}} \tag{7.19}$$

where $p_{\mathrm{free}}$ is the pressure contribution from the volume energy term with renormalization included, Eq. (7.8), and $p_{\mathrm{OCM}}$ is the state-independent pressure contribution for an effective one-component macroion system with the state-dependence of $u_{\mathrm{eff}}(r)$ disregarded,

$$\beta p_{\mathrm{OCM}} = n_{\mathrm{m}} - \frac{2\pi}{3} n_{\mathrm{m}}^2 \int_0^\infty dr r^3 g(r) \frac{\partial \beta u_{\mathrm{eff}}(r)}{\partial r}. \tag{7.20}$$

Figure 7.12(a) shows the various RLRT-calculated pressure contributions for the most structured suspension treated in the PM-MC simulations. We observe that $p_{\mathrm{vol}}$ is the dominant contribution in the full considered concentration range for the free-salt suspension. Note further that $p_{\mathrm{dens}}$ is negative and practically compensates the positive contribution $p_{\mathrm{OCM}}$ for most $\phi$ values. At large $\phi$, the macroion-induced pressure contribution $p_{\mathrm{m}} = p_{\mathrm{OCM}} + p_{\mathrm{dens}}$ becomes non-negligibly positive valued. In fact, for $\phi > 0.1$, $p_{\mathrm{m}}$ contributes up to 20% to the total pressure.

Figure 7.12(b) quantifies the contribution of $p_{\mathrm{dens}}$ to $p$ for different indicated couplings. The RLRT method predicts a non-negligible (negative) contribution of $p_{\mathrm{dens}}$ to $p$ with a larger relative contribution for weaker coupling. Neglecting $p_{\mathrm{dens}}$ would result in a nonphysically large contribution of the macroion-induced pressure $p_{\mathrm{m}}$ at low $\phi$. At low $\phi$, $p$ is mainly given by the microions, and $p_{\mathrm{m}}$ is only a small correction of $\mathcal{O}(n_{\mathrm{m}})$.

The effects of adding salt for $p$ and its constituents is analyzed in Fig. 7.13. For low salt concentrations in the counterion-dominated regime ($\kappa_{\mathrm{res}} a \lesssim 1$), $p$ stays constant and is practically equal to the pressure of a salt-free system. With increasing reservoir salt concentration, $p$ grow monotonically, approaching the reservoir pressure $p_{\mathrm{res}} = 2k_{\mathrm{B}}Tn_{\mathrm{res}}$ in the salt-dominated regime, where the Donnan effect is absent and $Z_{\mathrm{eff}} \approx Z$ holds with $\kappa_{\mathrm{eff}} \approx \kappa_{\mathrm{res}}$. As noted before in the salt-free case, $p_{\mathrm{vol}}$ is the main contributor to $p$, approaching

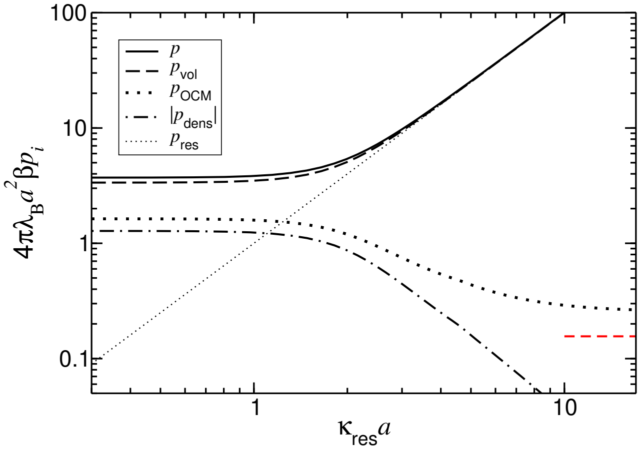

**Figure 7.13** Reduced suspension pressure, $4\pi\lambda_{\mathrm{B}}a^2\beta p$, and its additive constituents versus $\kappa_{\mathrm{res}}a$ ($\kappa_{\mathrm{res}}^2 \sim n_{\mathrm{res}}$) for $\phi = 0.2$. The pressure is calculated using the RLRT scheme. The red dashed line represents the pressure of a hard-sphere system, computed using the Carnahan-Starling equation of state at the same $\phi$. Other system parameters: $Z\lambda_{\mathrm{B}}/a = 7.12$, $Z = 40$, $\lambda_{\mathrm{B}} = 0.714$ nm.

$p_{\mathrm{res}} \approx p$ in the high-salinity limit. Although $p_{\mathrm{vol}}$ is dominant throughout in the counterion-dominated regime, $p_{\mathrm{m}} = p_{\mathrm{OCM}} + p_{\mathrm{dens}}$ gives a non-negligible positive contribution to $p$ visible even on the depicted logarithmic scale. It is seen in Fig. 7.13 that the negatively valued $p_{\mathrm{dens}}$ tends to compensate $p_{\mathrm{OCM}}$ for $\kappa_{\mathrm{res}}a \lesssim 1$. Similarly to $p$ and $p_{\mathrm{vol}}$, $p_{\mathrm{OCM}}$ and $p_{\mathrm{dens}}$ are constant in the low-salt region. With further increasing reservoir salinity, $p_{\mathrm{OCM}}$ tends to the hard-sphere pressure value (red dashed segment), while $p_{\mathrm{dens}}$ tends to zero.

In addition to the suspension pressure $p$, we have analyzed the osmotic compressibility, $\chi_{\mathrm{osm}}$, of the suspension as a second thermodynamic quantity of interest. It was discussed in section 5.2 that for a semi-open system in osmotic equilibrium with a microion reservoir, the osmotic compressibility factor, $\chi_{\mathrm{osm}}/\chi_{\mathrm{osm}}^{\mathrm{id}}$, is equal to the macroion-macroion static structure factor in the long wavelength limit, $S(q \to 0)$. Hence, the accuracy of the considered renormalization methods in predicting thermodynamic properties is linked to their respective accuracy on describing the pair structure. In Fig. 7.14(a), the RY-$S(0)$ obtained using $u_{\mathrm{eff}}(r)$ with EPC-mean input for $Z_{\mathrm{eff}}$ and $\kappa_{\mathrm{eff}}$ is plotted versus $\phi$ for different coupling parameters as indicated. At fixed coupling, $S(0)$ has a non-monotonic $\phi$ dependence with a maximum

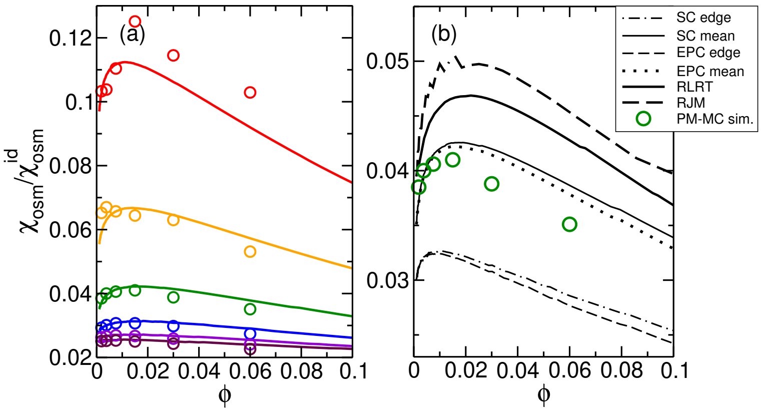

**Figure 7.14** (a) $\chi_{\mathrm{osm}}/\chi^{\mathrm{id}}_{\mathrm{osm}}$ versus $\phi$ for different coupling parameters using EPC-mean scheme. Different colors represent different coupling. From bottom to top: $Z\lambda_{\mathrm{B}}/a = 0.89$, 1.78, 3.56, 7.12, 14.23, 28.46. (b) $\chi_{\mathrm{osm}}/\chi^{\mathrm{id}}_{\mathrm{osm}}$ versus $\phi$ for different charge-renormalization schemes and $Z\lambda_{\mathrm{B}}/a = 7.12$. Circles are PM-MC results obtained from numerical derivative of the PM-MC pressure data in Fig. 7.11. Other system parameters as in Fig. 7.11.

at $\phi \approx 0.01$ for all considered cases. The position of this maximum approximately coincides with the concentration at which $Z_{\mathrm{eff}}$ has its minimum (cf. Fig. 7.11(b)). For fixed $\phi$, $S(0)$ increases with increasing coupling, i.e. the suspension becomes more compressible due to an accordingly decreasing $Z_{\mathrm{eff}}$. Figure 7.14(b) depicts $S(0)$ versus $\phi$ for different charge-renormalization schemes and fixed $Z\lambda_{\mathrm{B}}/a = 7.12$. Obviously, $S(0)$ is larger for the methods that predict stronger charge renormalization, i.e. smaller $Z_{\mathrm{eff}}$, except for the CM-based methods, where this tendency is reversed both for edge and mean linearizations.

The simulation data for $p$ from Fig. 7.11 [8] allows us to compute the compressibility factor from numerical differentiation according to Eq. (5.17). While the shape of $S(0)$ is qualitatively reproduced by the different methods including the location of the maximum, there are significant quantitative differences. The figure shows that the mean-linearization-based methods provide more accurate results for the osmotic compressibility factor than the ones invoking edge linearization.

In summary, we have shown that all considered renormalization schemes considerably improve the pressure predictions in the highly-coupling regime compared to calculations where charge renormalization is disregarded. The volume pressure gives the dominant contribution to $p$ under salt-free conditions, but the macroion-related part $p_{\mathrm{m}}$ is a non-negligible contribution at large macroion concentrations and for strong coupling. Although the accounted mean-field charge renormalization improves the pair structure description for stronger-coupled suspensions, for values $Z\lambda_{\mathrm{B}}/a \gtrsim 15$ the peak height $S(q_{\mathrm{m}})$ is overestimated by all renormalization schemes. On the plus side, charge renormalization allows for calculating $p$ quite accurately within $\sim 5\%$ deviations for $Z\lambda_{\mathrm{B}}/a \approx 30$, which is due to the fact that $p_{\mathrm{vol}}$ gives the main pressure contribution.

The accuracy of the methods used to determine the osmotic compressibility via $S(0)$ is linked to their performance for the pair structure. As a consistency test, it will be interesting to compare osmotic compressibility predictions with charge renormalization based on alternative routes for calculating $\chi_{\mathrm{osm}}$. This is left to future work.

In summary, we have analyzed the concentration-derivative contribution, $p_{\mathrm{dens}}$, to $p$, whose incorporation is still controversially debated. Depending on the charge renormalization scheme, this contribution is accounted for [66] or neglected [56] in computing $p$ via the generalized virial equation Eq. (7.11). We have argued that the $n_{\mathrm{m}}$-depencence of $u_{\mathrm{eff}}(r)$ arising from charge renormalization must be distinguished from the thermodynamically-relevant $n_{\mathrm{m}}$-dependence. We found that neglecting $p_{\mathrm{dens}}$ in the RLRT calculation of $p_{\mathrm{m}}$ leads to a wrong prediction for $p$. However, an incorporation of $p_{\mathrm{dens}}$ into the SDHA scheme does violate the limiting pressure behavior for $n_{\mathrm{m}} \ll 1$ and low coupling, and it gives wrong pressure results at large concentrations. It is clear that the good agreement with PM-MC pressure data is per se not a convincing argument for the omission of $p_{\mathrm{dens}}$, since this could be an artifact caused by the approximation in the employed mean-field method. As another point of principle, we have provided quantitative evidence that supports the fact that mean linearization is a better option than the more frequently employed edge linearization. In addition to being more consistent from a general viewpoint, it gives accurate results both for thermodynamic and structural properties.

# Chapter Eight

# CONCLUSIONS AND OUTLOOK

In this thesis, we have presented a comprehensive theoretical study of charged-stabilized colloidal suspensions of soft and permeable spherical particles (ionic microgels) and of impermeable, rigid particles. Our focus was on the exploration of effective macroion (colloid) interactions with associated effective interaction parameters, and their consequential effects on structural, thermodynamic and transport properties of the suspensions. Mapping the multi-component suspension onto an effective one-component system of dressed macroions by means of different mean-field methods, including DFT-PB, LRT and a MSA-based OZ integral equation scheme, we have obtained semi-analytic expressions for the electrostatic contributions to the free energy, effective pair potential and pressure terms of permeable and impermeable macroion systems. We have considered colloidal macroions carrying different bare charge distributions: ion-impermeable colloids with surface or internal charges, namely charged silica particles, and homogeneously-charged ion-permeable colloids.

Using the PM-based MSA integral equation scheme [9], we have given an alternative derivation of the effective electrostatic pair potential of ion-permeable colloids. This derivation is straightforward and fully analytical under linear MSA, and it offers the possibility to numerically obtain the effective interaction parameters accounting for nonlinear screening effects, by using the simple JA [9].

By taking advantage of the spherical PBCM approach of Denton and Tang [14] and the first-order TPT method of Weyer and Denton [15], based on a multi-center linear-response approach, we have combined the description of effective electrostatic interactions between ion-permeable colloids with a polymer network description, in order to model deswelling of microgel particles with uniform cross-linker distribution and uniform polymer backbone charge. Using these two methods, we thoroughly studied the influence of changing microgel concentration on deswelling, thermodynamics, structure, and dynamic properties of weakly cross-linked, ionic microgels suspended in a good polar solvent and being in osmotic equilibrium with a 1:1 electrolyte reservoir. We have assessed the respective pros and cons of the implemented PCBM and TPT methods by calculating microion density profiles, and single-particle and bulk osmotic pressures, and the state-dependent swelling ratios. Moreover, we consistently combined the results by these methods with our calculations of the net microgel valence, $Z_{\text{net}}$, and Debye screening constant, $\kappa$, characterizing the electrostatic part of the effective one-component microgel pair potential derived from LRT. On basis of the effective one-component model of microion-dressed microgels, we determined static structural properties, including $S(q)$ and $g(r)$, by implementing the self-consistent Rogers-Young integral equation method, and we used these structure functions as input to our calculations of dynamic suspension properties, with the salient hydrodynamic interactions included.

At salt concentrations large enough that salt ions dominate the electrostatic screening, the microion distributions inside and outside the microgels are rather uniform and the counterion-induced deswelling is consequently a weak effect. Therefore, our study focused on the counterion-dominated regime, where salt and microgel concentrations are low enough and microgel valences high enough that deswelling is pronounced even without particle overlap.

The TPT method neglects nonlinear electrostatic effects, but accounts for inter-microgel correlations. In contrast, the PBCM method accounts for nonlinear screening by mobile microions, but neglects inter-microgel correlations, except for the remnant concentration dependence of the cell radius. Unlike impermeable surface-charged colloidal particles, ionic microgels are characterized by electrostatic interactions whose strength, as measured at mutual contact, increases with decreasing microgel concentration. This behavior restricts the applicability of the TPT method to nonvanishing microgel concentrations.

While both methods predict the same trends for the effective microgel pair potential, there are quantitative differences in the swelling ratio, net valence, and interaction potential value at contact, whose values are in general higher in TPT than in PBCM. In the counterion-dominated regime, the range $1/\kappa$ of the electrostatic repulsion is equal in both methods. The greatest differences in the pair potential parameters occur at very low concentrations and high backbone valences, which can be partially attributed to the linear-response approximation inherent in the TPT. The relative variation in the microgel radius with changing microgel concentration is less pronounced in PBCM, whose account of nonlinear response confines the counterions more strongly to the microgel interior.

Differences in the predictions of the TPT and PBCM methods are more pronounced for static (i.e., thermodynamic and structural) properties than for dynamic ones, which is explained by the fact that dynamic properties depend only globally (i.e., functionally) on $S(q)$. The only exception is the collective diffusion coefficient, $d_{\mathrm{c}}$, which is directly proportional to the inverse of the static compressibility factor.

Owing to the dominance of the electrostatic interactions in the considered microgel systems, their dynamic behavior resembles that of charged-stabilized suspensions of impermeable solid particles. In particular, the peak, $H(q_{\mathrm{m}})$, of the hydrodynamic function has a non-monotonic concentration dependence, with a maximum higher than one for intermediate concentrations, reflected in a concomitant inflection point of the cage diffusion coefficient. The collective diffusion coefficient, $d_{\mathrm{c}}$, behaves likewise non-monotonically and has a maximum at the same concentration as $H(q_{\mathrm{m}})$. This maximum was shown to arise from the slowing effect of HIs, which becomes more influential with increasing concentration. The electric repulsion between the microgels distinctly enhances the zero-frequency viscosity at higher concentrations, as compared to suspensions of uncharged particles.

Our comparison with the corresponding results for a reference system of constant-sized microgels revealed that the major influence of deswelling on structural and dynamic properties is via the reduced volume fraction $\phi$, which grows only sublinearly with increasing concentration. The effect of counterion-induced deswelling on structural and dynamic properties is overall quite weak, for valences where nonlinear electrostatic contributions to the microion distributions are negligible, and changes of $\alpha = a(\phi_0)/a_0$ with concentration are accordingly small.

At higher concentrations, deswelling slightly enhances $S(0)$ and the hydrodynamic function $H(q)$ for all wavenumbers $q$. Deswelling reduces the zero- and high-frequency viscosity and slightly enhances collective diffusion. From the relation $d_{\mathrm{c}} = d_0 H(0)/S(0)$, one notices that the deswelling-induced enhancement of $d_0 \propto 1/a$ is nearly counterbalanced by the accompanying de-enhancement of $H(0)/S(0)$.

The most pronounced effect of deswelling is to shift the freezing (crystallization) transition to higher concentration values, as we have determined from an empirical freezing rule for the static structure factor peak height. This concentration shift is more pronounced for strongly charged microgels, in which case the nonlinear PBCM method can still be used to determine the swelling ratio $\alpha$. To determine the concentration shift, however, the PBCM must be combined with a charge renormalization procedure to determine renormalized values of the microgel net valence and screening constant from a linearized Poisson-Boltzmann equation in the cell model. The renormalized parameters are used in the linear-response pair potential (Eq. (2.61)), where they summarily account for the enhanced accumulation of counterions inside and close to the spherical backbone region. We have illustrated such a renormalization procedure using a linearization of the nonlinear PB equation around the potential at the cell boundary. While such a linearization is most commonly used in renormalization schemes applied to impermeable and permeable colloidal particles, it is not the only choice. As discussed, there are sound reasons to use instead a linearization around the mean (i.e., cell-volume-averaged) electrostatic potential value [57, 118].

For charge-stabilized suspensions of ion-impermeable, rigid colloids, we have assessed the pros and cons of different mean-field charge-renormalization schemes, which are applicable to suspensions with purely monovalent microions and larger macroion/microion size ratios. The evaluation has been done by the comparison with PM-MC simulation results of structural and thermodynamic properties of salt-free suspensions by [8]. In computing thermodynamic properties such as the suspension pressure and osmotic compressibility, we have also tested different prescriptions that the various renormalization methods provide for computing each of them.

The employed charge renormalization methods can be split into two groups depending on the invoked potential linearization: First, into edge linearization, for CM-based methods using linearization with respect to the electric potential value at the cell edge and for RJM using linearization with respect to the asymptotic value of the electric potential; and second, into mean linearization, for CM-based methods and RLRT, where the potential is linearized around the mean (volume-averaged) value. From analyzing the resulting effective interaction parameters, we have found that there is a clear distinction between the renormalized screening parameter based on edge and mean linearization according to $\kappa_{\text{eff}}(\text{mean}) > \kappa_{\text{eff}}(\text{edge})$ for most of the methods. Such a clear distinction, however, is not observed for the renormalized valence.

In analyzing the effect of adding salt on the renormalized interaction parameters, we detected that the largest differences between the renormalization schemes is for low salt concentrations in the counterion-dominated regime. As expected, the addition of salt attenuates the existing differences. While in the explored parameter space most of the renormalization methods predict effective interaction parameters in rather close agreement, RJM predicts remarkably smaller values of $Z_{\text{eff}}$ and $\kappa_{\text{eff}}$ than all the other methods. Consequently, RJM predicts a distinctly stronger counterion quasi-condensation on the colloid surfaces.

Interestingly, the EPC method predicts an effective valence, $Z_{\text{eff}}$, larger than the bare one, $Z$, for low coupling values and large concentrations. The PM-MSA and penetrating-JA results for $Z_{\text{eff}}$ also reproduce this high-concentration effect which, according to the PM-MSA, can be attributed to the reduced electrostatic screening caused by the excluded volume of nearby colloids. The prediction of $Z_{\text{eff}} > Z$ gives rise to an improved estimation of $g(r_{\text{m}})$ in comparison with PM-MC data [56].

In comparing the RY $g(r)$ and $S(q)$ with the PM-MC simulation results, we found a considerable improved agreement for high coupling values, $5 \lesssim Z\lambda_{\text{B}}/a \lesssim 30$, when charge renormalization is accounted for. Most of the considered charge-renormalization methods predict $g(r_{\text{m}})$ with an error of less than 5% for $Z\lambda_{\text{B}}/a < 15$, and an error of less than 10% for $Z\lambda_{\text{B}}/a < 30$. Regarding RJM that predicts a noticeable stronger condensation, RY-$g(r_{\text{m}})$ values with an error of less than 10% are found for the high coupling condition $Z\lambda_{\text{B}}/a > 5$.

According to what is observed for the renormalized interaction parameters, major differences in the structure functions are detected in the counterion-dominated regime. All charge renormalization methods give the correct hard-sphere limit at high salt concentrations.

The performance of the various renormalization methods for predicting thermodynamic properties was assessed by calculating the suspension pressure $p$ with its constituents and the osmotic compressibility $\chi_{\text{osm}}$. Our analysis shows that nonlinear electrostatic effects become relevant for coupling values $Z\lambda_{\text{B}}/a > 5$, in accordance with our findings for the structure properties.

We analyzed different prescriptions for computing the suspension pressure. In particular, we have analyzed the pair-potential density-derivative contribution, $p_{\text{dens}}$, to the macroion-related pressure contribution, $p_{\text{m}}$, whose incorporation is to some extent controversial. Depending on the invoked renormalization scheme, this contribution is accounted for or neglected when computing $p$ via the generalized virial equation, Eq. (7.11). We have discussed how the $n_{\text{m}}$-dependence of $u_{\text{eff}}(r; n_{\text{m}})$ should be interpreted: The density dependence of $u_{\text{eff}}$ arising from a charge renormalization procedure must be distinguished from the thermodynamically relevant one in the calculation of the suspension pressure. From the analysis of the RLRT method, we showed that $p_{\text{dens}}$ makes an important contribution to $p$. In contrast, the account of $p_{\text{dens}}$ in the SDHA scheme would violate the correct limiting-law behavior for

$p$ at $n_\mathrm{m} \ll 1$. Hence, $p_\mathrm{dens}$ is not included in the SDHA-based pressure.

Different from structural properties where the predictions by the various renormalization schemes start to deviate form the PM-MC results for $Z\lambda_\mathrm{B}/a \gtrsim 15$, the according predictions for $p$ are valid to good accuracy (i.e. 5%) even up to $Z\lambda_\mathrm{B}/a \approx 30$. This is explained by the fact that $p_\mathrm{vol}$ gives the major contribution to $p$.

Regarding the overall performance of the considered renormalization methods, the following comments are in order. The CM-SC method with edge linearization is most widely used for impermeable colloids due to its simplicity and easy implementation. The usage of the spherical CM approximation has the extra advantage to allow for estimating $p$ using the contact theorem. However, implementing mean linearization instead is not only conceptually preferable, as reported in [57], but it also leads to improved results of $g(r)$ and $S(q)$. Implementing this alternative linearization simply demands an extra integration step for computing the mean potential value without requiring any further modification in the numerical integration of the nonlinear PB equation. The SDHA combined with the EPC scheme from CM approximation provides the most accurate structural description at low coupling and high concentrations, where it correctly predicts $Z_\mathrm{eff} > Z$. This method is as easy to implement as the pure CM, but its validity additionally extends to high concentrations and salinities by using, e.g., the generalized virial theorem for pressure calculation. In this parameter range inter-colloid correlations become relevant and the contact theorem prediction for $p$ becomes poor. The originator of the RJM have argued [64] that the renormalized valence predicted by this method is more appropriate than that from CM-based calculations, since the DLVO-type $u_\mathrm{eff}(r)$ arises naturally within JA by integrating, for instance, the electrostatic stress tensor over the colloid surfaces [2, 36]. Despite this fact, we showed that the RJM significantly underestimates the pair structure in comparison with the PM-MC simulation data for $g(r)$. However, it accurately predicts the suspension pressure in a wide range of colloid concentrations. In our study, RLRT has proven to be overall quite accurate both regarding structural and thermodynamic properties. Different from the other considered methods, its renormalization mechanism relies on a thermodynamic argument and offers a clear picture of the phenomenology behind charge renormalization. While its implementation is more laborious, it provides an expression for the suspension free energy that includes the inter-colloid interactions.

Finally, we give an outlook on future developments based on this thesis. As shown in [119], it is possible to synthesize spherical microgels with different internal backbone charge distributions as well as different polymer-chain backbone structures. Due to mutual electrostatic repulsion and mixing with the solvent molecules, the charged sites on the polymer backbones tend to be accumulated at the periphery of a microgel [105, 119]. Furthermore, the role of the macroion charge distribution results crucial for understanding the role of the electrostatic interactions in viral aggregation [120]. Viral capsids are usually modeled as ion-permeable charged shells in presence of water-dissolved salt ions [121, 122]. These examples have motivated us to explore effective electrostatic interactions for different internal macroion charge distributions of ion-permeable colloids using the accordingly-modified mean-field methods presented in chapter 2. Results for the limiting case of a $\delta$-like-shell charge distribution at the microgel periphery have been obtained already and will be communicated in a future publication [123]. Deriving $u_{\text{eff}}(r)$ for a surface or shell charge distribution allows to model viral capsids and microgel suspensions with an according microgel architecture. The resulting effective potential $u_{\text{eff}}(r)$ in combination with the PBCM and TPT methods for the equilibrium microgel size allow to quantify the concentration-dependent deswelling, which is stronger than in the uniformly charged case studied in this thesis. On basis of this thesis, one can also explore the applicability of the various charge-renormalization methods for suspension having different internal backbone charge distributions. An interesting task will be to extent the RLRT method to suspensions of strongly-charged, ion-permeable colloids with homogeneous and inhomogeneous internal charge distributions, with the prospect to gain a clearer picture of nonlinear screening effects. An alternative way of incorporating nonlinear screening effects, applicable both to ion-permeable and impermeable macroions, is the derivation of $u_{\text{eff}}(r)$ by means of an effective macroion direct correlation function, $c_{\text{eff}}(r)$, using multi-species integral equation schemes such as the MSA in section 2.4. Following the procedure in [9], nonlinear effects can be incorporated using HNC instead of MSA closure. In this thesis, we have exemplified such a derivation by applying the MSA to ion-permeable colloids with a homogeneous charged distribution. The integral equation method can be extended to different radially-symmetric macroion charge distributions, allowing thus for an according analysis of structural and thermodynamic properties. This analysis can be the topic of future work.

The thesis has been focused on truly charged-stabilized systems, where particle overlap is very unlikely. For micellar and protein solutions as well as for microgel suspensions, it could be rewarding to explore conditions where the softness and elasticity of the particles matter. In case of weakly overlapping microgels, a Hertz potential can be used to account for elasticity effects.

In conclusion, the bottom-up methods presented in this thesis constitute a versatile toolbox for efficiently calculating thermodynamic, structural and dynamic properties of suspensions of permeable and impermeable charged particles. This toolbox is useful not only for the analysis of scattering and rheological data, but also for the optimization of technologically relevant processes such as pressure-driven filtration of dispersions [85, 124]. The present work allows to extend the modeling of ultrafiltration process [124] to protein solutions and to ionic microgel suspensions. Work on this extension is in progress.

# REFERENCES

[1] C. N. Likos, "Effective interactions in soft condensed matter physics", Phys. Rep. **348**, 267–439 (2001).

[2] W. B. Russel, D. A. Saville, and W. R. Schowalter, *Colloidal dispersions* (Cambridge University Press, 1995).

[3] B. Berne and R. Pecora, *Dynamic light scattering* (Dover Publications, 2000).

[4] J. C. Crocker and D. G. Grier, "Methods of digital video microscopy for colloidal studies", J. Colloid Interface Sci. **179**, 298–310 (1996).

[5] G. Nägele, "On the dynamics and structure of charge-stabilized suspensions", Phys. Rep. **272**, 215–372 (1996).

[6] J.-P. Hansen and H. Löwen, "Effective interactions between electric double layers", Annu. Rev. Phys. Chem. **51**, 209 (2000).

[7] P. Holmqvist, P. S. Mohanty, G. Nägele, P. Schurtenberger, and M. Heinen, "Structure and dynamics of loosely cross-linked ionic microgel dispersions in the fluid regime", Phys. Rev. Lett. **109**, 048302 (2012).

[8] P. Linse, "Structure, phase stability, and thermodynamics in charged colloidal solutions", J. Chem. Phys. **113**, 4359 (2000).

[9] B. Beresford-Smith, D. Y. Chan, and D. J. Mitchell, "The electrostatic interaction in colloidal systems with low added electrolyte", J. Colloid Interface Sci. **105**, 216–234 (1985).

[10] A. R. Denton, "Counterion penetration and effective electrostatic interactions in solutions of polyelectrolyte stars and microgels", Phys. Rev. E **67**, 011804 (2003).

[11] D. Gottwald, C. N. Likos, G. Kahl, and H. Löwen, "Ionic microgels as model systems for colloids with an ultrasoft electrosteric repulsion : Structure and thermodynamics", J. Appl. Cryst. **122**, 074903 (2005).

[12] J. Riest, P. S. Mohanty, P. Schurtenberger, and C. N. Likos, "Coarse-graining of ionic microgels: Theory and experiment", Z. Phys. Chem. **226**, 711–735 (2012).

[13] M. M. Hedrick, J. K. Chung, and A. R. Denton, “Structure and osmotic pressure of ionic microgel dispersions”, J. Chem. Phys. **142**, 034904 (2015).

[14] A. R. Denton and Q. Tang, “Counterion-induced swelling of ionic microgels”, J. Chem. Phys. **145**, 164901 (2016).

[15] T. J. Weyer and A. R. Denton, “Concentration-dependent swelling and structure of ionic microgels: simulation and theory of a coarse-grained model”, Soft Matter **14**, 4530–4540 (2018).

[16] P. J. Flory and J. Rehner, “Statistical mechanics of cross-linked polymer networks I. Rubberlike elasticity”, J. Chem. Phys. **11**, 512–520 (1943).

[17] P. J. Flory and J. Rehner, “Statistical mechanics of cross-linked polymer networks II. Swelling”, J. Chem. Phys. **11**, 521–526 (1943).

[18] P. J. Flory, *Principles of polymer chemistry* (Cornell University Press, 1953).

[19] J.-P. Hansen and I. R. McDonald, *Theory of simple liquids* (Elsevier, 2013).

[20] J. Gapinski, A. Wilk, A. Patkowski, W. Häußler, A. J. Banchio, R. Pecora, and G. Nägele, “Diffusion and microstructural properties of solutions of charged nanosized proteins: Experiment versus theory”, J. Chem. Phys. **123**, 054708 (2005).

[21] A. J. Banchio and G. Nägele, “Short-time transport properties in dense suspensions: From neutral to charge-stabilized colloidal spheres”, J. Chem. Phys. **128**, 104903 (2008).

[22] M. Heinen, F. Zanini, F. Roosen-Runge, D. Fedunová, F. Zhang, M. Hennig, T. Seydel, R. Schweins, M. Sztucki, M. Antalík, F. Schreiber, and G. Nägele, “Viscosity and diffusion: crowding and salt effects in protein solutions”, Soft Matter **8**, 1404–1419 (2012).

[23] F. Westermeier, B. Fischer, W. Roseker, G. Grübel, G. Nägele, and M. Heinen, “Structure and short-time dynamics in concentrated suspensions of charged colloids”, J. Chem. Phys. **137**, 114504 (2012).

[24] J. Riest, T. Eckert, W. Richtering, and G. Nägele, “Dynamics of suspensions of hydrodynamically structured particles: analytic theory and applications to experiments”, Soft Matter **11**, 2821–2843 (2015).

[25] F. Fahrenberger, Z. Xu, and C. Holm, “Simulation of electric double layers around charged colloids in aqueous solution of variable permittivity”, J. Chem. Phys. **141**, 064902 (2014).

[26] A.-P. Hynninen and M. Dijkstra, “Melting line of charged colloids from primitive model simulations”, J. Chem. Phys. **123**, 244902 (2005).

[27] E. Allahyarov and H. Löwen, “Nonadditivity in the effective interactions of binary charged colloidal suspensions”, J. Phys.: Condens. Matter **21**, 424117 (2009).

[28] R. Castañeda-Priego, V. Lobaskin, J. C. Mixteco-Sanchez, L. F. Rojas-Ochoa, and P. Linse, “On the calculation of the structure of charge-stabilized colloidal dispersions using density-dependent potentials”, J. Phys.: Condens. Matter **24** (2012).

[29] M. Heinen, E. Allahyarov, and H. Löwen, “Highly asymmetric electrolytes in the primitive model: Hypernetted chain solution in arbitrary spatial dimensions”, J. Comput. Chem. **35**, 275–289 (2014).

[30] A. R. Denton, “Effective interactions in soft materials”, in *Nanostructured soft matter: Experiment, theory, simulation and perspectives*, edited by A. V. Zvelindovsky (Springer, Berlin, 2007), pp. 395–433.

[31] M. Dijkstra, R. van Roij, and R. Evans, “Phase diagram of highly asymmetric binary hard-sphere mixtures”, Phys. Rev. E **59**, 5744–5771 (1999).

[32] R. van Roij, M. Dijkstra, and J. P. Hansen, “Phase diagram of charge-stabilized colloidal suspensions: van der Waals instability without attractive forces”, Phys. Rev. E **59**, 2010–2025 (1999).

[33] A. R. Denton, “Effective interactions and volume energies in charged colloids: Linear response theory”, Phys. Rev. E **62**, 3855–3864 (2000).

[34] R. Messina, C. Holm, and K. Kremer, “Strong attraction between charged spheres due to metastable ionized states”, Phys. Rev. Lett. **85**, 872–875 (2000).

[35] E. Gonzales-Tovar, M. Lozada-Cassou, and D. Henderson, “Hypernetted chain approximation for the distribution of ions around a cylindrical electrode. II. Numerical solution for a model cylindrical polyelectrolyte”, J. Chem. Phys. **83**, 361–372 (1985).

[36] Y. Levin, “Electrostatic correlations: from plasma to biology”, Rep. Prog. Phys. **65**, 1577–1632 (2002).

[37] C. Russ, M. Brunner, C. Bechinger, and H. H. von Grünberg, “Three-body forces at work: Three-body potentials derived from triplet correlations in colloidal suspensions”, Europhys. Lett. **69**, 468–474 (2005).

[38] A. Torres, A. Cuetos, M. Dijkstra, and R. van Roij, “Breakdown of the Yukawa model in de-ionized colloidal suspensions”, Phys. Rev. E **77**, 031402 (2008).

[39] L. Belloni, “Colloidal interactions”, J. Phys.: Condens. Matter **12**, R549–R587 (2000).

[40] R. Van Roij and J.-P. Hansen, “Van der Waals-like instability in suspensions of mutually repelling charged colloids”, Phys. Rev. Lett. **79**, 3082–3085 (1997).

[41] G. Nägele, “Dynamics of charged-particles dispersions”, in *5th Warsaw school of statistical physics*, edited by B. Cichocki, M. Napiórkowski, and J. Piasecki (Warsaw University Press, Warsaw, 2013).

[42] A. R. Denton, “Coarse-grained modeling of charged colloidal suspensions: From Poisson-Boltzmann theory to effective interactions”, in *Electrostatics of soft and disordered matter*, edited by D. S. Dean, J. Dobnikar, A. Naji, and R. Podgornik (Pan Stanford, Singapore, 2014), pp. 201–215.

[43] R. A. Marcus, “Calculation of thermodynamic properties of polyelectrolytes”, J. Chem. Phys. **23**, 1057–1068 (1955).

[44] A. R. Denton, “Phase separation in charge-stabilized colloidal suspensions : Influence of nonlinear screening”, Phys. Rev. E **73**, 041407 (2006).

[45] B. Lu and A. R. Denton, “Phase separation of charge-stabilized colloids: A Gibbs ensemble Monte Carlo simulation study”, Phys. Rev. E **75**, 061403 (2007).

[46] W. Olivares and D. A. McQuarrie, “A variational approach to the theory of ionic solutions”, J. Chem. Phys. **65**, 3604–3610 (1976).

[47] R. Piron and T. Blenski, “Simpler free-energy functional of the Debye-Hückel model of fluids and the nonuniqueness of free-energy functionals in the theory of fluids”, Phys. Rev. E **99**, 052134 (2019).

[48] L. Belloni, “Electrostatic interactions in colloidal solutions: Comparison between primitive and one-component models”, J. Chem. Phys. **85**, 519–526 (1986).

[49] H. Ruiz-Estrada, M. Medina-Noyola, and G. Nägele, “Rescaled mean spherical approximation for colloidal mixtures”, Physica A **168**, 919–941 (1990).

[50] L. Blum and J. S. Høye, “Mean spherical model for asymmetric electrolytes. 2. Thermodynamic properties and the pair correlation function”, J. Phys. Chem. **81**, 1311–1316 (1977).

[51] J.-P. Simonin and L. Blum, “Departures from ideality in pure ionic solutions using the mean spherical approximation”, J. Chem. Soc., Faraday Trans. **92**, 1533–1536 (1996).

[52] J.-P. Hansen and J. B. Hayter, “A rescaled MSA structure factor for dilute charged colloidal dispersions”, Mol. Phys. **46**, 651–656 (1982).

[53] M. Heinen, P. Holmqvist, A. J. Banchio, and G. Nägele, “Pair structure of the hard-sphere Yukawa fluid : An improved analytic method versus simulations , Rogers-Young scheme , and experiment”, J. Chem. Phys. **134**, 044532 (2011).

[54] T. E. Colla, Y. Levin, and E. Trizac, “A self-consistent renormalized jellium approach for calculating structural and thermodynamic properties of charge stabilized colloidal suspensions”, J. Chem. Phys. **131**, 074115 (2009).

[55] S. Alexander, P. M. Chaikin, P. Grant, G. J. Morales, P. Pincus, and D. Hone, “Charge renormalization, osmotic pressure, and bulk modulus of colloidal crystals: Theory”, J. Chem. Phys. **80**, 5776–5781 (1984).

[56]N. Boon, G. I. Guerrero-García, R. van Roij, and M. Olvera de la Cruz, “Effective charges and virial pressure of concentrated macroion solutions”, Proc. Natl. Acad. Sci. **112**, 9242–9246 (2015).

[57]E. Trizac, L. Bocquet, M. Aubouy, and H. H. von Grünberg, “Alexander’s prescription for colloidal charge renormalization”, Langmuir **19**, 4027–4033 (2003).

[58]E. Trizac, M. Aubouy, and L. Bocquet, “Analytical estimation of effective charges at saturation in Poisson-Boltzmann cell models”, J. Phys.: Condens. Matter **15**, S291–S296 (2002).

[59]M. Aubouy, E. Trizac, and L. Bocquet, “Effective charge versus bare charge: An analytical estimate for colloids in the infinite dilution limit”, J. Phys. A: Math. Gen. **36**, 5835–5840 (2003).

[60]M. Deserno and H. H. von Grünberg, “Osmotic pressure of charged colloidal suspensions: a unified approach to linearized Poisson-Boltzmann theory”, Phys. Rev. E **66**, 011401 (2002).

[61]E. Ruiz-Reina and F. Carrique, “Electric double layer of spherical particles in salt-free concentrated suspensions: Water dissociation and CO2 influence”, J. Phys. Chem. B **112**, 11960–11967 (2008).

[62]T. Colla, C. N. Likos, and Y. Levin, “Equilibrium properties of charged microgels: A Poisson-Boltzmann-Flory approach”, J. Chem. Phys. **141**, 234902 (2014).

[63]S. Pianegonda, E. Trizac, and Y. Levin, “The renormalized jellium model for spherical and cylindrical colloids”, J. Chem. Phys. **126**, 014702 (2007).

[64]E. Trizac and Y. Levin, “Renormalized jellium model for charge-stabilized colloidal suspensions”, Phys. Rev. E **69**, 031403 (2004).

[65]A. R. Denton, “Charge renormalization, effective interactions, and thermodynamics of deionized colloidal suspensions”, J. Phys.: Condens. Matter **20**, 494230 (2008).

[66]B. Lu and A. R. Denton, “Charge renormalization, thermodynamics, and structure of deionized colloidal suspensions”, Commun. Comput. Phys. **7**, 235–249 (2010).

[67]A. R. Denton, “Poisson–Boltzmann theory of charged colloids: limits of the cell model for salty suspensions”, J. Phys.: Condens. Matter **22**, 364108 (2010).

[68]J. C. Pàmies, A. Cacciuto, and D. Frenkel, “Phase diagram of hertzian spheres”, J. Chem. Phys. **131**, 044514 (2009).

[69]L. D. Landau and E. M. Lifschitz, *Theory of elasticity* (Elsevier, 1986).

[70]D. Paloli, P. S. Mohanty, J. J. Crassous, E. Zaccarelli, and P. Schurtenberger, “Fluid-solid transitions in soft-repulsive colloids”, Soft Matter **9**, 3000 (2013).

[71] P. S. Mohanty, D. Paloli, J. J. Crassous, E. Zaccarelli, and P. Schurtenberger, "Effective interactions between soft-repulsive colloids: Experiments, theory, and simulations", J. Chem. Phys. **140**, 094901 (2014).

[72] M. Urich and A. R. Denton, "Swelling, structure, and phase stability of compressible microgels Matthew", Soft Matter **12**, 9086–9094 (2016).

[73] L. Rovigatti, N. Gnan, A. Ninarello, and E. Zaccarelli, "Connecting elasticity and effective interactions of neutral microgels: The validity of the Hertzian model", Macromolecules **52**, 4895–4906 (2019).

[74] M. J. Bergman, N. Gnan, M. Obiols-Rabasa, J. M. Meijer, L. Rovigatti, E. Zaccarelli, and P. Schurtenberger, "A new look at effective interactions between microgel particles", Nat. Commun. **9**, 5039 (2018).

[75] M. Rubinstein and R. H. Colby, *Polymer physics* (Oxford University Press, 2003).

[76] N. Hoffmann, C. N. Likos, and H. Löwen, "Structure and phase behavior of polyelectrolyte star solutions", J. Chem. Phys. **121**, 7009 (2004).

[77] D. Henderson, "Analytic methods for the Percus-Yevick hard sphere correlation functions", Condens. Matter Phys. **12**, 127–135 (2009).

[78] G. Nägele, *The physics of colloidal soft matter* (Polish Academy of Science Publishing, 2004).

[79] G. Nägele, "Theories of fluid microstructures", in *Soft Matter: From synthetic to biological materials*, Vol. 31, Key Technologies (Forschungszentrum Jülich Publishing, Jülich, 2008).

[80] N. W. Ashcroft and D. C. Langreth, "Structure of binary liquid mixtures. I", Phys. Rev. **156**, 685–692 (1967).

[81] M. E. Brito, A. R. Denton, and G. Nägele, "Modeling deswelling, thermodynamics, structure, and dynamics in ionic microgel suspensions", J. Chem. Phys. **151**, 224901 (2019).

[82] A. A. Louis, "Beware of density dependent pair potentials", J. Phys.: Condens. Matter **14**, 9187–9206 (2002).

[83] H. Wennerstrom, B. Jonsson, and P. Linse, "The cell model for polyelectrolyte systems. Exact statistical mechanical relations, Monte Carlo simulations, and the Poisson–Boltzmann approximation", J. Chem. Phys. **76**, 4665 (1982).

[84] J. Dobnikar, R. Castañeda-Priego, H. H. von Grünberg, and E. Trizac, "Testing the relevance of effective interaction potentials between highly-charged colloids in suspension", New J. Phys. **8** (2006).

[85] R. Roa, D. Menne, J. Riest, P. Buzatu, E. K. Zholkovskiy, J. K. G. Dhont, M. Wessling, and G. Nägele, "Ultrafiltration of charge-stabilized dispersions at low salinity", Soft Matter **12**, 4638–4653 (2016).

[86] J. G. Kirkwood and F. P. Buff, "The statistical mechanical theory of solutions. I", J. Chem. Phys. **19**, 774 (1951).

[87] R. L. Henderson, "A uniqueness theorem for fluid pair correlation functions", Phys. Lett. A **49**, 197–198 (1974).

[88] L. S. Ornstein and F. Zernike, "Accidental deviations of density and opalescence at the critical point of a single substance", Proc. Akad. Sci. (Amsterdam) **17**, 793–806 (1914).

[89] C. N. Likos, "Colloidal interactions: From effective potentials to structure", Riv. del Nuovo Cim. **37**, 125–180 (2014).

[90] L. Verlet and J.-J. Weis, "Equilibrium theory of simple liquids", Phys. Rev. A **5**, 939–952 (1972).

[91] A. Santos, "Playing with marbels: Structural and thermodynamic properties of hard-sphere systems", in *5th Warsaw school of statistical physics*, edited by B. Cichocki, M. Napiórkowski, and J. Piasecki (Warsaw University Press, Warsaw, 2013).

[92] F. J. Rogers and D. A. Young, "New, thermodynamically consistent, integral equation for simple fluids", Phys. Rev. A **30**, 999–1007 (1984).

[93] H. Löwen, T. Palberg, and R. Simon, "Dynamical criterion for freezing of colloidal liquids", Phys. Rev. Lett. **70**, 1557–1560 (1993).

[94] G. Nägele, M. Kollmann, R. Pesché, and A. J. Banchio, "Dynamic properties, scaling and related freezing criteria of two- and three-dimensional colloidal suspensions", Molecular Physics **100**, 2921–2933 (2002).

[95] G. Nägele, "Colloidal hydrodynamics", in *Physics of complex colloids*, Vol. 184, edited by C. Bechinger, F. Sciortino, and P. Ziherl, Proceedings of the International School of Physics "Enrico Fermi" (2013).

[96] J. K. Dhont, *An introduction to dynamics of colloids* (Elsevier, 1996).

[97] M. Heinen, A. J. Banchio, and G. Nägele, "Short-time rheology and diffusion in suspensions of Yukawa-type colloidal particles", J. Chem. Phys. **135**, 154504 (2011).

[98] G. Nägele and J. Bergenholtz, "Linear viscoelasticity of colloidal mixtures", J. Chem. Phys. **108**, 9893 (1998).

[99] A. J. Banchio, M. Heinen, P. Holmqvist, and G. Nägele, "Short- and long-time diffusion and dynamic scaling in suspensions of charged colloidal particles", J. Chem. Phys. **148**, 134902 (2018).

[100] A. Pamvouxoglou, P. Bogri, G. Nägele, K. Ohno, and G. Petekidis, “Structure and dynamics in suspensions of soft core-shell colloids in the fluid regime”, J. Chem. Phys. **151**, 024901 (2019).

[101] G. C. Abade, B. Cichocki, M. L. Ekiel-Jezewska, G. Nägele, and E. Wajnryb, “High-frequency viscosity of concentrated porous particles suspensions”, J. Chem. Phys. **133**, 084906 (2010).

[102] P. Szymczak and B. Cichocki, “A diagrammatic approach to response problems in composite systems”, J. Stat. Mech. **2008**, P01025 (2008).

[103] E. Wajnryb, P. Szymczak, and B. Cichocki, “Brownian dynamics: divergence of mobility tensor”, Physica A **335**, 339–358 (2004).

[104] S. Das, J. Riest, R. G. Winkler, G. Gompper, J. K. Dhont, and G. Nägele, “Clustering and dynamics of particles in dispersions with competing interactions: theory and simulation”, Soft Matter **14**, 92–103 (2018).

[105] M. Braibanti, C. Haro-Pérez, M. Quesada-Pérez, L. F. Rojas-Ochoa, and V. Trappe, “Impact of volume transition on the net charge of poly- N -isopropyl acrylamide microgels”, Phys. Rev. E **94**, 1–8 (2016).

[106] S. Nöjd, P. Holmqvist, N. Boon, M. Obiols-Rabasa, P. S. Mohanty, R. Schweins, and P. Schurtenberger, “Deswelling behaviour of ionic microgel particles from low to ultra-high densities”, Soft Matter **14**, 4150–4159 (2018).

[107] V. A. Baulin and E. Trizac, “Self-assembly of spherical interpolyelectrolyte complexes from oppositely charged polymers”, Soft Matter **8**, 6755–6766 (2012).

[108] L. A. Aguirre-Manzo, M. Ledesma-Motolinía, L. F. Rojas-Ochoa, V. Trappe, J. Callejas-Fernández, C. Haro-Pérez, and P. González-Mozuelos, “Accounting for effective interactions among charged microgels”, Phys. Rev. E **100**, 032602 (2019).

[109] J. Gapinski, G. Nägele, and A. Patkowski, “Freezing lines of colloidal Yukawa spheres. I. A Rogers-Young integral equation study”, J. Chem. Phys. **136**, 024507 (2012).

[110] J. Gapinski, G. Nägele, and A. Patkowski, “Freezing lines of colloidal Yukawa spheres . II. Local structure and characteristic lengths”, J. Chem. Phys. **141**, 124505 (2014).

[111] Y. Levin, A. Diehl, A. Fernández-Nieves, and A. Fernández-Barbero, “Thermodynamics of ionic microgels”, Phys. Rev. E **65**, 036143 (2002).

[112] A. Fernández-Nieves, H. Wyss, J. Mattsson, and D. A. Weitz, eds., *Microgel suspensions: fundamentals and applications* (Wiley-VCH Verlag GmbH & Co. KGaA, Weinheim, 2011).

[113] M. Heinen, P. Holmqvist, A. J. Banchio, and G. Nägele, “Short-time diffusion of charge-stabilized colloidal particles: generic features”, J. Appl. Cryst. **43**, 970–980 (2010).

[114] J. Gapinski, A. Patkowski, and G. Nägele, "Generic behavior of the hydrodynamic function of charged colloidal suspensions", J. Chem. Phys. **132**, 054510 (2010).

[115] L. Belloni, "Ionic condensation and charge renormalization in colloidal suspensions", Colloids Surfaces A: Physicochem. Eng. Aspects **140**, 227–243 (1998).

[116] A. J. Banchio, G. Nägele, and J. Bergenholtz, "Collective diffusion, self-diffusion and freezing criteria of colloidal suspensions", J. Chem. Phys. **113**, 3381–3396 (2000).

[117] N. Boon, private communication, 2018.

[118] M. Deserno and H. H. von Grünberg, "Osmotic pressure of charged colloidal suspensions: A unified approach to linearized Poisson-Boltzmann theory", Phys. Rev. E **66**, 011401 (2002).

[119] J. Zhou, J. Wei, T. Ngai, L. Wang, D. Zhu, and J. Shen, "Correlation between dielectric/electric properties and cross-linking/charge density distributions of thermally sensitive spherical PNIPAM microgels", Macromolecules **45**, 6158–6167 (2012).

[120] C. P. Gerba and W. Q. Betancourt, "Viral aggregation: Impact on virus behavior in the environment", Environ. Sci. Technol. **51**, 7318–7325 (2017).

[121] D. G. Angelescu and D. Caragheorgheopol., "Influence of the shell thickness and charge distribution on the effective interaction between two like-charged hollow spheres", J. Chem. Phys. **143**, 144902 (2015).

[122] D. G. Angelescu, R. Bruinsma, and P. Linse, "Monte Carlo simulations of polyelectrolytes inside viral capsids", Phys. Rev. E **73**, 041921 (2006).

[123] M. E. Brito, M. O. Alziyadi, G. Nägele, and A. R. Denton, "Effective electrostatic interactions in suspensions of surface-charged ionic microgels", to be submitted.

[124] R. Roa, E. K. Zholkovskiy, and G. Nägele, "Ultrafiltration modeling of non-ionic microgels", Soft Matter **11**, 4106–4122 (2015).

[125] C. Beenakker and P. Mazur, "Diffusion of spheres in a concentrated suspension II", Physica A **126**, 349–370 (1984).

[126] U. Genz and R. Klein, "Collective diffusion of charged spheres in the presence of hydrodynamic interaction", Physica A **171**, 26–42 (1991).

# Appendix A

# Pairwise-additive (PA) approximation of short-time dynamic properties

The PA approximation of short-time diffusion properties used in this thesis is based on a truncated cluster expansion of the $N$-particle translational mobility matrix of colloidal spheres, with three-body and higher-order cluster contributions disregarded. The $N$-spheres hydrodynamic mobility tensors $\boldsymbol{\mu}_{jk}(\mathbf{X})$ are approximated here by [97]

$$\frac{1}{\mu_0}\boldsymbol{\mu}_{jk}(\mathbf{X})\Big|_{\mathrm{PA}} = \delta_{kj}\left[\mathbb{1} + \sum_{l\neq j}^{N} \mathbf{a}_{11}(\mathbf{r}_j - \mathbf{r}_l)\right] + (1-\delta_{jk})\,\mathbf{a}_{12}(\mathbf{r}_j - \mathbf{r}_k), \tag{A.1}$$

where $\mathbb{1}$ is the $3 \times 3$ unit matrix and $\mathbf{r}_j$ the center position of the colloidal sphere $j$. The two-particle tensors $\mathbf{a}_{11}$ and $\mathbf{a}_{12}$ describe, respectively, the hydrodynamic self-interaction of a sphere through flow reflections by other ones, and the interaction induced by the motion of a second particle. The axial symmetry of the two-sphere problem allows to split these tensors into longitudinal and transverse components,

$$\delta_{ij}\mathbb{1} + \mathbf{a}_{ij}(\mathbf{r}) = x_{ij}\hat{\mathbf{r}}\hat{\mathbf{r}} + y_{ij}(r)[\mathbb{1} - \hat{\mathbf{r}}\hat{\mathbf{r}}], \tag{A.2}$$

where $\hat{\mathbf{r}} = \mathbf{r}/r$. The mobility components $x_{ij}(r)$ and $y_{ij}(r)$ can be calculated recursively, leading to a power series in the reduced inverse pair distance $\sigma/r$.

Combining Eq. (A.1) with Eq. (5.41) and using the fact that we can write the equilibrium ensemble average of a function $f(r)$ in the thermodynamic limit as

$$\langle f(\mathbf{r})\rangle = \lim_{\langle N\rangle, V\to\infty} \frac{1}{V}\int_V d\mathbf{r}\, g(r) f(\mathbf{r}), \tag{A.3}$$

one obtains an expression for the short-time self-diffusion coefficient, $d_{\mathrm{s}}$, given in PA by

$$\left.\frac{d_{\mathrm{S}}}{d_0}\right|_{\mathrm{PA}} = 1 + 8\phi \int_1^\infty dx\, x^2\, g(r)[x_{11}(x) + 2y_{11}(x) - 3], \tag{A.4}$$

where $x = r/\sigma$. The distinct contribution, $H_{\mathrm{d}}$, to $H(q)$ is obtained in PA by

$$\begin{aligned} H_{\mathrm{d}}(y)|_{\mathrm{PA}} = &-\ 15\phi\frac{j_1(y)}{y} + 18\phi \int_1^\infty dx\, x\, \left[g(x) - 1\right] \times \left[j_0(xy) - \frac{j_1(xy)}{xy} + \frac{j_2(xy)}{6x^2}\right] \\ &+\ 24\phi \int_1^\infty dx\, x^2\, g(x)\, \tilde{y}_{12}(x)\, j_0(xy) \\ &+\ 24\phi \int_1^\infty dx\, x^2\, g(x)[\tilde{x}_{12}(x) - \tilde{y}_{12}(x)] \times \left[\frac{j_1(xy)}{xy} - j_2(xy)\right], \end{aligned} \tag{A.5}$$

where $y = q\sigma$ is the diameter-scaled wavenumber, and $j_n$ is the spherical Bessel function of first kind and order $n$. The short-range mobility parts, labeled here by a tilde, are

$$\tilde{x}_{12}(x) = x_{12}(x) - \frac{3}{4}x^{-1} + \frac{1}{8}x^{-3}, \tag{A.6}$$

$$\tilde{y}_{12}(x) = y_{12}(x) - \frac{3}{8}x^{-1} - \frac{1}{16}x^{-3}, \tag{A.7}$$

where the far-field terms up to the dipolar (Rotne-Prager) level have been subtracted.

# Appendix B

# Beenakker-Mazur (BM) method of short-time dynamic properties

In the zeroth-order BM-scheme expression for $H(q) = d_{\mathrm{s}}/d_0 + H_{\mathrm{d}}(q)$ used in thesis, the self-part is given by the microstructure-independent part [97],

$$\left.\frac{d_{\mathrm{s}}(\phi)}{d_0}\right|_{\mathrm{BM}} = \frac{2}{\pi}\int_0^\infty dy \left[\frac{\sin(y)}{y}\right]^2 \frac{1}{1+\phi\, S_{\gamma 0}(y)}. \tag{B.1}$$

The structure-dependent distinct part, $H_{\mathrm{d}}(q)$, is given by

$$H^{\mathrm{d}}(y)\Big|_{\mathrm{BM}} = \frac{3}{2\pi}\int_0^\infty dy' \left[\frac{\sin(y')}{y'}\right]^2 \frac{1}{1+\phi\, S_{\gamma 0}(y')} \times \int_{-1}^{1} d\mu\, (1-\mu^2)[S(|\mathbf{q}-\mathbf{q}'|)-1], \tag{B.2}$$

where $S(q)$ is the structure factor, $\mu$ the cosine of the angle between $\mathbf{q}$ and $\mathbf{q}'$, $y = q\sigma$ and $y' = q'\sigma$. The function $S_{\gamma 0}(y')$ consists of an infinite sum of wavenumber-dependent contributions depending on the volume fraction $\phi$, as well as on the scalar coefficients $\gamma_0^{(n)}$, with $n \in \{1, 2, 3, ...\}$. The explicit expressions of $S_{\gamma 0}(x)$ and $\gamma_0^{(n)}$ are given in Refs. [125, 126].

The employed modified BM expression for $\eta_\infty$ reads

$$\frac{\eta_\infty}{\eta_0} = \frac{1}{\lambda_0 + \lambda_2}\,, \tag{B.3}$$

where

$$\lambda_0 = \left[1 + \frac{5}{2}\phi\, \tilde{\gamma}_0^{(2)}\right]^{-1} = 1 - \frac{5}{2}\phi + \frac{215}{168}\phi^2 + \mathcal{O}(\phi^3), \tag{B.4}$$

$$\lambda_2 = \frac{30\phi}{4\pi}\left[\lambda_0\, \tilde{\gamma}_0^{(2)}\right]^2 \int_0^\infty dy\, \frac{j_1^2(y/2)[S(y/\sigma)-1]}{1+\phi\, S_{\gamma 0}(y/2)} \tag{B.5}$$

and

$$\tilde{\gamma}_0^{(2)} = \frac{\gamma_0^{(2)}}{n_\mathrm{m}} = 1 + \frac{167}{84}\phi + \mathcal{O}(\phi^2)\,. \tag{B.6}$$

# Appendix C

# Suspension pressure using RLRT

We summarize here how the suspension pressure, $p$, in a suspension of impermeable charged macroions of hard-core diameter $\sigma = 2a$ is calculated in RLRT method. As explained in the context of Eq. (5.9), for pairwise additive effective potential energy, $p$ is obtained from

$$\beta p = \beta p_{\text{free}} + n_{\text{m}} - \frac{2\pi}{3} n_{\text{m}}^2 \int_0^\infty dr r^3 g(r) \frac{\partial \beta u_{\text{eff}}(r)}{\partial r} + 2\pi n_{\text{m}}^3 \int_0^\infty dr r^2 g(r) \frac{\partial \beta u_{\text{eff}}(r)}{\partial n_{\text{m}}}. \tag{C.1}$$

with renormalized effective pair potential

$$\beta u_{\text{eff}}(r) = \begin{cases} \infty, & 0 \leq r \leq \sigma \\ \lambda_{\text{B}} Z_{\text{eff}}^2 \left( \frac{\exp(\kappa_{\text{eff}} a)}{1+\kappa_{\text{eff}} a} \right)^2 \frac{\exp(\kappa_{\text{eff}} r)}{r}, & r > \sigma \end{cases} \tag{C.2}$$

where the renormalized $\kappa_{\text{eff}}$ and $Z_{\text{eff}}$ are calculated using RLRT (see section 3.3). Here, $p_{\text{free}}$ is the pressure contribution due to free, i.e. not surface-condensed, microions related to the volume energy pressure. By accounting for charge-renormalization, $p_{\text{free}}$ is given in RLRT by

$$\beta p_{\text{free}} = \tilde{n}_+ + \tilde{n}_- - \frac{Z_{\text{eff}}(\tilde{n}_+ - \tilde{n}_-)\kappa_{\text{eff}}\lambda_{\text{B}}}{4[1 + \kappa_{\text{eff}}(a + \delta)]^2}. \tag{C.3}$$

where $\delta$ characterizes the thickness of the shell of quasi-condensed counterions and $\tilde{n}_\pm = n_\pm/(1 - \phi)$. The remaining three terms in Eq. (C.1) correspond to the three additive parts conforming the macroion pressure contribution, $p_{\text{m}}$,

$$\beta p_{\text{m}} = n_{\text{m}} + \beta p_{\text{m}}^{(1)} + \beta p_{\text{m}}^{(2)}. \tag{C.4}$$

The first term in Eq. (C.4) is the ideal-gas contribution. The second term is

$$\begin{aligned} \beta p_{\mathrm{m}}^{(1)} &= -\frac{2\pi}{3} n_{\mathrm{m}}^2 \int_0^\infty dr r^3 g(r) \frac{\partial \beta u_{\mathrm{eff}}(r)}{\partial r} \\ &= 4\pi n_{\mathrm{m}} \phi\, g(\sigma^+) + \frac{2\pi}{3} n_{\mathrm{m}}^2 \int_{\sigma^+}^\infty dr\, r^2 g(r) \beta u_{\mathrm{eff}}(r) (\kappa_{\mathrm{eff}}\, r + 1) \end{aligned} \tag{C.5}$$

where, in the second equality, we have singled-out the contribution due to the contact value of $g(r)$. The concentration derivative of $u_{\mathrm{eff}}$ in the third contribution of Eq. (C.4) is taken by accounting only for the variations of $u_{\mathrm{eff}}$ with $n_{\mathrm{m}}$ that are relevant thermodynamically, disregarding the natural $n_{\mathrm{m}}$-dependence of the renormalized interaction parameters $\kappa_{\mathrm{eff}}$ and $Z_{\mathrm{eff}}$ arising from the charge-renormalization process. These derivatives should be also taken keeping the thermodynamic variables constant according to the statistical ensemble chosen for the calculation. Furthermore, the electroneutrality condition must be maintained. Using for simplicity a (full) canonical-ensemble description in conjunction with the electroneutrality condition $Z_{\mathrm{eff}} N_{\mathrm{m}} = N_+^{\mathrm{eff}} - N_-^{\mathrm{eff}}$, where $N_\pm^{\mathrm{eff}}$ are the number of freely-moving microions, we find

$$\frac{\partial Z_{\mathrm{eff}}}{\partial \phi} = 0. \tag{C.6}$$

The only concentration dependence of the effective pair potential arises here from the effective screening parameter $\kappa_{\mathrm{eff}}$. Within RLRT, the latter is given by

$$\kappa_{\mathrm{eff}}^2 = 4\pi\lambda_{\mathrm{B}} \left( \frac{N_+^{\mathrm{eff}}}{V(1-\phi_{\mathrm{eff}})} + \frac{N_-^{\mathrm{eff}}}{V(1-\phi_{\mathrm{eff}})} \right), \tag{C.7}$$

where $\phi_{\mathrm{eff}} = \phi(1+\delta/a)^3$. Assuming $\delta$ to be independent of $n_{\mathrm{m}}$, it follows

$$\begin{aligned} \beta p_{\mathrm{m}}^{(2)} &= 2\pi n_{\mathrm{m}}^3 \int_{\sigma^+}^\infty dr\, r^2 g(r) \frac{\partial \beta u_{\mathrm{eff}}}{\partial n_{\mathrm{m}}} \\ &= \frac{8\pi^2}{3} n_{\mathrm{m}}^3 a^3 \int_{\sigma^+}^\infty dr\, r^2 g(r) \beta u_{\mathrm{eff}}(r) \gamma \left( \alpha - \frac{r}{a} \right), \end{aligned} \tag{C.8}$$

where

$$\alpha = \frac{2\kappa_{\mathrm{eff}} a}{1+\kappa_{\mathrm{eff}} a} \tag{C.9}$$

$$\gamma = \frac{\partial \kappa_{\mathrm{eff}} a}{\partial \phi} = \frac{\kappa_{\mathrm{eff}} a}{2\phi\left(1-\phi(1+\delta/\sigma)^3\right)} \tag{C.10}$$

with $x = \kappa_{\text{eff}} a$.

The pressure results for a charge-renormalized system, computed using Eq. (C.4), are in total agreement with results utilizing both the first-order thermodynamic perturbation expansion (Gibbs-Bogoliubov) and the OCM-MC results from Ref. [67].

# List of Abbreviations

| | |
|---|---|
| BM | Beenakker and Mazur |
| CM | Cell Model |
| DFT | Density Functional Theory |
| DH | Debye-Hückel |
| DLVO | Derjaguin-Landau-Verwey-Overbeek |
| EHS | Effective Hard Spheres |
| EPC | Extrapolated Point Charge |
| EPC edge | EPC and linearization with respect to the edge potential |
| EPC mean | EPC and linearization with respect to the mean potential |
| GSE | Generalized Smoluchowski Equation |
| HIs | Hydrodynamic Interactions |
| HNC | Hypernetted Chain (Closure) |
| HS/hs | Hard Spheres |
| JA | Jellium Approximation |

| | |
|---|---|
| KB | Kirkwood-Buff |
| LRT | Linear Response Theory |
| MC | Monte Carlo |
| MCT | Mode-Coupling Theory |
| MSA | Mean Spherical Approximation (Closure) |
| OZ | Ornstein-Zernike |
| PA | Pairwise-Additive approximation |
| PB | Poisson-Boltzmann |
| PBCM | Poisson-Boltzmann Cell Model |
| PM | Primitive Model |
| PY | Percus-Yevick (Closure) |
| rdf | radial distribution function |
| RJM | Renormalized Jellium Model |
| RLRT | Renormalized Linear Response Theory |
| RMSA | Rescaled Mean Spherical Approximation (Closure) |
| RPA | Random Phase Approximation (Closure) |
| RY | Rogers-Young (Mixed Closure) |
| SC | Surface Charge |
| SC edge | SC and linearization with respect to the edge potential |

| | |
|---|---|
| SC mean | SC and linearization with respect to the mean potential |
| SDHA | Shifted Debye-Hückel Approximation |
| TPT | Thermodynamic Perturbation Theory |

# Acknowledgments

First of all, I would like to thank Gerhard Nägele for the supervision and support. His broad knowledge and thorough working have been a valuable influence on my development. I truly appreciate his dedication. In particular, I specially value his willingness and constant predisposition to help me every time I needed it. I want to thank Jan Dhont for the opportunities and tools that allowed me to develop and grow scientifically and professionally. I am deeply grateful to Alan Denton for the collaborations that we have engaged. I appreciate his openness and his good and positive predisposition. His work has constituted an important base for the thesis, but, most importantly, it has been inspiring. I would also like to express my gratitude to Jürgen Horbach for having accepted to review the thesis.

Many thanks to every single one of the current and former members ICS-3/IBI-4 for creating a nice and friendly atmosphere in the working place. I acknowledge their help along this period. I thank the student crew for the important peer support in this process. And a special thank to Emmanuel and Olivera, from whom I have learnt a lot as colleagues and, especially, as friends.

I thank to my family and friends, who have been always there despite the distance. And finally, from the bottom of my heart, I thank Gastón for being by my side in this journey. *Muchas gracias por acompañarme y por haber estado siempre.*

# Eidesstattliche Versicherung

Ich versichere an Eides Statt, dass die Dissertation von mir selbstständig und ohne unzulässige fremde Hilfe unter Beachtung der “Grundsätze zur Sicherung guter wissenschaftlicher Praxis an der Heinrich-Heine-Universität Düsseldorf” erstellt worden ist.
Des Weiteren wurde die Dissertation in der vorgelegten oder in ähnlicher Form noch bei keiner anderen Institution eingereicht und ich habe bisher keine erfolglosen Promotionsversuche unternommen.

Düsseldorf, den 10.11.2020

Mariano E. Brito